

Developing a multiscale optical interrogation of interneuron dynamics in the rodent sensory cortex

Dissertation zum Erlangen des Grades Doktor der Naturwissenschaft

Am Fachbereich Biologie der Johannes-Gutenberg-Universität in Mainz



JOHANNES GUTENBERG
UNIVERSITÄT MAINZ

Vorgelegt von Pierre-Hugues Prouvot geboren den 12 Juli 1989 in Paris, Frankreich

Mainz 2023

Dekanat:

Berichterstatter 1:

Berichterstatter 2:

Tag der mündlichen Prüfung: 8. mai 2023

Declaration

I hereby declare that this thesis is my original work and that it has not been previously submitted to any other German or foreign university or comparable institution for the conferral of an academic degree.

I hereby declare that I have not unsuccessfully ended another doctoral or equivalent program in the subject area of the current doctoral program.

I hereby declare that I wrote the dissertation submitted without any unauthorised external assistance and used only sources acknowledged in the work. All the textual passages, which are appropriated verbatim or paraphrased from published and unpublished texts, as well as all information obtained from oral resources are duly indicated and listed in accordance with bibliographical rules. In carrying out research, I complied with the rules of standard scientific practice as formulated in the statutes of Johannes Gutenberg University Mainz to ensure standard scientific practice.

I am aware that an untruthful declaration will have legal consequences.

Lausanne 22/11/22 Pierre-Hugues Prouvot

Place, Date, Name



Signature

Zusammenfassung

Sensory processing in the cortex is dependent on the intricacies of the columnar microarchitecture as well as the local excitatory-inhibitory balance itself influenced by the global arousal state of the brain. Fast spiking cortical interneurons expressing Parvalbumin occupy a central position in this information processing. We established and employed optogenetics, calcium imaging and electrophysiological recording techniques to link the global arousal state with very local sensory responses in the barrel cortex. This with the secondary objective of setting the groundwork for minimally invasive all optical physiology. We then used these techniques to more precisely focus on the impact of Parvalbumin interneurons on sensory processing in the barrel cortex. In a first phase we employed optical calcium record in combination with Local Field Potential recordings to compare sensory responses between optogenetic and sensory stimulation in different conditions of anesthesia. We found that calcium fiber photometry is a reliable proxy for electrical activity and that panneuronal optogenetic stimulation results in cortical activation comparable to peripheric stimulation. We showed that consistent with previous data in the visual cortex the primary sensory cortex of the forepaw responds differently under deep (1.5%) isoflurane or under medetomidine anesthesia. Presenting all or none slow waves in the former and individual response to repetitive stimuli in the latter. We then investigated the role of Parvalbumin interneurons in sensory processing in the barrel cortex using a combination of in vivo multi electrode recordings and optogenetics. We established specific expression of Archaeorhodopsin and Channelrhodopsin 2 in PV interneurons. We found that inhibition of PV interneurons upon sensory stimulation enhances the neuronal response maximally when concomitant with the first 20ms post stimulation. Enhancing PV activity yielded the opposite results by reducing sensory evoked neuronal activity. Prolonging the inhibition yielded a secondary rebound response peaking around 40ms post stimuli. Optogenetic modulation of PV neurons induced a change in multi-unit activity but not LFP in neighboring barrels while not significantly affecting the principal barrel. This indicated an unexpectedly strong lateral inhibition produced by PV interneurons. We developed a model to estimate the number of neurons efficiently modulated by optogenetics and applied it in the barrel cortex and the olfactory bulb with satisfactory results. We used Intrinsic Optical Imaging to identify individual barrel position first to measure their changes in a PRG-1 KO mouse model and found a significant reduction in barrel size. Then we used the same technique to significantly improve the precision of targeting of virus injections. We achieved a proof of principle single barrel

targeting of opsins. We then established a general method for two-photon calcium imaging in the barrel cortex of anesthetized mice. Having failed to record sensory evoked activity reliably we established a complete protocol for recordings of sensory evoked activity in awake headfixed animals on an air-cushioned spherical treadmill. We established a protocol for identification of individual barrel using epifluorescence imaging of Gcamp fluorescence changes allowing us to achieve recording and stimulation in specifically targeted barrels. Finally, we established recordings of whisker evoked activity in awake behaving mice opening the possibility of transversal recordings and potentially awake all optical physiology.

Die sensorische Verarbeitung im Kortex hängt von den Feinheiten der säulenförmigen Mikroarchitektur sowie dem lokalen Erregungs-Hemmungs-Gleichgewicht ab, das selbst durch den globalen Erregungszustand des Gehirns beeinflusst wird. Schnell feuernde kortikale Interneurone, die Parvalbumin exprimieren, besitzen eine zentrale Position in diesem Informationsverarbeitungsnetzwerk. Hier haben wir optische und elektrophysiologische Aufnahmetechniken etabliert und kombiniert eingesetzt, um den globalen Erregungszustand mit sehr lokalen sensorischen Reaktionen im Barrelkortex zu vergleichen. Diese Methoden setzten wir als Grundsteine von eine minimal invasive optik-exklusive Physiologie ein. In einer ersten Phase haben wir eine optische Kalziumaufzeichnung in Kombination mit lokalen Feldpotentialaufzeichnungen (LFP) verwendet, um sensorische Aktivierung zwischen optogenetischer und sensorischer Stimulation unter verschiedenen Anästhesiebedingungen zu vergleichen. Wir fanden heraus, dass die Kalziumfaserphotometrie ein zuverlässiger Proxy für die elektrische Aktivität ist und dass die panneuronale optogenetische Stimulation zu einer kortikalen Aktivierung führt, die mit der peripheren Stimulation vergleichbar ist. Wir haben gezeigt, dass in Übereinstimmung mit früheren Daten im visuellen Kortex der primäre sensorische Kortex der Vorderpfote unter tiefer (1,5 %) Isofluran- oder unter MedetomidinAnästhesie unterschiedlich reagiert.

Unter hoher Isoflurananästhesie beobachteten wir langsame Wellen, während unter Medetomidin individuelle Reaktionen auf sich wiederholende Reize sichtbar waren.

Anschließend untersuchten wir die Rolle von Parvalbumin-Interneuronen bei der sensorischen Verarbeitung im Barrelkortex unter Verwendung einer Kombination aus in-vivo Mehrelektrodenaufzeichnungen und Optogenetik. Wir fanden heraus, dass die Hemmung von PV-Interneuronen nach sensorischer Stimulation die neuronale Reaktion maximal

verstärkt, wenn sie mit den ersten 20ms nach der Stimulation einhergeht. Die Steigerung der PV-Aktivität führte zu gegenteiligen Ergebnissen, indem die sensorisch evozierte neuronale Aktivität reduziert wurde. Die optogenetische Modulation von PV-Neuronen induzierte eine Änderung der Multi-Unit-Aktivität, aber nicht im LFP von benachbarten Barreln. Das Hauptbarrel wurde ebenfalls nicht signifikant durch optogenetische Stimulation beeinflusst. Jedoch zeigte sich eine unerwartet starke seitliche Hemmung, die durch PV-Interneuronen erzeugt wird. Wir entwickelten und setzten ein Modell der Menge Neuronen bei Optogenetik effizient betroffen ein. Dieses Modell setzten wir dann im Barrel Kortex und Riechkolben mit befriedigenden Ergebnissen ein. Wir verwendeten daraufhin Intrinsic Optical Imaging, um zunächst die Position einzelner Barrel zu identifizieren. Wir stellten fest, dass in einem PRG-1 KOMausmodell die Barrelgröße significant verringert ist. Dann verwandten wir dieselbe Technik und erreichten ein Proof-of-Principle-Single-Barrel-Targeting mit Opsinen. Wir etablierten dann eine allgemeine Methode für die Zwei-Photonen-Kalzium-Bildgebung im Barrelkortex von anästhesierten Mäusen. Dazu haben wir ein Protokoll zur Identifizierung einzelner Barrel mithilfe der Epifluoreszenz-Bildgebung von Gcamp-Fluoreszenzänderungen erstellt. Nachdem es uns allerdings nicht gelungen war, die sensorisch evozierte Aktivität zuverlässig in anästhesierten Tieren aufzuzeichnen, haben wir ein vollständiges Protokoll für die Aufzeichnung der sensorisch evozierten Aktivität bei wachen, kopffixierten Mäusen auf einem luftgepolsterten Styroporball erstellt. Schließlich haben wir Aufzeichnungen der durch Schnurrhaare hervorgerufenen Aktivität bei wachen verhaltenden Mäusen erstellt, was generell die Möglichkeit transversaler Aufzeichnungen eröffnet.

Table des matières

Zusammenfassung	4
Foreword.....	12
Introduction	14
Main Question	15
Outline of the research project	16
Hypotheses	16
Methodological approach	17
All optical approach to physiology.....	17
Main results	18
The mouse somatosensory cortex.....	19
Anatomy of the barrel cortex.....	19
Physiology of the barrel cortex.....	20
The whisker field.....	21
Thalamocortical projections	22
Intracortical connectivity.....	22
Cortico-cortical projections	23
Subcortical projections	23
General anesthesia	25
Anesthesia modulates the resting state of the brain.....	26
Drug choice depending on experimental context	27
Functional rhythms in the brain.....	31
Neuromodulation of brain state	33
Sleep and anesthesia	34
Inhibition in the cortex	34
Two-Photon laser scanning microscopy	40
Basic principles	40
Calcium imaging	45
Acquisition of fluorescent signals	49
Current state of the field	51
History of electrophysiology	52
Experimental stimulation of neuronal activity	53
Optical physiology.....	54

Electrophysiology.....	58
Viral transduction of neurons.	59
Materials and methods.....	61
Mouse line and viruses	61
Mouse lines for optogenetics and electrophysiology	61
Viral transduction vectors.....	62
Surgical preparations	62
Virus injection	62
Acute imaging preparations.....	64
Chronic imaging preparations	65
Histology	66
Immunohistochemistry	66
Quantifications of expressing neurons	66
Electrophysiology.....	67
Multi electrode array recordings	67
Single channel field potential recordings	72
Patch Clamp recordings of photostimulation	72
Optogenetics	73
Light sources and modulation	73
Controls for optogenetic stimulation.....	75
Stimulation design.....	75
Computational modeling of light distribution in brain tissue.....	76
Data Evaluation and Statistics	80
Calcium imaging	80
Fiber photometry	80
Anesthetized two-photon recordings.....	82
Intrinsic Optical Imaging.....	82
Awake recordings	84
Animal habituation	84
Imaging data analysis	84
Results	86
Study 1: Local field potential correlates of fiber photometry during sensory stimulation	86
Optic-fiber based recordings are suitable for recording of slow oscillation associated calcium waves.....	86

Electrical dynamics underlying calcium changes.....	89
Panneuronal optogenetic stimulation presents similar properties to sensory stimulation in the somatosensory cortex	89
Optical artifacts in optical recordings.....	95
Study 2: Optogenetic activation and inhibition of Parvalbumin positive interneurons in the barrel cortex.....	98
Combining Depth-Resolved Multichannel Recordings and Optogenetic Manipulation of PV Interneurons in Mouse Barrel Cortex	98
Interneuron-Specific Expression of ArchT in Layers II/III and V in Mouse Barrel Cortex..	101
Temporal Profile of Transient PV-Mediated Disinhibition	103
Spatial Profile of Transient PV Inhibition	107
Inhibiting PV Interneurons Causes Broad-Spectrum Hyperexcitability	109
Spatial Profile of Transient PV Inhibition	113
Effect of Activation of PV Interneurons on Sensory-Evoked Response	117
Modelization of efficient optogenetic modulation	120
A Small Number of Inhibited Interneurons Exert Significant Influence on the Cortical Representation of Sensory Stimuli.....	122
Study 3: Efficient optogenetic inhibition of spiking activity of ArchT-expressing newborn granule neurons in the olfactory bulb	127
Evaluation of the number of inhibited newborn neurons	128
Estimating the number of optogenetically silenced newborn neurons.....	130
Study 4: Mesoscale imaging of the whisker field	131
Using Intrinsic Optical Imaging to target virus expression to a single barrel.....	132
Two-photon calcium imaging under anesthesia	135
Implementation of two-photon calcium imaging	135
Neuropil signal is an indicator of global brain state.....	141
Visually evoked activity in awake recordings	144
The recording system	144
Implantation surgery for chronic imaging.....	146
Recording of whisker evoked activity in the primary barrel field.....	150
Discussion.....	155
Technical implementation of two-photon microscopy	155
Animal consciousness	157
anesthesia and brain states.....	157
Awake recordings	158

Technical considerations into the design of a two-photon microscope	159
Microscope	161
Accessories	163
Optogenetics	163
Possible improvements to two-photon microscopy systems	163
Upstream labelling of data and mechanical states	164
Future proofing computer interfaces	166
Slow wave activity in the context of largescale networks	167
Advantages and drawbacks of awake experiments	168
Physiological state	168
Movement artifacts	169
Ethical considerations	170
Parvalbumin interneurons show unexpected effects on local networks	171
Lateral effects	172
Sensory modulation	172
Other types of interneurons	173
Excitation-inhibition balance	173
Towards a better understanding of optogenetic modulation	175
The kubelka-munk approach	175
Assessing the Scope of Optogenetic Network Modulation	175
More comprehensive modelizations	176
Prospective re-analysis the data	177
Outlook	182
All optical physiology	182
Optogenetics	182
Two-photon calcium imaging	183
Brain states in new and old datasets	186
Supplementary analysis of imaging datasets	186
Parvalbumin interneurons show unexpected effects on local networks	187
Pathophysiological considerations epilepsy and schizophrenia	189
Towards a better understanding of optogenetic modulation	190
Quantification of optogenetic stimulation in the olfactory bulb	191
More comprehensive approaches	191
Prospective re-analysis of this data set	193

The nature of the fiber photometry signal	194
Current limitations of GECIs.....	196
Genetically encoded neurotransmitter sensors	197
APPENDIX	199
References	203
Glossary:.....	244
List of figures	246
Aknowledgments.....	249

Foreword

I would invite the reader of this thesis to consider that this work was started from scratch in an empty laboratory. This situation gave us considerable freedom over our experimental design but also required us to implement almost any new method we wished to use from the ground up using information available in the literature and in neighboring teams. The laboratory became in 2017 the Mainz Animal Imaging Center (MAIC) part of the Leibniz Institute for Resilience (LIR) research and the technical development presented here is now used on the platform. Hence, we will consider the details of each technical paradigm we implemented in the hope that it will help anyone wanting to use these methods in the future.

The work presented has been in large part detailed in four publications:

Schwalm M, Schmid F, Wachsmuth L, Backhaus H, Kronfeld A, Aedo Jury F, **Prouvot PH**, Fois C, Albers F, van Alst T, Faber C, Stroh A. *Cortex-wide BOLD fMRI activity reflects locally-recorded slow oscillation-associated calcium waves*. *Elife*. 2017 Sep 15;6:e27602. doi: 10.7554/eLife.27602. PMID: 28914607; PMCID: PMC5658067.

Schmid F, Wachsmuth L, Schwalm M, **Prouvot PH**, Jubal ER, Fois C, Pramanik G, Zimmer C, Faber C, Stroh A. *Assessing sensory versus optogenetic network activation by combining (o)fMRI with optical Ca²⁺ recordings*. *J Cereb Blood Flow Metab*. 2016 Nov;36(11):1885-1900. doi: 10.1177/0271678X15619428. Epub 2015 Nov 30. PMID: 26661247; PMCID: PMC5094300.

Cheng J, Sahani S, Hausrat TJ, Yang JW, Ji H, Schmarowski N, Endle H, Liu X, Li Y, Böttche R, Radyushkin K, Maric HM, Hoerder-Suabedissen A, Molnár Z, **Prouvot PH**, Trimbuch T, Ninnemann O, Huai J, Fan W, Visentin B, Sabbadini R, Strømgaard K, Stroh A, Luhmann HJ, Kneussel M, Nitsch R, Vogt J. *Precise Somatotopic Thalamocortical Axon Guidance Depends on LPA-Mediated PRG-2/Radixin Signaling*. *Neuron*. 2016 Oct 5;92(1):126-142. doi: 10.1016/j.neuron.2016.08.035. Epub 2016 Sep 15. PMID: 27641493; PMCID: PMC5065528.

Yang JW, **Prouvot PH**, Reyes-Puerta V, Stüttgen MC, Stroh A, Luhmann HJ. *Optogenetic Modulation of a Minor Fraction of Parvalbumin-Positive Interneurons Specifically Affects Spatiotemporal Dynamics of Spontaneous and Sensory-Evoked Activity in Mouse*

Somatosensory Cortex in Vivo. Cereb Cortex. 2017 Dec 1;27(12):5784-5803. doi: 10.1093/cercor/bhx261. PMID: 29040472; PMCID: PMC5939210. **(co-first authorship)**

As well as two technical book chapters:

Fois C, **Prouvot PH**, Stroh A. *A roadmap to applying optogenetics in neuroscience*. Methods Mol Biol. 2014;1148:129-47. doi: 10.1007/978-1-4939-0470-9_9. PMID: 24718799.

Yang JW., **Prouvot PH.**, Stroh A., Luhmann H.J. (2018) *Combining Optogenetics with MEA, Depth-Resolved LFPs and Assessing the Scope of Optogenetic Network Modulation*. In: Stroh A. (eds) *Optogenetics: A Roadmap*. Neuromethods, vol 133. Humana Press, New York, NY. 10.1007/978-1-4939-7417-7_8 **(co-first authorship)**

(Schmid, Wachsmuth, Schwalm, P.-H. Prouvot, et al. 2016; Schwalm et al. 2017a; J. W. Yang et al. 2017) the data presented here is partially from experiments we performed for these publications.

Introduction

My work will be presented here in four studies following a thematic and chronological order. Our goal was to start with simpler methodological approaches to optical physiology in the sensory cortices, all the while we established more complex methods in parallel. As a result, my data and methods increase in complexity as we move across scales.

I will first present the data we acquired at the largest scale using fiber photometry and Local Field Potentials recordings (LFPs) (Study 1). Next, I will present the data acquired using the same optical method with a more complex electrical recording: our combination of optogenetics with in vivo multi electrode recordings to investigate sensory processing more in depth. We will concentrate on the role of Parvalbumin positive (PV) interneuron inhibition in the barrel cortex. I will also use the opportunity to evaluate the extent of optogenetic modulation in vivo. This project concentrates more on a physiological question than on technical development, therefore a large part of this introduction will concentrate on Study 2.

Using the insight into optogenetic modulation we gained, I used the same approach in another project: I designed a more in-depth protocol to understand the extent of optogenetic modulation in newborn neurons in the olfactory bulb (Study 3).

Finally, in parallel to these different projects we worked our way through developing and improving methodologies for two-photon microscopy in anesthetized and awake mice (Study 4). The introduction will concentrate on the physiology of the barrel cortex first and then the optical recording techniques necessary for all optical physiology, namely two-photon imaging and optogenetics.

Study 1: I will present data from experiments we performed directly for Schmid et al. 2017 and 2016 in a collaborative study combining functional Magnetic Resonance Imaging of Blood Oxygenation Level Dependent signal (BOLD fMRI) and calcium fiber photometry as a preliminary study informing our later work. These publications concentrated on the fMRI correlates of sensory activity under general anesthesia. I provided Local field potential recordings as a complementary readout to fiber photometry during sensory and optical stimulations as well as data analysis of LFP and calcium signal.

Study 2: We then present most data from a collaborative publication we co-authored with Dr. [REDACTED] from Ag. [REDACTED]. Our main question for this work was: How is sensory

evoked activity shaped by Parvalbumin Interneurons in the somatosensory cortex? We implemented a combination of multichannel recording with optogenetics in vivo and showed that a small number of Parvalbumin interneurons can exert their inhibition more powerfully across barrels than locally. I developed a straightforward approach to evaluate the number of neurons affected by optogenetic modulation. I provided experimental design, virus injections, immunohistochemistry, technical installation, optogenetics modelling and part of the data analysis while Dr █████ provided electrophysiological recordings and analysis.

Study 3: I applied my model of efficient optogenetic modulation to an unpublished study of adult-born neurons migrating from the subventricular zone to the olfactory bulb. This work was done in collaboration with Ag █████ and led by █████ PhD. I provided the experimental design for optogenetics control experiments, technical installation, part of data analysis and modelling of optogenetics stimulation.

Study 4: I will present unpublished data concerning our work surrounding the installation and technical improvements of the two-photon microscopes of our team in the Ag. Stroh, in particular the improvements from initial prototypes of the Trimscope II from LaVision Biotec for in vivo anesthetized recordings and how we implemented awake two-photon calcium imaging of sensory evoked activity. In this perspective we implemented Imaging of Intrinsic signals (IOI) that we used for (Cheng et al., 2016) and epifluorescence imaging for identification of cortical sensory regions. I collaborated with Dr. █████ and Dr. █████ for intrinsic imaging. All other recordings and most technical installation were done by me.

Main Question

Parvalbumin positive interneurons produce a strong local inhibition on somata of pyramidal cells. Deficiencies in PV interneurons are thought to be implicated in sensory impairments in schizophrenia and epilepsy among others. Understanding their role in sensory processing is a step towards a better understanding of these impairments. Given their position in the network, reducing their activation should give rise to a very local disinhibition inducing a large in amplitude but spatially narrow increase in the response amplitude upon sensory (whisker) or optogenetic stimulation. On the opposite, inducing their depolarization would induce a strong local reduction in the response amplitude. Based on previous information on cortical PV

interneurons this would imply a role in suppression of local “noise” to facilitate detection of minor inputs and neuronal computation by making activity sparser.

In order to question this hypothesis, we needed to establish several methods. A method for reading out the activity, a method to manipulate a local population of PV interneurons and a method for identifying the responsive area. We also needed to choose an anesthetic regimen presenting neural activity resembling our physiological conditions of interest.

I will first establish my research questions, then guide the reader through the basic anatomy and physiology of the regions we recorded. I will establish the basics of the anesthetics we will be using and our rationale for choosing them. Then I will explain the basics of the recording and manipulation methods we chose before diving into the experimental details and the results. Finally, I will discuss the significance of our findings and outline leads for future projects.

Outline of the research project

Hypotheses

We started by using Chr2 in the somatosensory region of the forepaw in mice under anesthesia. We wanted to investigate if ChR2 direct activation of all neurons in a small region of S1 is comparable to activity evoked by stimulation of the sensory terminals. We also wanted to compare LFP recordings with calcium fiber photometry signal.

H1: Calcium recordings represent a reliable proxy for electrical activity. H2:
Optogenetic evoked activity resembles sensory evoked activity.

We investigated the role of parvalbumin interneurons in sensory processing. Based on the position of PV interneurons in the barrel cortex microcircuit and limits of opsin expression we expected optogenetic modulation to affect sensory response in the following way:

H1: Inhibition of PV interneurons during sensory processing broadens the cortical response in time.

H2: Direct stimulation of PV interneurons sharpens the cortical response in time.

H3: Parvalbumin positive interneurons mostly affect the barrel their cell body is situated in.

We established two-photon calcium recordings in the sensory cortex:

H1: Surface calcium imaging can be used as reliably as intrinsic optical imaging to identify individual barrels.

H2: Calcium imaging is a reliable readout of electrical activity across scales and the neuropil signal can be assimilated to fiber photometry.

Methodological approach

We first combined electrical readouts of neuronal activity with optogenetics and/or fiber photometry of calcium changes in the somatosensory cortex of rats and mice. This approach was in the context of a combination of fiber photometry with fMRI. We used LFP recordings to evaluate the correlation of calcium events with electrical events when stimulating the nerve terminals electrically or the local network of neurons directly using ChR2. Then we combined optogenetics with multi-channel silicon probes recordings in the barrel cortex. Both these studies required testing for optical artifacts, titration of the stimulation, characterization of exogenous expression of opsins and evaluation of the impact of the optogenetic stimulation.

All optical approach to physiology

We attempted to combine optical readouts of neuronal activity with optical stimulation of neurons at different scales. At the macro-scale this consisted in recording and stimulating through the same fiber. At the microscopic scale this consisted in combining two-photon calcium imaging with sensory stimulation and later optic fiber optogenetics in anesthetized mice. We implemented acute two-photon calcium imaging using OGB1-AM or Gcamp6f and sufficient expression of ArchT-GFP and ChR2-mCherry avoiding cytotoxicity. To identify barrel columns with as low invasivity as possible we implemented Intrinsic Optical Imaging of blood oxygenation and then surface calcium recordings. Using this we achieved precise targeting of opsin expression to single barrels.

Main results

Electrophysiological recordings and optogenetics

We achieved a combination of single electrode recordings with optogenetic stimulation of all neurons. Our results show that optogenetic stimulation can broadly mimic sensory stimulation in anesthetized animals and that it can be used to elicit cortical slow waves or individual sensory response depending on anesthesia. We also showed that the cortical calcium response to electrical stimulation of the paw adapts across repetitive stimulations depending on the stimulation frequency in the same way as the LFP response.

We achieved a combination of multisite silicon probe recordings with specific optogenetic modulation of Parvalbumin expressing interneurons. When applying this method in the context of the barrel cortex we found that parvalbumin positive interneurons exert a strong local and lateral modulation on the sensory response and modulate the intensity of slow waves under anesthesia.

We proposed a simple method to evaluate the number of optogenetically modulated neurons in the context of PV neurons in the Barrel cortex but also in newborn neurons of the olfactory bulb. We showed that a low number of modulated neurons is sufficient to significantly affect the sensory response.

Multi scale optical interrogation of networks

We achieved OGB1-AM based two-photon calcium recordings in the Barrel cortex but we struggled to apply the same method to virus injected mice because of surgical difficulties. We successfully combined fiber photometry of calcium fluorescence and used it to show that the calcium signal closely correlates to the LFP signal during sensory stimulation and slow waves. We successfully identified the loci of individual barrels using Intrinsic Optical Imaging in acute preparations and surface calcium imaging in chronic preparations.

We implanted mice with a glass cranial window in a custom implant and recorded from them up to 4-month post implantation. We achieved chronic two-photon calcium imaging in awake head fixed mice approaching chronic all optical physiology in mice.

The techniques that were available to us and the ones we implemented all provide interesting improvements to spatial and genetic specificity. They also presented unknown parameters because of their novelty. It was immediately interesting to implement them in an animal model that was already well defined to build upon a well-established literature. Our system of choice

was the somatosensory cortex and more specifically the barrel cortex for the main study. I will mostly present the properties of the barrel cortex, but I will mention differences with other sensory cortices we studied here. Fortunately for us most sensory cortices present a mostly conserved canonical columnar structure.

The mouse somatosensory cortex

Anatomy of the barrel cortex

The somatosensory area of the cortex responsible for whisker perception is called the barrel cortex in rodents. This region of the cortex is characterized by a clear somatotopy. In particular where each individual whisker projects to a spatially well-defined region in layer IV (Schiffman et al., 1970; Woolsey & Van der Loos, 1970). These regions, when revealed by cytochrome oxidase staining, are in the shape of small barrels, hence the name barrel cortex. This cortical region has been extensively studied since its discovery in large part because of this characteristic (Van Der Loos & Woolsey, 1973). Even if whiskers are relatively common in mammals well defined barrel cortices as well as whiskers are much more unusual (Fox & Woolsey, 2008). Both happen to be absent in primates which limits the translational aspect of research in the barrel field. However, the interest in this region stems from its well-defined cortical columns and it represents an invaluable tool to understand how sensory information is processed from the sensory organ to the formation of a conscious percept. It is also extremely useful in developmental biology to understand the development of connectivity in the cortex. This columnar structure is reproduced all over the sensory cortices (Douglas & Martin, 1991, 2004; Gilbert & Wiesel, 1983b, 1983a).

Understanding the connectivity in this region can help us understand the general mode of processing of information in the cortex. The structure-function relationship of the barrel cortex is helping guide investigations in less accessible or more complex cortices. Moreover, whiskers are easy to access on the snout of rats and mice and removing one or multiple whiskers to study adaptation is reversible and does not harm the animal. This is critically different from, for example tactile perception in the limbs or with the visual system where mono-ocular isolation is an invasive intervention (Frenkel & Bear, 2004). It is also interesting that organization within a single column is still somatotopic with orientation selectivity encoded in a pinwheel fashion centered more or less in the center of the barrel (Kremer et al., 2011). This part of the cortex is positioned laterally to the midline and between bregma and lambda. It rests caudally within S1 and takes up a large portion of it. It is organized in somatotopic column defined in layer IV

identified by the identification name of the corresponding whisker. This identification system uses letters to define the dorso-ventral row of the whisker and numbers to define the antero-posterior column. Each whisker and barrel are then defined with a letter and a number from A1 to E10 even though these last outlying whiskers are rarely studied for practical reasons, their small size making them hard to stimulate individually. The somatotopic organization exists in other sensory and motor areas albeit less simple to identify.

Physiology of the barrel cortex

Physiologically the barrel cortex like all sensory cortices presents strong short- and long-term adaptation to stimuli. When a whisker is cut, its associated barrel regresses and neighboring barrels increase in size to compensate (Welker et al., 1989). Short term local inhibition between barrels allows for sharpening of sensory stimuli allowing mice to detect weak stimulation of single whiskers (De Kock et al., 2007). Subtle stimulations such as fine textures, small direct deflections, or weak air puffs.

All in all, the barrel cortex is a great tool to isolate cortical columns and study development and organization of cortical columns in detail. In our case specifically the clear vertical and lateral organization fits nicely our combination of perpendicular readouts. Thanks to the easy identification of the columnar structures that are barrels we can investigate a processing unit of the cortex in relative isolation. The cellular organization of the barrel cortex differs across layers. Layer IV in particular, is different from other sensory areas in that it is organized in barrels. Like in other sensory regions this is the main input layer from thalamic regions. The barrels themselves are ovoid and limited to layer IV as revealed by the mitochondrial cytochrome oxidase staining cell bodies are primarily positioned in the septa while the barrels themselves contain mainly local neurites and afferents from the thalamus. This cellular organization makes them lightly visible in the absence of staining. Because the sensory cortex is organized in vertical columns this has repercussions on other layers as the excitatory projections are mainly vertical (Andermann & Moore, 2006; Feldmeyer et al., 2002), as a result the neuropil in layer II/III and V also presents a functional barreloid organization. As a matter of fact the pinwheel organization of direction selectivity present in layer IV is reproduced if slightly shifted in layer II/III (Andermann & Moore, 2006; Kremer et al., 2011). The organization of excitatory and inhibitory neurons across barrels is well known across layers but much less between functional columns and septa.

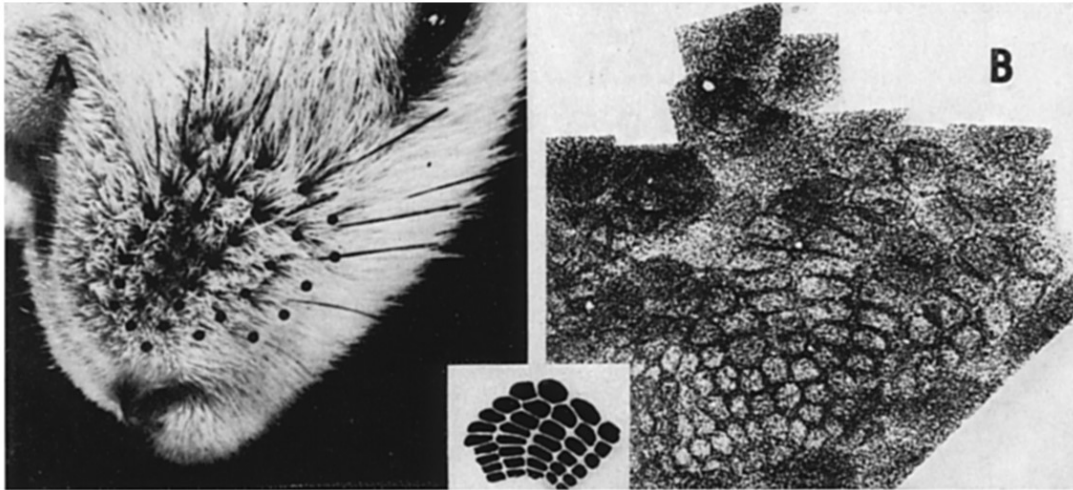


Figure 1-1: Whisker field and barrel cortex A) Photograph of the whisker organization on a mouse's snout. B) Micrograph of cytochrome oxidase staining of the barrel field in tangential sections, The somatotopic organization of barrels is clearly visible (Fig. adapted from Woolsey & Van der Loos, 1970 with permission from Elsevier).

The whisker field

All sensory pathways start with the sensory organ, touch is no exception. Whisker sensation is a part of touch but is organized considerably more specifically than normal fur. The sensory unit of this pathway is the whisker or vibrissae is composed of an elongated hair situated on the snout of the animal. Whiskers are present in a wide variety of mammals and don't always signify the presence of a barrel cortex on the contrary, a barrel cortex always indicates the presence of whiskers. Most rodents possess barrels (Killackey, 1973; Rice, 1985; Rice et al., 1985; Van Der Loos & Woolsey, 1973; Woolsey et al., 1975) as well as other animals in different orders like moles (Catania & Kaas, 1997), wallabies (Waite et al., 1991) or Australian opossum (Lee Weller, 1972). Somewhat surprisingly cats and racoons do not (Rice, 1985; Woolsey et al., 1975), while mustelids like ferrets sometimes do (Mosconi & Rice, 1991). These specialized hairs take their root in specialized follicles formed of concentric membranes and innervated by the so-called superficial vibrissae nerve close to the skin surface and by the deep vibrissae nerve around the capsule. These nerves provide sympathetic, parasympathetic and sensory innervation and terminate in a variety of Merkel, reticular, free and meandering endings along the follicle, the superficial vibrissal nerve (SVN) innervating the superficial part around the skin surface while the deep vibrissal nerve (DVN) innervates the deeper regions of the sheath. The whisker follicles are erectile thanks to the vascular sinus at their basis controlling the rigidity of the sheath (Rice, 1993). The SVN and DVN nerves innervate each a single follicle per fiber, without branching with up to 200 axons per follicle (Woolsey et al., 1975). The infraorbital

nerve carries the whisker innervation until it merges with the other branches of the fifth cranial nerve at the trigeminal ganglion whose projections then innervate the brainstem. Three trigeminal nuclei are innervated by the projections originating from the whiskers all named after the fifth (V) cranial nerve. Nucleus oralis (Vo), Nucleus interpolaris (Vi) and Nucleus caudalis all named after their position within the brainstem. The spatial representation of the whisker field is conserved within these nuclei so well that somatotopic structures called barreltes can be detected by cytochrome oxidase staining along it.

Thalamocortical projections

Neurons from the principalis and interpolaris trigeminal nuclei then respectively project to two nuclei of the somatosensory thalamus, the Ventro-Postero-medial (VPM) and Principal (Pom) in what are called the lemniscal and paralemniscal pathways because VPM and Pom then project differentially and separately to the cortex. The trigeminal nuclei also project to the cerebellum and the superior colliculus in addition to the cortex. Within the cortex thalamic projections in important terminal layer IV clumps delimiting the barrels all the while sending some collaterals at the border of layer V and VI. This intrabarrel input represents an important (19%) proportion of intrabarrel synapses. Of interest for us is that about 8% of the synaptic connections on GABAergic interneurons comes directly from the thalamus. Layer IV vaso-intestinal peptide (VIP) immunoreactive interneurons in particular receive multiple (up to six) inputs from the same thalamic axon. The cells in the barrels and the barrel walls are organized asymmetrically with most neurites pointing towards the center of the barrel. The cells in the outer septa are particularly representative presenting dendrites only on the side of the barrel center.

Thalamic collaterals also project to the cerebellum and to the superior colliculus. In the thalamus these whisker projections are organized in a strict grid of barreltes strikingly similar across mammals. This grid is precisely inverted in layer IV of the barrel cortex to form the final somatotopic map.

Intracortical connectivity

The highest proportion of synapses (over 70%) are formed by intracortical input, highlighting the high processing potential of this sensory area. The main cortical circuit goes as follows. Cells from the input layer IV project to all other layers, providing a pre-processed and potentially gain-controlled input. Layer II/III and V cells then interconnect within a column.

Layer II/III excitatory synapses on pyramidal cells tend to evoke weak excitatory post synaptic potentials (EPSPs) suggesting a necessary integration of multiple inputs to evoke action potentials (Feldmeyer et al., 2006). One exception to the barrel-centered orientation of layer IV neurons is that septal excitatory cells show some long-range connections that stay within the septa and do not enter the barrels (Feldmeyer et al., 1999). In layer II pyramidal neurons then send their dendrites either directly horizontally or climbing to layer I and then branching horizontally, which provides major lateral inter-barrel connectivity (Gottlieb & Keller, 1997). Layer V can be subdivided into Va and Vb depending on electrophysiological properties of pyramidal neurons, cell density and connectivity. Layer Vb pyramidal cells receive direct input from the thalamus and very little connection from layer IV to the contrary of Va. The internal connectivity of layer V is like layer II/III in that it is not limited by barrel limits, individual cells can project across multiple barrels (Bernardo et al., 1990). Finally layer VI is the main layer providing major projections back to the VPM and POM, approximately 50% of pyramidal cells in this layer present a reverse morphology, with the apical dendrite projecting towards the white matter away from the cortical surface (Woolsey et al., 1975; Z. W. Zhang & Deschênes, 1997) while some cells project their axons to more superficial layers.

Cortico-cortical projections

The major outputs of the barrel cortex are in the primary motor cortex (MI) and in the secondary sensory cortex (SII). These projections are reciprocal, and these three regions are on equivalent level hierarchically. The projections to SII keeps the topography but is mirrored along the A row and individual barrels project to regions overlapping in a row (Alloway et al., 2006; Chakrabarti & Alloway, 2006).

In MI the projections originate mostly from the septal areas interestingly (Alloway et al., 2004). The projections from Pom are also landing in the septa indicating parallel circuits passing through the barrels and septa. The barrel circuit receives input from VPM and connects with both MI and SII while the septal circuit receives input from Pom and connects with SII.

Subcortical projections

Retrograde tracer studies showed that the barrel cortex also retrogradely projects to the thalamus and the pons. Cells from layer Vb project majorly to the pons but also to other subcortical targets like the superior colliculus. Mercier et al 1990 showed that 25% of the pons projecting neurons also send collaterals to the superior colliculus (Mercier et al., 1990). It is thought that a large

proportion of these long-distance retrograde connections are collateral. These corticopontine projections also conserve the somatotopic organization, mainly along rows.

The projections to the striatum originate majorly from barrels in layer Va and partially from layer Vb and forms once again a somatotopic map. Some septal layer V neurons project diffusely and bilaterally (Wright et al., 1999, 2000). Because the septa already receive contralateral connections this appears to be a bilateral coordination network.

The main purpose of this work is to study the barrel cortex, but we also briefly studied other sensory areas within collaborative projects. We performed fiber-based calcium recordings as well as single channel Local Field Potential recordings in the hind paw primary somatosensory region during work centered around BOLD-fMRI recordings. The rationale for recording there was the size of the regions and the simplicity of the electrical stimulation. Since these recordings were part of a project centered around functional magnetic resonance imaging (fMRI) we needed an easy stimulation modality and electric stimulation of the paws fit our use perfectly. The somatosensory cortex of the paws is quite like the barrel cortex but usually studied for different purposes. The somatotopy is as well defined, but not in as repetitive a pattern, moreover paws are often easily accessible for stimulation. Only a small subset of mammals possesses whiskers and a barrel cortex, but all possess limbs and a large number possess paws making this area of study more easily translatable across the mammalian kingdom (Catania & Kaas, 1997; Kaas, 2009).

We also briefly recorded in the visual cortex, while implementing recordings using virtual reality (VR). It can be difficult to access whiskers for stimulation when the animals are awake. Mice naturally move their whiskers to explore the environment, making it potentially difficult to keep the stimulation to a single whisker without directly attaching the arm of the stimulator to the whisker or inserting it in a tube, which would in turn interfere with whisking. Recently research groups have started presenting an object between two identified whiskers (J. L. Chen et al., 2013). While awake however mice open their eyes and use them to explore their environment. Since the virtual reality system allows us to control the visual environment of the mice, we decided to move our area of study to the visual cortex when using the VR system. The visual cortex of mice has a similar columnar organization as the barrel cortex although columns are more intricate and much harder to identify in vivo as well as post hoc (J. C. Horton & Adams, 2005). One of the striking similarities is the pinwheel organization of orientation

selectivity inside cortical columns which is strikingly similar in mouse barrel and visual cortex (Kondo et al., 2016; Kremer et al., 2011).

General anesthesia

To record the brain of animals from within it is often necessary to perform some form of craniotomy. To that end it is necessary and ethical to anesthetize them. There are two cases in which we need to perform craniotomies and thus anesthetize the animals. During surgeries to prepare for recordings and for the duration of the subsequent recording or during surgeries to perform virus injection.

The virus injection requires only a tiny opening of the skull to allow the passage of a capillary. These surgeries last 30min to 1 hour depending on the complexity of the injection site (depth, size of the target, superficial features to avoid). The ideal anesthetic for these procedures has a short lifespan and/or is reversible. We typically used isoflurane because of the very short recovery time and because we had easy access to it. It however requires a bulky infrastructure (O₂ supply, mixing tank, exhaust) and a mask covering the nose of the animal restricting access to snout, whiskers and olfactory bulb. It is also a potent odorant. Two excellent alternatives are Ketamine/Xylazine at a typical small dose (90mg/kg Ketamine and 10mg/kg Xylazine), and medetomidine-midazolam-fentanyl mix. Ket/Xyl lasts 30-45min and can be reinjected if complications lengthening the surgery arise. The animal then recovers slowly in a few hours, making the experience slightly more traumatic than isoflurane. Med-mix lasts 1-2hours but can be reversed using the antidote atipamezole-naloxone after which the animals wake up fully in 5-10min. Making it very adapted to short procedures, avoiding keeping the animal unconscious for too long and reducing the physiological stress of unconsciousness to the strict minimum. The only obstacles to using this anesthetic are the legal regulations around opioids which, depending on the country can make it harder to access. It can also be counter indicated to certain studies because it contains the opioid fentanyl. Finally, Urethane is ill advised for survival experiments because of its high carcinogenicity and its very long lifetime in the body. Moreover, it doesn't fully suppress reflexes and requires supplementary analgesia (Gargiulo et al., 2012). In the case of recordings of neuronal activity, we considered four criteria regarding anesthetics: survivability, length, depth control and access to the snout.

If the animal is expected to survive and recover from the experiment urethane is ill advised because it is carcinogenic. In general, anesthesia duration on a single dose goes as follows from shortest to longest. Ketamine/Xylazine – Medetomidine - Urethane - Isoflurane. Urethane and

Ketamine/Xylazine need to be reinjected periodically to prolongate the anesthesia. Med-mix can be used in a single injection or be continuously perfused at low dose, conveniently allowing depth control. Urethane lasts very long on a single, low volume, injection but the resulting anesthesia fluctuates spontaneously in depth, mimicking natural sleep but limiting experimental control and reproducibility. Isoflurane, if the experiment does not require access to the snout (whiskers, olfactory system), is extremely convenient for easy induction and depth control because of its volatile nature. Control of anesthetic depth is quasi-immediate when changing the mixing ratio of pure oxygen to isoflurane. Recovery is fast and it does suppress reflexes. Being mildly respiratory depressant and odorant, it is not ideally suited to study blood oxygenation, respiratory or olfactory systems. We used isoflurane for some initial experiments but then switched to urethane anesthesia when we needed access to the whisker field. It was also chosen for compatibility with data from our collaborators.

We discussed anesthesia depth in this part because it is of utmost importance to the activity to be recorded.

Anesthesia modulates the resting state of the brain

The very first electric recordings of the brain in the 19th century were time series recorded in a single point of the nervous system. As such the first spectral analyses showed rhythms correlated with activity of the subject (Jensen et al., 2014). Activity in the brain happens in multiple dimensions, three spatial dimensions, the temporal dimension, and variations in intensity. However, recordings are done in two or three dimensions and often the analysis, for simplicity's sake deal only with two-dimensional data varying in intensity and time. Naturally researchers have since the beginning been interested in the frequency domains of the data. As such, rhythms in the brain are grouped in typical spectral bands based on spectral analysis and based on their physiological correlates (attention state, activity, neuronal correlate). Our team has been interested in slow rhythms associated with deep sleep and anesthesia. Both states present a particular spectral band below 1Hz that represents specific field of study as they typically only appear during slow wave sleep (NREM sleep) and under anesthesia (Adelsberger et al., 2014; Steriade & Amzica, 1998; Stroh et al., 2013). The function, mechanisms of initiation and propagation of slow waves are not very well understood.

Periods where 0-2Hz frequency bands dominate in the cortex and thalamus can be classified under slow wave state while periods during which higher frequency ranges and more continuous activity we classify as persistent up state (Grienberger et al., 2012; Steriade et al., 1993; Stroh

et al., 2013). Slow wave state is characterized by epochs of relative neuronal silence interleaving epochs of depolarization serving as windows of opportunity for action potentials, resulting in so-called spindles. These bursts of higher frequency activity (9-16Hz) are not always present during slow waves. Slow waves, detected on a network wide level are correlated with epochs of depolarization on a single cell level. These depolarizations represent windows of opportunity for action potentials. It is sometimes called burst suppression state because of the presence of these bursts followed by refractory periods of neuronal silence (Clement et al., 2008; Ward-Flanagan et al., 2022). What triggers these changes and what makes the depolarization and hyperpolarization periods meta stable is an interesting subfield of research. The main current cellular explanation is that inward rectifying potassium currents due to hyperpolarization activated potassium channels lower the sensitivity of spiny stellate cells while in pyramidal neurons a concomitant change in synaptic input is necessary (Wilson, 2008). A convenient way to control the brain state experimentally in order to study specific aspects is by using anesthesia. For practical reasons most of experimental physiology is performed in anesthetized animals. This was our case for a large portion of this work. Obviously, anesthesia greatly affects sensory physiology and anesthetized recordings greatly differ from awake. However, the great strength of these recordings lies in the ability to control the physiological state of the animal quite precisely and if one considers the effects of the drugs used, they represent an invaluable tool to study the functional mechanisms of the brain. In an early part of this work, we investigated how isoflurane and medetomidine affect the physiological state of the brain. We tried to consider anesthesia state as a variable with explanatory value in our subsequent experiments.

Drug choice depending on experimental context

The main reason to perform anesthesia is to render the animal unconscious thus insensitive to pain and to suppress noxious reflexes, and reflexes in general. We refer to this depth of anesthesia as the surgical plane it is considered reached when the animal loses muscle tone, consciousness and doesn't present any reaction to air puffs to the eye or to a tail or paw pinch. Once certain this is reached, we also administer the painkiller lidocaine locally to avoid unnecessary pain if the anesthesia depth is reduced. Lidocaine blocks voltage activated sodium channels, blocking any action potentials and thus local pain and sensory signals for approximately an hour (X. Yang et al., 2020). We chose different anesthetic agents depending on the neuronal activity they produce, their administration mode and the duration of their

effects. In this section we will detail what anesthetics are available for rodent surgery, their relative advantages and their impact on recorded activity.

Ketamine-Xylazine

Ketamine is a drug mainly used for anesthesia and sedation in mammals. Its main known action is as a NMDA receptor antagonist and prevents central sensitization in dorsal horn neurons reducing pain transmission. It can be used to initiate and maintain anesthesia, its main advantage being that it is not respiratory depressant. Ketamine is often used in veterinary medicine. It is often used in animal experiments in conjunction with Xylazine, an agonist of alpha-2 adrenergic receptors, making it a muscle relaxant and light respiratory depressant. The combination of these drugs is sometimes called the “rodent cocktail” usually administered intraperitoneal and provides a convenient way of anesthetizing laboratory rodents for two reasons. It has a high tolerance threshold and a short recovery time with few side effects. We used this cocktail for short experiments and sometimes surgeries. Longer experiments using this cocktail require continuous perfusion or multiple IP injections increasing the mortality rate drastically. Which is the reason why we phased it out from two-photon experiments (Levin-Arama et al., 2016). Neuronal activity under Ketamine-Xylazine doesn’t reach burst suppression or slow-wave state until a very high dose much larger than the one necessary to reach a surgical plane (Ward-Flanagan et al., 2022). The EEG under this anesthetic remains quite active with a frequency spectrum resembling more NREM sleep than strict burst suppression. Reflexes do not disappear completely at low dose indicating that sensory evoked activity should remain present when slowly reducing the dose to below the surgical plane during recordings.

Medetomidine

Medetomidine is an alpha-2 adrenergic agonist. It is used only in veterinary medicine as an anesthetic. In the case of rodents, it is administered subcutaneously either alone or in combination with analgesic drugs. It can be perfused intraperitoneally or intravenously, punctually or continuously depending on the control needed on the depth of anesthesia. In some recordings presented here we used it alone with the topical analgesic lidocaine because we intended to study lighter modes of anesthesia that do not present slow oscillations. We call this state persistent up state at low isoflurane or under medetomidine. It is sometimes also used in a cocktail containing Midazolam (hypnotic) and Fentanyl (hypnotic and painkiller). In a very potent hypnotic and painkiller cocktail reversible with naloxone-flumazenil-atipamezole

(Fleischmann et al., 2016). The reversibility makes it usable and interesting for short surgeries. Medetomidine by itself can be useful to perform recordings under persistent up state following an induction and surgery using isoflurane. Using it mixed with Fentanyl and midazolam is ill advised for anesthetized recordings because of the complex neurophysiological effects of mixing drugs. It is also ill advised for chronic recordings because of the addictive effects of the opioid fentanyl.

Urethane/ethyl-carbamate

Surprisingly unrelated to polyurethane, ethyl-carbamate occurs naturally in low doses in some fermented products (Zimmerli & Schlatter, 1991). It produces very long-lasting anesthesia up to 8 hours in rodents with a single administration IP or subcutaneous (Field & Lang, 1988; Hara & Harris, 2002; Maggi & Meli, 1986). It depresses activity in the neocortex less than other drugs like isoflurane. The level of brain activity varies largely over its very long duration and is mostly independent of the surgical plane. The rhythms observed and their variety mimicking natural sleep somewhat (Clement et al., 2008). The animals alternate between stages comparable to NREM and REM sleep with a period of approx. 8 minutes (Silver et al., 2021). It is hard to argue that the slow wave phase of urethane anesthesia resembles NREM sleep since the electro-encephalogram (EEG) is so similar and even sleep specialists seem to mostly agree on this (Pagliardini et al., 2013; Sharma et al., 2010; Ward-Flanagan & Dickson, 2019). The REM-like phase however is more controversial because it does not reproduce all hallmarks of REM like eye movement, strong muscle atonia with twitches and a termination followed by a short wake (Jouvet, 1965). Some argue that it resembles more wake or persistent up state (Ward-Flanagan & Dickson, 2019) in part because it is unsure if it affects the ventral tegmental to basolateral amygdala dopaminergic circuit of rem (Hasegawa et al., 2022), the dorsal pontine cholinergic circuit (El Mansari et al., 1990) or the ventral medulla to ventro-lateral periaqueductal grey GABAergic switch (Weber et al., 2018). Until the true mechanisms of REM switching are understood and how anesthesia affects it however it is hard to answer this question.

Ethyl-carbamate is only ever used in animal experiments since it was discovered to be potentially carcinogenic to humans and effectively mutagenic in mice, plants (Field & Lang, 1988) and drosophila (Vogt, 1948). A vast literature demonstrates its carcinogenicity (IARC Working Group on the Evaluation of Carcinogenic Risks to Humans. & International Agency for Research on Cancer., 2010; Mirvish, 1969; Schlatter & Lutz, 1990) in mammals through a

variety of administration methods. As a result, we only ever used it for terminal experiments. This drug has been used in a number of experiments and a lot of the historical findings and definitions of brain states have been made under urethane anesthesia (Deschênes et al., 2005; Sheroziya & Timofeev, 2014; Steriade, 1993; Steriade et al., 1993). More specifically our collaborators at Ag Luhmann have been using this anesthetic for a very large portion of their experiments in the sensory cortex (Reyes-Puerta, Kim, et al., 2015; Reyes-Puerta, Sun, et al., 2015; J. W. Yang, Kilb, et al., 2018). Naturally we used it for our collaborative project to be able to relate it to their previous findings.

Isoflurane

Isoflurane is a halogenated ether used in human and veterinary medicine as a general anesthesia (Pauc & Dripps, 1973). It is volatile at room temperature administered as a gas and as such requires specific equipment and precautions. The volatility of isoflurane and its short lifetime in the organism make it a perfect candidate for experiments requiring fast modulation of anesthesia depth. It is possible to reach burst suppression easily with it but also to use it at low dose to try and preserve some level of desynchronized activity (Lissek et al., 2016; Ward-Flanagan et al., 2022). While it is very volatile and changing the dose can be done easily the physiological result can be slower, in particular when reaching very deep anesthesia during long surgeries it is possible for the animal to take upwards of 20minutes to recover. Monitoring breathing and heart rate continuously is essential to avoid this. Isoflurane is analgesic; however, it is often used in conjunction with a topical anesthetic like lidocaine. It is a GABA receptor positive allosteric modulator and an NMDA receptor antagonist it is also a glycine receptor potentiator amongst other things. It is a respiratory depressant and can decrease blood pressure and affect cardiac rhythm (Alagesan et al., 1987; Grasshoff & Antkowiak, 2006). The specific equipment consists in a gas mixer allowing for modulation of the mix ratio. The isoflurane can be mixed with normal air, but we used it mixed with pure oxygen to counter the hypoxia it induces. We used it for continuous anesthesia during experiments and surgeries but also commonly using a so-called induction box to induce anesthesia to facilitate the use of other anesthetics. Precautions need to be taken to prevent the experimenter from breathing it in as the effects of chronic exposure are not well known. Chronic exposure to Halothane being carcinogenic, precautions should apply (Alagesan et al., 1987). This means excellent ventilation in the room, an exhaust with negative pressure on the mask, a filter for halogenated products in

the exhaust, working under the hood when inducing anesthesia and being very careful when refilling the mixer.

Functional rhythms in the brain

Since the very first experiments of EEG researchers have noticed the prevalence of certain frequencies in the recordings. Early on certain spectrograms have been associated with different states of consciousness. The most prominent frequency bands are named after Greek letters. They are in order of frequency delta (1–4 Hz), theta (4–8 Hz), alpha (8–12 Hz), beta (12–30 Hz), and gamma (30–100 Hz) rhythms in adult humans (Hiltunen et al., 2014; Malmivuo & Plonsey, 1995). These frequencies originate from different sources filtered by the conducting medium and are convoluted into the EEG or LFP signal. Separating them by using Fourier transforms allows us to investigate the different types of activity in the brain.

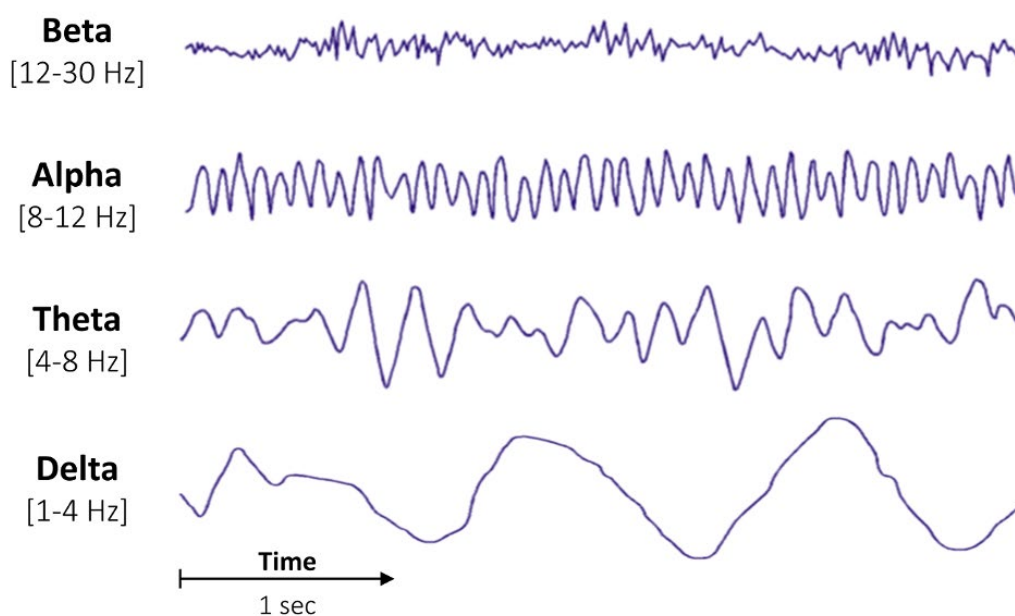


Figure 1-2: Frequency bands in EEG.

Visual example of different frequency components of the EEG spectrum. Delta is present during deep NREM sleep, deep anesthesia and during some tasks requiring sustained concentration. Theta is present during wake and is amplified when idling or during voluntary response suppression, it is also dominant during REM sleep. Alpha is associated with relaxed reflexion. Beta is particularly high during alertness and stressful situation. Additionally, Gamma frequencies over 32hz are present during cross modal sensory processing and pattern matching. (Fig from Malmivuo & Plonsey, 1995 Reproduced with permission of the Licensor through PLSclear)

Neuronal activity encompasses a large spectrum from less than a Hz to the fastest unit of activity, for example action potentials from fast spiking interneurons that can reach over 100Hz (Hu et al., 2014). Classically in electrophysiological recordings the spectrum is separated into frequency bands for ease of analysis and because each band corresponds to different physiological sources. This naturally depends on the recording method with Single cell recordings being the most precise allowing for distinction of single action potentials and EEG or Electrocorticogram (EcoG) being less precise as these recordings integrate activity over a large region. Here we recorded single electrode local field potentials, because of the filtering parameters we used (low pass 300Hz). But also because of the combination of the uncompensated capacitance and the resistance of the 2M Ω pipette creating a low pass filter, the data we acquire is intrinsically heavily filtered (Barbour, 2014). Moreover, the intrinsic properties of brain matter and the integration factor of the signal makes these recordings dominated by slow events under the spiking threshold (Kajikawa et al., 2011). On the opposite, maybe counter-intuitively the fluorescence induced by calcium changes is heavily dominated by spiking induced calcium changes (Grienberger & Konnerth, 2012; Rochefort, 2009). This is due to the proportions of calcium influx to the cytoplasm during action potentials (~100 to ~1000 nanomolar in a matter of milliseconds) being much higher and sudden than other calcium signaling events (Berridge et al., 2000). Naturally local depolarization can be observed at a high enough resolution. Spiking related events appear with very distinct kinetics in the cell body whereas slower lower intensity signaling events are almost impossible to distinguish. As an optical method, the sampling frequency of calcium imaging is always limited by the speed of optical detectors. Photomultiplier tubes are very fast nowadays and allow good single point recording frequency which is promising for fiber photometry. Otherwise spatially resolved methods like laser scanning and cameras are more limited to the 10-200Hz sampling frequency range (Grienberger & Konnerth, 2012; Kremer et al., 2008; Pisanello et al., 2019).

We reviewed different methods to record different phenomenon but what are the questions we want to answer here? We have the capacity to observe different scales and one of our goals is to link these scales to provide a more integrative understanding of past experiments and to be able to infer the global context from local recordings. Because up until recently the overwhelming majority of recordings of the brain in animals have been conducted under anesthesia for practical and ethical reasons and because anesthesia in some manners resembles sleep, it is interesting to understand global states of activity under anesthesia.

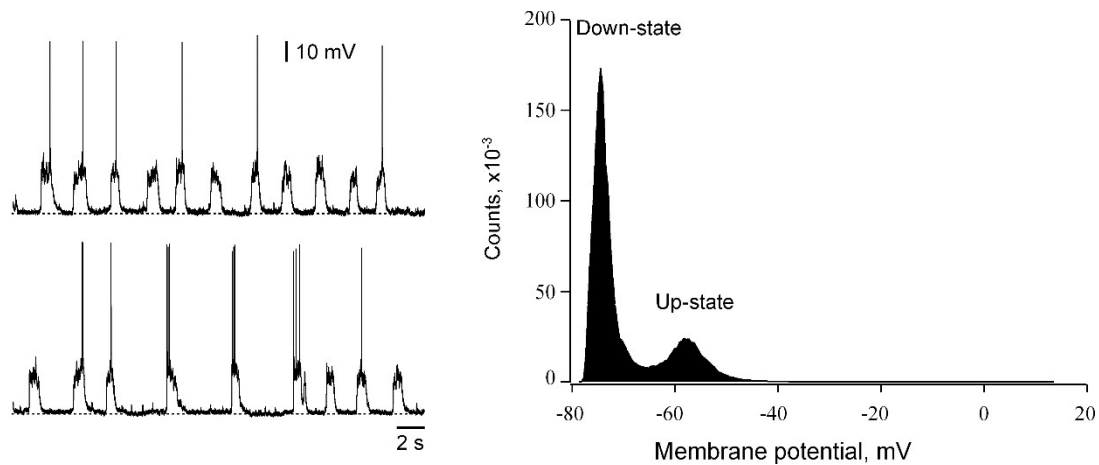


Figure 1-3: Membrane potential changes during slow waves Right: Whole-cell recordings in layer 2/3 Isoflurane anesthesia (approx. 1.1-1.2%) Single cells show periodic depolarizations acting as windows for action potentials. Left: distribution of membrane potentials in slow wave state showing the typical two peaks. A persistent up state would only show a single peak (Fig adapted from Rochefort, 2009).

Neuromodulation of brain state

The brain states observed under anesthesia resemble parts of natural sleep. During natural sleep in most vertebrates the brain alternates between wake, rapid eye movement sleep (REM) and non-rapid eye movement sleep (NREM). Wake is characterized during EEG recordings by muscular tone in the EMG and high frequency persistent activity in the EEG or LFP. REM sleep is characterized by a complete loss of muscular tone, electrical activity resembling wake and rapid eye movements. In healthy individuals it also only appears after a period of NREM. NREM finally is characterized by slower higher amplitude currents in the EEG, hence why it is sometimes called slow wave sleep. The mechanisms of switch between those conditions are understood to be controlled in brainstem and hypothalamus but the precise details are still hotly debated (Jouvet, 1965; S. H. Lee & Dan, 2012; Luppi et al., 2013). The apparent bistability of pyramidal neurons seems to be dependent on hyperpolarization activated potassium channels and synaptic input (Wilson, 2008). This synaptic input can be intracortical or thalamic as both can evoke a travelling up state under anesthesia (Stroh et al., 2013). Neuromodulation by acetylcholine from the basal forebrain probably plays a major role in this arousal state since it is the major excitatory neuromodulator in the cortex and is linked to natural changes in arousal during sleep and wake. The basal forebrain being itself under control from the locus coeruleus and the orexinergic system (Dale et al., 2022; Fu et al., 2014; Lu et al., 2008).

Sleep and anesthesia

The comparisons between sleep and anesthesia seem straightforward but are hotly debated and few people effectively bridge the two fields. Finding out the common points would illuminate our understanding of consciousness and open ideas in sleep clinical research. The main mode of studying the common points in the clinic consist in measuring how much different anesthetics affect REM and NREM sleep debts. It appears that propofol can attenuate sleep deprivation accrued debt as effectively as natural sleep (Tung et al., 2004), while sevoflurane only reverses NREM sleep debt (Pal et al., 2011) like most volatile anesthetics. Conversely sleep deprivation facilitates anesthesia (Tung et al., 2002). In rodents anesthesia similar to that produced by GABA agonist agents can be induced by direct injection of muscimol the pontine central grey just ventral of the sublateral dorsal tegmentum, pointing to possible common mechanisms of transition with REM sleep (Devor et al., 2016; Minert et al., 2017). On the contrary, applying excitatory agents to the thalamus and importantly lateral hypothalamus, where orexin cells reside, facilitates emergence from anesthesia (Alkire et al., 2007; Kelz et al., 2008). Because of these fundamental overlaps, studies of anesthesia and sleep could help put each other in perspective.

Inhibition in the cortex

Information in the brain is conveyed inside cells by ionic currents and at the synaptic level by neurotransmitters. The principal neurotransmitters are glutamate to convey excitation and depolarize the post synaptic neuron and GABA to convey inhibition/hyperpolarization to the postsynaptic neuron. One neuronal type provides one main type of neurotransmitter and as such one type of influence allowing for a classification between excitatory and inhibitory neurons. Very early on Ramon y Cajal and Golgi theorized the general principles of neuronal connectivity from microanatomical data. Typically, information between brain regions is transmitted by excitatory cells, typically pyramidal cells. While inhibitory cells project on a shorter scale within anatomical and functional regions or between neighboring regions.

First, we can separate excitatory and inhibitory neurons, glutamatergic vs GABAergic. Excitatory neurons generally convey information intracortically, in between brain regions as well as towards the peripheral nervous system. Inhibitory neurons on the other side mostly convey information inside specific regions inside a layer or inside a cortical column and more rarely between regions. The properties and anatomy of inhibitory neurons are relatively well known or at least well studied but the sheer vastness of their variety and the multiplicity of brain

regions makes the classification and in-depth description difficult. Confronted with this large variety researchers in the field have long tried to classify neurons using at first their morphological properties and more recently their genetical markers (Gentet, 2012; Gentet et al., 2012; Jiang et al., 2015). From the microanatomical studies of Golgi and Ramon y Cajal, and later, studies of the cerebellum early neuroscientists discovered that structure and function are tightly related. Functional models of the cerebellum can give us insight into the less well-known functional anatomy of the cerebral cortex. Where the cerebellum has a very strict and simple anatomy with a computational unit repeated in parallel to the input and only three layers, the cerebral cortex has a multiplicity of layers and sub layers with intricate connections between them. Generally, in the cerebral cortex a few classes of interneurons are defined, SOM, PV and VIP or alternatively martinotti, basket/chandelier and multipolar. If we consider the morphology the classification can become quite complex as shown in figure 1-4. Only considering interneurons from the superficial layers I, II and III the variety is quite staggering. The morphological classification is well suited to single cell recordings and biocytin staining since it stems from studies those type of stainings. After the experiment the experimenter can visually identify the morphology of a neuron and relate it to its function. Some of these neuronal phenotypes have been described very early using histological stainings by the same Ramon y Cajal and Golgi.

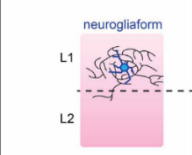
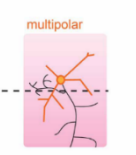
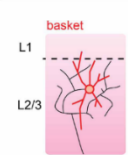
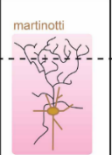
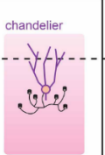
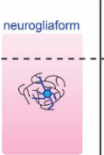
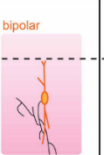
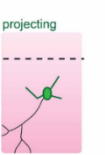
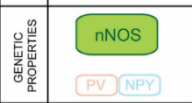
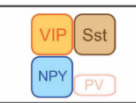
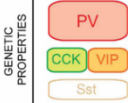
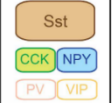
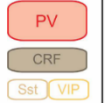
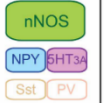
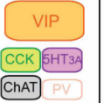
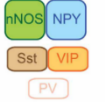


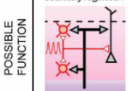


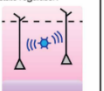
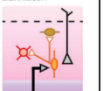
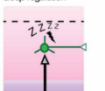
									
MORPHOLOGY	SA: local, small AA: local, dense, horizontal extent	SA: large, L1 + L2 AA: local, L2		SA: local, small or large, multipolar AA: local, large, can be trans-laminar	SA: local, deeper main dendrite AA: large, mainly to L1	SA: L1 + L2 AA: local, characteristic shape	SA: small, local, small somata AA: local, dense	SA: local, vertical, fusiform somata AA: local + trans-laminar to deeper layers	SA: local, small, large somata AA: long-distance
CONNECTIVITY	Pre: TC, CC Post: dendrites of L2/3 + L5a/b PC L1 NGFC	Pre: TC, L2/3 PC Post: L2/3 PC, L2/3 BC + ChC		Pre: L4 SC L2/3 PC, BC, BPC Post: perisomatic region of L2/3 PC BC	Pre: L2/3 PC Post: distal dendrites of L2/3 PC	Pre: L1 MpC, TC, CC Post: axon initial segment (AIS) of L2/3 PC	Pre: L2/3 PC, L5a PC Post: dendrites of L2/3 PC, volume transmission	Pre: L2/3 PC, TC L2/3 BC Post: mainly other L2/3 GABAergic neurons	Pre: L2/3 PC Post: S2, ipsi- and contralateral cortex
ELECTRICAL PROPERTIES	FP: low, delayed, AC AP: average, slow AHP IR: moderate	FP: low, AC, may be bursting or irregular AP: average, large AHP IR: moderate - large		FP: high, nAC AP: narrow, fast AHP IR: low	FP: moderate, AC AP: average, fast AHP followed by slow AHP IR: large, lh sag	FP: high, nAC AP: narrow, fast AHP IR: low - moderate	FP: low, delayed, AC AP: average, slow AHP IR: moderate	FP: low, irregular, bursting, AC AP: broad, small AHP IR: large	FP: moderate, AC AP: average, fast AHP IR: large
GENETIC PROPERTIES									
MOUSE MODELS	nNOSCre	VIPCre CRCre		G42 PvCre	GIN SstCre	G42 PvCre Nko2.1	GAD65 nNOSCre	G30 VIPCre ChATCre	GAD65 nNOSCre FosGFP
POSSIBLE FUNCTION									

Figure 1-4: Overview of the different types of superficial cortical interneurons, their structure, connectivity and genetic markers. Left: layer I interneurons, Right Layer II/III interneurons Basket and chandelier cells both express Parvalbumin but with different morphologies and connectivity. Note that almost all interneurons presented here express Parvalbumin at varying levels from (Fig. adapted from Gentet, 2012).

Anatomy and electrical properties are partially related, the main electrical parameter linked to anatomy is the membrane capacitance since it is directly related to the surface area of the cell membrane (Gentet et al., 2000; Rall, 1962). Myelination is also an anatomical parameter very closely related to electrical properties of a neuron (Clements & Redman, 1989). The membrane conductance and composition of intracellular medium are however harder to infer directly from anatomy. Single-cell electrophysiology has been used for decades to characterize neurons and is still the golden standard technique.

The rise to prominence of optogenetics and other genetically targeted methods gave more importance to a genetic definition of neuronal populations. When designing an optogenetic or GECI experiment the way to target your cell population is by using the internal expression machinery of the cell and in particular endogenously active promoters to drive expression of a gene of interest. As a result, it is essential to identify cell populations by their active promoters and their expression profile. This has historically been done using FISH and immunohistochemistry. Fortunately, these parameters are closely related to the anatomical and

electrical properties of neurons. The fine subtleties of anatomical descriptions still need to be related more clearly to expression profiles. Generally, we consider three populations of cortical interneurons (Rudy et al., 2011).

Parvalbumin interneurons

Expressing Parvalbumin at high levels this class regroups basket and chandelier cells. It is the most common class of interneurons in the cortex representing up to 50% of the neuronal population in layer IV where they receive input largely from VPM (Porter et al., 2001). They project vertically across layers and only within 200 μ m laterally remaining within the confines of a single barrel. Basket and Chandelier cells connect pyramidal cells on their cell bodies or on the axonal cone respectively. As a result, they produce a strong inhibition capable of fully inhibiting action potentials. PV interneurons are particularly well connected by gap junctions forming a large electrically coupled network (Gibson et al., 1999). Other types of interneurons are electrically coupled as well but these connections do not exist between different cell types. In layer II/III chandelier cells present a large receptive field and project the furthest laterally, they have however little sensitivity to direct whisker stimulation (Zhu et al., 2004). In layer V/VI seem to contain mostly vertically projecting PV interneurons. As a rule of thumb chandelier cells project within a column and basket cells can project laterally in relation with their size.

Somatostatin positive interneurons

The category of interneurons expressing somatostatin includes Martinotti and multipolar cells in the cortex. Martinotti cells are typically ascending to layer I sending collaterals along the way. They form inhibitory synapses on dendritic spines of pyramidal neurons majorly in layer I but not exclusively. These axonal projections can extend up to several millimeters laterally, providing a major source of lateral inhibition (Markram et al., 2004).

Vaso-intestinal peptide positive interneurons

These neurons are mainly present in layer II/III (~60% of the population) and provide inhibition to the other interneuron populations (Dávid et al., 2007; Pfeffer et al., 2013; Staiger et al., 2004) by projecting vertically across layers within the confines of a single column. This population is the main source of direct disinhibition in the cortex. The circuit involving VIP to SST

interneurons is particularly well described in multiple sensory regions (S. Lee et al., 2013; Li et al., 2014; Prönneke et al., 2015).

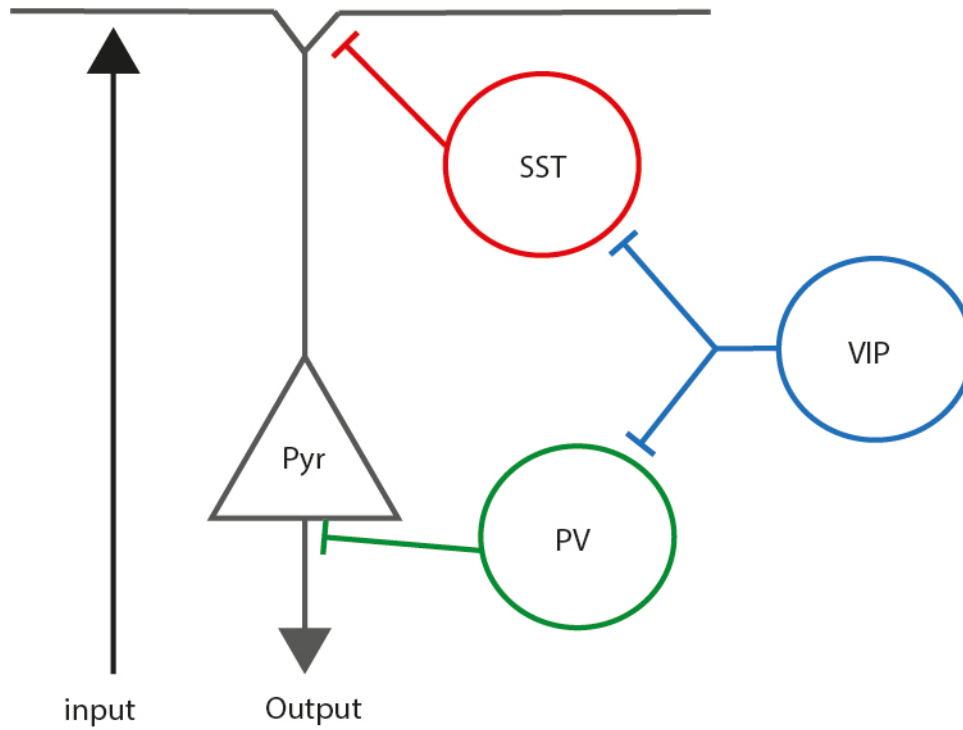


Figure 1-5: Generalized schematic of interneuron connectivity in the mouse cortex. PV interneurons provide strong inhibition at the axonal cone. SST interneurons provide dendritic inhibition to pyramidal neurons. VIP interneurons provide somatic inhibition to both other types of interneurons. This is a simplified view to visualize the most common targets of each type. (Fig. PH. Prouvot)

Characteristics of parvalbumin expressing interneurons

As the name implies, they classically express the endogenous calcium buffer parvalbumin. The genetic definition of cell types might not be the most relevant from a functional point of view, but it is of extreme interest since the advent and routinization of transgenesis using mouse lines viral transduction and even crispr-cas9. In our case since our technical focus is on optogenetics we will refer to these neurons as PV as this is the promoter we use to target them with opsins. Parvalbumin is not unrelated to the functionality of these neurons since the calcium buffering it provides allows these cells to fire at frequencies much higher than pyramidal neurons (Galarreta & Hestrin, 2002) by buffering calcium entering the cell with a high affinity.

The parvalbumin protein

The parvalbumin protein is expressed by the corresponding neurons and fast contracting muscles. Although the name means small albumin it is unrelated to the serum albumin protein, being structurally closer to calmodulin and troponin C other calcium binding proteins. It has a low molecular weight of 9-11kDa. Parvalbumin binds calcium with a high affinity and buffers calcium entering the cell with a high affinity allowing fast spiking rates in the neurons expressing it (Klausberger et al., 2005) and fast contraction rates in muscles cells (Celio & Heizmann, 1982; Pechère et al., 1977). This characteristic explains why parvalbumin interneurons fall in the fast spiking category (Kawaguchi & Kubota, 1997; Kosaka & Heizmann, 1989; Uematsu et al., 2008). Parvalbumin expressing GABAergic interneurons represent up to 25% of all GABAergic neurons in the cortex. They form powerful synapses onto cell bodies of pyramidal cells (Cauli et al., 2000; Klausberger et al., 2005; Rudy et al., 2011).

Parvalbumin interneurons in the context of the barrel cortex

PV interneurons in the barrel cortex seem to possess similar properties as in other sensory areas. The main specificity here lies in the somatotopy of barrels and the spatial restriction of their dendritic trees to a small cortical column. We expect these neurons to have spatially restricted in their input and output being a key local component of the computational unit that is a barrel. A consequent amount of recent literature investigated PV interneurons in sensory cortices but at the time only few functional studies were done in the barrel cortex.

What do PV neurons do in the context of sensory processing in the barrel cortex? How far across layers and across barrels does local modulation of PV neurons impact sensory evoked activity? Does PV neuron modulation impact resting state dynamics of the cortex? These questions are the subject of study 2.

To investigate microcircuits in the barrel cortex and answer these questions we devised a collaborative approach. On one side of the collaboration, we would combine multi-channel recordings with optogenetics to investigate PV interneurons modulation in a plane crossing all cortical layers. On the other side we would use two-photon calcium imaging to record activity in a plane tangential to the cortical surface. This double approach would give us a tridimensional insight into the modulation produced by PV interneurons.

Two-Photon laser scanning microscopy

Basic principles

Two-photon imaging is a fluorescence imaging technique, more precisely a laser scanning fluorescence imaging technique. In principle it resembles confocal laser scanning microscopy, with the difference that the excitation is limited in space instead of limiting the detection to the focal plane.

In a confocal microscope a focused laser beam scans the sample and excites fluorophores in an hourglass shape with a statistically stronger excitation close to the focal point due to the increase in power density. The collected light is then sorted through a pinhole so that only photons emitted on the focal plane and travelling in the appropriate direction can reach the detector. The result is an image composed almost exclusively of light emitted from the focal spot.

Two-Photon microscopy is based on the principle described by Maria Goepper-Mayer in her thesis “Über Elementarakte mit zwei Quantensprüngen” (Göppert-Mayer, 1931). She described broadly that it is theoretically possible to excite a fluorophore with two photons of half the energy and twice the normal excitation wavelength if these two photons hit the fluorophore within an extremely short time window. In her honor the absorption probability of a photon by a fluorophore is measured in a unit carrying her name the GM ($10^{-50} \text{ cm}^4 \cdot \text{s} \cdot \text{photon}^{-1}$).

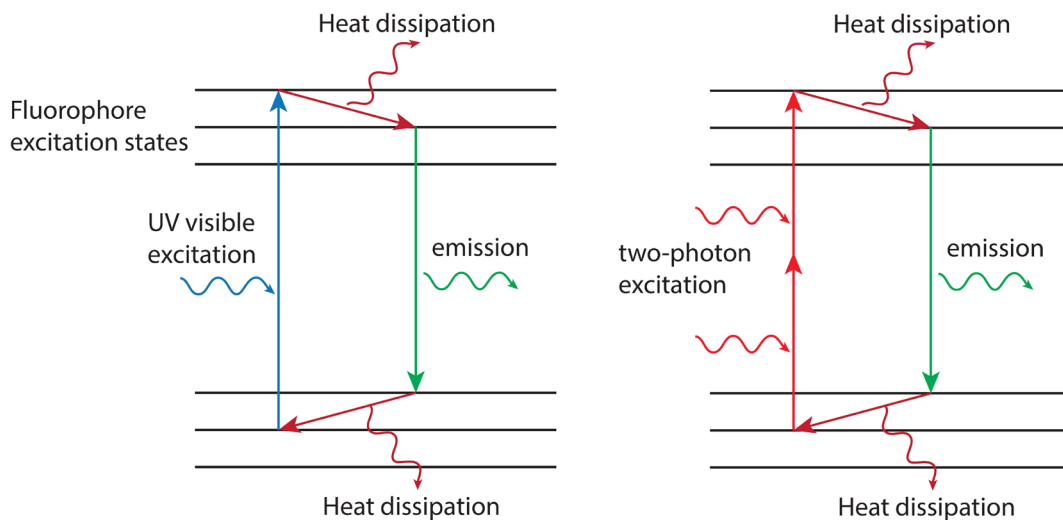


Figure 1-6: Principle of two-photon excitation compared to classical fluorescence. Illustration of the metastates of excitation in a fluorophore. Left: the fluorophore is excited by a single photon carrying sufficient energy to move a labile electron into a metastable state. After some heat dissipation the electron then returns to its stable orbital by emitting a photon of the corresponding wavelength and heat. Right: The same phenomenon can be attained when two photons of half the energy and thus twice the wavelength excite the fluorescent molecule within the right time window (fig. PH. Prouvot).

The two-photon cross section of fluorophores is much lower than for single photon excitation. In classical fluorescence, the relationship between excitation light intensity and fluorescence intensity (linearly related to excitation probability) is linear, if a single photon reaches the fluorophore, it produces fluorescence. In two-photon excitation, the relationship is quadratic as the fluorescence intensity is dependent on the square of the number of photons arriving at the fluorophore due to the compounding probabilities of two photons being absorbed sequentially. As a result, achieving this is statistically improbable using traditional continuous wave (CW) laser and the technique only became realistically feasible with the invention of femtosecond pulsed lasers. These lasers emit pulsed coherent light with all the power concentrated in our case during the 140fs pulse repeated at around 80Hz in the case of our chameleon Ultra.

The femtosecond pulsed lasers consist in an optical resonator pumped by a lower wavelength CW laser, in our case a Verdi 532nm ultra-fast laser head. The resonator consists typically in a Titanium-sapphire gain medium between two reflectors, a high reflector and the output reflector, one of them being typically tuneable. The gain medium we used is a sapphire crystal containing atoms of titanium. In a similar way to fluorescence when illuminated at 532nm some electrons on outer orbitals around the titanium atoms get excited to a higher excitation state and upon relaxation to their basal state they emit light, further participating in the back and forth within the cavity. By adjusting the cavity length, that is by synchronizing multiple longitudinal modes of the light it is then emitted in pulses centering the belly of the chosen wavelength mode. The synchronization is achieved by centering the node of the chosen wavelength on the mirrors at each extremity of the cavity by setting the cavity length to a multiple of the desired wavelength. The result is that only the chosen wavelength will emit in pulses while the rest will stay desynchronized. Moreover, only photons travelling perpendicular to the reflectors will be reflected multiple times and will participate in the amplification. This results in very coherent light at the cost of significant loss in power. Strangely the frequency of the modes is equal to the frequency separation of adjacent longitudinal modes. These lasers are tuneable insofar as an integral number of half wavelength will fit between the two reflectors (the reflector and the output coupler).

To let the pulses exit the cavity with the right timing and further avoid contamination by unwanted wavelength one can use a precisely timed shutter, a passive dye that only becomes transparent at high power (like during the top of the pulse) or in the case of coherent one can take advantage of electrical effects on refractive index caused by high power traversing a glass lens. At very high intensities the refractive indices of glass change transforming a lens into a

Kerr lens. Because this so-called Kerr lens is only formed at very high power it only happens during the pulse and not during continuous emission. This enables the design of a system where the beam shape changes depending on its power this beam can then be let through a slit only when it is narrowed enough by the Kerr lens.

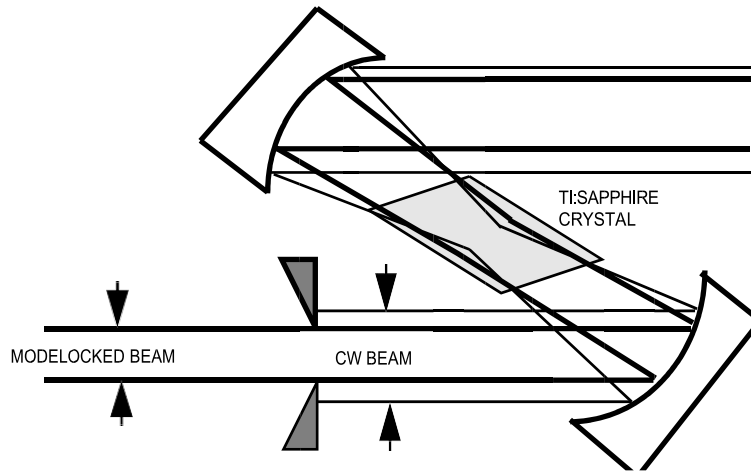


Figure 1-7: Schematic of the cavity within a chameleon ultra laser head. Thin lines represent the beam in continuous wave mode while thick lines represent the mode locked beam able to cross the output slit thanks to the Kerr effect (Fig courtesy of Coherent inc.).

To initiate modelocking an intracavity mirror is vibrated in order to synchronize as many phases as possible and allow the initial formation of the Kerr lens. Once the Kerr lens has been achieved so does passive modelocking and the intracavity mirror can be stopped. The result is a quasi-soliton laser.

Chirping and dispersion in refractive media

Different wavelength of light travel at different speed depending on the refractive index of the medium they are travelling in this relationship between wavelength and refractive index happens to be nonlinear. Lasers are not perfect sources, they emit light in a very narrow range but nonetheless a range of different wavelength. This is no different in the case of a mode locked laser, as a results when traversing the glass of lenses in the light path the different wavelength compositing the pulse traverse each lens at different speeds and are diffracted at different angles. Bluer components of the beam will travel at a different speed than red components. This results in spatial and temporal changes in the beam. In the case of two-photon microscopy the temporal changes are particularly important. This change is called chirp and is for once not an acronym. Moreover, the Kerr effect described previously will happened in every lens traversed by the beam, it needs to be accounted for in the design of the lenses. It also participates in temporal

widening since the peak of the pulse carries more energy than the edges it will produce a different Kerr lens.

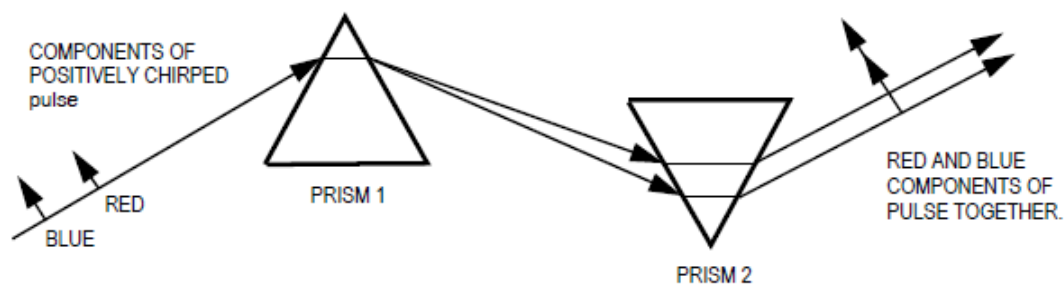


Figure 1-8: Schematic of the mechanism of chirp compensation showing the time delay between red shifted wavelength and how it is compensated using spatial diffraction. After passing through an optical system the red wavelength tend to lead the blue ones. This system uses two prisms to separate the frequencies in space first and re-join them in time second. (Fig. courtesy of Coherent inc.)

A simple system to compensate for chirp that is employed twice in the two-photons used here, is a pair of prisms. By shifting the chromatic elements in space using a glass prism one can introduce delay between them, shining this delayed and spatially broadened beam on a second prism one can spatially narrow the distance between chromatic components and at the same time narrow temporal delay between them because the more dispersed wavelength will have a longer distance to travel than the less dispersed ones. This chirping compensation mechanism is used within the chameleon laser head to compensate for the optical elements traversed within it. It is also used once in the design of all our microscopes to pre-chirp, that is preventively narrow the pulse, to compensate for the multiple optical elements it will traverse. Because these systems are particularly complex and need to fit in a reasonable space, they contain a lot of lenses and mirrors, and it is important to take it into account. An ideal system could of course be extremely long and linear to use the minimal number of optical elements but that would be unpractical.

Two-Photon calcium imaging

Reducing the focal spot is advantageous compared to confocal microscopy because it restricts photobleaching to the imaging plane and can potentially improve resolution. However, the price of the necessary equipment is comparatively very high, and the light source is tunable only in a narrow range. For multicolor static imaging of thin fixed samples, the vast majority of samples, confocal microscopy remains very advantageous. That is in part because CW single

photon laser manufacturing is very flexible and because the combination of precise focus and pinholes provides an excellent speed to resolution ratio.

This technique is mainly interesting for biology because of the light absorbing properties of biological tissues (Favre-Bulle et al., 2015; Peixoto et al., 2020; Scheffold, 2014). They are highly absorbent of lower wavelength such as UV, blue and green for example and much less in the red and, naturally the infrared (Bevilacqua et al., 1999). This is already intuitively understood when looking at an intense white light through closed eyes or hands and seeing only red coming through. It is one of the mechanisms used by heart rate and blood oxygenation finger monitors. Thus, shifting the excitation wavelength towards higher wavelength allows for better penetration of the excitation light into the tissue. Coupled with the limitation of excitation to the focal plane it becomes possible to image a specific plane within biological tissue with minimal impact on the out-of-focus tissue. The emitted light of usual fluorophores is however not red and is heavily absorbed and diffracted by the tissue. The detection system needs to be extremely sensitive to detect emitted light. The technique necessitates high numerical aperture objectives and extremely sensitive PMTs. Because in an ideal situation of absolute darkness all collected light comes from the excitation spot instead of cameras, photomultiplier tubes operating on similar principles to avalanche photodiodes are used. The principle consists in using a scintillator screen to convert photons to electrons and then use a sequence of dynodes held at steps of different potentials to amplify the electrical signal. Those present the advantage of being extremely sensitive due to the high gain afforded by sequential amplification within the detector. Nowadays PMT such as the ones produced by Hamamatsu can detect single photons. In a detector like the Kamiokande series it is possible to work in absolute darkness but in the laboratory this requires careful isolation around the imaging sample and filtering of the light by a series of filters in front of the detectors. The main limiting factor here is then scattering of emitted light within tissue. One can increase excitation power but risk heating the tissue or average over multiple repetitions to improve SNR and risk bleaching the fluorophore. The result is an efficient imaging depth limited to 300-600 nm depending on the application.

The word “minimal” in “minimal impact of excitation” must be stressed here since the laser is still depositing energy in the tissue along the whole path, which can and will heat the tissue especially below the focal plane. Using these techniques and committing normal simple mistakes one quickly understands the risks involved with high power lasers and biological tissue. It is important to keep in mind these potential secondary effects of this imaging technique.

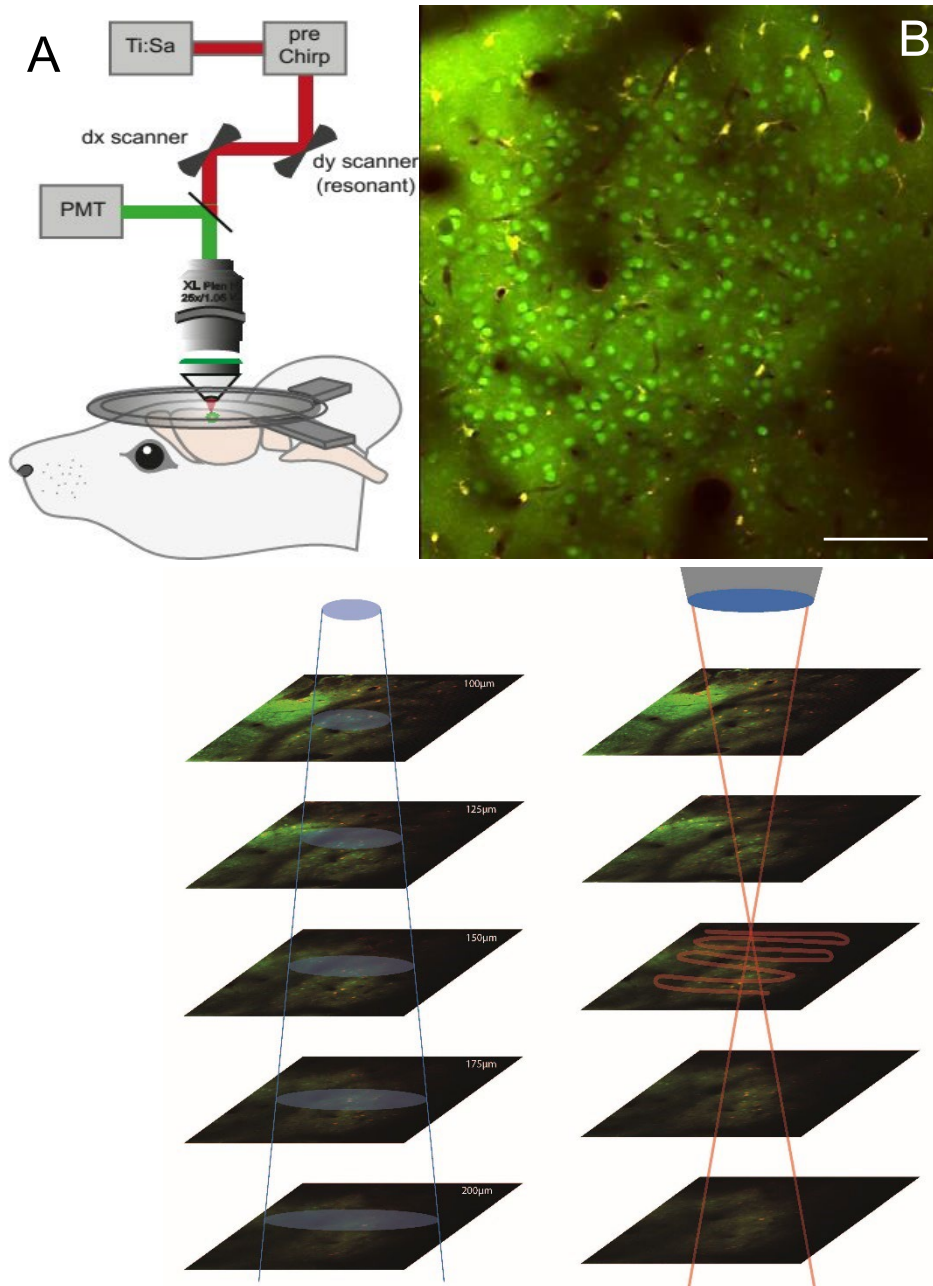


Figure 1-9: Methods of calcium photometry Top: Conceptual difference between bolus imaging using fiber photometry or epifluorescence and laser scanning microscopy. Considering the same staining, fiber photometry records a mix of signal from a rounded up frustum under the detector. On the contrary two-photon microscopy images a single plane optical section perpendicular to the objective. Bottom: schematic of a basic two-photon imaging system and a representative image of an OGB1 bolus staining co-stained with SR101 specific for astrocytes. Scale bar=100µm (Fig. PH. Prouvot)

Calcium imaging

Calcium imaging is the method consisting in using fluorescent calcium sensors to record changes in intracellular calcium in relation to neuronal activity. The fluorescence changes are

often used as a proxy for action potentials. This method depends on two parameters: the internal calcium dynamics in neurons and fluorophores dependent on calcium.

Calcium in aqueous solution is a divalent ion with a relatively large atomic weight around 40. Because of its double charge and size, it doesn't cross the cellular membrane easily and can only cross through ionophore channels. Calcium is an important second messenger inside cells with heavy implication in gene activation, mitochondrial activity, neurotransmitter release and cytoskeleton modification. Because it is so essential, it is strongly buffered in the cytoplasm with typical concentration in the nanomolar range compared the micromolar range of other ions. Multiple mechanisms are implicated in this buffering (Helmchen et al., 1996; Stosiek et al., 2003). Pumping out of the cell by membrane calcium ATPase or transport by the sodium calcium exchanger. Some calcium is then also pumped in the endoplasmic reticulum and mitochondria. By themselves however these mechanisms are slow and supplementary buffering by calcium chelators like parvalbumin or calbindin happens to reduce free calcium ions while the slower pumping mechanisms excrete it (Grienberger & Konnerth, 2012). Calcium chelators can serve to detect intracellular calcium or simply to buffer it fast. Calcium buffers are Parvalbumin, Calbindin, Calretinin and are present depending on cell type (Schwaller, 2010). Genetically encoded calcium sensors are based on Calmodulin and S100 family proteins as we will see (T. W. Chen et al., 2013; Tian et al., 2009).

Calcium imaging has evolved from technical advances in fluorescence microscopy. There are two main methods to optically measure activity in a cell, directly measuring the voltage across the membrane or measuring one of the ionic concentrations within the cell. Calcium is a very convenient ion for this purpose because its concentration within the cell is kept low (nM range) and is tightly controlled through buffering and transport. Importantly it an extremely important messenger within the cell, allowing neurotransmitter release and triggering a variety of secondary molecular pathways. Accordingly, the only time when calcium concentration raises in a live neuron is when strong electrical activity like action potentials is triggered. As a result, following the calcium concentration within a neuron can be used as a proxy for action potentials, especially when focusing on the cell body.

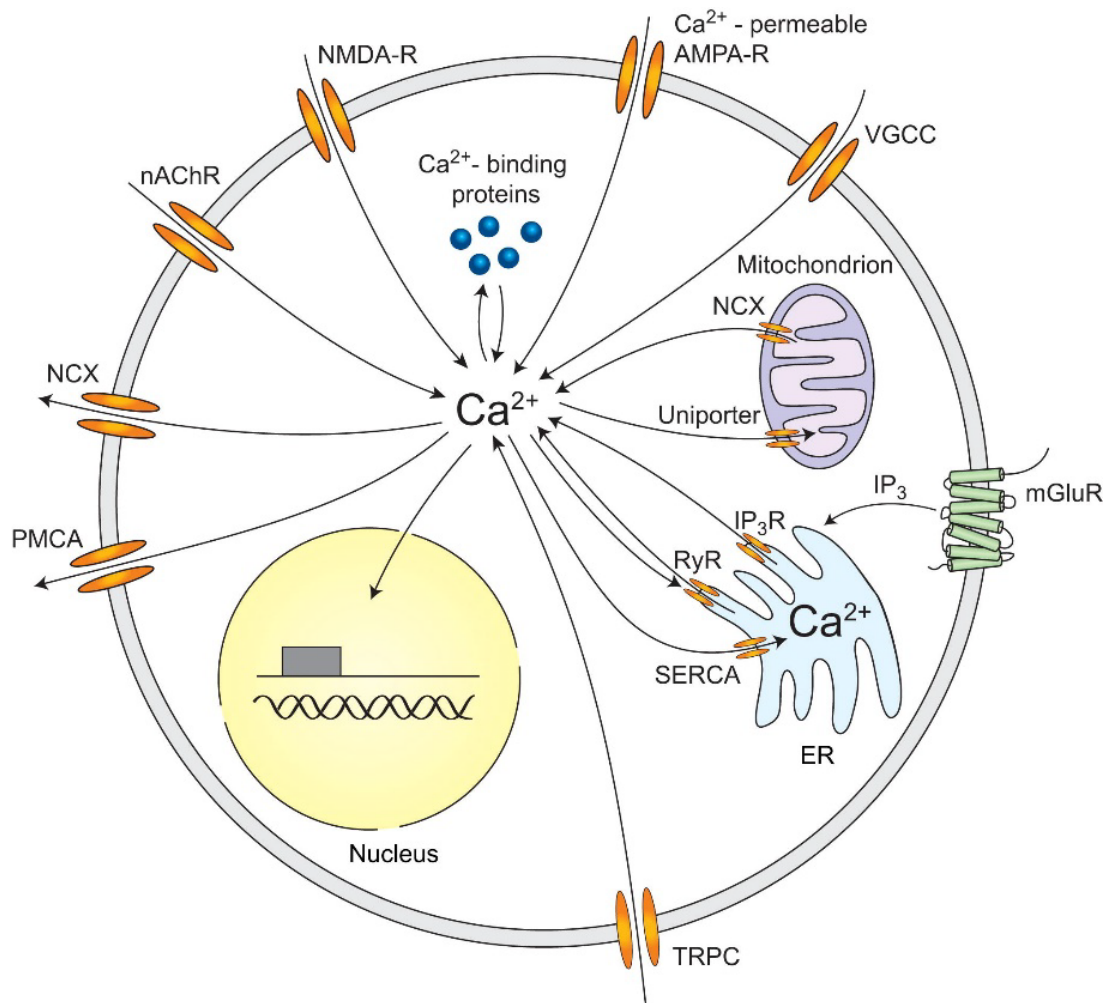


Figure 1-10: Overview Sources of calcium entry into the cytoplasm.

There are multiple ways calcium can enter the cytoplasm, from the extracellular medium, the mitochondria or the endoplasmic reticulum. Extracellular medium entries: cholinergic receptors, NMDA receptors, Calcium permeable AMPA receptors, voltage gated calcium channels, TRP channels. Mitochondrial entry: sodium calcium exchangers. Endoplasmic reticulum entry: Ryanodine receptors, Inositol-3-phosphate receptors (Fig. from Grienberger & Konnerth, 2012 reproduced with permission from Elsevier).

Brief history of calcium imaging

All fluorescent calcium sensors are calcium chelators introduced inside the cells of interest. The first chemically constructed sensors have been derived from the EGTA family of calcium chelator molecules. Older ones like fluo-4 Fura-2 (Grynkiewicz et al., 1985) became very popular thanks to their sensitivity and the new possibilities they opened. The general mechanism is that the fluorescent dye bound to the chelator is quenched when free of calcium but conformational changes caused by the binding of calcium unquench it resulting in an increase in fluorescence. These original indicators also stemmed from a need to measure calcium concentrations on a larger scale *in vitro* and they are so-called ratiometric sensors. Like

most sensors their fluorescence spectrum shifts when binding calcium. Measuring the ratio of fluorescence between both spectra allows (after calibration) to obtain a true value of the calcium concentration (Mank et al., 2006).

More recently a green, fluorescent version based on BAPTA (Oregon green bapta-1) has become the standard synthetic calcium indicator in neuroscience thanks to its sensitivity, reliability and the existence of an acetomethylester (AM) variant that helped it cross the membrane. This hydrophobic ester group gets cleaved by intracellular esterases, trapping the sensor in the cytoplasm (Kerr & Plenz, 2004; Stosiek et al., 2003). Now instead of having to load cells individually using electroporation or patch clamp it became possible to load hundreds of cells using the multicell bolus loading method (Garaschuk, Milos, & Konnerth, 2006; Stosiek et al., 2003).

The same mechanism of action is used in some genetically encoded calcium indicators. Those use calcium chelators already present in cells and tag them with a fluorescent protein. In our case we used GCaMP, which is a chimera composed of the Calmodulin protein bound to a GFP protein. The conformational changes of the calmodulin due to calcium binding setting the GFP to its normal configuration, restoring its normal fluorescent properties (T. W. Chen et al., 2013; Nakai et al., 2001; Tian et al., 2009). Note that calmodulin possesses four calcium binding sites and that binding on one of them modifies the affinity of the remaining free sites. This has the unfortunate consequence of making the GCaMP family of sensors nonlinear sensors of calcium. The other type of GECI uses Förster resonance energy transfer (FRET) to transmit energy between two fluorophores that only become close enough upon calcium binding (Mank et al., 2006). These sensors have the excellent advantage of allowing ratiometric measurements, they are the only possibility for actual precise measurement of calcium concentration using GECIs. The issue with them is that they require two excitation and detection wavelengths which greatly limits the speed of imaging for scanning techniques and is a non-starter for two-photon imaging where the wavelength is set requires time in the scale of seconds to be changed (T. W. Chen et al., 2013). They are also large proteins requiring a longer sequence to be transfected which can be inconvenient.

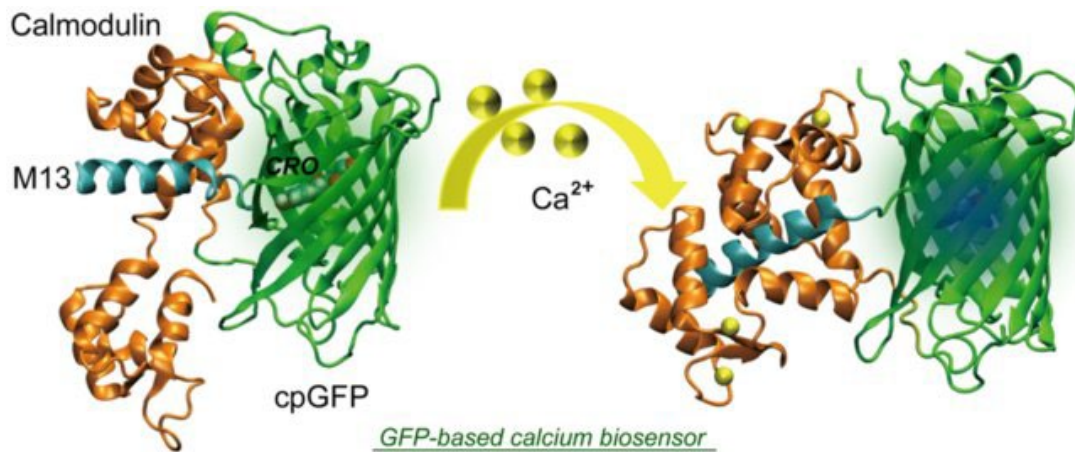


Figure 1-11: Molecular mechanisms of Gcamp. Structural changes upon calcium binding in the GFP-calmodulin based fluorescent calcium sensor GCamp. Note the changes in calmodulin configuration restoring the structure of the GFP. Also note the 4 calcium binding sites of the calmodulin responsible for the non-linearity of fluorescent response to calcium binding. (Fig Adapted from Tang & Fang, 2019).

Voltage indicators

Voltage indicators present a more direct readout of electrical activity of neurons, but they present many disadvantages for our purpose. Because the voltage difference is across the membrane all voltage indicators are within the cell membrane and use a variety of mechanisms like flipping across the lipid bilayer in relation to voltage changes or binding to the membrane depending on the voltage difference (Baker et al., 2005; Villette et al., 2019). The issue with membrane-bound sensors is that they are only present in the very thin plane that is the cell membrane, compared to calcium sensors present in the whole cytosol. This makes them extremely challenging to image using two-photon microscopy since the imaging plane will only intersect the cell membrane and almost never correspond exactly with it. The kinetics of voltage changes are also extremely fast, and these sensors follow them closely by design, They are in fact faster than the framerates typically used for two-photon microscopy and a single event would cover only a fraction of a single frame (Panzera & Hoppa, 2019).

Acquisition of fluorescent signals

The first applications of calcium imaging naturally used the available epifluorescence microscopes that were used for other types of fluorescence imaging. Epifluorescence microscopy usually employs CMOS (complementary metal-oxide-semiconductor) cameras. The framerate of these cameras can now easily go up to 100Hz, but usual structural imaging applications do not require high framerates and as an economical trade-off most systems are

equipped with high sensitivity low speed cameras. The inherent limits of epifluorescence imaging are the penetration of light in the sample, the definition of the imaging plane and contaminations by out of focus light. These issues do not appear in the single layer of cell cultures and epifluorescence still is a very advantageous method in this case. Confocal microscopy allows for a nice limitation of the imaging plane and some level of penetration in the sample and this technique is a good option to image in thin samples with multiple cell layers like brain slices. Finally, to image deep in the tissue one can either use a light source penetrating deeper in the tissue like in two-photon imaging or move the guiding optics inside the tissue. The result is using optic fiber implanted inside the tissue to excite and record fluorescence. By inserting an optic fiber deep in the tissue, we can record optical signals normally only accessible through electrophysiology or fMRI. This method is quite economical in its simple form needing a single light source and detector as well as simple optics. The main advantageous aspect of this method in our study was the non-metallic nature of optic fiber making it compatible with fMRI studies. Electrophysiology recordings during fMRI sessions are non-trivial and require a lot of adaptation in the recording equipment, data analysis and MRI sequence. In part because the magnetic field of the MRI induces currents in the recording electrodes that are magnitudes larger than the recorded signals. The electrodes being metallic also heavily distorts the MRI magnetic field resulting in artefacts in the MR image. Optic fibers are composed of glass and plastic, they produce very little distortion of the magnetic field resulting in less imaging artifacts than metallic probes. The light transmitted and collected is not affected by the magnetic field either. The only adaptation that fiber optic recordings eventually necessitate is eventually a coil modified with a groove to accommodate the fiber, but this can be bypassed depending on the recording region. The last potential advantage of optical recordings over electrophysiological recordings is the possibility to genetically define the population one wants to record from.

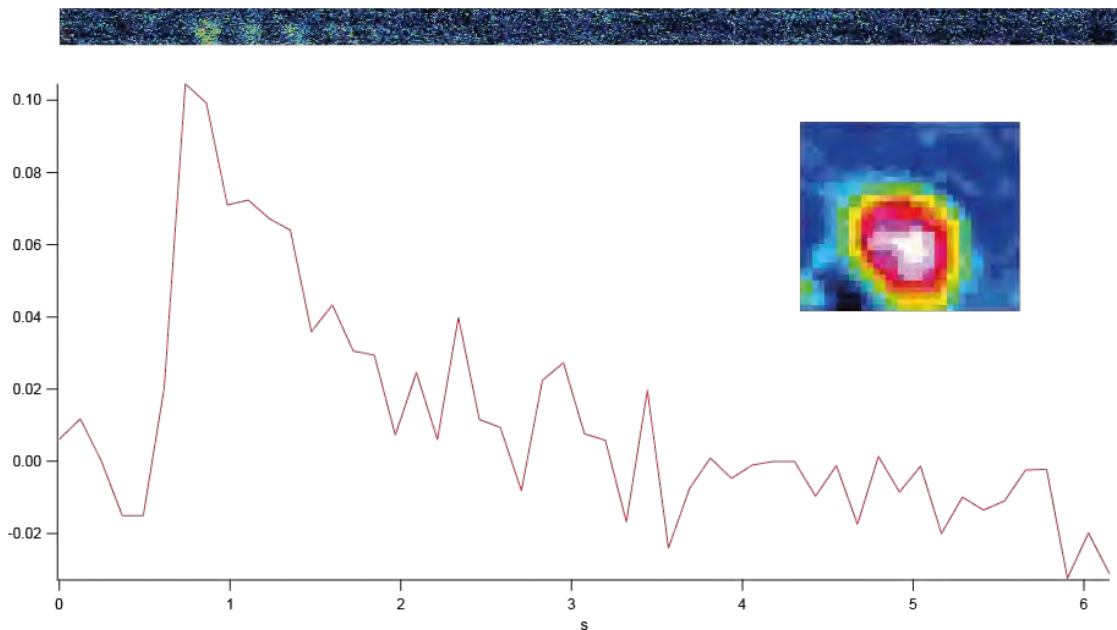


Figure 1-12: OGB-1 Fluorescence correlate of action potentials in a neuron. Top line: timelapse of fluorescence ($\Delta F/f_0$) change over 6 seconds in false colors. Bottom graph: fluorescence intensity change over time in the same neuron over the same period. Dynamics are similar with other sensors with only the peak value and characteristic decay time changing with affinity. (Fig. PH Prouvot)

Current state of the field

Two-photon calcium imaging represents the best available mix of spatial and temporal resolution for calcium imaging. One of the main advantages resides in the visualization of inactive cells and the identification of cells in time without the need for advanced classification methods like spike sorting. This method also presents excellent spatial resolution in the lateral (usually tangential) direction, it only allows recording in one tangential plane at a time unfortunately. Thanks to an emergent property of these recordings, we can also get a global readout of activity thanks to averaged signals from the neuropil. We can also use this method in combination with gene delivery techniques to record from a genetically defined cellular population. Disadvantages to 2P calcium imaging do exist, the readout is limited to a single plane, often tangential to the brain surface even though some techniques exist to mitigate it like GRIN lenses (M. Yang et al., 2019), implantable microprisms (Andermann et al., 2013) or AODscopes (Villette et al., 2019). Timing the system with external modalities can be difficult. Online readout of activity quantitatively is not always possible depending on the system. Finally, two-photon microscopes are complex machines requiring maintenance and that can be complex to operate.

Recently three photon microscopy has been achieved by increasing the excitation wavelength further and exciting fluorophores with three simultaneous photons. The result of shifting the excitation light further in the infrared is even deeper penetration (N. G. Horton et al., 2013; Wang et al., 2018). This comes at the cost of a more difficult detection of emitted light, which can be partially alleviated by using red-emitting fluorophores. The larger distance between the objective and the light source increasingly being a problem here. The final problem of using three-photon is that increasing the excitation wavelength pushes it into the absorption spectrum of water which peaks around 1600nm greatly limiting the potentially usable fluorophores. The increased absorption even before the peak could also result in extra heating of the sample.

History of electrophysiology

The concept of organisms producing electrical currents has been known before the discovery of electricity since certain species of teleost fish have been known to produce currents as far as antiquity. Ancient Egyptian and Greek naturalists reporting of their effect on the human body (Moller, 1991). The true beginning of the scientific investigation of electrical signals in organisms can be dated to the experiments of Volta and Galvani discovering respectively the anatomy of organs producing electricity in *Scophthalmus maximus* (a type of flatfish colloquially called turbot) and that electrical currents can induce muscular contractions. These discoveries constitute the first experiments of electrical stimulations. In the middle of the 19th century Carlo Matteucci measured the first membrane potential difference in tangential sections of muscle, around the same time Emil du Bois-Reymond recorded the first fluctuations in membrane potential in stimulated nerves and muscles. By the end of the century two students of Bois-Reymond posited the mechanisms of creation and transmission of nervous potentials. The recent equation describing the diffusion potential of two solutions of different concentrations by Walther Nernst then allowed Julius Bernstein to describe the resting potential of nerves. The experiments of Wilhelm Ostwald combined with the theory of an isolating membrane separating two different ionic solutions then allowed him to set the basics of modern electrophysiology in 1912. Electrophysiology as a discipline appeared only with the advent of sufficient signal amplification and was greatly facilitated by the invention of operational amplifiers in 1967 by Karl D. Swartzel and Georg Erdi at Bell labs.

The next founding experiments happened when Kenneth Stewart Cole and H. J. Curtis developed their experimental model of squid giant axon which was then improved upon by Hodgkin and Huxley when they invented voltage clamp (Hodgkin et al., 1952) and measured

for the first-time sodium and potassium conductance. This paved the way to an application of similar methods in mammalian neurons by Ernst Neher and Bert Sackmann when they invented patch clamp recordings (Hamill et al., 1981), breaking further ground for electrophysiology as we know it now. Interestingly being at the intersection of multiple disciplines like physics, chemistry and biology for a long time (and arguably even now) electrophysiology has been dependent on methodological improvements in either of these domains. On one side theoretical discoveries like the Nernst equation and on the other side improvements in the field of electronics for the recording equipment.

Experimental stimulation of neuronal activity

It is natural that modulating the recorded activity became an essential issue in experimental investigation of the brain. The earliest way of doing so is by using drugs either produced chemically or naturally occurring. Electrophysiology has developed an important pharmacopeia to modulate every possible aspect of neuronal activity in vivo or in vitro. Pharmacological modulation is intrinsically limited by its kinetics, the kinetics of diffusion in the medium and of the affinity to the targeted receptors. Some drugs are very fast acting but even in brain slices the modulation onset happens on the scale of tens of seconds and the offset is dependent on the kinetics of the drug.

The fast alternative to chemical modulation has for the longest time been electrical stimulation. By inducing an electrical current either in the vicinity of neurons or directly across the membrane in whole cell configuration it is possible to induce action potentials (Barbour, 2014; Stüttgen et al., 2017). This is still the gold standard to study connection between individual neurons using patch clamp. Volume electrical stimulation of multiple neurons has multiple disadvantages. By inducing a current between two electrodes one certainly can excite neurons or passing fibers of interest but it is almost impossible to avoid unwanted stimulation due to the intertwined nature of the brain (Komarov et al., 2019; Meffin et al., 2012). As a result, one can stimulate excitatory passing fibers as well as inhibitory, resulting in contradictory effects.

In 1976 the team of Kaplan developed a method to optically control the release of neurotransmitters (Kaplan & Ellis-Davies, 1988). This innovation consisted in “caging” a neurotransmitter in a chemical “cage” that would block the active site preventing its binding to receptors. A pulse of light at a specific wavelength would induce photolysis of the cage resulting in the release of the neurotransmitter (E. B. Brown et al., 1999; Kantevari et al., 2006). This technique is still useful in vitro because of the extremely fast kinetics of the release and of the

high spatial resolution. High enough to stimulate single synapses, it is still in use for in vivo studies of synaptic physiology (Ellis-Davies, 2019; Pettit et al., 1997). The next improvement came from unicellular organisms and would greatly facilitate all optical physiology.

Optical physiology

The concept of optical physiology is dependent on several technological advancements. The discovery of opsins by Oesterhelt and Stoeckenius, began in 1971 (Oesterhelt & Stoeckenius, 1971) and their investigation of their mechanisms or applications continued until the breakthrough in 2005. In that year two publications by the teams of Karl Deisseroth and Alexander Gottschalk demonstrated optical control of neural activity using channelrhodopsin in mammalian neurons and *C. Elegans* respectively (Boyden et al., 2005; Nagel, Brauner, et al., 2005; Nagel, Szellas, et al., 2005). Giving credit where it is due let us not forget the considerable groundwork laid by Georg Nagel, Ernst Bamberg and Peter Hegemann who identified and characterized the Channelrhodopsin 2 currently in use across the world and that organized this historical collaboration (Nagel, Brauner, et al., 2005; Nagel et al., 2003; Nagel, Szellas, et al., 2005).

Current commonly used opsins have a variety of mechanisms from halorhodopsin pumping chloride into the cytoplasm and bacteriorhodopsin that pumps protons out of it, (both inhibitory in neurons) to channelrhodopsin that lets positive ions flow both ways (mostly depolarizing and excitatory) and its variants. Later the genetically engineered chloride channel for fast control of hyperpolarization was published in 2014 (Berndt et al., 2011, 2016; Wietek et al., 2014). And in 2015 a naturally occurring chloride channel was discovered (Berndt & Deisseroth, 2015; Govorunova et al., 2015). The second step was the expression of those in neural systems (addressing expression level, retinal levels). Original heterologous expression was achieved in the 80s-90s (Hoffmann et al., 1994; Nagel et al., 2003), the first expression in mammalian neurons was published by the team of Karl Deisseroth in 2005 (Boyden et al., 2005; F. Zhang et al., 2007) all in all it was found that no other component than the nagel 2003 single gene expression of the opsin was enough for modulation of activity by light. Interestingly optical activation of neurons was reported earlier by the team of Gero Miesenböck in *Drosophila* using a different system (Zemelman et al., 2002). And in *Caenorhabditis elegans* by the team of Alexander Gottschalk (Nagel, Brauner, et al., 2005).

Excitatory opsins induce excitation of the illuminated cell. We used channel-type opsins, specifically Channelrhodopsin 2 H134R. This opsin is a channel permeable unspecifically to positive ions like sodium and potassium and to a lesser extent calcium, when illuminated with blue light the peak being around 488nm (Nagel et al., 2002). We used the H134R variant because of its improved photocurrent to the wild type (Berndt et al., 2011). The kinetics of ChR2 are peculiar presenting a peak and a fast transition to a steady state current. The dose response curve is also sigmoid which we had to keep in mind when choosing the excitation power. For the stimulations to be modulated the chosen power should be within this linear range. If the stimulation power is already at maximum, it becomes impossible to modulate the response both ways. The kinetics of longer excitations have been described in detail by Kuhne et al in 2019, briefly ChR2 can follow two isomerization paths upon illumination, a fast C1-O1 (Glu90-anti) cycle or a slower C2-O2 (Glu90-syn) cycle. Because the conductance of the O2 state is lower and its kinetics slower it tends to accumulate during continuous illumination supplanting the C1-O1 cycle as the dominant one until the opsin population in the cell membrane reaches a steady state between both states.

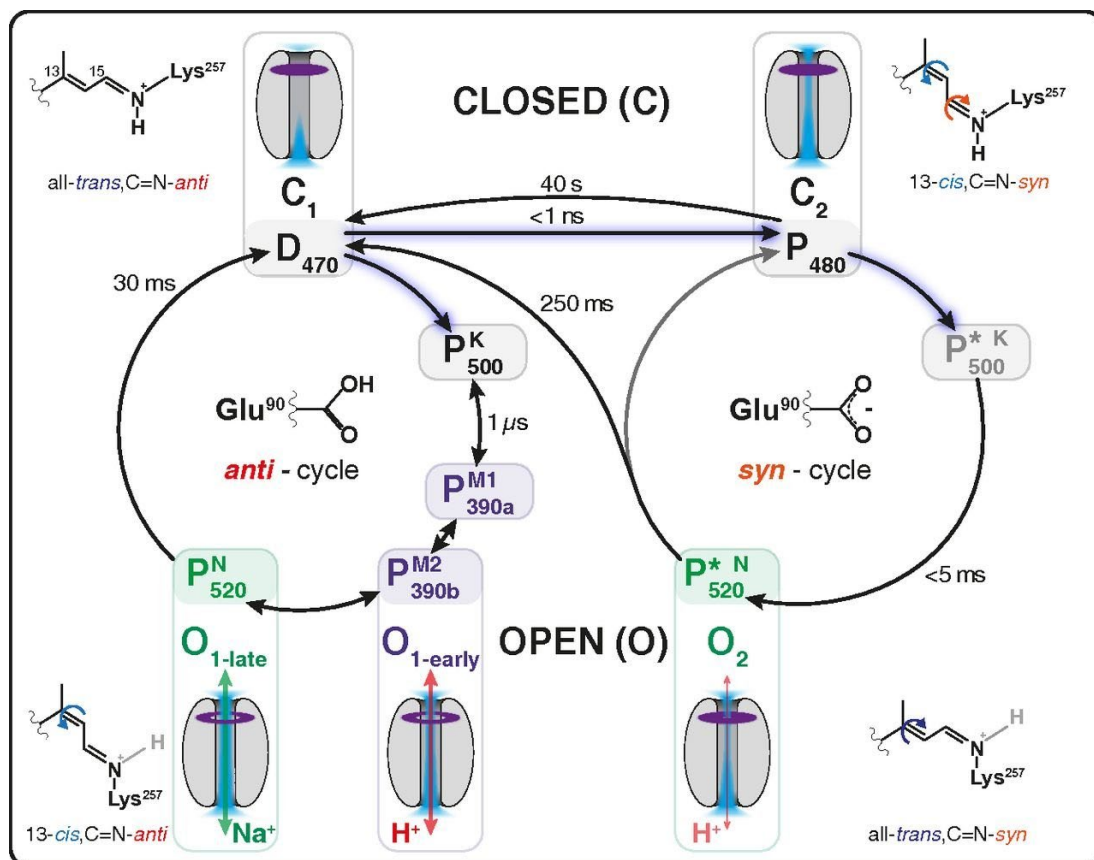


Figure 1-13: Schematic of the ChR2 photocycle proposed by Kuhne et al., 2019. Top left classical photocycle of sequential opening of closing of the channel with time constants. two possible photocycles with different time constants can be entered from the closed state resulting in adaptation upon continuous illumination.

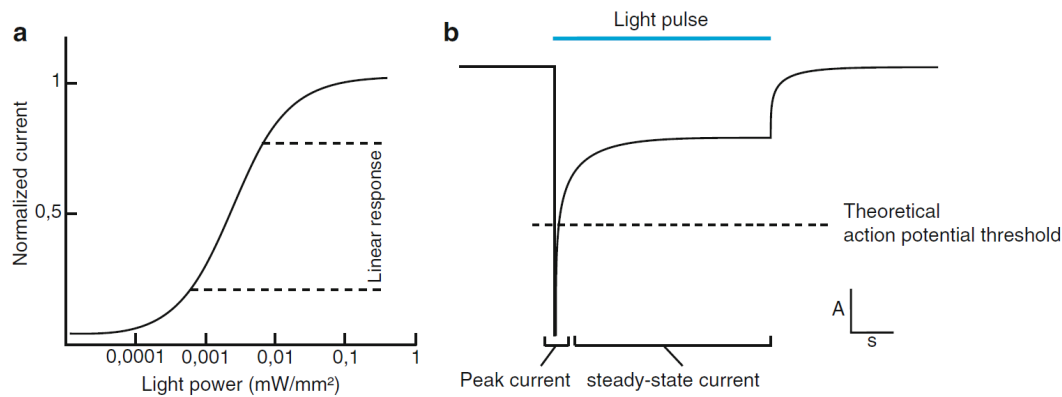


Figure 1-14: Kinetics of ChR2 A: Dose response curve for an excitatory opsin adapted from (Prigge et al. 2012). For the subsequent effective and low-impact optogenetic experiments, we chose a light power density in the linear section of the dose–response curve. B: Typical inward current elicited by longer illumination (light pulse indicated by blue bar) in a cell that would be recorded in voltage clamp (adapted from Stroh, 2018, figure by PH. Prouvot) displaying the typical peak and steady state currents predicted by the model from Kuhne et al., 2019.

Proton pumps

To inhibit action potentials in neurons one needs to hyperpolarize the intracellular compartment. Achieving that artificially can be done in multiple manners but only a few naturally occurring opsins have suitable characteristics. The two main mechanisms are entry of positive ions (proton pumps) or exit of negative ions (chloride channels). A chloride conducting variant has been mutated from channelrhodopsin, producing small but significant hyperpolarizing currents (Wietek et al., 2015). Unlike channelrhodopsin this channel lets chloride ions through when illuminated at 470nm resulting in a hyperpolarizing current at the resting membrane potential. We did not use chloride pumps for these projects because we preferred the more reliable, higher photocurrent proton pumps. It is important to remember that depending on the reversal potential of chloride ions their entry can be excitatory or inhibitory and prolonged opening of the channel can allow the cell to reach that reversal potential (Delpire & Staley, 2014).

Proton pumps operate under a more complicated mechanism but have simpler kinetics. We will concentrate on Archhodopsin here because it is the inhibitory opsin used in this work. This pump was isolated as archaerhodopsin-3 from *Halorubrum sodomense* and then improved upon by the Boyden group. The current induced by ArchT is slower to reach a steady state but stays stable and doesn't present any sharp peak. ArchT, that we used in this work, is an active proton pump gated by photon capture. The photocycle requires the capture of a photon for the pumping of a proton. Unlike it is the case for channels, when the light is turned off, photons are no longer

supplied, and the pumping stops in under a millisecond. It also present a simple cycle with no branching into an inactivated state (Han et al., 2011).

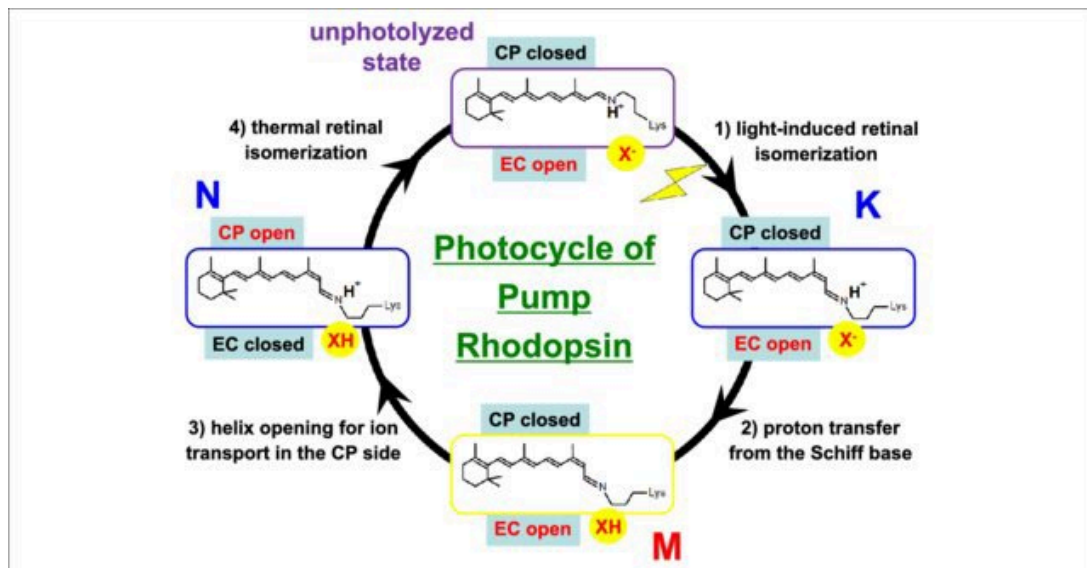


Figure 1-15: General photocycle of pump rhodopsins, presenting the retinal isomerization configurations relative to the photon absorption and proton pumping. Here bacteriorhodopsin hence the bacterial retinal, the mechanism is similar for other bacteriorhodopsins. CP: Cytoplasmic domain, EC: Extracellular domain. X represents the counterion of the Schiff base of the retinal. The cycle consists in four stages of opening and closing of the Cytoplasmic (CP) and Extracellular (EC) domains of the channel and protonation of the retinal. CP and EC opening is exclusive as is normally the case for ion pumps. When EC is open a proton can attach to the retinal at the same time as the counterion of the Schiff base is deprotonated. The retinal is then isomerized, allowing for the transfer of the proton to the Schiff base. Proton that is then transferred to the cytoplasmic side and released to the cytoplasm. (Fig from Kandori, 2015) CC BY.

Optogenetics in the somatosensory cortex

Applying optogenetics in the somatosensory cortex is straightforward given the advancements already made. The cortex is easily accessible through surgery and each region is large enough to be targeted reliably. The main property of the cortex to take into account is the unexplained impermeability of layer IV to certain virus transduction (AAV 1-2-8-9 Aschauer et al., 2013; Watakabe et al., 2015), it seems that the virus load does not cross layer IV and that very few neurons get transduced inside this layer. This is important to consider when performing the virus injections. To achieve expression across layers II/III and V/VI it is preferable to inject in multiple steps. It can also be taken advantage of to achieve layer specific expression above or below layer IV.

Electrophysiology

Recordings of local field potentials

In this work we acquired electrical signals using two methods very similar in principle. We started by using single point local field potential recordings for practical reasons. First the electrode is inserted in a glass pipette containing a conductive solution. The advantage is twofold, one it is easier prepare, glass pipettes are simple to produce, and it is possible to adjust their resistance (especially compared to gold plated tungsten electrodes). Second the equipment necessary is very simple, the amplifier doesn't need to be of excellent quality and replacing the wire or the glass pipette is fast and simple. We chose to use low pass filtering for most of these recordings since we were mostly interested in slow modulations of brain activity, this in turn allowed us to work in less-than-ideal conditions regarding electrical noise. A lot of these experiments were performed using a mobile setup installed temporarily on a surgical table and had to be re-installed and de-noised for every single recording. The technical work required albeit lower than for a lot of electrophysiology experiments is still non negligible to be able to dismantle and reassemble the whole system for each experiment. The LFP signal is an average signal of electrical activity in a volume around the recording electrode. The signal is typically low pass filtered to avoid noise and singular fast events like action potentials. The signal recorded have long been thought to be very local but the last decade has shown us that events can propagate and be recorded millimeters or in extreme cases centimeters away from their source. The activity recorded then is a mixture of local potentials and further away conducted potentials (Kajikawa et al., 2011). Field potentials also are not necessarily related to action potentials and are arguably even dominated by subthreshold synaptic activity (Herreras, 2016). As a result, we will limit our interpretation of single channel LFP recordings by themselves, using them mostly for comparison to calcium recordings.

Multi electrode arrays in vivo

On the other side of the complexity spectrum of electrophysiology is multi-electrode array recordings. These systems are composed of arrays of silicon recording sites arranged in various manners. A well-known type is in vitro multi-electrode arrays arranged in a recording chamber used to record from cell cultures and brain slices. While extremely useful for in vitro multi-site and even transversal recordings we will not discuss those in detail here. For this work we used so-called Michigan probes developed by the company Neuronexus. These arrays of electrodes can range from 1 to 256 recording sites depending on the complexity of the experiments. These

setups represent a significant monetary investment, be it for the amplifiers and software or for the probes themselves. Moreover, these expensive probes are consumables owing to their considerable fragility. Single channels of a silicon probe routinely become damaged after a few experiments and lose their conductivity and the lifetime of a probe varies depending on the number of recording sites available. Because of that it becomes essential to invest significant time into getting the best out of those experiments, de-noising must be as good as possible in order to record all available frequencies as well as possible. One of the advantages provided by having numerous recording sites is the complexity of the data acquired. The analysis can become as complex as needed from surface level analysis of the filed potentials all the way to spike sorting and complex analysis of single cell response patterns. All the silicon probes recordings presented here have been performed by [REDACTED] while we provided the optogenetics, histology, virus injections, analysis design and technical help during the experiments.

Viral transduction of neurons.

Innovations in the techniques of protein transduction played a major role in the accessibility of optogenetics and later calcium imaging. There are three main ways to induce expression of a heterogenous protein in an organism.

In utero electroporation consists in extracting embryos during pregnancy and using electrodes to induce an electrical current to permeabilize the membrane of cells in the region of interest to allow negatively charged DNA of plasmids to enter the cells (Borrell et al., 2005; Langevin et al., 2007; Shimogori & Ogawa, 2008). It takes advantage of the small volume of embryonic brain to achieve large expression in adults. It is also not limited in the size of gene transfected. The disadvantage is the technicity of the method and the resulting expression being often sparse. One also needs to know well the developmental path of the region of interest.

Transgenic lines consist in generating animals, often mice, innately expressing a heterogenous protein. This is nowadays achieved either by transfecting the gene of interest into the zygote to achieve expression in the future germ lines. Nowadays the cripr-cas9 system is often used to achieve precise insertion into the genome (Cho et al., 2009; Zariwala et al., 2012). This technique is the most time consuming and requires multiple generations of animals, explaining why it is limited to those that reproduce fast (mice, zebrafish, drosophila).

The resulting expression is extremely stable and in the whole organism or whole organ depending on the promoter. Finally, it can cause developmental defects because of the proteins expressed are active and can perturb endogenous functions. As it is the case for in the case of cognitive impairments of the early Gcamp mouse line (Steinmetz et al., 2017).

We did not use these methods instead we took advantage of the recent improvements viruses for transduction. Different viruses types can be used, lentiviruses, adenoviruses, herpes simplex and modified rabies virus. Each type has different tropism, infection properties and carrying capacities. We only used viruses in our project because they represent a good trade-off of cytotoxicity to load capacity (around 4.7kb) (Dumitriu et al., 2007). Lentiviruses are also commonly used because of their high carrying capacity (6kb) but their biosafety level (BSL-2 vs BLS-1 for AAVs) and their random genomic integration makes them less than ideal (Sakuma et al., 2012).

We used either direct promoters or the Cre-lox system to achieve cell-specific expression of our constructs. The Cre-lox system allows for cell type specific expression even in the case where the cell specific promoter only induces weak expression. By expressing the Cre recombinase under a cell specific promoter and the protein of interest flanked by loxP sites under a strong pan neuronal promoter one can combine a strong expression with precise cell specificity (Hamilton & Abremski, 1984; Hoess et al., 1985). Here we used a mouse line expressing the Cre recombinase under the control of the parvalbumin promoter to induce expression of opsins driven by a pan-neuronal promoter.

In certain cases, not presented here, we used a double virus approach. This workaround can be used when the mouse line of interest does not exist or to induce expression stronger than by using cell specific promoters directly. The easiest to obtain expression of a protein from a plasmid is to have the reading sequence of the protein in sequence with the selective promoter. This methodology produces good expression, but the expression level is limited by the promoter. In the case of cell specific promoters like DBH or VGAT the issue is that these promoters do not drive very high expression. This workaround is to have the protein of expression in sequence with a strong pan-neuronal promoter but have it reversed and between flox cassettes. The cell specificity is then provided by driving Cre expression under a more specific promoter. The Cre expression can be provided by a secondary virus or by a mouse line. This double virus approach while it allows for a smaller stockpile of viruses necessitates titration of virus combinations to avoid cytotoxicity.

Materials and methods

Mouse line and viruses

Mouse lines for optogenetics and electrophysiology

All experiments were designed to minimize the number of animals used. All procedures related to the care and treatments of animals were approved by a local ethics committee (number 23 177-07/G10-1-010) and followed the European and German national regulations (European Communities Council Directive, 86/609/EEC).

Mice used for project electrophysiology and optogenetics combination

A total of 18 PV-Cre mice (13 males and 5 females, 1.5-9 months, B6, 129P2-Pvalb, Ref. 017 320, Jackson laboratories) were used for photoinhibition experiments. Six PV-Cre mice (male, 4-5 months) were used for photoactivation experiments. Three C57BL/6 mice (male, 11.5 months) and 6 PV-Cre mice (4 males, 2 females, 2-4.5 months) were used for testing the photoelectrical effect on the LFP. In total, 13 PV-Cre mice (6 males, 7 females, 2-10 months) were used for immunohistochemistry.

Mice used for chronic calcium imaging

For the two-photon imaging experiments presented here we used C57/Bl6 J mice for OGB-1 imaging experiments 6 mice (4 males, 2 females) for Gcamp6f visual cortex recordings 6 for barrel cortex recordings (all females) and 6 SJL/J mice for testing holder configurations and recordings of spontaneous activity (all females). All mice were aged 3-10 month old. Under the same ethical committees as the first section.

Mice used for intrinsic optical imaging

Conditional PRG-2^{-/-} (coPRG-2^{-/-}) mice lines were obtained by flanking exon 1 of prg-2 with LoxP sites allowing for removal by Cre recombinase expression. For our experiments we used a constitutive PRG-2 KO mouse line generated by mating coPRG-2^{-/-} mice with a Del-Cre line (Schwenk et al., 1995). By breeding PRG-2^{+/-} mice, we generated littermates of wild type and PRG-2^{-/-} mice. Gbx2-Cre-ERT2 (Gbx2CreER) mice (L. Chen et al., 2009; Normand et al., 2013) were provided by J. Li (UConn Health Center). R26loxPSTOP-loxP-tdTomato (R26tdTomato) mice (Madisen et al., 2010) were purchased from Jackson laboratories (stock #007905). Genotyping for CreER was performed as described (A. Brown et al., 2009),

genotyping for the R26tdTomato allele was performed as described on the jax.org website. To inactivate PRG-2 in thalamic neurons, E12.5 pregnant PRG2^{fl/fl}/Gbx2CreER/R26tdTomato female mice were administered 4mg of tamoxifen (20mg/ml in corn oil) by oral gavage as described (Brown et al. 2009). The morning of the day a vaginal plug was detected, was considered as embryonic day E0.5.

Rats used for fiber and LFP recordings

We performed LFP and Calcium recordings on 11 female Fisher rats with a body weight between 160 and 180 g. Three additional rats received Calcium recordings only. Animal husbandry and experimental manipulation were carried out according to animal welfare guidelines of the Westfalian Wilhelms-University and the Johannes Gutenberg-University Mainz and were approved by the Landesamt für Natur-, Verbraucher- und Umweltschutz Nordrhein- Westfalen, Recklinghausen, Germany, and the Landesuntersuchungsamt Rheinland-Pfalz, Koblenz, Germany.

Viral transduction vectors

To express ArchT-GFP, archT-dtomato and ChR2-dtomato we used adeno associated viruses from the virus vector core of Penn state university (Philadelphia PA US, Now addgene). The gene of interest were under the control of LoxP cassettes allowing them to be expressed only under the condition that the Cre recombinase was present in the transfected cells. We used different methods to achieve high enough expression rates in our cells of interest all based on the Cre-Lox system. To achieve expression in PV interneurons we used a mouse line expressing the Cre recombinase under the control of the Parvalbumin gene in combination with a virus containing the floxed gene of interest. In the case of co-expression of gcamp6f and opsin coexpression we used the same strategy for the opsin but the gcamp6f was under the control of a camKII promoter to achieve specific expression in pyramidal cells. We used Serotype 2 rAAV2-FLEX-ArchT-GFP, rAAV2-FLEXArchT-tdTomato, or rAAV2-FLEX-ChR2mCherry We used serotype1 AAV1.CamKII.GCamP6f.WPRE.SV40 for gcamp6f expression.

Surgical preparations

Virus injection

To obtain expression of either ArchT or ChR2 into Parvalbumin interneurons the standard procedure consisted in using a transgenic mouse line expressing the Cre recombinase under the

control of the PV promoter. Injections or viral solutions were conducted under deep isoflurane anesthesia (Forene, Abbott, Wiesbaden, Germany). PV Cre mice were placed on a warming pad (37 C) and fixed in a stereotactic frame (Kopf Instruments). At the level of the somatosensory barrel cortex (AP: -2mm, ML: 3.5mm) Or the somatosensory forepaw in rat (S1FL: 0 mm AP, +3.5 mm ML, -0.5, -0.7 and 0.9 mm DV), the skull was thinned with a dental drill (Ultimate XL-F, NSK, Trier, Germany), and a small cranial of 0.5mm opening was prepared under a dissecting microscope using a small injection needle.



Figure 2-1: Simplified methodology for cortical virus injections without using a stereotactic frame. 1. Isoflurane anesthesia of the mouse. 2. Longitudinal incision of the cranial skin. 3. revealing the skull surface and marking coordinates from bregma to identify region of interest. 4. using temporary glue to affix a metal holder to the skull surface. (Fig. from JW. Yang and PH. Prouvot from J. W. Yang, Prouvot, et al., 2018 reproduced with permission from Springer Nature).

The dura was kept intact. A microtiter pipette pulled by a horizontal puller (Sutter Instruments, Novato, CA) to a tip diameter of around 5 μ m (Fig. 1e2) (Ringcaps Hirschmann Laborgeräte GmbH, Eberstadt, Germany) was connected to a flexible plastic tube of a 200 ml syringe. A piece of Parafilm was placed on the craniotomy, and then 1–2 μ l of virus solutions containing 2x10¹¹ viral particles per ml, rAAV2-FLEX-ArchT-GFP, rAAV2-FLEXArchT- tdTomato, or rAAV2-FLEX-ChR2-mCherry in PBS were placed on the Parafilm. About 300 nl viral solution (0.6x10⁸ viral particles) were slowly injected using manual pressure within 3min at 300 and 600 μ m cortical depth from the pia before leaving the pipette in place 5min and slowly retracting the pipette. The skin incision was closed with Vetbond tissue adhesive (3 M, Maplewood, Minnesota, USA), and the mice were returned to the cage for recovery. Functional experiments were conducted no earlier than 2 weeks after surgery for details see (Mocanu & Shmuel, 2021; J. W. Yang, Prouvot, et al., 2018).



Figure 2-2: Protocol for the virus injection. 1. Representative picture of the craniotomy size for a single injection. 2. Picture of the tip of the pipette approx. 20 μ m outside 10 μ m inside diameter. 3. Method for front loading of the virus. The pipette is connected to a 50ml syringe to apply

negative pressure manually. 4. Injection of the virus. 5. Mouse after closing of the wound and a few hours of recovery. (Fig from JW Yang and PH. Prouvot from J. W. Yang, Prouvot, et al., 2018 reproduced with permission from Springer Nature).

Acute imaging preparations

The mice were put under isoflurane anesthesia 2.5% for induction subsequently reduced to 2% once the breathing rate reduced to 60-70bpm and anesthetic state was stable. The mice were fixed in a stereotactic frame (Kopf Instruments) on a heating pad at 37°C. A small craniotomy was prepared at the level of the barrel cortex as described in the previous section with the difference being that the craniotomy spanned an area of about 2x2mm. A 0,5mm spherical drill tip was used to progressively thin the skull surface around a square 2x2mm in area. The remaining thinned perimeter was progressively and carefully breached using a 31-gauge needle. Once the whole perimeter was breached the freed piece of bone was carefully lifted and removed using the same needle and Dumont forceps taking care to keep the dura intact.

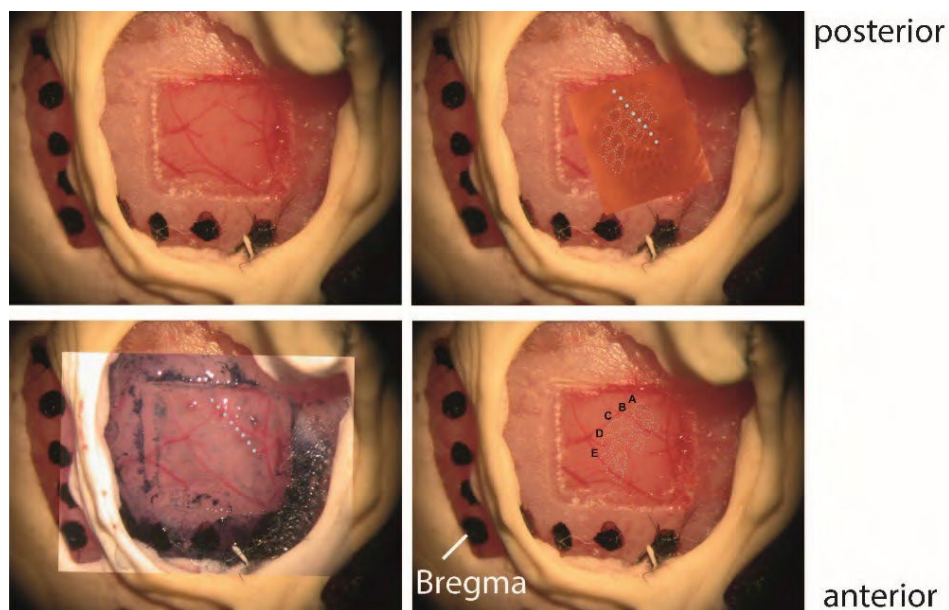


Figure 2-3: Stereotactic positioning of the barrel cortex black dots mark millimeters from bregma. Barrels can be identified post hoc from the positions of blood vessels. (Fig. from JW. Yang)

Particular care was taken to keep the animal in a physiological state during the whole procedure. Body temperature was kept at 37°C using a heating plate and probe in a feedback loop. The breathing rate was kept around 90-110bpm by counting manually and adjusting the Isoflurane concentration. A custom-made recording chamber was then glued onto the skull using cyanoacrylate glue (Vetbond 3M) and acrylic cement (Cyano Fast and Cyano Veneer Pulver.

Hager & Werken GmbH & Co. KG, Duisburg, Germany). We tested a variety of chambers before settling on the current model and method of attachment the different models are compared in Figs 6-10 to 12 multiple chambers. The mouse was then transferred into the imaging set-up, the implant was affixed and a warming plate as well as a piezo element for monitoring of breathing rate were placed under the mouse. Anesthesia was reduced to about 0,7% letting the breathing rate increase to 100-120bpm to allow recovery of a persistent up brain state. The recording chamber was perfused with commercial Phosphate buffer solution (sigma). A small volume of solution containing OGB-1 AM (500 μ M; Life Technologies/ Molecular Probes) was loaded in a 4-6M Ω glass pipette which was inserted down to 200300 μ m below the pial surface at which point the solution was pressure injected. Supplementary details can be found in (Ellwardt et al., 2018).

Chronic imaging preparations

For chronic and awake experiments, we used a classical chronic window preparation. Mice were anesthetized under 2% isoflurane and put in a stereotactic frame. A circle of skin was cut out up to about 1-2 mm from the muscle laterally and dorsally, frontally depending on the implant used we exposed the frontal skull plates covering the olfactory bulb or stopped at eye level. The edges of the skin were sealed with histological glue (Vetbond 3M St Paul, USA) after bleeding stopped, this prevented post-surgical bleeding, facilitates cicatrisation and greatly improves the durability of the implant. A 3mm diameter window was opened in the skull using a dental drill using a similar method as in the previous section. If a virus was to be injected, it was at this point (see Virus injections above). Then after cleaning of the surface of the dura using dental sponges (Gelfoam Pfizer Karlsruhe Germany) a glass coverslip of 4mm diameter was firmly held in place and glued along the periphery using histological glue, taking care not to let glue reach the pial surface. For more precise application the glue it was either applied with the smallest syringe needle gauge available (usually gauge 28) or with a glass capillary similar to the ones for virus injections but broken to have a shorter tip and larger opening of around 50-100 μ m. Great care was taken to leave PBS between the coverslip and the tissue surface, the excess was absorbed using surgical wipes. In short when removing PBS aim to leave a small dry space along the edges of the window while applying a little pressure to protect the opening. The head restraining implant was then glued to the skull using UV-hardening glue (UV2108 Polytec PT Germany), applying it in two to three layers to ensure proper hardening of each layer. We took care to form a cap covering the exposed parts of the skull. We tested two different

head restraining implants for this preparation (Fig. 6-11, 6-12), one provided by Phenosys with the VR system and the other one designed by the group of [REDACTED] in Heidelberg and reproduced by our in-house workshop. The second one was chosen for stability reasons detailed in the results section.

Histology

Immunohistochemistry

After the electrophysiological and imaging experiments, mice were transcardially perfused with 4% paraformaldehyde (PFA) under lethal ketamine/xylazine anesthesia to characterize the opsin expression. Brains were removed, fixed overnight in 4% PFA, and transferred to 30% sucrose solution. Coronal brain sections of 70 μm thickness were prepared using a vibratome (Leica, Wetzlar, Germany). For permeabilization, slices were incubated with 0.1% Triton X100 and 5% normal donkey serum (Invitrogen, Life Technologies, Carlsbad, CA) in phosphate buffer solution for 90 min. Slices were incubated with goat anti-PV (1:200, Swant, Marly, Switzerland) or rabbit anti-CamKII (1:200, Epitomics, Burlingame, CA) at 4 °C overnight. On the next day, slices were incubated with the secondary antibodies Cy-2 donkey anti-goat (1:200, Jackson Immuno Research, West Grove, PA), or Cy-2 donkey anti-rabbit (1:200, Jackson Immuno Research, West Grove, PA), and a fluorescent Nissl stain (red 615 nm, Neurotrace, Molecular Probes, Life Technologies, Carlsbad, CA). Slices were mounted using anti-bleaching Vectashield (Vector Laboratories, Burlingame, CA).

Quantifications of expressing neurons

To assess the number and density of optogenetically inhibited cells, we first imaged the area of expression in coronal brain slices of 5 mice using a confocal microscope (SP8, Leica, Mannheim, Germany) and a 20x objective (HCX PL APO dry, Leica), with a numerical aperture of 0.70. Expression was confined to layers II/III and V, only very few cells could be observed in layer IV, in line with previous studies (Schmid et al., 2016; Stroh et al., 2013). Next, we quantified neurons exhibiting strong, membrane-bound ArchT-tdTomato (n = 3 mice) or ArchT-GFP (n = 2 mice) or ChR2-mCherry (n = 5 mice) fluorescence using an epifluorescence microscope (Olympus BX51, Japan, equipped with a 20 NA = 0.75 UPlanSApo Olympus objective) and dedicated software (StereoInvestigator, Microbrightfield, Williston, USA) in a randomized approach (Schmid et al., 2016). The quantifications resulted in average cell densities in layers II/III and layer V, as stated in the results section.

Our colleague Sophie Peron from the Berninger Ag performed similar quantifications in the case of opsin expressing newborn neurons in the olfactory bulb as follows.

The sections were washed in TBS (0.1M, pH 7.6) and incubated for 90 minutes in blocking solution (5 % Donkey serum, 0.3 % Triton X-100 in TBS 0.1M, pH 7.6) and then overnight at 4°C with primary antibodies diluted in blocking solution. The following antibodies were used in this study: rabbit anti-GABA (1:300, Sigma A2052, Sigma-Aldrich Chemie GmbH, Munich, Germany), rabbit anti-glutamate (1:75, Sigma Aldrich, G6642) and mouse anti-NeuN (1:500, Millipore, Burlington, Massachusetts, USA, MAB377). Sections were washed and appropriate secondary antibody diluted in blocking solution was applied for 1 hour at room temperature. Sections were counterstained with DAPI and mounted in Vectashield (VECTOR Laboratories, Burlingame, CA, USA) after washing. Confocal imaging was conducted using a Leica SP8 (Leica, Wetzlar, Germany) confocal microscope.

Electrophysiology

Multi electrode array recordings

Extracellular in vivo recordings were performed in the barrel cortex 1–3 months after virus injection. The mouse was anesthetized using urethane (1.5 g/kg, intraperitoneal injection), headfixed in a stereotactic frame and placed on a warming pad at a constant body temperature of 37 C. During recording, additional urethane (10-20% of the initial dose) was given when the mice showed any sign of distress. A silver wire was inserted into the cerebellum as ground electrode. A 2x2mm² craniotomy was performed over the barrel cortex, centered at the previous small craniotomy of virus injection. According to the location of the previous virus injection, an 8-shank 128-channel electrode (200 μm horizontal shank distance and 75 μm vertical interelectrode distance, impedances 1-2MΩ, NeuroNexus Technologies, Ann Arbor, MI) or 4shank 80-channel electrode (150μm horizontal shank distance and 50μm vertical interelectrode distance, 1–2MΩ) was inserted perpendicularly into the barrel cortex to record the LFP and MUA (Fig. 1A). After 60-90 min of electrode insertion, single whisker stimulation was performed to identify the targeted barrel columns. A single whisker was stimulated using a miniature solenoid actuator (modified from Krupa et al., 2001). The movement of the tip of the stimulator bar was measured precisely using a laser micrometer (MX series, Metralight, CA, USA) with 2500Hz sampling rate. The stimulus takes 26ms to reach the maximal 1mm whisker displacement, with a total duration of 60ms until it reaches baseline. Because the single whisker

was stimulated approximately 2mm distal from the base, the peak stimulus velocity is 1114°/s. In addition to the 1mm whisker displacement, we also use 0.4 and 1.6mm whisker displacement to test the effect of different stimulus strengths on the evoked response amplitude during the PV interneuron inactivation (Fig. 2-4). The positioning of the principal shank (PS) electrode in the center of the transduced area was confirmed in all experiments by postmortem confocal analysis (Fig. 3-1 and 3-2) in either tangential or coronal slices.

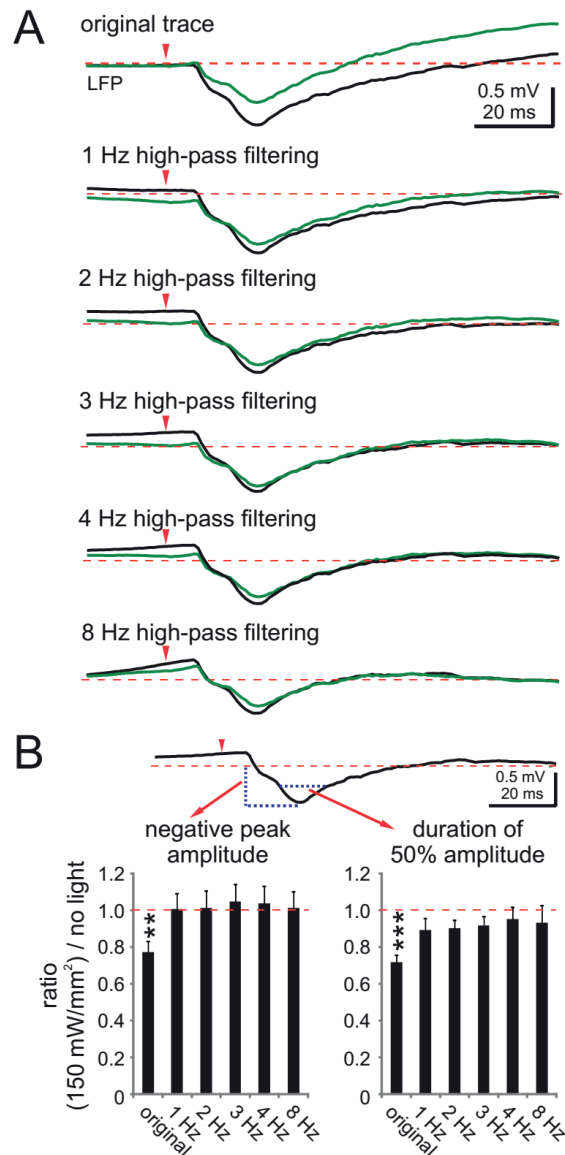


Figure 2-4: Determination of optimal filter settings for elimination of light induced artifacts. (A) Average of 80 evoked LFP responses to single whisker stimulation with (green trace) and without (black trace) light pulse illumination in deep layer II/III of non-ArchT expressing control mice (n=8, 3 C57BL/6 and 5 PV-Cre mice). The light-induced artifact could be reduced by high-pass filtering (1 to 8 Hz). (B) The amplitude of the negative peak and the duration of 50% amplitude of evoked response were calculated both for unfiltered and high-pass filtered traces. Bar diagrams show the ratio of amplitude and duration comparing light on (150 mW/mm²) and no light conditions. 4 Hz high-pass filtering and usage of negative peak amplitude values were used in all analyses presented in this study. Statistically significant

*differences are indicated by ** $p < 0.01$ and *** $p < 0.001$, paired t-test (Fig by JW. Yang J.-W. Yang et al., 2017 by permission with Oxford university press).*

For the ArchT experiments, we observed optically induced artifacts in our LFP recordings independent of ArchT, brought about by photons interacting with electrons in the metallic recording probe, termed Becquerel or photoelectric (PE) effect, as already reported by others (Cardin et al., 2010; Laxpati et al., 2014). To assess the scope of optically induced artifacts, we performed control experiments in 3 wild type mice and 6 PV-Cre mice without ArchT expression. Light illumination (100 ms, 150mW/mm²) altered evoked LFP recordings following single whisker stimulation. The PE effect was most notable in the 3 upper electrodes, corresponding to layer I and upper layer II/III (Fig. 2-5A).

We systematically compared the effects of different filtering settings (1, 2, 3, 4, 8 Hz high-pass filtering) on the evoked LFP and found 4 Hz high-pass filtering almost entirely compensate for the PE effect (Figs 2-4 and 2-5B). Light illumination (1 s, 150mW/mm²) also altered spontaneous LFP recordings. Fast Fourier transform (FFT) analysis shows a clear effect on the delta band (Fig. 8-1A 2-5). Again, 4 Hz high-pass filtering removed the PE effect in spontaneous LFP recordings (Fig. 4-1B). However, to minimize any potential contamination of our data, we used only electrodes located in deep layer II/III for our analysis, barely affected by the PE effect, but applied 4 Hz high-pass filtering to all data. We ensured filtering of the becquerel effect had an undiscernible effect on sensory evoked activity by applying light stimulation on non-expressing mice upon whisker stimulation. (Fig.2-5). For the ChR2 experiments, activating PV interneurons induced very large LFP responses at the very onset of illumination, representing the strong initial response (Stroh et al., 2013), strongly influencing the calculation of evoked LFP peaks. To overcome this issue, we additionally performed illumination without sensory stimulation. We then subtracted this early nonsensory-related component of the LFP response from the sensory-evoked LFP response. Data were imported and analyzed offline using MATLAB software version 7.7 (Mathworks, Natick, MA, USA). MUA was extracted from 800 to 5000 Hz filtered raw signals by applying a threshold at 7.5 times the baseline standard deviation (SD).

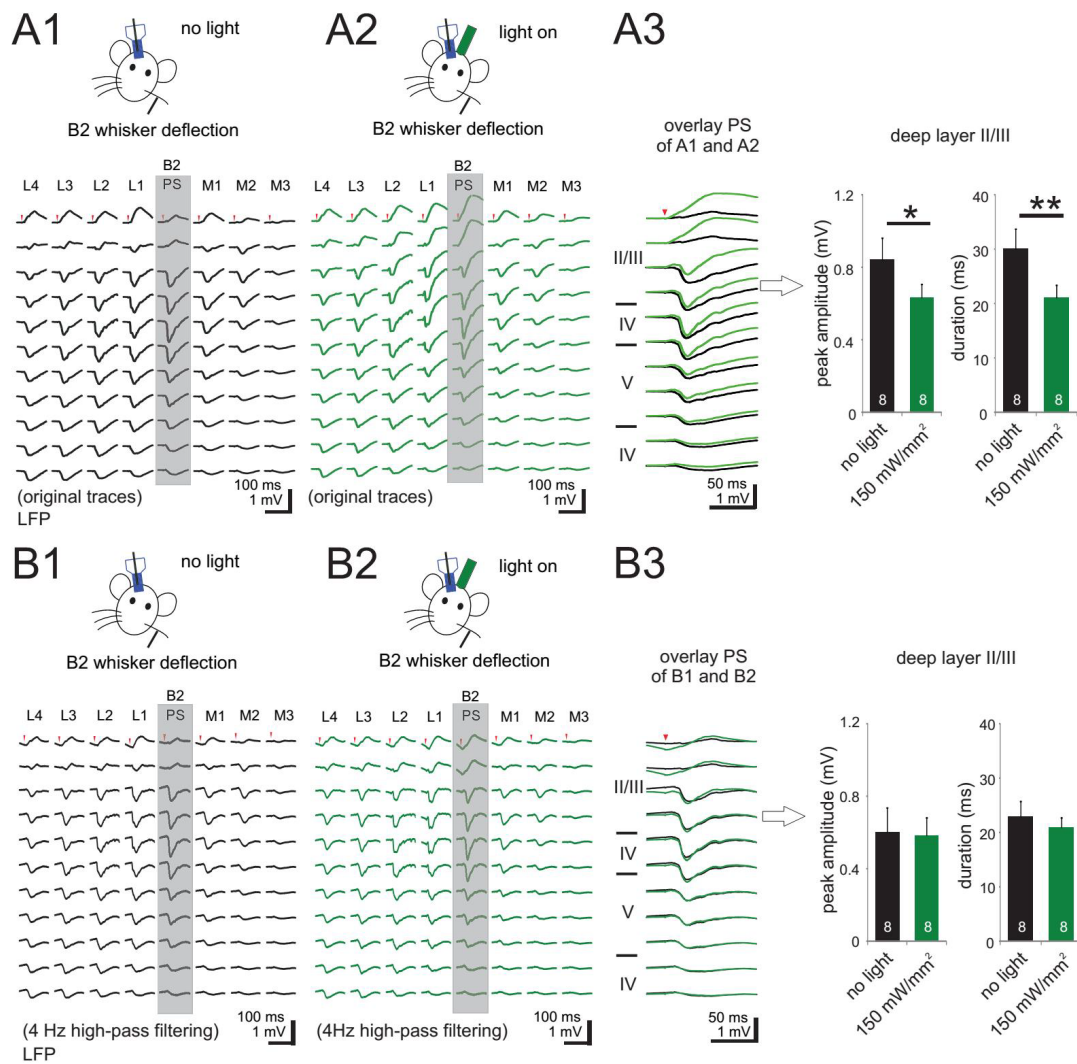


Figure 2-5. Effect of green light pulse illumination on evoked response by single whisker stimulation in non-ArchT expressing control mice. (A) Average LFP response to 10 stimulations of the B2 whisker under control conditions (A1, no light) and combination with 150 mW/mm² green light pulse illumination (A2, light on). (A3) Overlaying the evoked response in principal shanks of A1 and A2 shows strong expression of light-induced artifacts especially in superficial electrodes. Right, bar diagram showing that light illumination significantly reduces both the peak amplitude and the duration of the evoked response in the fourth channel located in deep layer II/III ($n=8$, 3 C57BL/6 and 5 PV-Cre mice). (B) Same as in A, but after high-pass filtering at 4 Hz. High-pass filtering eliminated the light-induced reduction of both peak amplitude and response duration in all but the three most superficial electrodes. (Fig by JW. Yang adapted from J.-W. Yang et al., 2017 by permission with Oxford university press)

Current source density analysis

Current source density (CSD) depth profiles were calculated from averaged sensory-evoked LFP responses. First, we duplicated the LFP traces in the uppermost and lowermost channels of each shank. One-dimensional CSD profiles were then calculated from the LFP according to a 3-point formula (Freeman and Nicholson 1975). The CSD values I_m were derived from the

second spatial derivative of the extracellular field potentials f and calculated by the finite-difference formula:

$$I_m = \frac{-(f(x-h) - 2f(x) + f(x+h))}{h^2}$$

where, h is the distance between successive measuring points (75 μm for 8-shank 128-channel electrode arrays and 50 μm for 4-shank 80-channel electrode arrays) and x is the coordinate perpendicular to the cortical layer. In the CSD profiles, current sinks are indicated by downward deflections and sources by upward deflections. To facilitate visualization of CSD profiles, we generated color image plots by linear interpolation along the depth axis. The blue color represents current sinks and red color represents current sources (Fig. 4-1C).

Up State Detection

The slow oscillations (Up–Down state transitions) were detected by the method described by (Compte et al., 2008). Briefly, LFPs in layer II/III were used to identify Up and Down states. First, raw LFP was down sampled to 1 kHz. Second, the envelope of the LFP (Figs 4-8 and 4-7A, dashed trace) was calculated by Hilbert transform and further smoothed using a 100 ms moving average. Third, the 1.5-fold of mean value of the envelope was employed as the threshold (Figs 4-8A and 4-7A, blue line) for the detection of transitions between Up and Down states. Up states shorter than 50ms were discarded.

Spike sorting

Spike detection and sorting were performed as described in detail previously (Reyes-Puerta, Kim, et al., 2015; Reyes-Puerta, Sun, et al., 2015). First, the raw data were high-pass filtered (0.8–5 kHz). Nonoverlapping groups of 2–4 channels were selected and at least one channel was left unused between neighboring groups to ensure that a sorted unit was present only in one group. Spike detection was performed in each recorded channel independently using 7.5-times the standard deviation of the signal. When a threshold crossing was detected in either of the channels within a group, all sampled amplitude values from all channels in the time range from -0.5 to $+0.5$ ms relative to the waveform negative peak were extracted. These spike waveforms were then used to compute feature vectors (negative peak amplitude and 2 first principal components derived from the waveforms). The feature vectors were then used to perform spike sorting using KlustaKwik and Klusters (Harris et al., 2000; Hazan et al., 2006). Several criteria were used to ensure the isolation quality of the sorted neurons (for details see Reyes-Puerta,

Kim, et al., 2015; Reyes-Puerta, Sun, et al., 2015). Cells were subsequently classified as putative inhibitory (INH) interneurons or putative excitatory (EXC) pyramidal neurons based on the mean spike waveform (Fig. 10C, D). For each neuron, 3 parameters were calculated and used to separate INHs and EXCs by k-mean clustering method: (1) spike half-width (ms), (2) the trough to right (late) peak latency, and (3) asymmetry index (Fig. 8-4).

Single channel field potential recordings

In the context of a collaboration with the team of Pr. Faber at the Universitätsmedizin Münster we traveled with a mobile LFP recording system in order to perform joint Fiber photometry of calcium signals and LFP recordings in the same region to control the correlation between electrical and calcium signals. The mobile system consisted of an EXT-02F external amplifier (npi electronic Tamm Germany) and a custom Fiber photometry system both coupled into a DAC converter. The rat was mounted in a stereotactic frame for the surgery and the recordings and was anesthetized either with Isoflurane through a gas mask or with a mix of medetomidine continuously perfused IP? The stereotactic frame was set on a steel plate itself and grounded to it, the steel plate itself was mounted on rubber pads to prevent movement artifacts. The headstage of the EXT-02F was attached to a scientifica patchstar micromanipulator (scientifica Maidenhead UK) for precise approach and positioning of the electrode.

In a series of control experiments (n = 3) simultaneous local field potential (LFP) recordings and calcium measurements (as described above) were performed outside the MR scanner. A pipette with a tip resistance of 0.2 MOhm filled with Phosphate Buffered Saline (Sigma, Munich, Germany) was inserted through a second craniotomy at a depth of 300 µm, lateral to the optic fiber insertion site. A reference electrode was inserted into the cerebellum, 1 mm posterior from Lambda and signals were amplified using an extracellular amplifier (EXT02F/2, npi Electronics, Tamm, Germany). Signals were filtered at 300 Hz (low pass), digitized at 2 kHz and recorded together with the optical signals using LabView.

Patch Clamp recordings of photostimulation

A cohort of animals was injected in the SVZ with ArchT-tdTomato, as described in the corresponding section. The mice were anesthetized with isoflurane and the brains were dissected and transferred in cold standard artificial cerebrospinal fluid (ACSF) solution of the following composition (in mM): NaCl, 125; KCl, 2.5; NaHCO₃, 25; CaCl₂, 2; MgCl₂, 1; NaH₂PO₄, 1.25 and glucose 25; saturated with 5 % CO₂ and 95 % O₂, pH 7.4. Coronal 300

μm thick OB slices were cut from the OB and transferred to a protective ACSF (34°C, 10-15 min) containing (in mM): 92 N-methyl-D-glucamine (NMDG), 2.5 KCl, 1.25 NaH₂PO₄, 30 NaHCO₃, 20 HEPES, 25 glucose, 2 thiourea, 5 Na-ascorbate, 3 Na-pyruvate, 0.5 CaCl₂, and 10 MgSO₄, pH 7.4 (www.brainslicemethods.com). The slices were left to equilibrate to room temperature in standard ACSF for at least 1 h, and then placed in a recording chamber, perfused (1 ml/min in standard ACSF) and mounted on a Zeiss microscope (Axio Imager 2, Germany) equipped with an epifluorescence lamp. The ArchT-expressing neurons were visualized with a 40X (0.75 NA) objective and subsequently patch-clamp whole-cell recordings were performed at room temperature with glass electrodes filled with (in mM): K-gluconate, 125; NaCl, 5; Na₂ATP, 2; MgCl₂, 2; EGTA, 10; HEPES, 10; biocytin, 10 and Alexa 488 hydrazide, 0.2 (Invitrogen) to allow the morphological analysis; pH 7.4. Current- and voltage-clamp recordings were obtained using Axopatch 200B (Molecular Devices, CA, USA). Current and voltage steps were generated with pClamp10 (Molecular Devices), which was also used for further analysis. Seal resistances were between 4 and 18 G Ω . Series resistance and whole-cell capacitance were not compensated. To stimulate ArchT-tdTomato-expressing newborn neurons, light flashes (0.1, 1 or 10 s, from 10 to 160 mW/mm² at the fiber tip) were delivered by the mean of an optic fiber (200 μm in diameter) and controlled by TTL pulses generated by the pClamp10.

Optogenetics

Light sources and modulation

For optogenetic stimulation we used OBIS lasers from coherent at respectively 488nm and 552nm for ChR2 and ArchT. These lasers were encased in a custom build system. Both lasers were directed at a dichroic mirror in order to collimate them in a single optical fiber. An ultrafast (1ms) shutter was installed the beam path to allow for fast and simple temporal modulation of the beam. The lasers power is modulated by the OBIS proprietary software. An alternative solution for temporal and power control is available using a combination of TTL and analogic signals directly to the laser control units but for our usual purpose the shutter was sufficient. The light for excitation of ArchT was delivered by a 60mW solid-state laser at 552nm wavelength (Sapphire, Coherent, Dieburg, Germany), and for ChR2 stimulation, a 50mW solid state laser at a wavelength of 488nm (Sapphire, Coherent, Dieburg, Germany) was used. Both lasers were placed in a custom-built optical setup. The laser beams were coupled to a 200 μm multimode fiber with a numerical aperture of 0.39 (Thorlabs, Munich, Germany) by means of

a fiber collimator (Schäfter + Kirchhoff, Hamburg, Germany). To ensure reproducibility of the power density used, the output power at the end of the fiber was measured prior to each experiment with a powermeter (Nova 2, Ophir, Newport, Irvine, CA). The initial power density was calculated with $I_0 = i/\pi r^2$, where i is the initial power and r the radius of the fiber core (0.1 mm). The light pulsing was controlled by a mechanical shutter (Uniblitz, Rochester USA) connected to a stimulator (Master8, A.M.P.I., Jerusalem, Israel). To keep the geometric shape of light illumination, the tip of the fiber was cut precisely using a diamond pen (fiber scribe S90R Thorlabs). The fiber was positioned parallel to the electrodes along the center of the electrode array by means of a micromanipulator and barely touched the cortical surface (Fig. 41).

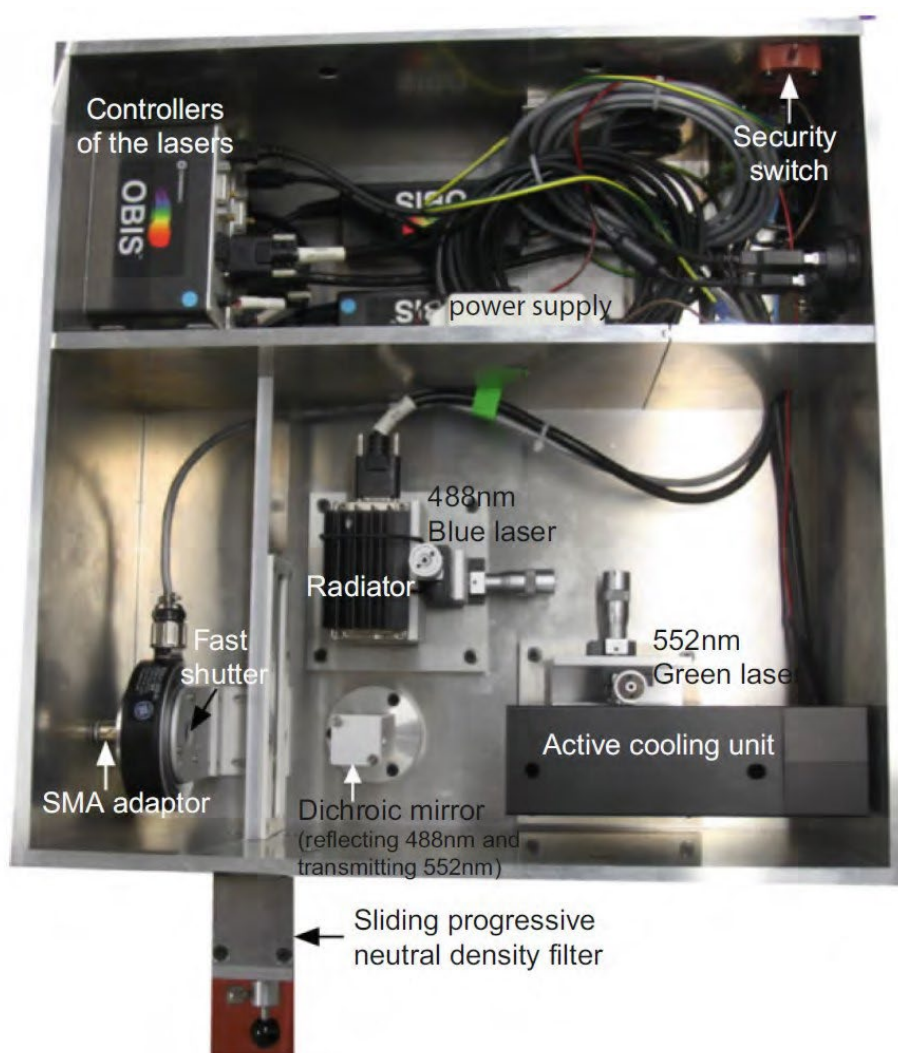


Figure 2-6: The laser system designed in-house for optogenetic stimulation.

Two OBIS lasers at 488 and 552nm are beamed into a dichroic mirror and coupled into a collimator for an optic fiber through an ultrafast shutter allowing for easy control of the beam. Both lasers are placed on platforms movable by micrometer screws to allow for precise alignment into the collimator to optimize power transmission. The 488nm laser uses passive cooling while the 552nm uses an active radiator as it produces more heat by design. A

progressive neutral density filter can be inserted into the path to provide fine control of the power since power control of the laser becomes unreliable under 10% power. Analog modulation is possible using SMB coaxial connectors on the control units (Fig by PH. Prouvot device design by A. Stroh build by R. Necel from J. W. Yang, Prouvot, et al., 2018 reproduced with permission from Springer Nature).

Controls for optogenetic stimulation

Quantification of ArchT-expressing cells

The sections were imaged with a Zeiss Axio Imager (Carl-Zeiss AG, Oberkochen, Germany) using a 20x objective. Quantification of reporter-positive cells was performed on equally spaced sections (300 μm) throughout the OB. The OB surface (in mm^2) for each section was measured to calculate the density (in cells/mm^3) of reporter-positive cells.

Evaluation of the number of inhibited newborn neurons

We combined electrophysiological results, quantification of ArchT-expressing newborn neurons and already established modeling of light distributions to evaluate the number of inhibited newborn neurons in the in vivo experiments (Rungta et al., 2017). For the calculations of light penetration, we used the same online tool provided by the Deisseroth lab (<http://web.stanford.edu/group/dlab/cgi-bin/graph/chart.php>). We used a 200 μm fiber with a numerical aperture of 0.39, an initial power density of 95 mW/mm^2 and a wavelength of 552 nm. ArchT-positive cell density was evaluated in equally spaced sections (every 300 μm ; 7 animals) resulting in a density of $410 \pm 8 \text{ cells}/\text{mm}^3$. Using the aforementioned model for light propagation in tissue, we conclude, that the light density falls below this value at a depth of 600 μm . We then calculated the illuminated volume as a frustum with a 0.1 mm radius top section, and multiplied this value by our cell density, to get the final number of cells that are inhibited on average in the in vivo experiments.

Stimulation design

Opsins display a sigmoid dose-response curve to light. For excitatory cation channels, stimulation should be applied at a frequency preventing the inactivation of the peak current, e.g., a brief pulse train of 10 ms pulsed at up to 30 Hz for ChR2, spaced by at least 10 s. For proton and chloride pumps the illumination should be continuous as their sustained activity relies on the continuous absorption of photons. The first step of any recordings including optogenetic manipulation is to establish a dose-response curve or when available utilize the

ones in the literature. The optimal power should be in the linear range of the curve, use the minimal power sufficient to elicit a direct effect on the target neurons and the network. We stayed aware that using highest power levels may lead to phototoxicity. In the case of inhibitory opsins establishing the dose response curve is more delicate but should be done by quantifying the decrease in response relative to a constant stimulation. This stimulation can be physiological e.g. sensory stimulation or artificial such as a constant current injection in patch clamp recordings.

Here, we found that inhibiting PV interneuron enhanced the evoked response by single whisker stimulation. We applied increasing intensities of 552 nm light and chose 150 mW/mm² as the suitable light intensity for our experiment due to its efficiency in enhancing the sensory evoked responses, and still ranging in the linear dose-response curve (Fig. 2-7).

In the case of olfactory bulb experiments our collaborators performed patch clamp recordings of the expressing neurons guided using fluorescence to determine a coarse dose-response curve of inhibition in these neurons as they have only recently started being described in the literature.

Computational modeling of light distribution in brain tissue

In order to estimate the number of cells modulated during an illumination in optogenetic experiments we used a simple model of light propagation derived from the Kubelka-Munk theory (Vo-Dinh et al., 2003; Yizhar et al., 2011; Yona et al., 2016).

To calculate the average number of optogenetically modulated neurons, not only the relative density of opsin-expressing cells needs to be estimated, but also the light distribution in tissue. Each opsin is characterized by its dose-response curve. Using this curve, it is possible to determine the current imposed on the cell during the optogenetic stimulation provided the power density at a certain depth is known. It is then possible to estimate at which depth the stimulation ceases to be efficient. The dose response curves of the most common opsins can be found in the literature. We use the Kubelka-Munk model for a geometrical estimation of light spread but note that this model is only partially reflecting the actual light distribution. This model underestimates the later spread of light close to the fiber tip, while it is relatively accurate in determining the efficient penetration depth. To determine the effective penetration depth, defined as the depth at which the light power density falls below the activation threshold of the respective opsin (Schmid et al., 2016; Yizhar et al., 2011). The optical fiber is defined by a few

key parameters, such as the diameter of the core and the numerical aperture. We can consider the initial light source as a circle defined by the core diameter.

(a) The numerical aperture is related to the half angle at which light will exit the fiber: $NA = ni \sin \theta$ where ni is the scattering coefficient of the media (1.36 for the gray matter) (Sun *et al.*, 2012). Thus $\theta = \arcsin (NA/ni)$. In our case $\theta = 16.6^\circ$

(b) The intensity decreases with depth following:

$$\frac{I(z)}{i(z=0)} = \frac{\rho^2}{(z + \rho)^2}$$

(c) The geometrical factor ρ is defined as:

$$\rho = r * \sqrt{(ni/NA)^2 - 1}$$

(d) The final equation including scattering:

$$\frac{I(z)}{i(z=0)} = \frac{\rho^2}{(Sz + 1)(z + \rho)^2}$$

with $Sz = 11.2 \text{ mm}^{-1}$ in mice and 10.3 mm^{-1} in rats.

(e) Plot the results as depth against power (see Fig. 2-7) 3.

Once the penetration depth is known, calculate the size of the truncated cone corresponding to the stimulated volume:

$$V = \pi r^2 \left(\frac{h}{3}\right)$$

(Fig. 2-7). 4. Then calculate the overlapping volume between this frustum and the expressing regions (in the cortex layer II/III and V).

The formula to calculate a frustum directly is:

$$V = \left(\frac{1}{3}\right)\pi h(r^2 + rR + R^2)$$

where r is the radius of the smaller top circular surface and R the radius of the largest bottom one. To calculate the height of an n th layer R_n one can use Pythagoras formula in the triangle with R_n at its base, θ as its known angle and h the height from the fiber tip plus the height of the virtual triangle within the fiber.

$$\tan \theta = R_n/h$$

as a result

$$R_n = h * \tan \theta$$

This can be repeated for each layer to obtain h and R_n and then calculate the volume of each frustum until the power becomes insufficient for modulation anymore.

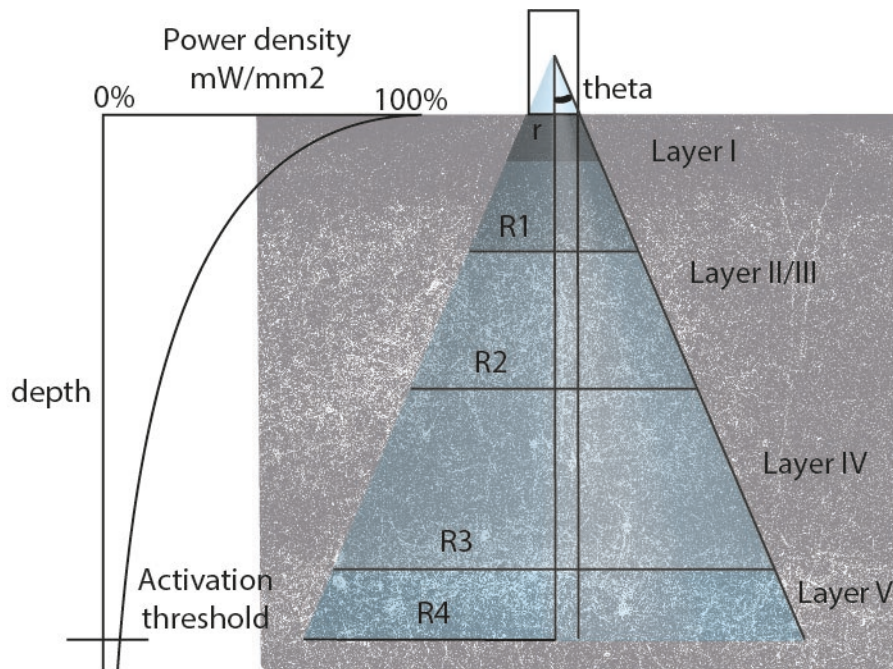


Figure 2-7: General representation of calculating the efficiently excited volume. Left: Exponential attenuation in brain tissue relative to depth, the activation threshold of the opsin of choice is marked as example. Right: Schematic of the ideal spread of light exiting an optic fiber in a vacuum, superimposed on cortical expression of ChR2. Theta is the initial angle related to the Numerical Aperture. R1 to 4 indicate lower and upper radius of the frustum of light in each layer (Fig PH. Prouvot from J. W. Yang, Prouvot, et al., 2018 reproduced with permission from Springer Nature).

Also note that ChR2 has been used at higher frequencies in the literature, but frequencies higher than 30 Hz become hard to use reliably in our hands. Not all cell types can spike at such a high frequency, additionally the refractory period of the Channelrhodopsin (Fig. 1-15) starts to decrease response intensity and rate. It is always best to check the literature beforehand and especially the original articles for each opsin. In most cases the dose response curves are available in the literature. However whole cell electrophysiology after your specific viral transduction strategy in the respective brain region remains the gold standard for controls in optogenetics experiments, be it in slices or in vivo. (Fig. 5-2) The main parameters to control for patch clamp are: (a) The dose response curve between light density and photocurrent (obtained by ramping up the light power between stimulation and measuring the current in voltage clamp). (b) The power necessary for efficient silencing or excitation of the cells of

interest (how much light power is necessary to inhibit action potential firing in current clamp in our case).

Here we started by estimating the minimal photocurrent needed to effectively silence ArchT expressing PV interneurons. Considering a typical membrane resistance of $R_m = 90\text{M}\Omega$ (M et al. 2002) and assuming that a membrane potential hyperpolarization of 25mV is required for action potential inhibition, a photocurrent of at least 250 pA is required in this case. For ArchT (Han et al., 2011), this inward photo current is reached at about $1.5\text{mW}/\text{mm}^2$ illumination density. We estimated the light power density sufficient for effective ChR2 activation according (Prigge et al., 2012). They demonstrated that light power densities as low as $0.875\text{mW}/\text{mm}^2$ reliably evoked spiking in cultured pyramidal neurons expressing ChR2. With $45\text{mW}/\text{mm}^2$ as initial power at the fiber tip, this density is reached about $650\ \mu\text{m}$ in depth of the tissue. Indeed, we can identify spiking responses in our MUA data upon illumination with $45\text{mW}/\text{mm}^2$ up to a depth of $675\ \mu\text{m}$ (Fig. 4-14). We used 2 models for assessing the light density distribution in brain tissue: the spherical model (Schmid et al., 2016), as an extreme example of lateral scattering, and the Kubelka-Munk-model, underestimating lateral scattering, but more realistic for penetration depth. In layer II/III, the spherical model results in an area of above-threshold light illumination with a lateral radius of $380\ \mu\text{m}$, exceeding the lateral spread of ArchT expression of $320\pm 10\ \mu\text{m}$. Consequently, the entire layer II/III expressing volume ($0.097\pm 0.007\text{mm}^3$) is effectively illuminated. Assuming a conical spread of light from the tip of the fiber following the Kubelka-Munk model, the area of above threshold illumination comprises of a frustrum with an upper radius of $100\ \mu\text{m}$ and a lateral angle of 16.6 with $\text{NA} = 0.39$, refractive index, $n_i = 1.36$ for mouse grey matter. Applying a power density of $150\text{mW}/\text{mm}^2$ at the fiber tip, the inhibition threshold of $1.5\text{mW}/\text{mm}^2$ is reached at a depth of $800\ \mu\text{m}$ in dorsoventral direction. The area of ArchT expression commences at layer II/III at about $100\ \mu\text{m}$ of cortical depth, ceasing at around $430\ \mu\text{m}$. This results in an efficiently inhibited volume of 0.0376mm^3 in layer II/III, which is considerably smaller than the volume of expression ($0.097\pm 0.007\text{mm}^3$). In layer V, the volume efficiently illuminated is larger than the volume of expression for ArchT ($0.0684\pm 0.0041\text{mm}^3$), therefore we can assume inhibiting the entire expressing population in layer V. The actual cell numbers were obtained by multiplying the calculated volumes with the measured cell densities. For assessing the relative proportion of ArchT-expressing neurons with regard to the neuronal population of the entire cortical column, we related the volume of the cortical layers harboring ArchT expressing neurons to the

volume of the entire column. For ChR2 stimulation using $45\text{mW}/\text{mm}^2$ as initial power at the fiber tip, the spherical model results in a lateral radius of $290\mu\text{m}$ of effective illumination, amounting to a volume of 0.024mm^3 in layer II/III. Using the conical model, the volume efficiently stimulated in layer II/III is 0.0376mm^3 . In layer V the volume efficiently illuminated is 0.0863mm^3 , as for ArchT excitation we used only the conical model for layer V, as the spherical model cannot be employed for deeper regions, as described (Schmid et al., 2016).

We then re-used this same model in the context of newborn neurons in the olfactory bulb. In this case we based our threshold calculations on values acquired using patch-clamp recordings of expressing cells. We established a dose response curve between light intensity, calculating the light density at the cell level, and evoked current (Fig. 5-2). We used these values to define a threshold of efficient optogenetic inhibition and used this value in the same model as earlier.

Data Evaluation and Statistics

Data in the text and figures are presented as means \pm SEM. Statistical analyses were performed with GraphPad Prism (GraphPad Software, Inc.; La Jolla, CA, USA) or MATLAB. We performed D'Agostino & Pearson omnibus normality tests to test for normal distribution of the data when appropriate. Paired t test and repeated-measures ANOVA were used when the data were normally distributed. The Friedman test, Mann–Whitney–Wilcoxon test and Wilcoxon signed-rank test were used when data exhibited non-Gaussian distributions. The Kolmogorov–Smirnov test was employed to compare 2 non-normal distributions.

Calcium imaging

Fiber photometry

The fiber photometry experiments were performed jointly with single channel electrophysiology recordings described earlier, we used a custom-built fiber photometry system briefly described in Fig. 2-8 for optical fiber-based Ca^{2+} recordings and optogenetic stimulation. The light for excitation of the fluorescent Ca^{2+} indicator, Oregon Green 488 BAPTA-1 (OGB1, Invitrogen, Life Technologies, Carlsbad, CA) and for stimulation of ChR2 was delivered by a blue 20mW solid-state laser at 488nm (Sapphire, Coherent, Dieburg, Germany). An acoustooptic modulator (AOM 3080-125, Crystal Technology, Palo Alto, CA) was used for rapid control of laser intensity. The laser beam was coupled into a $200\mu\text{m}$ optic multimode fiber using a fiber collimator (Thorlabs, Grünberg, Germany). The emitted fluorescent light was guided back through the fiber, separated from the excitation light with a dichroic mirror and

detected by an avalanche photodiode (LCSA500-01, Lasercomponents GmbH, Olching, Germany). The signal was sampled at 2 kHz using a multifunction data acquisition board (PCI 6259, National Instruments, Austin, TX) and a custom-written LabView (National Instruments) script.

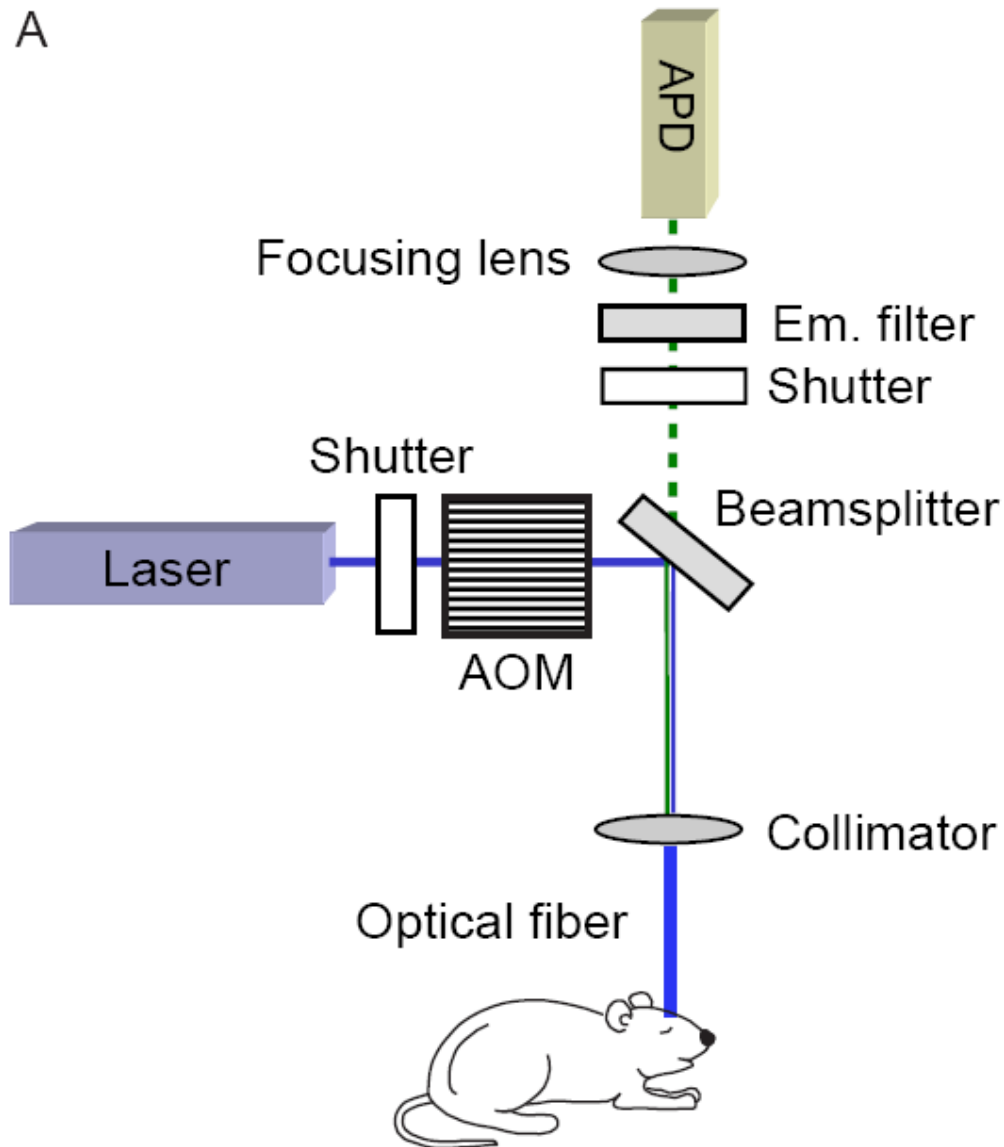


Fig 2-8: Basic design of our fiber photometry system.

Illumination from a 488nm CW laser is controlled by a shutter and an electro optical modulator and reflected by a beamsplitter mirror. Emitted light is collected through the same path and passed through a 500nm long pass filter before being focused into an avalanche photodiode (adapted from: Adelsberger et al., 2014 Reproduced with permission from Cold Spring harbor Laboratory press).

Anesthetized two-photon recordings

Mice aged 1.5-12 month were put under isoflurane anesthesia 1,5-2% and a prepared for the recording like described earlier the only difference being the chamber implanted being the one described in Fig. 6-10. After making sure the chamber was properly fixed the isoflurane level was increased to 2% and the animal was quickly transferred from the stereotactic frame to the holding clamp on the microscope table. The anesthetic mask was fixed on the snout of the mouse and the isoflurane level was set at 1,5% and slowly decreased to 0,8-1% over 5-10 minutes while controlling the breathing rate and reflexes of the animal to ensure it did not wake up. To control for oxygen saturation of the animal we controlled either by an infrared sensor or by visually identifying gasping events. In case it dropped, or the animal started gasping we increased the flow rate of oxygen/isoflurane mix. A heated 37°C phosphate buffer solution (Sigma-Aldrich) was immediately perfused into the chamber.

Once the animal was fixed and stable, we filled a patch pipette with a tip resistance of about 25M Ω with OGB-1 AM dissolved in 20% DMSO/Pluronic F-127 to a stock concentration of 10mM then mixed 1/10 in commercial Phosphate Buffered Saline for a usable solution of 1mM. We fixed the pipette into a patch clamp pipette holder attached to a headstage. The secondary opening used to apply pressure was connected to a pressure controller (npi electronic) We lowered the pipette under visual control to the surface of the brain, selected a region devoid of large blood vessels within the barrel cortex and inserted the pipette diagonally about 300 μ m laterally and about 300 μ m in depth. We applied 20psi for 3-5min at depth and continued with the applied pressure while retracting the pipette.

Intrinsic Optical Imaging

Surgical preparation

For IOI experiments 23 to 28 postnatal days aged mice were used (n = 7 WT and 7 PRG-2 KO animals). Mice were anesthetized with intraperitoneal injection of mixture of Urethane (1g/kg) and Chlorprothixene (7mg/kg.), mixed in the ratio of 3:1 respectively. Heart and breathing rates were continuously monitored during the experiment. Body temperature was maintained at 37°C using a heating pad (ATC 2000, World Precision Instruments, Florida). Xylocaine gel (2%, AstraZeneca, Germany) was applied on the skin before surgery. After scalp dissection, a custom-built head post was attached to the right side of the skull with cyanoacrylate adhesive and dental cement to facilitate head fixation during imaging. Since vasculature was clearly visible, there was no need of skull thinning. All whiskers on the contralateral side of the snout

were cut except C2. To stimulate the C2 whisker, a custom built magnetic driven whisker stimulator driven by TTL voltage pulses was used. Whisker stimulation was synchronized with imaging using an A/D converter (Micro3 1401, Cambridge Electronic Design Limited, UK) controlled with the spike2 software.

Image acquisition

For image acquisition, an Andor Zyla 5.5 sCMOS camera (5.5 megapixels) was used, which was mounted on an upright Olympus Microscope. The camera was controlled by MicroManager (Vale's Laboratory, UCSF) software. To obtain pictures of superficial blood vessels, we used 120 W Fluorescence Microscope Excitation Light Source (X-cite 120Q, Excelitas Technologies), filtered through 488nm filter. A Nikon 10X objective with a numerical aperture of 0.45 and a field of view of 1.8 x 1.6 mm was used for imaging while no excitation or emission filter was applied. For functional imaging, the focal plane was moved 300-400 μ m deeper from the pial surface and red LED (625nm, Thor labs, USA) was used to emphasize rapid changes in blood oxygenation levels. The light intensity was adjusted every time, just below the camera saturation. To calculate the area of the intrinsic signal evoked by single whisker (C2) stimulation, full resolution data frames were acquired at a frame rate of 15 fps and with spatial binning of 3 X 3. Individual trials were 15 sec long, with an initial 5 sec baseline, a subsequent 5 sec stimulation (5 Hz) and 5 sec post stimulus recording. 30 trials were averaged in order to improve signal-to-noise ratio. Additionally, 10 trials were taken without stimulation (as baseline recording) for normalization.

Two-photon calcium imaging

We performed High-speed two-photon Ca^{2+} imaging in layer II/III (150 to 350 μ m from the pial surface) with an upright LaVision BioTec TrimScope II resonant scanning microscope, equipped with a Ti:sapphire excitation laser (Chameleon Ultra II, Coherent) and a 25x (1.1 N.A., MRD77220, Nikon) or 40x (0.8 N.A., NIRAPO, Nikon) objective. The laser was tuned to 800nm or 920nm for OGB-1 and Gcamp6f respectively and fluorescence emission was isolated using a band-pass filter (525/50, Semrock) and detected using a GaAsP photomultiplier tube (PMT; H7422-40, Hamamatsu). The TriM Scope II scan head, equipped with a resonant scanner, imaged time-lapses (512 \times 512pixels, \sim 440 \times 440 μ m field of view) at a maximum frame rate of 30.4Hz. Time lapses were recorded for 5–10min on average. Inspector software (LaVision BioTec) was used for microscope control and image acquisition.

Data analysis

The images recorded were analyzed using a plugin (Intrinsic Signal Processor VSD1) for ImageJ (National Institutes of Health, Bethesda, MD; <http://rsb.info.nih.gov/ij>). Multi-frame image stacks were averaged across 30 trials. Next, the images of baseline periods and stimulation periods were each averaged. After Gaussian filtering of 10 in the X and Y dimensions, we compared baseline and response either by calculating their ratio or by dividing their difference by the baseline ($\Delta R/R_0$) (Harrison et al., 2009).

Awake recordings

Animal habituation

Keeping balance on an air-cushioned ball is not a natural exercise for mice and requires training. The procedure for head fixation also proved stressful on naïve mice. To reduce stress and facilitate imaging sessions we trained the mice to the procedure for five days before imaging. The training consisted in gentle handling for 10-20 minutes per mouse alternating between mice in the same cage. Briefly, the mice were not single housed because females fight less for social dominance. The implants are small and sit relatively flush on the head, as such the risk of the implant getting detached was low. We preferred keeping the mice housed together to reduce stress caused by single housing. Once the mice were habituated to the experimenter, we began gently holding the implant in place while manipulating the mice, first only on the cage floor then similarly when holding them. Once the mice stopped struggling against the fixation they were brought to the trackball (air cushion turned off) and left to explore while gently securing them by the tail. The next day after handling the mice for a few minutes (5-10 depending on the stress level displayed) they were brought to the holder and head fixed in the final configuration (cushioning turned on). The first session lasted only 5 minutes and the next two sessions 10 and 20 minutes. Once the mice were calm in the head fixation and learned to balance on the ball the VR system could be turned on to allow them to move and explore freely. Finally on day 4 or 5 the first imaging session could be performed on quiet resting or exploring mice.

Imaging data analysis

Images were initially imported into ImageJ as z-stacks. To perform normalization, we computed the average fluorescence image and subtracted it from each frame in the stack. We then divided

the result by the same average image. The result was a $\Delta F/F_0$ image containing grey values between zero and one allowing us to compare values more easily between recordings.

ROIs were manually drawn on the average image and saved using Fiji's built-in ROI manager. Typically, ROIs were drawn very conservatively around the cell bodies staying slightly within the cell limits. Two additional ROIs were drawn, one including part of the neuropil and excluding the cell bodies and one including the whole field. The average grey value within each ROI was then extracted across the Z direction resulting in a column for each ROI. These values were then imported in IGOR or MATLAB for further analysis with custom scripts.

Results

Study 1: Local field potential correlates of fiber photometry during sensory stimulation

Optic-fiber based recordings are suitable for recording of slow oscillation associated calcium waves

In the continuation of a collaborative project with Ag Faber at the university of Münster we sought to combine fiber photometric recordings with fMRI in what is now called ofMRI or opto-fMRI. This project was intended to study brain states under anesthesia, in particular the whole-brain BOLD fMRI correlates of slow waves events. Within this project I performed LFP recordings in combination with fiber photometry of calcium signals to ensure the calcium signals we recorded were indeed correlated with the LFP signals. I also used the same combination to assess sensory and optogenetically evoked activity. The results and methodological development during this initial project provided a basis for the subsequent studies of activity in the barrel cortex. I will not present data acquired with BOLD-fMRI as I was not implicated in data acquisition or analysis and it doesn't fit within the scope of this dissertation.

We employed an optic fiber-based approach to detect Ca^{2+} transients simultaneously to fMRI scans within a 9.4 T small animal MR scanner (Schmid et al., 2016; Schulz et al., 2012). To monitor intracellular Ca^{2+} as proxy of action potentials. The synthetic dye Oregon Green 488 BAPTA-1 (OGB-1) was injected stereotactically resulting in an ovoid stained region with a diameter of about $600\mu\text{m}$ using the multicell bolus loading technique (Stosiek et al., 2003). The tip of the optical fiber with a core diameter of $200\mu\text{m}$ was implanted dorsal to the stained region in primary somatosensory cortex (S1 front limb, S1FL). As mentioned above, OGB-1 stains both neurons and astrocytes, as confirmed by co-staining with the astrocytic marker SR101 (Nimmerjahn et al., 2004) (Fig. 1-9). In addition, we employed the genetically encoded Ca^{2+} indicator GCaMP6f under control of a pan-neuronal promoter hSyn and the CamKII promoter limiting expression to excitatory neurons. Experiments were conducted under isoflurane anesthesia (1.1–1.8%) inducing and maintaining slow wave activity with recurrent slow wave events at similar frequencies (Chang et al., 2013; Grienberger et al., 2012; Jercog et al., 2017; Lissek et al., 2016; Stroh et al., 2013). Ca^{2+} waves were reliably recorded during simultaneous fMRI recordings (8 out of 10 experiments in 7 out of 8 animals), occurring at frequencies

ranging between 9 and 15 events/min (mean 10.9 ± 1.3 events/min), in line with previous in vivo recordings (Busche et al., 2015; Egger et al., 2015; Stroh et al., 2013) (Fig. 3-1H,I). For OGB-1, the typical and rather uniform Ca^{2+} waves exhibited sharp rise times (72 ± 14 ms, and rather variable durations and amplitudes of 1356 ± 85 ms and $2.6 \pm 0.1\Delta f/f$, respectively ($n = 30$ traces, five animals). For GCaMP6f (hSyn) the rise times exhibited slower kinetics (163 ± 14 ms, $n = 30$ traces, two animals, Fig. 3-1J) (Stroh et al. 2013b) presumably due to four Ca^{2+} binding sites of the calmodulin, which need to be occupied to reach maximum fluorescence change, while similar values for durations and amplitudes of slow waves were observed as compared to OGB-1 (Fig. 3-1K,L,M). To test, whether indeed OGB-1 and GCaMP6f both reveal the same slow wave events, we conducted two-fiber experiments outside of the MR scanner, in two animals expressing GCaMP6f under control of the CaMKII promoter in S1FL and being injected with OGB-1 2 mm posterior to that site on the same hemisphere. (Fig. 3-1N). Indeed, we found the associated slow waves to be highly correlated (Fig. 3-1N,O). The Ca^{2+} waves were separated by periods of network quiescence of variable durations (Fig. 3-1H,I,N,P), equivalent to down states in electrophysiological recordings (Poulet & Petersen, 2008; Seamari et al., 2007; Steriade et al., 1993).

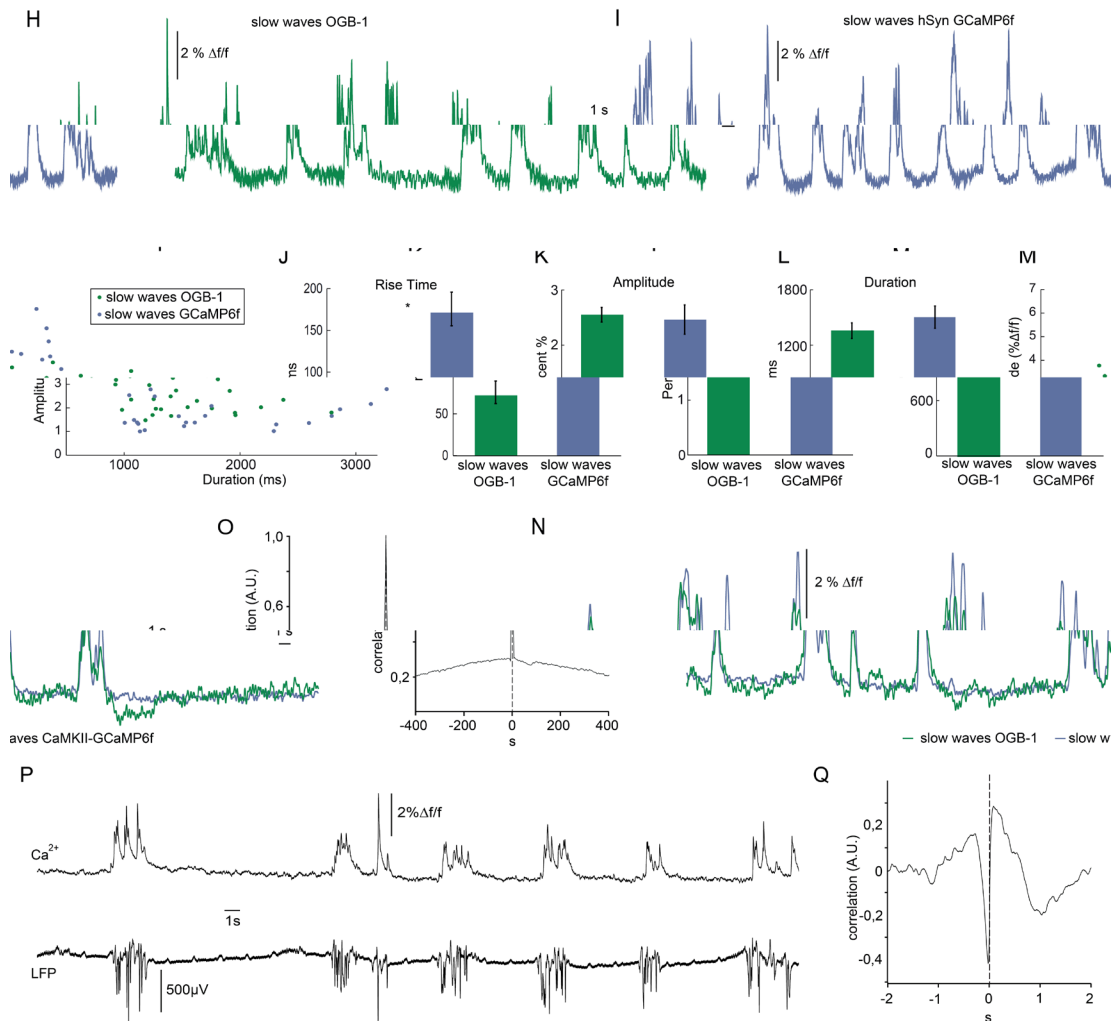


Figure 3-1. Optical recordings of slow oscillation-associated comparing signal between OGB1, Gcamp6f and LFP.

(H) Calcium trace upon OGB-1 staining recorded in the MR scanner during slow wave activity. Optically recorded spontaneous stereotypical calcium waves are interrupted by periods of network quiescence. (I) Optical recordings in GCaMP6f expressing rats similarly reveal slow calcium waves. (J-M) Quantifications of slow calcium wave parameters in OGB-1 stained vs. GCaMP6f expressing rats reveal significant differences only in rise times ($p=0.0001$), whereas amplitude and durations are not significantly different ($p=0.13$; $p=0.61$). (N) Simultaneous optical calcium recordings outside the MR scanner using two optic fibers implanted into left hemisphere with OGB-1 staining (green trace) and with CaMKII-GCaMP6f staining. An overlay of recorded traces shows that with both indicators the occurrence of a slow wave is reflected by similar transients. (O) Cross-correlation of simultaneously recorded optical calcium signals obtained in (N) indicates high similarity between both signals. (P) Simultaneous optical calcium and LFP recordings outside of the MR scanner indicating correlation of slow calcium waves with electrically recorded slow oscillations under isoflurane anesthesia. (Q) Cross-correlation of optically and electrically recorded traces result in a prominent peak with almost zero timeshift, indicating a close similarity of the two signals. (LFP recordings by PH. Prouvot Calcium recordings by L. Wachsmuth and F. Schmidt analysis M. Schwalm and PH. Prouvot fig adapted from Schwalm et al., 2017) CC BY.

Electrical dynamics underlying calcium changes

Since optic fiber recordings were relatively new at the time of these experiments we combined fiber recordings with LFP recordings to investigate similarities and differences between them. The first step was to combine these recordings, we started by injecting OGB-1 and implanting the optic fiber as usual but this time we also performed a second craniotomy next to the first one to insert the recording pipette at a 45° angle and record as close as possible to the fiber recording site. We then were able to record both modalities simultaneously. In line with previous results (Busche et al., 2015; Stroh et al., 2013), the observed population Ca^{2+} transients were correlated with electrically recorded slow oscillations in the local field potentials (Fig. 3-1P,Q). We performed this control experiment in mice injected with OGB-1 but only after having controlled the similarity of events between OGB-1 and GCaMP6f. To that effect we recorded under slow wave state (isoflurane 2% and compared rise time amplitude and duration of these events. As expected, given the intrinsic kinetics of the sensors the rise time proved significantly different around 70ms for ogb1 and 170ms for gcamp6f. The amplitude and duration were no different with both sensors. A change in duration could have been expected given the different release kinetics of the sensors but given the long duration of events it is undetectable here. We then performed simultaneous recordings in the same hemisphere with GCaMP6f and OGB-1 in order to directly compare both conditions. As depicted in Fig. 3-1 N both traces overlap almost perfectly, which is confirmed by the correlogram centered at 0 in panel O. Note the slight delay due to the slight delay in calcium relative to electrical activity. Finally, having confirmed the comparability of OGB-1 and gcamp6f recordings we compared OGB-1 and LFP recordings. In Fig. 3-1 P a representative example of Ca^{2+} and LFP is depicted showing a clear correlation between electrical activity and Ca^{2+} transients.

Panneuronal optogenetic stimulation presents similar properties to sensory stimulation in the somatosensory cortex

One of the goals of this study was to evaluate the possible sources of slow wave evocation. The natural way to do so was to use sensory modulation and we decided to use ChR2 to investigate if excitatory neurons could start a slow wave in the cortex when stimulated in high enough numbers (Stroh et al., 2013). The difference with previous studies by here was the concomitant use of fMRI to provide a global readout showing us the extent of activation. The implication for anesthetized sensory stimulation is that in the right conditions sensory stimulation could evoke a slow wave and have a much larger effect on the network than the localized recorded

activity. It would be possible, under anesthesia, to unknowingly affect the context of the recording while looking only at a very local response. OGB-1-AM was injected in the same region previously injected with a ChR2 carrying AAV in order to stimulate and record using the same optical fiber. The result in Fig. 3-5 B show the expected issue that the optogenetic stimulation physically saturates the detector with fluorescence making the peak of the response hidden by an artifact in the average of multiple stimulations (Fig 3-5 B). However, the decay typical of this calcium sensor is visible confirming the existence of a Ca^{2+} transient induced by ChR2. When looking at individual trials it is also possible to distinguish what could be the peak of the response when heavily filtering. Note the large noise band making it difficult to decipher the position of the actual peak. This transient seems to be larger than a forepaw evoked transient. We also compared three different intensities of stimulation. 0.5mA 1mA and 1.5mA. Increasing from 0.5 to 1mA significantly increased the response amplitude which was not further increased by 1.5mA.

We then evaluated response adaptation in the calcium response, given the properties and behavior of intracellular calcium we needed to ensure a good correlation between the adaptation properties of calcium and LFP signal. In the context of the fMRI study, it was also necessary to perform repetitive stimulation to evoke a response large enough to be detected that would not immediately induce adaptation. We tested 3-7 and 9Hz stimulations using co-recordings. Adaptation occurred as soon as 7Hz in both LFP and calcium signals prompting us to choose 3Hz for subsequent repetitive sensory stimulations (Fig. 3-2). Interestingly the LFP signal shows a tendency to adapt proportionally less, this could be due to a rapid change in internal buffering properties of the neurons. We then tested pan neuronal optogenetic stimulation at a rate of 3Hz for comparison with sensory stimulation. Optogenetic stimulation recapitulated the sensory calcium signal and showed similar intensity with no adaptation at 3Hz as well (Fig. 3-3).

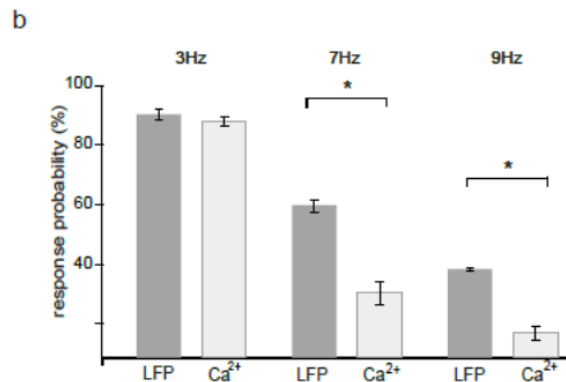
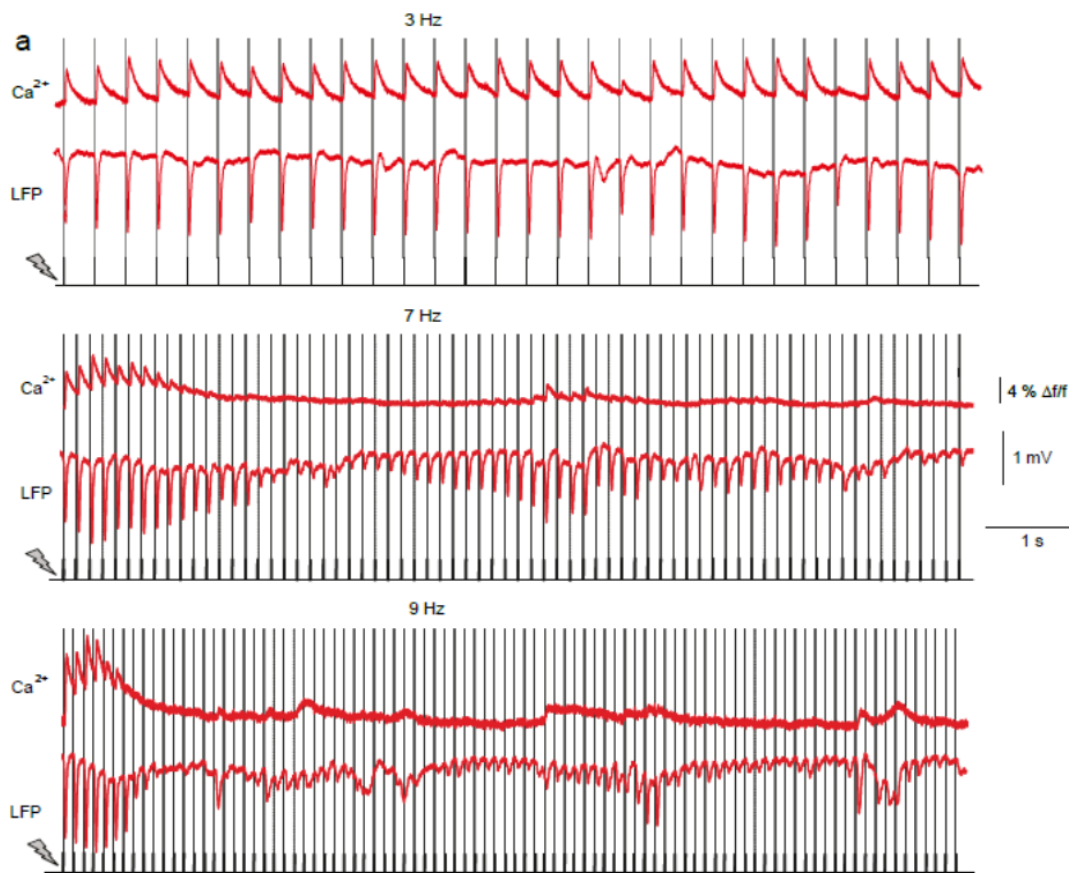


Figure 3-2: Correlation of simultaneous Ca^{2+} and LFP recordings. a: Representative traces upon pulsed forepaw stimulation at 3 Hz, 7 Hz and 9 Hz for 10 s. Note the differential adaptation of LFP and Ca^{2+} responses b: Quantification of probabilities of response in Ca^{2+} vs. LFP recordings. Response was defined as signal amplitudes exceeding 10 % of maximal response amplitude. At 7 and 9 Hz, the response probability was significantly lower in Ca^{2+} recordings compared to the LFP ($p < 0.01$, t-test, three animals, 57 trials total for 9Hz and 56 trials for each of the other two frequencies) (Data acquisition PH. Prouvot, C. Fois and F. Schmid data analysis PH. Prouvot and C. Fois adapted from Schmid et al., 2016) CC BY

We then used either deep isoflurane anesthesia or medetomidine to compare sensory evoked activity under slow-wave state or what we call persistent up state. Fig. 3-4 A shows that slow oscillation-associated calcium waves evoked by sensory stimulation are indistinguishable from spontaneously occurring waves in Fig. 3-1. For slow wave activity, we observed electric forepaw stimulation to reliably evoke slow waves locked to stimulus onset (A) with a mean latency of $143 \text{ ms} \pm 7 \text{ ms}$ (30 events, 3 animals, Fig 3-4 E), in reasonable agreement with studies in mice using visual or auditory stimulation (Grienberger et al., 2012; Stroh et al., 2013). Regarding signal characteristics, stimulus-evoked calcium waves were not distinguishable from spontaneous waves (Fig 3-4 H), again in agreement with previous studies (Stroh et al., 2013). Stimulating with multiple pulses with a frequency of 3 Hz and pulse train duration of 4 s led to calcium waves with latencies similar to those waves induced by single pulses (Fig 3-4 C). Subsequent pulses within a given pulse train did not evoke additional waves, suggesting a refractory behavior of those waves, as previously shown in mice (Stroh et al., 2013). Waves followed all-or-none characteristics, with a probability of induction of $72 \pm 8\%$ (5 animals, 12 traces). In the persistent activity condition, we detected neuronal calcium responses upon sensory stimuli with a significantly shorter latency of $20 \text{ ms} \pm 4 \text{ ms}$ and a significantly shorter duration of $55 \pm 3 \text{ ms}$, in agreement with previous studies (Schmid et al., 2016) versus $959 \pm 36 \text{ ms}$ in slow wave state (30 events, 3 animals, Fig 3-4 E, F). The amplitudes of persistent activity responses slow waves did not differ significantly (Fig 3-4 F), but varied between individual animals due to different staining efficiencies. It must be noted that amplitudes of calcium transients can only be meaningfully compared within one experiment, as the fluorescence amplitudes depend on many local parameters, such as the concentration of the calcium indicator in the region and the relative position of the optic fiber. Responses during persistent activity exhibited significantly shorter rise times compared to slow waves (G), suggesting a different mechanism of activity initiation.

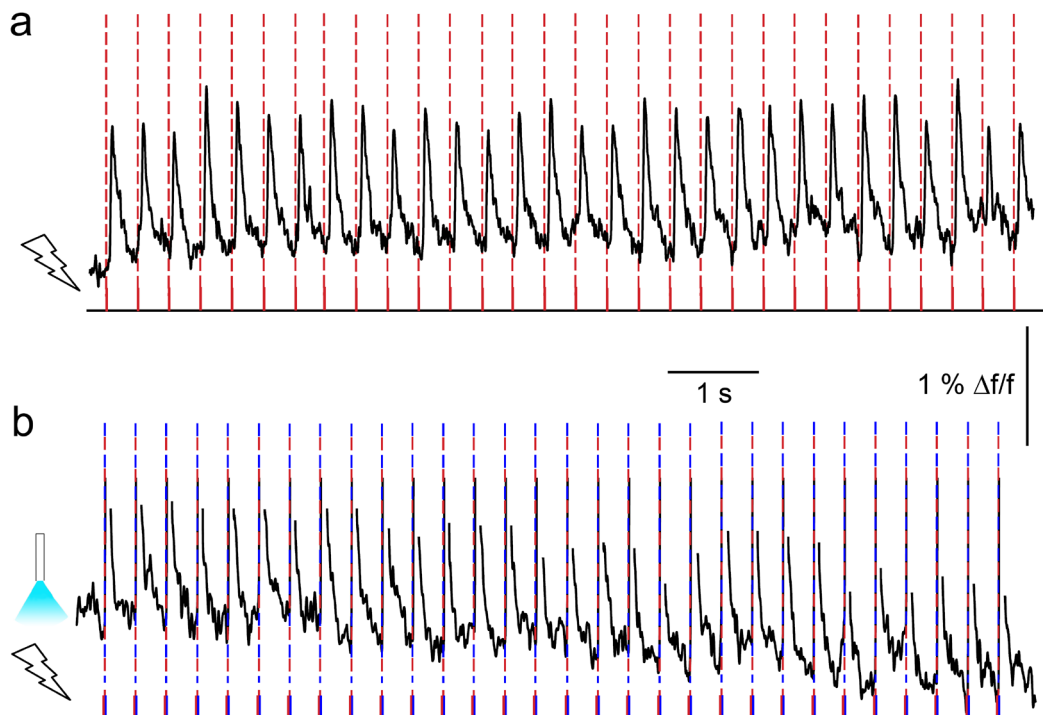


Figure 3-3: Similar signals between sensory and optogenetic stimulation. Amplitude of Ca^{2+} transients can be determined despite optic artefact. a, b,: Primary Ca^{2+} responses induced by forepaw stimulation, pulse train at 3 Hz, 10 s duration, without (a) and with additional optical pulses, 10 ms durations (b). Note that the stimulation artifact has been removed (Data acquisition PH. Prouvot, C. Fois and F. Schmid data analysis E. Rosales and PH. Prouvot adapted from Schmid et al., 2016). CC BY

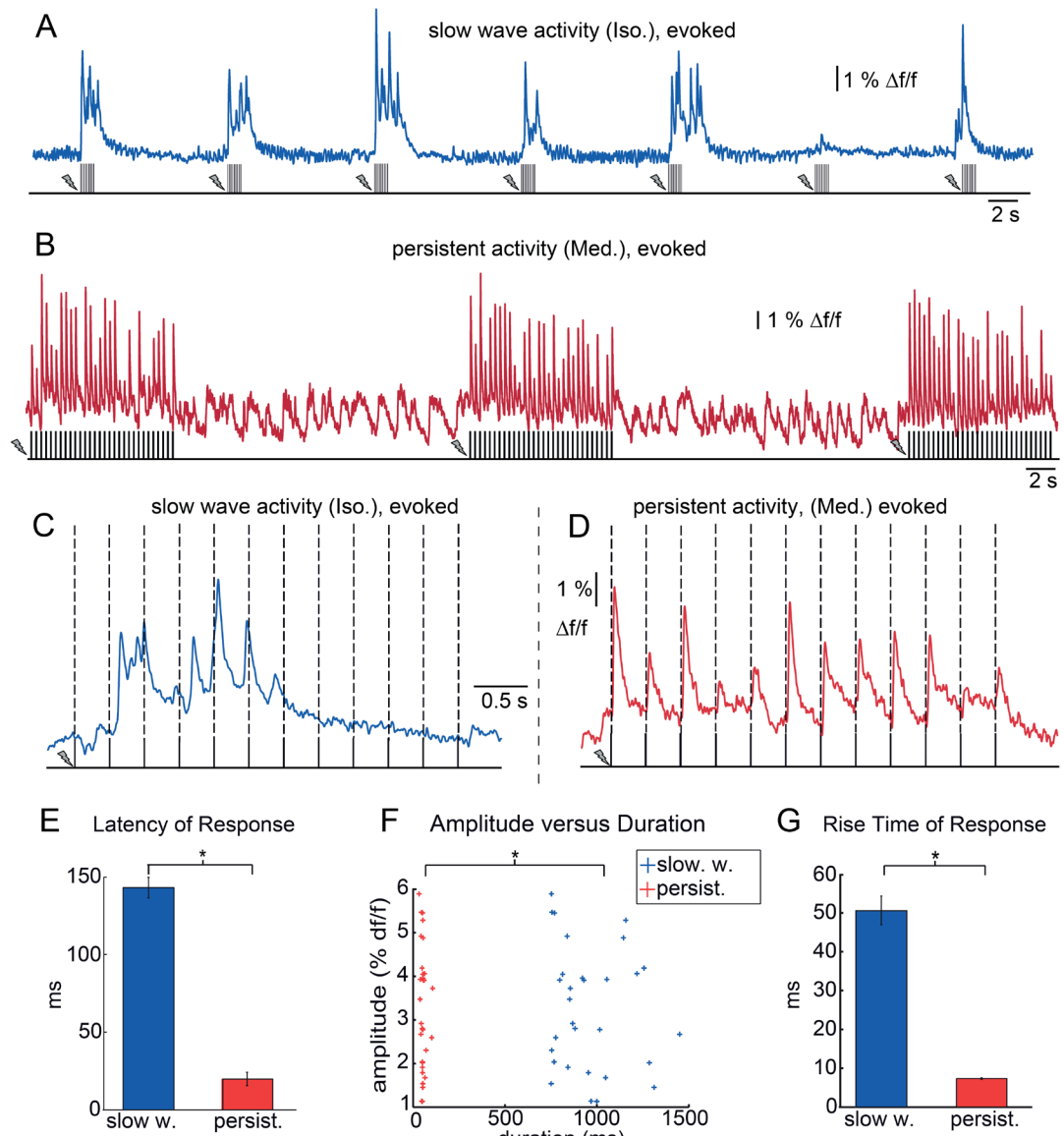


Figure 3-4: Neuronal response patterns upon sensory stimulation for slow wave and persistent activity. (A) Calcium trace recorded during slow wave activity (blue). Electric forepaw stimulation at 9 Hz for 1 s every 10 s. Calcium waves were evoked in an all-or-none manner. The last pulse train started during the occurrence of a spontaneous wave. (B) Calcium trace recorded during persistent activity (red). Electric forepaw stimulation at 3 Hz for 10 s every 30 s resulted in short-latency calcium transients upon each pulse. (C) Individual sensory evoked slow calcium wave, note that wave is locked to the onset of the first stimulus with a latency of 140 ms (stimulation paradigm: 3 Hz, 4 s). (D) Sensory-evoked calcium responses during persistent activity (stimulation paradigm: 3 Hz, 4 s). Each pulse evoked an individual response. (E) Latencies of evoked calcium waves during slow wave activity (blue) vs. responses during persistent activity (red). Latencies differ significantly by more than 100 ms. (F) Scatter plot displaying mean response amplitudes versus durations measured at 50 % of maximum peak in the two conditions. Duration of responses (slow wave vs. persistent response) differs significantly by more than 900 ms. (G) Mean rise times of responses in the the two conditions differ significantly. Asterisks indicate significant difference (rank sum test, $p < 0.0001$, 30 events, 3 animals). (H) . (Fig by M. Schwalm, recordings by F. Schmid analysis PH. Prouvot Schwalm et al., 2017) CC BY

Optical artifacts in optical recordings

In a similar way that electrical stimulation interferes with electrical recordings, optical stimulation can interfere with optical recordings. Because electrical stimulation usually is very short and amplifiers do not suffer from saturation induced shut down, stimulation artifacts can be an asset in electrophysiology even as they are often unavoidable. In optical recordings and the main issue is caused by the order of magnitude difference between the power necessary for exciting a fluorophore and the power necessary for optogenetic stimulation. Very low power density can be used to excite a fluorophore (down to $1\text{mW}/\text{mm}^2$ at the fiber) but power densities of $10\text{-}100\text{mW}/\text{mm}^2$ at the fiber tip are often necessary to excite an opsin (enough to saturate classical fluorophores). Moreover, to minimize photobleaching, excitation light is always reduced to the minimum necessary in imaging experiments. Most problems arise when stimulating cells in the same area that is recorded. Because the detectors are calibrated to be as sensitive as possible to detect light emitted by the fluorophores, they can easily be saturated. Because of their sensitivity Photomultiplier tubes they often possess safety features allowing them to shut down when overexposed. By their very mechanisms light detectors convert photons hitting their surface into current and the gain has to be calibrated to keep that current in a range not damaging to the electronic components. In the case of photomultiplier tubes in particular the current is amplified in a series of Dynodes to enable detection of extremely low light. The resulting sensitivity exposes them to saturation and if safety shut down measures were not put in place repetitive or long-term exposure to high light power would damage the electronics irreversibly. This results in loss of data for a few milliseconds to a second while the detector shuts down and recovers. The light saturating the detector can have two sources, most commonly it can be light simply reflected and diffused by the sample (tissue or even coverslip), in some cases when the excitation spectrum of the opsin and the fluorophore overlap the excitation light can saturate the fluorophore and thus the detector. Often, this can be worked around when designing the experiment by selecting opsin and fluorophore with nonoverlapping excitation spectra. In the case there is still some overlap the light sources should be selected to be in the non-overlapping parts of the excitation spectra. The next safety measure that should always be put in place is using dichroic filters reflecting excitation light, naturally from the fluorescence excitation but also from the optogenetic excitation to prevent any light not coming from emission from the fluorophores to reach the detector. Given the strong power necessary for optogenetic excitation this is not always sufficient so as an extra safety measure an ultrafast shutter can be put in place in front of the detector (like in the case of our two-photon

microscopes). That shutter should be synchronized with the stimulation to protect the detector from saturation. This of course prevents recording during the stimulation and should be only used when one absolutely needs to record and stimulate in the same region (depending on the sample size this can be unavoidable) and cannot use clearly separated wavelength with the right set of filters. While it prevents recording during a short time it also prevents saturation of the detector and recording can resume much faster than when the detector needs to recover from oversaturation. On the long term the more safety measures the longer detectors will be able to operate without degradation.

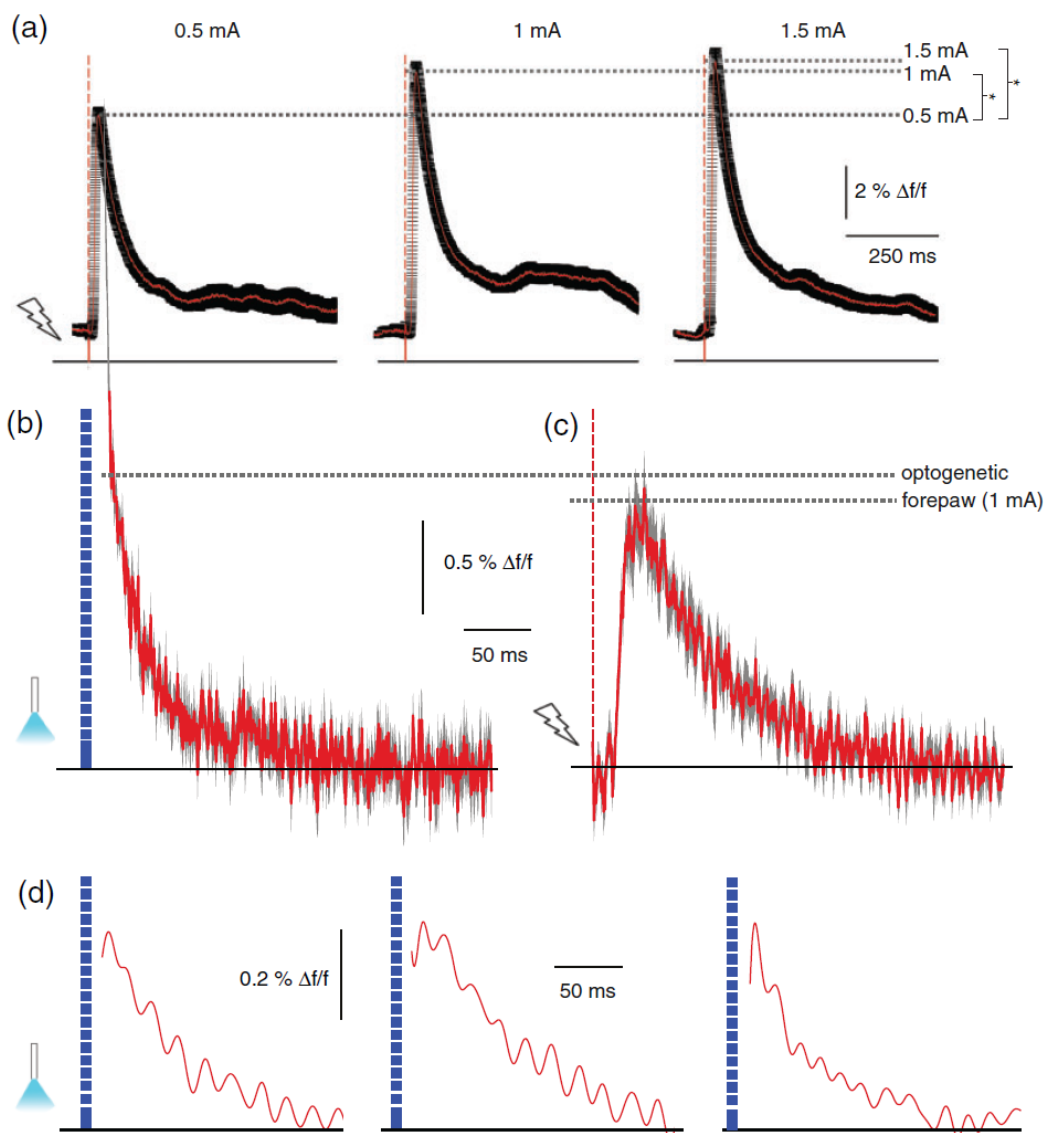


Figure 3-5: Cortical optogenetic stimulation did not result in a widespread secondary recruitment of the neuronal network. (a) Primary Ca^{2+} responses induced by forepaw stimulation, single pulses at different stimulation strength. Mean (red line) \pm SEM (black line), significant increase of peak amplitudes comparing 0.5 to 1 mA ($p < 0.001$, 21 versus 18 transients) and comparing 0.5 to 1.5 mA ($p < 0.001$, 18 versus 23 transients). (b) Average

primary responses upon optogenetic stimulation with a pulse duration of 10 ms in a different animal expressing ChR2 in somatosensory cortex, mean (red line) SEM (black line), 11 transients. Ca²⁺ transients were recorded after single stimulation pulses without preceding fluorescence excitation to exclude influence of constant illumination. Note that the stimulation artifact has been removed. (c) Average responses of same animal upon 1 ms, 1 mA electric forepaw stimulation, identical scaling as in (b), mean (red line) \pm SEM (black line), 11 transients. Importantly, fluorescence intensity changes can only be compared within the same experimental subject. (d) Single Ca²⁺ transients from three different animals upon optogenetic stimulation. Exponential detector recovery was removed and data were low-pass filtered. Data are shown starting at 6ms after the end of the optic pulse (Fig. E Rosales PH. Prouvot adapted from Schmid et al., 2016). CC BY

In the present recordings where we combined fiber photometry of OGB1-AM or Gcamp6f and ChR2 excitation we ran into the expected issue that our 488nm light source is the correct wavelength for both molecules. Because of the same excitation wavelength for Ca²⁺ indicator and ChR2, the detector was saturated by the high fluorescence emission of the indicator during the high-intensity optic stimulation pulses, as in previous studies (Grienberger et al., 2012; Stroh et al., 2013). We used low light initial intensities (1.3mW/mm²) for constant excitation of OGB1 versus high intensities (80mW/mm²) for pulsed excitation of ChR2. For analysis of Ca²⁺ signal following optogenetic stimulation, the signal resulting from detector saturation was removed using two different approaches. After the high-intensity light pulse the saturation decayed. This decay could be fitted with a monoexponential function with a time constant of 0.9954 ± 0.0038 ms (R^2 square 0.9998). In a basic approach, the stimulus artifact was removed for the first 25 ms after onset of the stimulation pulse (10 ms).

In this initial project we recorded the calcium and electrical correlate of sensory activation on a large scale and under isoflurane and medetomidine anesthesia. We found a clear correlation of sensory and spontaneous calcium transients with the local field potentials and a certain dose response correspondence of the calcium signal with intensity of sensory or optogenetic stimulation. In data not shown here we also showed a correlation of slow waves with global BOLD activation. I was then interested in the more local circuits implicated in the sensory response. The optogenetic stimulation presented here was pan-neuronal and we decided to take advantage of the possibilities of cell specificity offered by optogenetics to study the spatial scale of sensory response using methods with a higher resolution.

Study 2: Optogenetic activation and inhibition of Parvalbumin positive interneurons in the barrel cortex

The first pendant of this collaborative project consisted in using electrical recordings to investigate the effects of PV neurons on the barrel cortex network. More specifically we used in collaboration with ██████████ in the team of ██████████ Multi electrode array recordings in vivo to obtain a readout that is effectively perpendicular to two-photon calcium imaging. This combination would have allowed us to obtain a 3D overview of the network.

Here we combined optogenetics with spatially resolved multielectrode recordings in mouse barrel cortex in vivo, complemented by an assessment of the local density of inhibited neurons. We resolve 3 distinct functional components of the network: LFP, reflecting subthreshold synaptic activity and suprathreshold action potential firing, multiunit activity (MUA), reflecting only suprathreshold activity, and lastly single units, allowing for the differentiation between putative excitatory and inhibitory neurons (Reyes-Puerta, Sun, et al., 2015). In the lightly anesthetized mouse expressing ArchT or ChR2 in PV interneurons (ArchT/PV or ChR2/PV mice) in layers II/III and V, we recorded spontaneous and single-whisker evoked activity upon optogenetic modulation. We correlated the functional findings with an estimation of the relative density of optogenetically modulated neurons. We find that a small number of light-modulated PV interneurons exert control over a large number of excitatory and inhibitory neurons, extending to neighboring barrel columns and affecting both spontaneous activity over a broad frequency range as well as shaping the spatiotemporal dynamics of whisker-evoked neuronal activity.

Combining Depth-Resolved Multichannel Recordings and Optogenetic Manipulation of PV Interneurons in Mouse Barrel Cortex

The effects of transient PV-mediated disinhibition on neocortical network function were studied by intracortical multielectrode array (MEA) recordings in 18 adult mice in vivo. In barrel cortex of lightly anesthetized mice, we combined 4- or 8-shank multichannel recordings with optic fiber-based optogenetic inhibition of PV interneurons. The electrode shanks were inserted at the site of ArchT expression and in neighboring cortical columns. The optic fiber was then placed parallel to the recording shanks, in the center of the ArchT-expressing area, barely touching the cortical surface (Fig. 4-1A). The virus injection site was identified using the

injection scar, the pattern of blood vessels and when available epifluorescence. We inserted the electrodes centered on the supposed expression of virus expression.

Electrode shanks were marked with DiI for post hoc identification of recording sites by confocal microscopy. Postmortem histology indicated that electrode shanks indeed penetrated the ArchT-GFP expressing area and covered all cortical layers (Fig. 4-1B). Stimulation of single whiskers was performed alongside multichannel recordings to identify the whisker corresponding to the barrel closest to the center of the electrode array. To identify the expression site we visually identified the scar left from the injection. We used the pattern of blood vessels on the surface for better reproducibility of the injection. Only the whisker evoking the maximal response in the middle shank (PS) was retained for subsequent stimulation, all other whiskers were trimmed. CSD analysis allowed the identification of the principal column and cortical layers (Fig. 4-1C). Neighboring electrodes lateral (L) and medial (M) to the PS electrode recorded the activity in the neighboring columns.

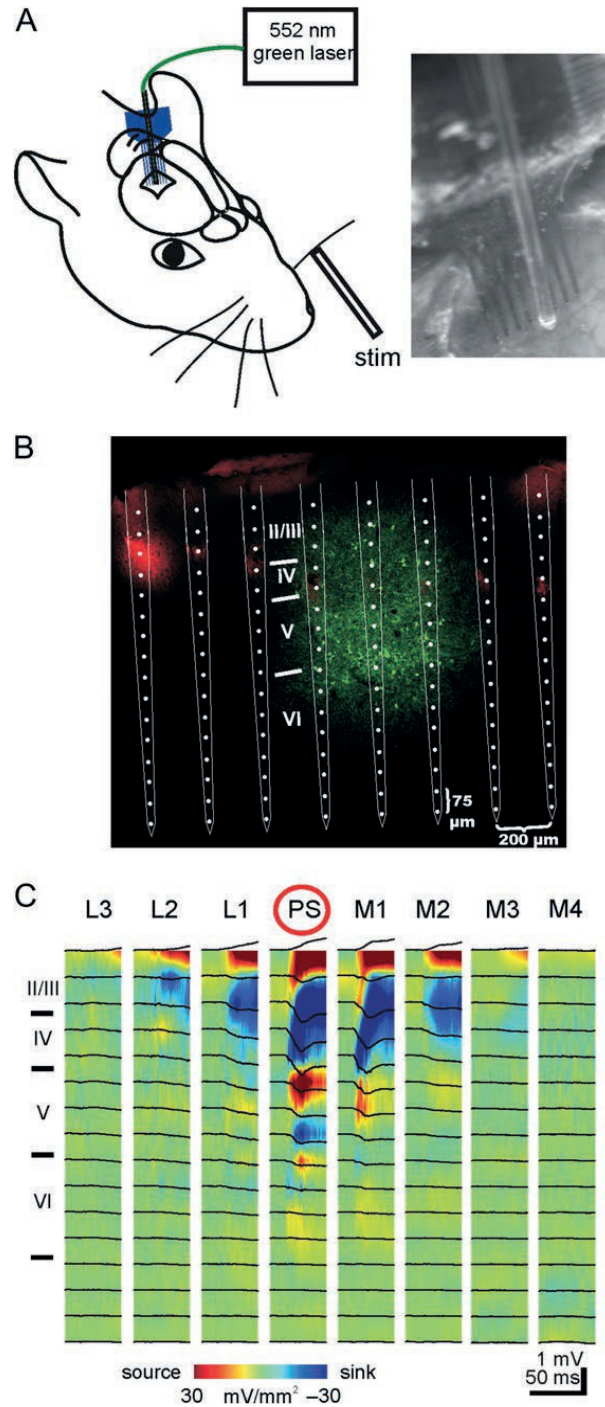


Figure 4-1: Experimental setup for combining in vivo multielectrode recordings, optogenetic manipulation and mechanical stimulation of single whiskers in adult mice. (A) Schematic illustration of the experimental setup for data recording using 8-shank 128-channel probes, selective mechanical stimulation of a single whisker and photo-illumination using an optical fiber connected to a 552 nm green laser. Right panel shows a photograph of the cortical surface with electrode array and optical fiber. (B) Fluorescent image of ArchT-GFP expression pattern (green) and position of DiI-covered electrode tracks (red). An 8-shank 128-channel electrode probe is superimposed on this image according to the position of the DiI tracks. (C) Local field potential responses (black lines) and corresponding color-coded current-sink-source density (CSD) depth profile following stimulation of whisker E1. Blue color represents current sinks and red color represents current sources. The shank showing the largest stimulus-evoked

response amplitude was located in the E1-column and denoted the principal shank (PS). Activity profiles recorded at electrodes located lateral (L) and medial (M) from the PS are also illustrated. (Fig. adapted from J.-W. Yang et al., 2017 by permission with Oxford university press)

Interneuron-Specific Expression of ArchT in Layers II/III and V in Mouse Barrel Cortex

Floxed ArchT-tdTomato encoding AAVs were stereotactically injected in barrel cortex of PVCre transgenic mice to achieve selective expression of the inhibitory opsin in PV interneurons like described earlier. Notably, expression was almost exclusively constrained to layers II/III and V. In layer IV, only very few ArchT-positive neurons could be found, even though it was along the injection path, and we sometimes even injected within it. This is interesting since the majority of reports on PV interneurons in the barrel cortex concentrate on layer IV as this is where they are most numerous (Ascoli et al., 2008; Rudy et al., 2011), this will be a point to keep in mind when analyzing the results of modulation. The area of expression constituted a cylinder with a diameter of $640 \pm 20 \mu\text{m}$ ($n = 5$ mice), and a dorsoventral extent ranging at $300 \mu\text{m}$ in layer II/III and $200 \mu\text{m}$ in layer V (Figs 4-1B and 4-2A). We covered on average one to two barrels per injection given these measurements. Within this area, neurons exhibited strong, membrane bound expression of ArchT-tdTomato/-GFP (Fig. 4-2B, C). We then assessed the cell type specificity of ArchT expression. Upon immunostaining and quantification of coexpression in confocal micrographs, we identified $90.9 \pm 2.8\%$ ($n = 272$ cells from 4 mice) of the ArchT-expressing neurons as clearly PV positive (Fig. 4-2D–F; K, left chart), the remaining cells exhibited only weak PV immunofluorescence. To test for an unspecific expression in excitatory neurons, we conducted a co-staining for anti-CaMKII. Not a single region of ArchT expression contained neurons which were co-stained for both CaMKII and ArchT-tdTomato, demonstrating the high specificity of viral expression (Fig. 4-2G–I; K, middle chart; 441 cells in $n = 3$ mice). Lastly, we assessed the relative proportion of PV interneurons in the local neuronal network. Upon staining for neuronal nucleic acids and anti-PV immunofluorescence, a percentage of $5.1 \pm 1.5\%$ out of all neurons were PV positive, in line with a previous study (Lefort et al., 2009) (Fig. 4-2J; K, right panel; $n = 2$ mice, 6395 cells).

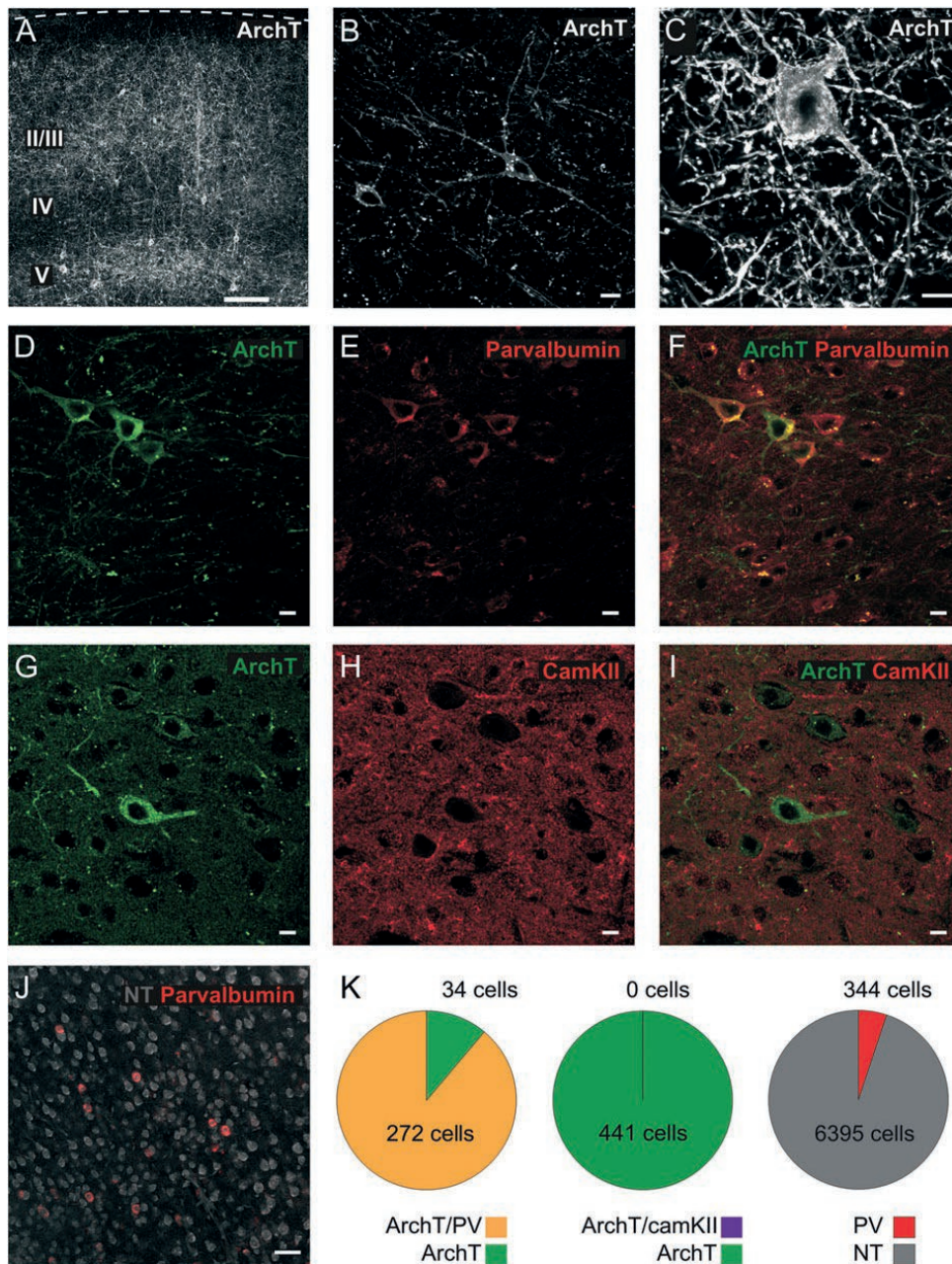


Figure 4-2: Layer and cell type specificity of ArchT expression in mouse barrel cortex. (A–C) Confocal micrographs of coronal sections of somatosensory cortex from PV-cre mice injected with AAV-floxed-ArchT-tdTomato/GFP reveal ArchT expressing cells mainly confined to layers II/III and V. Scale bars: 100 μm in A and 10 μm in B and C. (D–F) ArchT-GFP-expressing cells (green, D); PV-expressing cells (anti-PV immunostaining, red, E); merged photo from D and E. Scale bars: 10 μm . (G–I) ArchT-GFP-expressing cells (green, G); co-staining with anti-CamKII (red, H); merged photo from G and H. Scale bars: 10 μm . (J) Co-staining with a fluorescent Nissl stain (Neurotrace) and a Parvalbumin antibody. Scale bar: 50 μm . (K) Pie charts depicting the ratios of co-stainings: left ArchT/PV ($90.9 \pm 2.8\%$, from 4 mice), middle ArchT/CamKII (0%, from 3 mice), right PV/NT ($5.9 \pm 0.7\%$, from 2 mice). (Fig PH. Prouvot adapted from J.-W. Yang et al., 2017 by permission with Oxford university press)

We verified the expression of floxed ChR2 in the same PV-Cre mouse line using only confocal micrographs. The expression system being unchanged we considered the specificity of expression to be similar. Expression of ChR2-mCherry was limited to layer II/III and V like previously (Fig 4-3). Notably the protein tends to form punctae in the cell membrane of the expressing neurons, this is a property of mCherry which tends to form clusters in the cell membrane. Expression was uniform and no dead overexpressing cells were detected.

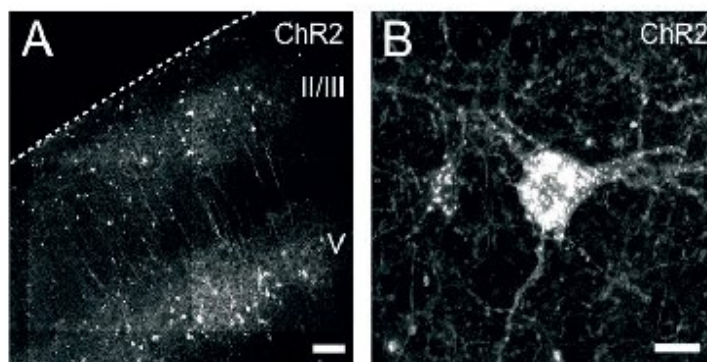


Figure 4-3: Expression of ChR2 Confocal micrographs of coronal sections of somatosensory cortex from PV-cre mice injected with rAAV2-FLEX-ChR2-mCherry reveal ChR2 expressing cells mainly confined to layers II/III and V. Scale bars: 100 μ m in panel A and 10 μ m in panel B (Fig PH. Prouvot adapted from J.-W. Yang et al., 2017 by permission with Oxford university press)

Temporal Profile of Transient PV-Mediated Disinhibition

The two opsins used in the work ArchT and ChR2 have very different working mechanisms. ArchT is a proton pump using photons to continuously pump H^+ protons out of the cell, as such it is continuously active as long as it is illuminated. The dynamics of ArchT are also quite flat, after a short time to reach a plateau the hyperpolarizing current they provide in neurons is continuous with only a slight decrease over time. It makes sense generally to illuminate ArchT expressing cells continuously. ChR2 on the other hand is a light gated cation channel it opens and closes in a cycle and is only gated open by photons of the right wavelength. The kinetics of ChR2 depolarization are non-linear, first there is a peak with an exponential decay to a plateau of steady state depolarization. Typically, researchers want to evoke action potentials directly and potentially drive a neuron's firing at a certain frequency. In this case using short pulses avoids saturating the opsin and depolarizes the cell only shortly driving ideally a single action potential per pulse. In our case for the sake of comparison with the effects of ArchT continuous hyperpolarization we did illuminate ChR2 continuously so the first 10-20ms of illumination represent the peak of excitation before the steady-state plateau is reached.

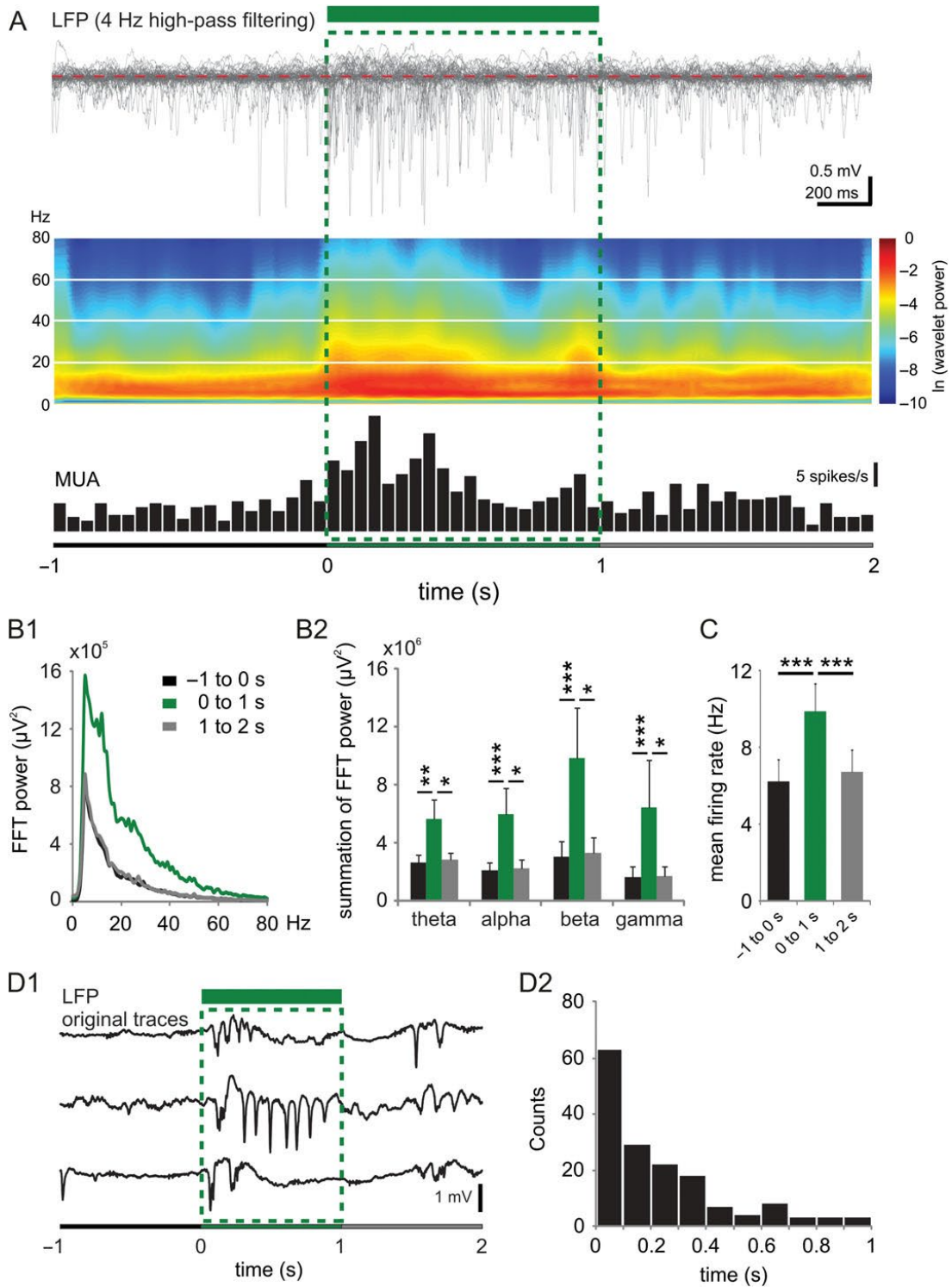


Figure 4-4: Optogenetic inactivation of PV inhibitory interneurons causes increase in spontaneous neocortical activity. (A) Spontaneous LFP activity (4Hz high-pass filtering) recorded in deep layer II/III at the site of virus transfection before, during (green horizontal bar) and after light stimulation. Upper panel: Fifty superimposed traces of 3 s duration were aligned according to the onset time of the green light pulse (1 s duration, 150mW/mm², every 10 s). Three periods were defined: before (-1 to 0 s), during (0 to 1 s) and after green light pulse (1 to 2 s). Middle panel shows the corresponding wavelet plot averaged from fifty spontaneous LFPs in the upper panel. Lower panel shows corresponding PSTH plot of

*spontaneous multiunit activity (MUA). (B1) Fast Fourier transformation (FFT) of spontaneous LFP activity during the 3 periods (average over 9 animals). Note the prominent and reversible increase of FFT power over a wide frequency band during optogenetic inactivation of PV interneurons (green line). (B2) Bar diagram illustrating significant increase of FFT power from theta to gamma band during green light pulse (Friedman test: * $P < 0.05$, ** $P < 0.01$, and *** $P < 0.001$). (C) Bar diagram showing significant increase of mean firing rate during optogenetic inactivation of PV inhibitory interneurons recorded on the same electrodes (repeated measures ANOVA test: *** $P < 0.001$). (D1) Three representative unfiltered traces revealing prominently induced slow oscillations during 1 s of inactivating PV interneurons. (D2) The temporal distribution of the onsets of slow oscillations upon optogenetic silencing of PV interneurons. A total of 160 events were detected from 9 animals that fulfilled 2 criteria: first, no Up state for at least 500ms immediately before the onset of illumination; second, occurrence of Up state within the 1 s of illumination. (Fig. by JW. Yang adapted from J.-W. Yang et al., 2017 by permission with Oxford university press)*

In order to estimate the optimal time window of disinhibition required for obtaining a significant effect on the synaptic LFP responses, single whisker stimulation was combined with laser pulses of increasing duration, starting 100ms before the whisker stimulus (Fig. 4-6A). A 100ms long laser pulse, which was terminated at the time point of whisker stimulation, had no effect on the evoked LFP response as compared with the whisker stimulation without light (0ms trace in Fig. 6A), demonstrating that the ArchT mediated hyperpolarization rapidly stopped when the laser was turned off. Gradually increasing the duration of the pulse to produce an overlap with the period of the LFP synaptic response had a significant effect at 15ms poststimulus ($P < 0.05$, $n = 9$ mice; Fig. 6B). A further increase in response amplitude to $213 \pm 32.8\%$ could be observed at 20ms overlap, when the disinhibition induced excitation reached a plateau. In agreement with the effects on the LFP peak amplitude and duration (Fig. 4-5C) these data suggest that the PV-mediated disinhibition increases the network excitability already 15-20ms poststimulus and a further prolongation in disinhibition does not have any stronger effect.

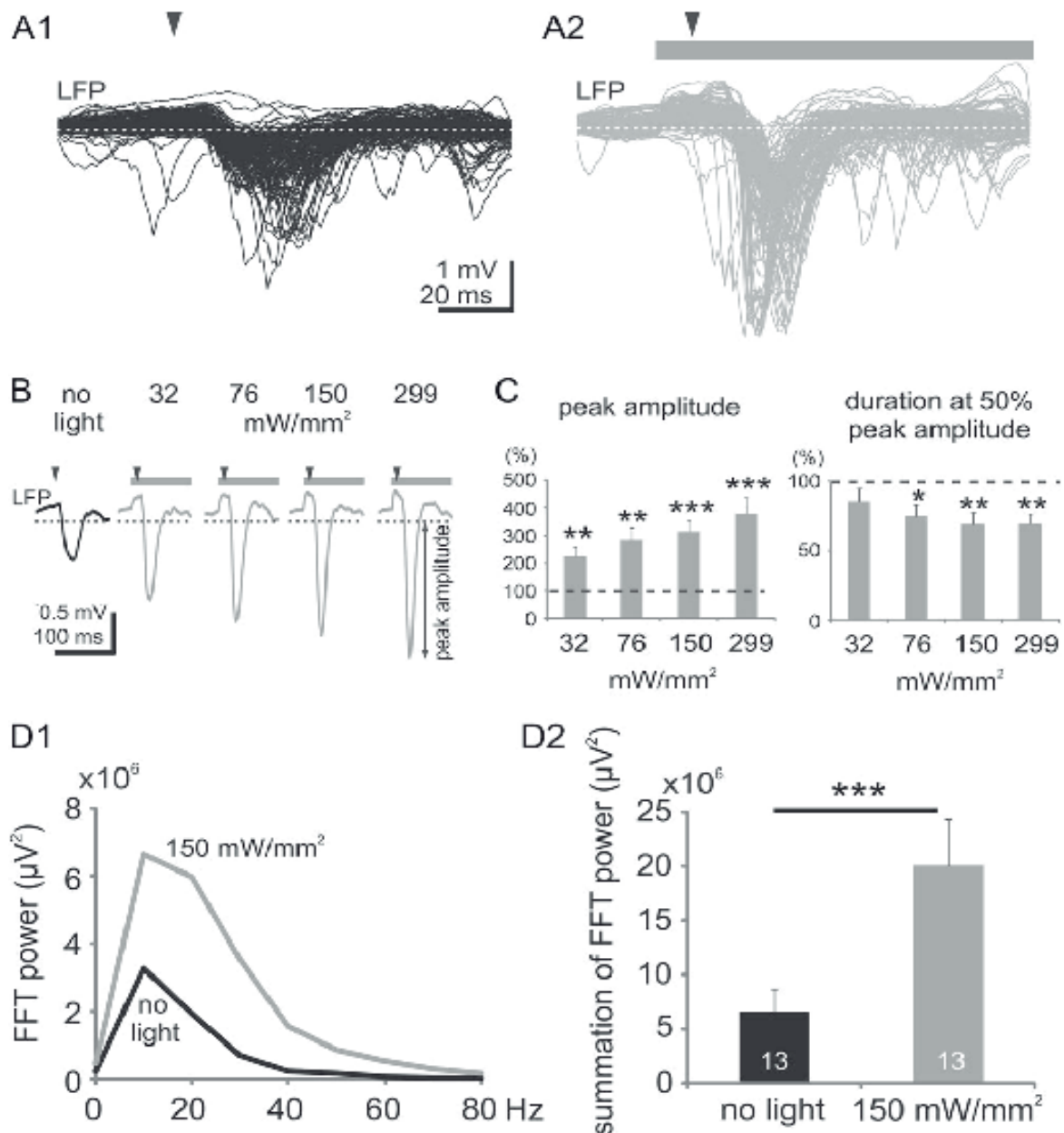


Figure 4-5: Optogenetic inactivation of PV interneurons causes amplitude and broad spectrum increases in stimulus-evoked cortical responses. (A) 130 superimposed traces ($n = 13$ animals) of evoked LFP activity (4 Hz high-pass filtering) recorded in deep layer II/III of the principal barrel column to single whisker stimulation under control condition (A1, no light) and during optogenetic inactivation of PV interneurons (A2, light on, 150 mW/mm²). In this and the following figures, downward arrowheads indicate time point of single whisker deflection. The dashed lines mark baseline of LFP recordings. (B) Enhancement of sensory-evoked response in layer II/III to increasing laser intensities (average of 130 evoked LFP responses from 13 mice). In this and the following figures, the peak amplitude was measured from baseline (dashed lines) to maximum negative peak amplitude. (C) Normalized increase in response peak amplitude (left) and decrease in response duration at half maximal amplitude (right) with increasing laser intensities ($n = 13$ mice). Responses were normalized and compared with control (no light; horizontal dashed lines). Paired t test, * $P < 0.05$, ** $P < 0.01$ and *** $P < 0.001$). (D1) Fast Fourier transformation (FFT) of evoked LFP responses during no light (black line) and light on (gray line) conditions (average of 13 mice). Note the prominent increase of FFT power over a wide frequency band during optogenetic inactivation of PV interneurons. (D2) Bar diagram

*illustrating significant increase of FFT power during light pulse (Wilcoxon signed-rank test, *** $P < 0.001$). (Fig. JW. Yang adapted from J.-W. Yang et al., 2017 by permission with Oxford university press)*

Since the ArchT kinetics are very fast, a 10ms laser pulse was positioned at various time points before and after the whisker stimulus to further assess the temporal profile of the PV-mediated disinhibition (Fig. 4-6C, D). No effect on the LFP response could be observed when the pulse was applied 10ms before the stimulus (-10ms trace in Fig. 4-6C). When the pulse was applied during the first 10ms poststimulus, the response peak amplitude increased significantly ($P < 0.01$) to $253.5 \pm 69.3\%$ (Fig. 4-6C, D). A similar response increase could be observed when the pulse was given during the second 10ms interval poststimulus. At later intervals of over 20ms, the peak amplitude in the LFP response was no longer influenced by a 10ms disinhibition interval. These data indicate that the PV-mediated disinhibition has the most potent impact on cortical excitability during the first 20ms after onset of the whisker stimulation. We could not entirely explain the rebound observed when the stimulation was presented after the primary response peak it persisted at +20 and +30ms. Because it is induced by disinhibition it could be due to continuous input into the barrel that would be inhibited under normal conditions. It could be continuous glutamatergic input from the thalamus, or a secondary response from another region that would normally be suppressed by cortico-cortical projections. Our main indication here is that it is stronger at +20ms and produces a secondary peak larger than the initial one, moreover because we are recording LFP in this context it is probably related to broad synaptic activity. This would lead to the idea of a continuous 30ms excitatory (glutamatergic or cholinergic) input into Layer II/III and/or V normally suppressed by Parvalbumin interneurons maybe to sharpen the timing of activity in the cortex. This result would indicate that Parvalbumin interneurons indeed sharpen the primary activation in the barrel cortex.

Spatial Profile of Transient PV Inhibition

Under control no-light conditions, mechanical deflection of whisker C1 with a duration of 60ms (Fig. 2-4) elicited the typical activation pattern to single whisker stimulation with large LFP responses recorded at the PS electrode located in the C1 column (Fig. 4-9A1). Smaller responses were recorded at the lateral shanks L1–L3 and the medial shanks M1–M4. Identical whisker stimulation with simultaneous PV-mediated disinhibition of the excitatory network evoked at all recording sites much larger LFP responses (Fig. 4-9A2). Interestingly, an increase of the response peak amplitudes could be also observed at the electrode shanks located up to

600 μ m lateral (L1–L3) and up to 600 μ m medial (M1– M3) (Fig. 4-9B, C) clearly outside of the expressing region containing cell bodies. These data indicate that the local and transient PV-mediated disinhibition induced a widespread excitability increase, affecting several neighboring columns in barrel cortex. Whereas the LFP reflects the local synaptic activation, the MUA reveals the suprathreshold activation of neurons located near the recording site. Therefore, the whisker stimulation induced MUA was analyzed under control no-light conditions and during PV-mediated disinhibition (Fig. 4-9D). Under control, deflection of a single whisker evoked a large MUA response in the activated principal column and smaller responses in the neighboring columns (Fig. 4-9D1, upper row in Fig. 4-9E). With simultaneous PV-mediated disinhibition at the PS, the maximum MUA response in the principal column did not change in any cortical layer, but interestingly increased at all lateral and medial recording sites (Fig. 4-9D2, lower row in Fig. 4-9E and Fig. 8-3). The spatial MUA profile shows a Ushaped pattern reaching an increase of 200% in peak MUA firing rate at 400 and 600 μ m lateral and medial from the activated column (Fig. 4-9F). These MUA data and the spatial profile of the synaptic LFP responses indicate that PV-mediated disinhibition induces a widespread increase in synaptic excitation, but an increase in suprathreshold spiking activity only in neighboring columns. Next, we addressed the question over which intervals and at which time points the PV mediated disinhibition exerts these strong network effects.

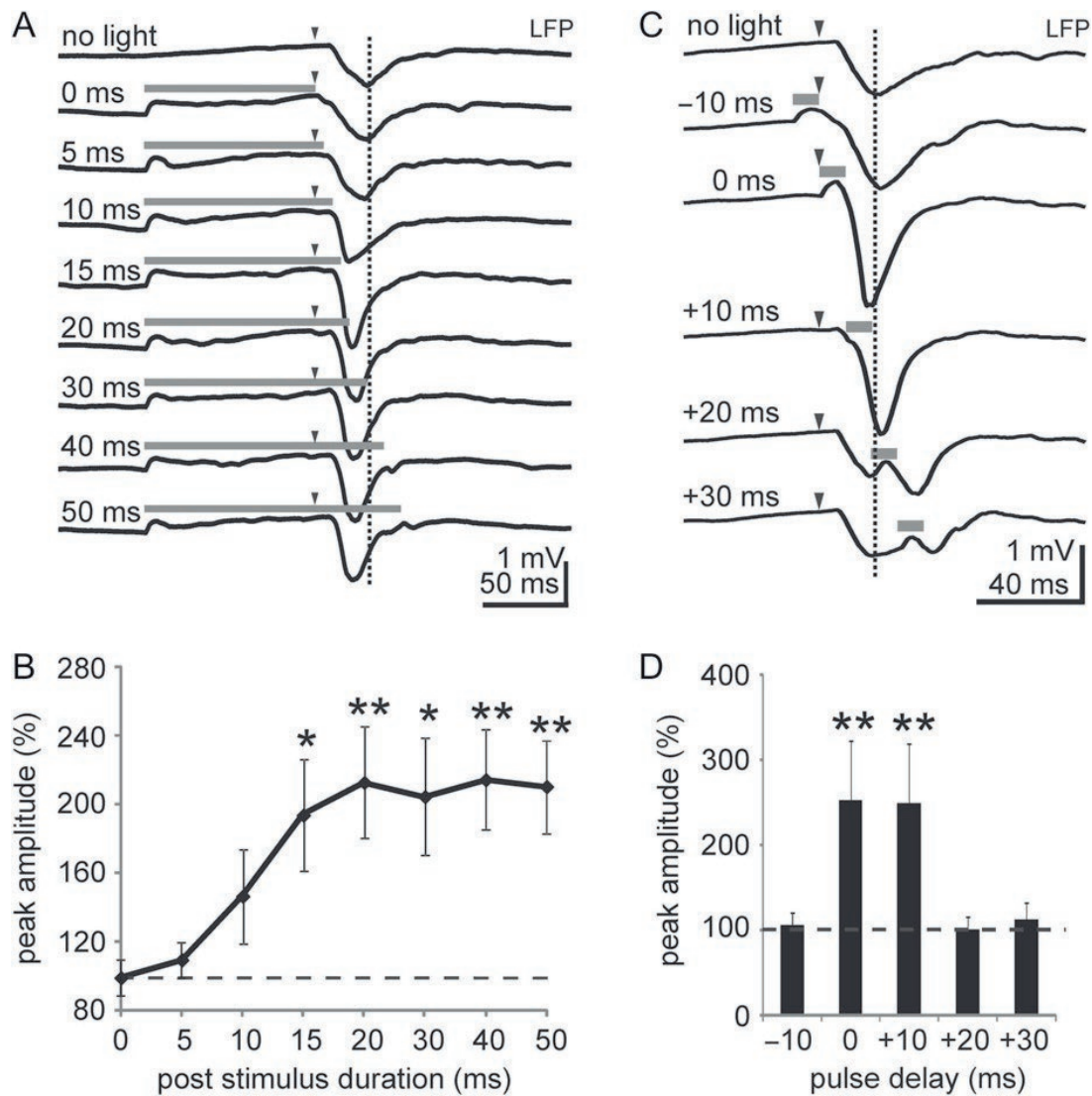


*Fig 4-6: Effect of increasing disinhibition duration and influence of different timing of transient disinhibition on sensory-evoked cortical responses. (A) Average of 90 evoked LFP responses to single whisker stimulation combined with different durations of inhibiting PV interneurons ($n = 9$ mice). Note increase in response amplitude and decrease in delay of peak amplitude with increasing duration of optogenetic disinhibition, which starts 100 ms before whisker stimulation and ends 0–50 ms after the stimulus (gray horizontal lines). (B) Normalized peak amplitude of LFP response at increasing disinhibition intervals. (C) Timing of 10 ms disinhibition and effect on evoked LFP response (average of 80 evoked LFP responses from 8 mice). (D) Normalized first peak amplitude indicated by black dash line of LFP response at different disinhibition time points. Statistically significant differences (Wilcoxon signed-rank test) versus the control (no light) condition are indicated by $*P < 0.05$ and $**P < 0.01$. (Fig. JW. Yang adapted from J.-W. Yang et al., 2017 by permission with Oxford university press)*

Inhibiting PV Interneurons Causes Broad-Spectrum Hyperexcitability

Spontaneous LFPs were recorded in deep supragranular layers by electrodes of the PS, and a 1s green laser light pulse at 150mW/mm² was applied to the cortical surface every 10s in ArchT/PV mice. During this transient disinhibition, spontaneous LFPs were enhanced over a broad

frequency range from theta up to the gamma band; moreover, this transient network hyperexcitability was associated with a prominent increase in MUA (Fig. 4-4A, B1). The average FFT power from theta to gamma of the LFP increased significantly during the light-induced disinhibition and rapidly recovered to control level following light offset (Fig. 4-4B2). This effect was specific to ArchT/PV mice, nonexpressing control mice did not show any change in FFT power upon light illumination (Fig. 4-1B). This pronounced rise in spontaneous LFP power was associated with a significant ($P < 0.001$, $n = 9$ mice) increase in the mean firing rate from $6.2 \pm 1.2\text{Hz}$ to $9.9 \pm 1.5\text{Hz}$ during light-induced disinhibition (Fig. 3C). As found for LFPs, the MUA also rapidly reached control values after switching off the light pulse (Fig. 4-4C). These results demonstrate that a transient inhibition of PV expressing interneurons causes a strong and rapid increase in synaptic excitation and action potential firing of neurons in supragranular layers. These effects are transient and tightly follow the timing of the light-induced disinhibition. For assessing the impact of activating PV interneurons on spontaneous activity, we performed 5s of illumination at $45\text{mW}/\text{mm}^2$ without sensory stimulation in animals injected with AAVs encoding for ChR2. Opposite to the enhancement effect on the FFT power by inhibiting PV interneurons, their activation induced a strong, significant decrease in theta to gamma frequency bands (Fig. 4-5A and B). Under urethane anesthesia, cortical dynamics show prominent slow oscillations (Up–Down state changes) (Reyes-Puerta et al., 2016; Steriade et al., 1993). To evaluate if inhibiting PV interneurons directly impacts slow oscillations, we used a threshold-based algorithm to identify the onsets of Up states based on the work of (A et al. 2008). Indeed, the detected Up states are reflected by MUA firing through all cortical layers (Fig. 8-2), in line with a previous study of ours (Stroh et al., 2013). Notably, of 160 detected Up state onsets in a time window of 1 s during ArchT stimulation, 63 onsets followed the beginning of illumination with a latency of less than 100ms (Fig. 4-4D1). The distribution of onsets is significantly different from a homogeneous temporal distribution (Fig. 4-4D2), which would be assumed if there would be no induction of Up states ($P = 0.031$, 2 sample Kolmogorov–Smirnov test). This strongly suggests that ArchT-mediated inhibition of PV interneurons is capable of inducing Up states, in line with a very recent study (Zucca et al. 2017). Yet, inhibiting PV interneurons did not alter the overall occurrence of Up states, but significantly increases their duration (Fig. 4-7C). We next performed experiments activating PV interneurons using ChR2, see below, and could reduce the occurrence of up states but not their duration (Fig. 4-8C). To address the question whether a similar increase in excitability can also be observed in sensory-evoked cortical activity, the responsiveness to single whisker stimulation in supragranular layers at the PS under no-light conditions and during transient PV-mediated disinhibition was

studied. Indeed, we observed a prominent increase in response amplitude upon illumination with 150mW/mm^2 green light (Fig. 4-5A), again only in ArchT/PV mice (Fig. 2-5). The increase in response amplitude during disinhibition was dependent on the light intensity (Fig. 4-5B, C), but the relative change of response amplitude remained unaffected by the different sensory stimulation strength (Fig. 2-4). Compared with the response under no light condition, at a low intensity of 32mW/mm^2 the peak amplitude already increased significantly ($P = 0.0048$, $n = 13$ mice) to $223.4 \pm 35.8\%$. Higher intensities of 76, 150 and 299mW/mm^2 induced a further enhancement of the peak amplitude, and at an intensity of 150mW/mm^2 , the response amplitude increased significantly ($P = 0.0002$, $n = 13$ mice) to $314.8 \pm 41.5\%$ during PV-mediated disinhibition. This effect was accompanied by a gradual decrease in the duration of the response from $85.9 \pm 9.1\%$ of control at 32mW/mm^2 to $69.4 \pm 7.3\%$ at 299mW/mm^2 (Fig. 4-5C, right). Based on these experiments, we have chosen 150mW/mm^2 for all subsequent optogenetic experiments, to achieve a reliable inhibition and at the same time reduce the probability of unspecific effects (Fois et al., 2014). The decrease in the duration and the sharp increase in the peak response of the LFP indicate that the initial component at 10–30ms after whisker stimulation is most strongly affected. As spontaneous neocortical activity, sensory-evoked responses also showed a prominent increase in the FFT power over a broad frequency range from theta up to the gamma band (Fig. 4-5D1) during the 100ms time window of light illumination (150mW/mm^2), again only in ArchT/PV mice (Fig. 8-1C, Ds Fig. 2-5). The FFT power increased significantly ($P = 0.0002$, $n = 13$ mice) from $6.7 \pm 2 \times 10^6 \mu\text{V}^2$ to $20 \pm 4.2 \times 10^6 \mu\text{V}^2$ during the light-induced disinhibition (Fig. 4D2). In summary, these data demonstrate that spontaneous as well as sensory-evoked activity in barrel cortex are prominently enhanced when PV-expressing interneurons are transiently inhibited. Next, we studied the spatiotemporal dynamics of this disinhibition by recording LFPs and MUA with a MEA covering all cortical layers and several barrel-related columns.

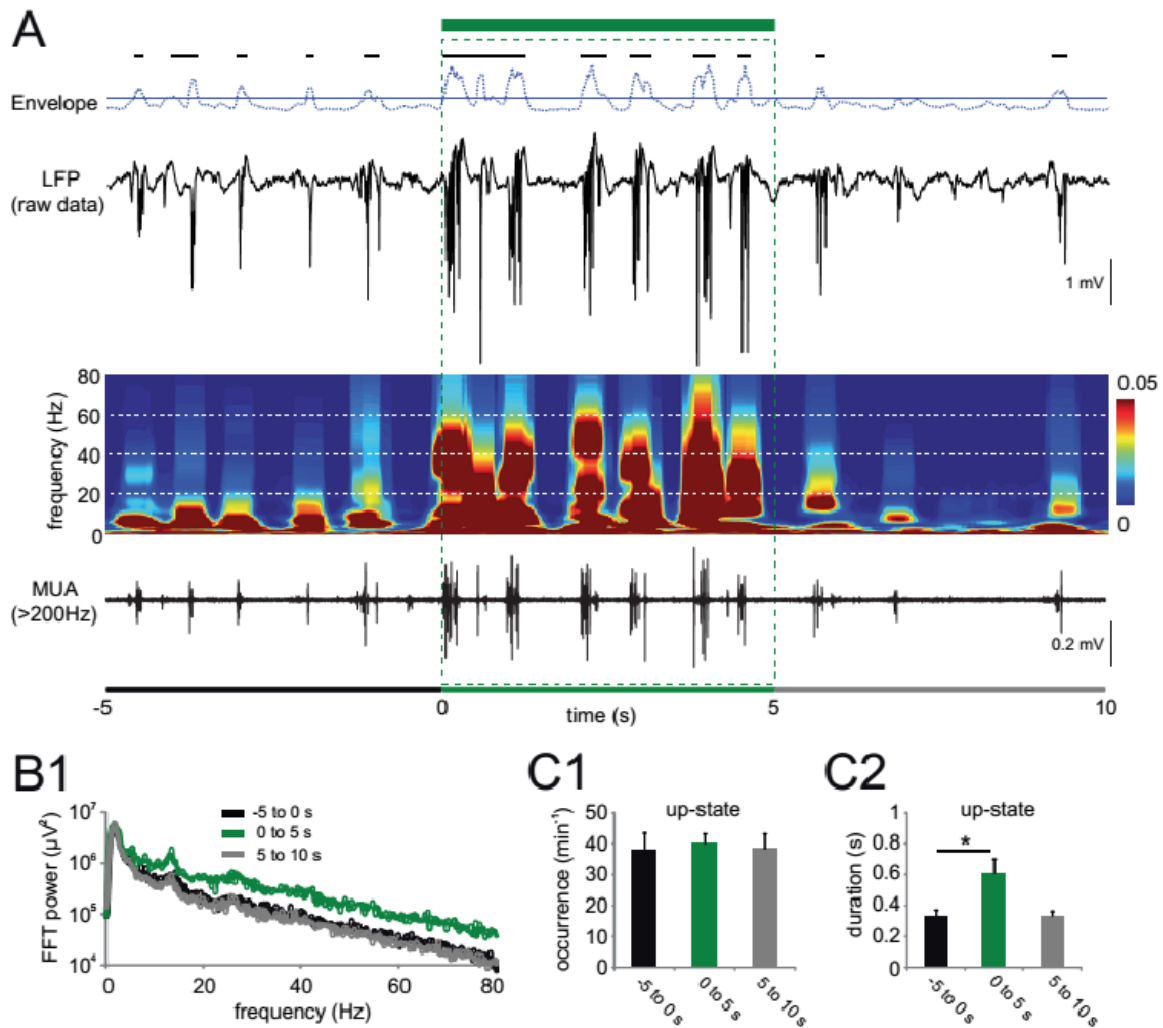


Figure 4-7: Impact of inhibiting PV interneurons on slow oscillations (A) Upper panel: Spontaneous LFP activity (raw trace) recorded in deep layer II/III of principal shank before, during (green horizontal bar; 5 s duration, 150 mW/mm², every 20 s) and after PV in activation from one P76 mouse. Three periods were defined: before (-5 to 0 s), during (0 to 5 s) and after green light pulse (5 to 10 s). The envelope of the recorded LFP was extracted and thresholded (blue line) from the raw signal to detect the Up states of the slow oscillation (black bars). Middle panel shows the corresponding wavelet plot from the LFP in the upper panel. Lower panel shows the corresponding multi-unit activity (MUA). (B) Fast Fourier transformation (FFT) of spontaneous LFP activity during the three periods (average over 4 animals). Note the prominent, reversible, and significant shift of the distribution towards higher FFT power over a wide frequency band during optogenetic inactivation of PV interneurons (green line, two sample K.-S. test, $p < 0.001$). (C1) The occurrence of Up states was not influenced during 5 s inactivation of PV interneurons (C2) The duration of Up states significantly increases during inhibiting PV interneurons (Friedman test: * $p < 0.05$, $n = 4$). (Fig. adapted from J.-W. Yang et al., 2017 by permission with Oxford university press)

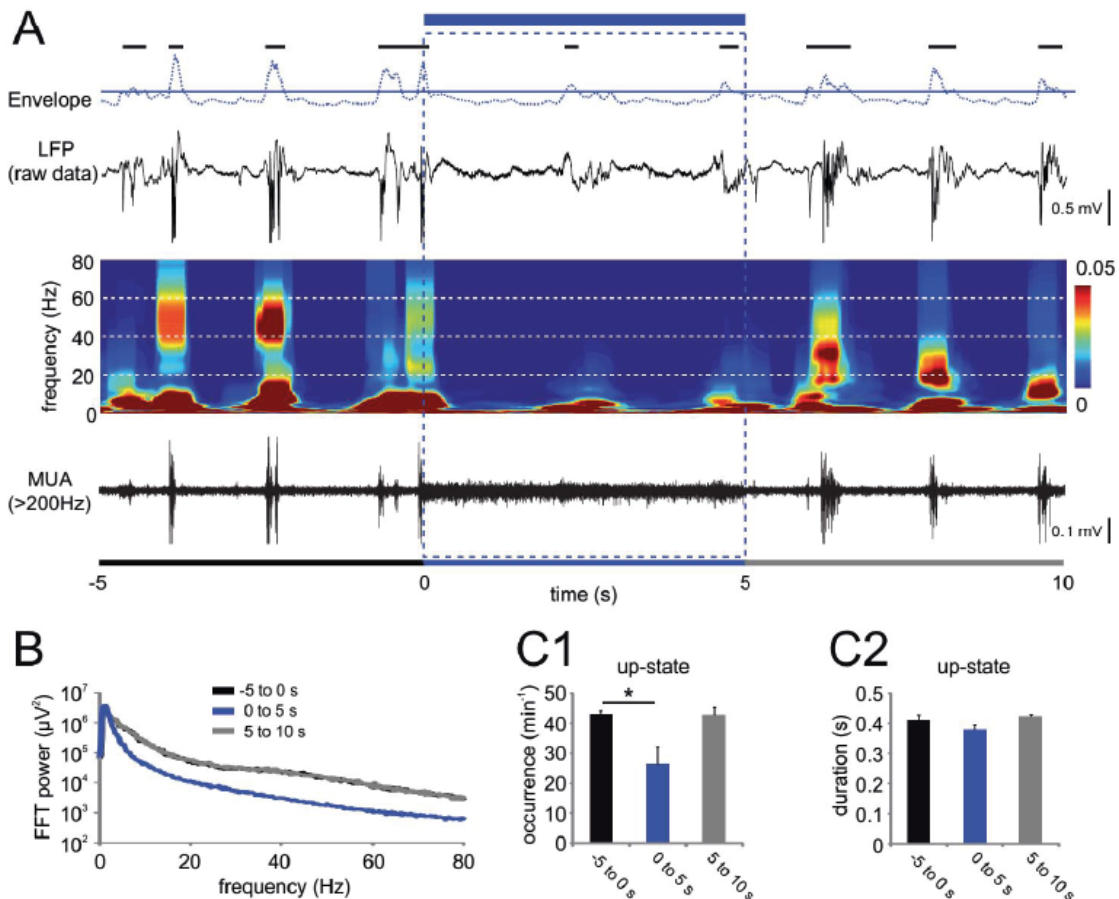
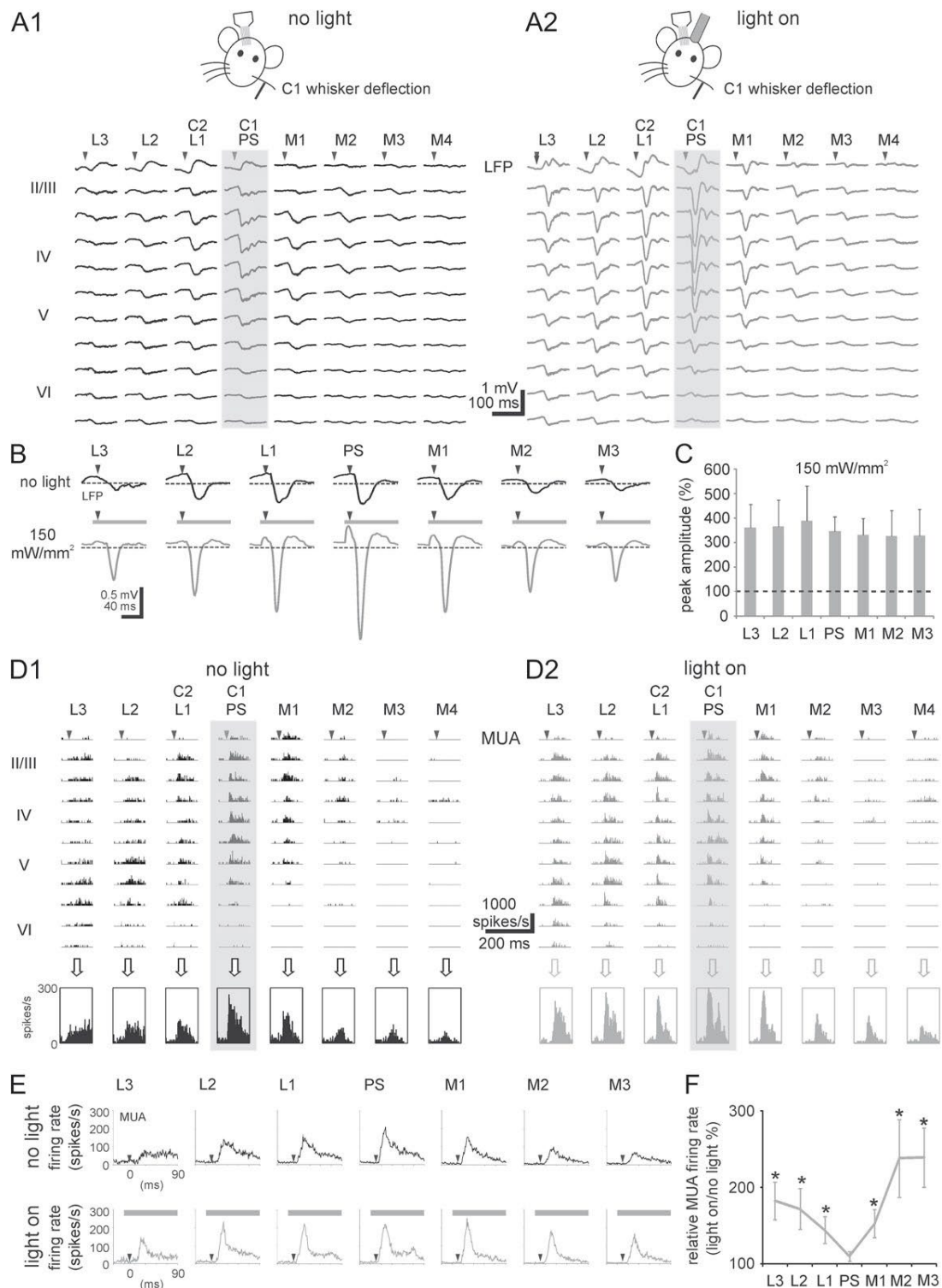


Figure 4-8. Impact of activating PV interneurons on slow oscillations (A) Upper panel: Spontaneous LFP activity (raw trace) recorded in deep layer II/III of principal shank before, during (blue horizontal bar, 5 s duration, 45 mW/mm², every 20 s) and after PV activation from one P136 mouse. Three periods were defined: before (-5 to 0 s), during (0 to 5 s) and after blue light pulse (5 to 10 s). The envelope (dashed trace) of the recorded LFP was extracted and thresholded (blue line) from the raw signal to detect the Up states of the slow oscillation (black bars). Middle panel shows the corresponding wavelet plot from the LFP in the upper panel. Lower panel shows the corresponding multi-unit activity (MUA). (B1) Fast Fourier transformation (FFT) of spontaneous LFP activity during the three periods (average over 6 animals). Note the prominent and reversible decrease of FFT power over a wide frequency band during optogenetic activation of PV interneurons (blue line, two sample K.-S. test, $p < 0.001$). (C1) Reduced occurrence of Up states during 5 s activation of PV interneurons (Friedman test: * $p < 0.05$, $n = 6$) (C2) The duration of Up states was not affected during activating PV interneurons. (Fig. adapted from J.-W. Yang et al., 2017 by permission with Oxford university press)

Spatial Profile of Transient PV Inhibition

Under control no-light conditions, mechanical deflection of whisker C1 with a duration of 60ms (Fig. 2-4) elicited the typical activation pattern to single whisker stimulation with large LFP responses recorded at the PS electrode located in the C1 column (Fig. 4-9A1). Smaller responses were recorded at the lateral shanks L1–L3 and the medial shanks M1–M4. Identical whisker stimulation with simultaneous PV-mediated disinhibition of the excitatory network

evoked at all recording sites much larger LFP responses (Fig. 4-9A2). Interestingly, an increase of the response peak amplitudes could be also observed at the electrode shanks located up to 600 μ m lateral (L1–L3) and up to 600 μ m medial (M1–M3) (Fig. 4-9B, C). These data indicate that the local and transient PV-mediated disinhibition induced a widespread excitability increase, affecting several neighboring columns in barrel cortex.



*Figure 4-9. Optogenetic inactivation of PV interneurons causes a global increase in neocortical responses to single whisker stimulation. (A) Average LFP response to 10 stimulations of the C1 whisker under control conditions (A1, no light) and during optogenetic inactivation of PV interneurons (A2, light on). Note largest responses at principal shank (PS) located in the cortical column representing the C1 whisker. (B) Prominent increase in response amplitude (average of 80 evoked LFP responses from 8 mice) during optogenetic inactivation of PV inhibitory interneurons could be observed at all recording electrodes located up to 600 μ m medial and lateral from the principal shank (PS). (C) Bar diagram illustrating that the increase in the response peak amplitude at lateral (L1–L3) and medial (M1–M3) shanks is not significantly different from that at principal shank (PS) ($n = 8$ mice). (D) Peristimulus time histograms (PSTHs) of MUA elicited by stimulation of whisker C1 under control conditions (no light, D1) and during optogenetic inactivation of PV inhibitory interneurons (light on, D2). Pooled MUAs recorded at different shanks are shown in lower row. (E) Average of pooled evoked MUAs recorded at the 7 different shanks under control conditions (upper panel, black) and during optogenetic disinhibition (lower panel, gray) ($n = 8$ mice). (F) The relative MUA firing rate was calculated by the ratio of mean MUA firing rate (light on/no light conditions) within ± 5 ms of maximum evoked MUA response. Note that response in principal column (PS) is not changed whereas MUA firing rate at neighboring recording sites is increased during disinhibition. (Paired t test, * $P < 0.05$, $n = 8$ mice). (Fig by JW. Yang adapted from J.-W. Yang et al., 2017 by permission with Oxford university press)*

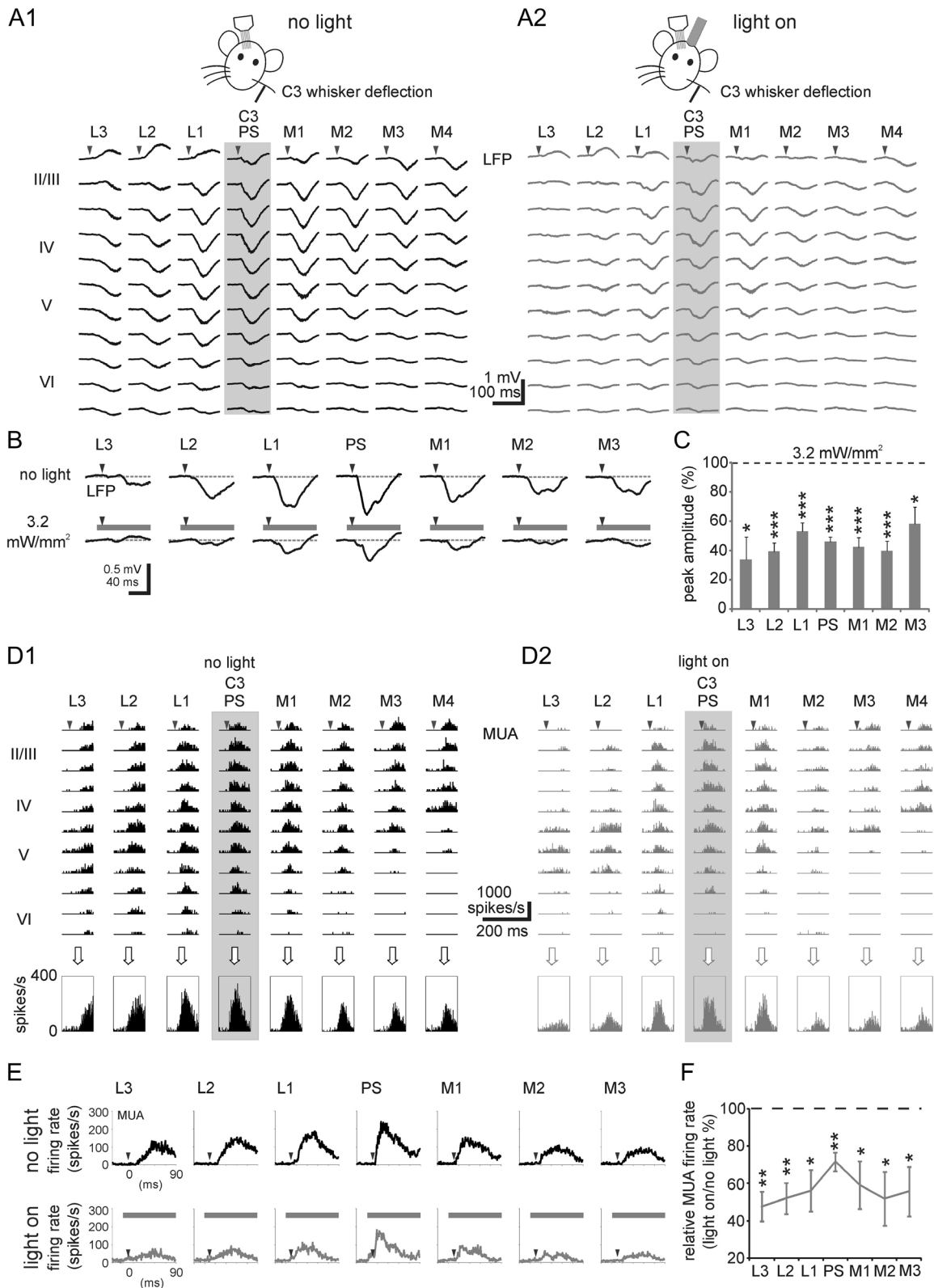


Figure 4-10: Optogenetic activation of PV interneurons lead to global decrease in neocortical responses to single whisker stimulation. (A) Average LFP response to 10 stimulations of the C3 whisker under control conditions (A1, no light) and during optogenetic activation of PV interneurons with an illumination density of 3.2mW/mm² (A2, light on). (B) Prominent decrease in response amplitude (average of 60 evoked LFP responses from 6mice) during optogenetic activation of PV interneurons could be observed at all recording electrodes located up to 600

μm medial and lateral from the principal shank (PS). (C) Bar diagram illustrating that the significant decrease of the LFP response peak amplitudes up to 600 μm lateral and medial of the PS (Paired t test, $*P < 0.05$ and $***P < 0.001$, $n = 6$ mice). (D) Peri-stimulus time histograms (PSTHs) of MUA elicited by stimulation of whisker C3 under control conditions (no light, D1) and during optogenetic activation of PV interneurons (light on, D2). Pooled MUAs recorded at different shanks are shown in lower row. (E) Average of pooled evoked MUAs recorded at the 7 different shanks under control conditions (upper panel, black) and during optogenetic activation of PV interneurons (lower panel, gray) ($n = 6$ mice). (F) The relative MUA firing rate was calculated by the ratio of mean MUA firing rate (light on/no light conditions) within $\pm 5\text{ms}$ of maximum evoked MUA response. There was a significant decrease of the MUA response up to 600 μm lateral and medial of the PS (paired t test, $*P < 0.05$ and $**P < 0.01$, $n = 6$ mice). (Fig. adapted from J.-W. Yang et al., 2017 by permission with Oxford university press)

Whereas the LFP reflects the local synaptic activation, the MUA reveals the suprathreshold activation of neurons located near the recording site. Therefore, the whisker stimulation induced MUA was analyzed under control no-light conditions and during PV-mediated disinhibition (Fig. 4-9D). Under control, deflection of a single whisker evoked a large MUA response in the activated principal column and smaller responses in the neighboring columns (Fig. 4-9D1, upper row in Fig. 4-9E). With simultaneous PV-mediated disinhibition at the PS, the maximum MUA response in the principal column did not change in any cortical layer, but interestingly increased at all lateral and medial recording sites (Fig. 4-9D2, lower row in Fig. 4-9E and Fig. 8-3). The spatial MUA profile shows a U-shaped pattern reaching an increase of $\sim 200\%$ in peak MUA firing rate at 400 and 600 μm lateral and medial from the activated column (Fig. 4-9F). These MUA data and the spatial profile of the synaptic LFP responses indicate that PV-mediated disinhibition induces a widespread increase in synaptic excitation, but an increase in suprathreshold spiking activity only in neighboring columns. Next, we addressed the question over which intervals and at which time points the PV-mediated disinhibition exerts these strong network effects.

Effect of Activation of PV Interneurons on Sensory-Evoked Response

We now investigated the impact of PV activation on single whisker-evoked responses in supragranular layers of the PS. For that, we expressed ChR2-mCherry in PV interneurons as described for ArchT experiments. Expression of ChR2 was again mainly constrained to layers II/III and V. The area of ChR2 expressing neurons constituted a cylinder with a diameter of $1335 \pm 40\mu\text{m}$ ($n = 5$ mice, Fig. 4-3). For ChR2, we found a cell density of $3093 \pm 399\text{cells}/\text{mm}^3$ in layer II/III, and $4297 \pm 488\text{cells}/\text{mm}^3$ in layer V. In our functional experiments, opposite to inhibiting PV interneurons, we observed a prominent decrease in response amplitude upon

illumination with 45mW/mm^2 blue light (Fig. 4-12A). The decrease in response amplitude during activating PV interneurons was strongly dependent on the light intensity (Fig. 4-12B, C). Compared with the response under no light condition, already at a low intensity of 3.2mW/mm^2 the peak amplitude was significantly decreased ($P < 0.001$, $n = 6$ mice) to $45.7 \pm 4.8\%$. Higher intensities of 6.4, 22, 45, and 105mW/mm^2 induced a further decrease of the peak amplitude, eventually abolishing most of the sensory-evoked response. This effect was accompanied by a significant decrease in the duration of the response at higher light intensity of 22, 45, and 105mW/mm^2 (Fig. 4-12C). Next, we studied the influence of transient PV activation on the spatial profile of evoked response. For that, we chose a low light intensity, which had shown to reduce but not completely abolish the evoked responses in the principal column. Notably, illuminating the principal column with 3.2mW/mm^2 light intensity induced a significant decrease of the LFP response peak amplitudes up to $600\mu\text{m}$ lateral and medial of the PS (Fig. 4-10A–C). The evoked MUA activity, reflecting neuronal spiking, also decreased during the PV activation (Fig. 4-10D–F). These data indicate that the local and transient activation of PV interneurons induced a widespread excitability decrease, affecting several neighboring columns in barrel cortex. We further studied the temporal profile of the impact of transiently activating PV interneurons on sensory-evoked responses. Differing from inhibiting PV interneurons (Fig. 4-11A, B), activating PV interneurons with a 100ms laser pulse terminated directly prior to the onset of whisker stimulation already decreased the evoked LFP response (0ms trace in Fig. 4-11A). Gradually increasing the duration of illumination—now overlapping with the whisker stimulus did not further decrease the response amplitude Fig. 4-11B). Applying short light pulses of 10ms only effectively modulated sensory-evoked responses when applied either directly at or 10ms after the onset of whisker stimulation (Fig. 4-11C, D). These data mirror the temporal profile of PV-mediated disinhibition (Fig. 6C, D). Next, we were interested in the question, how many PV-expressing interneurons need to be modulated to have such prominent effects on cortical excitability.

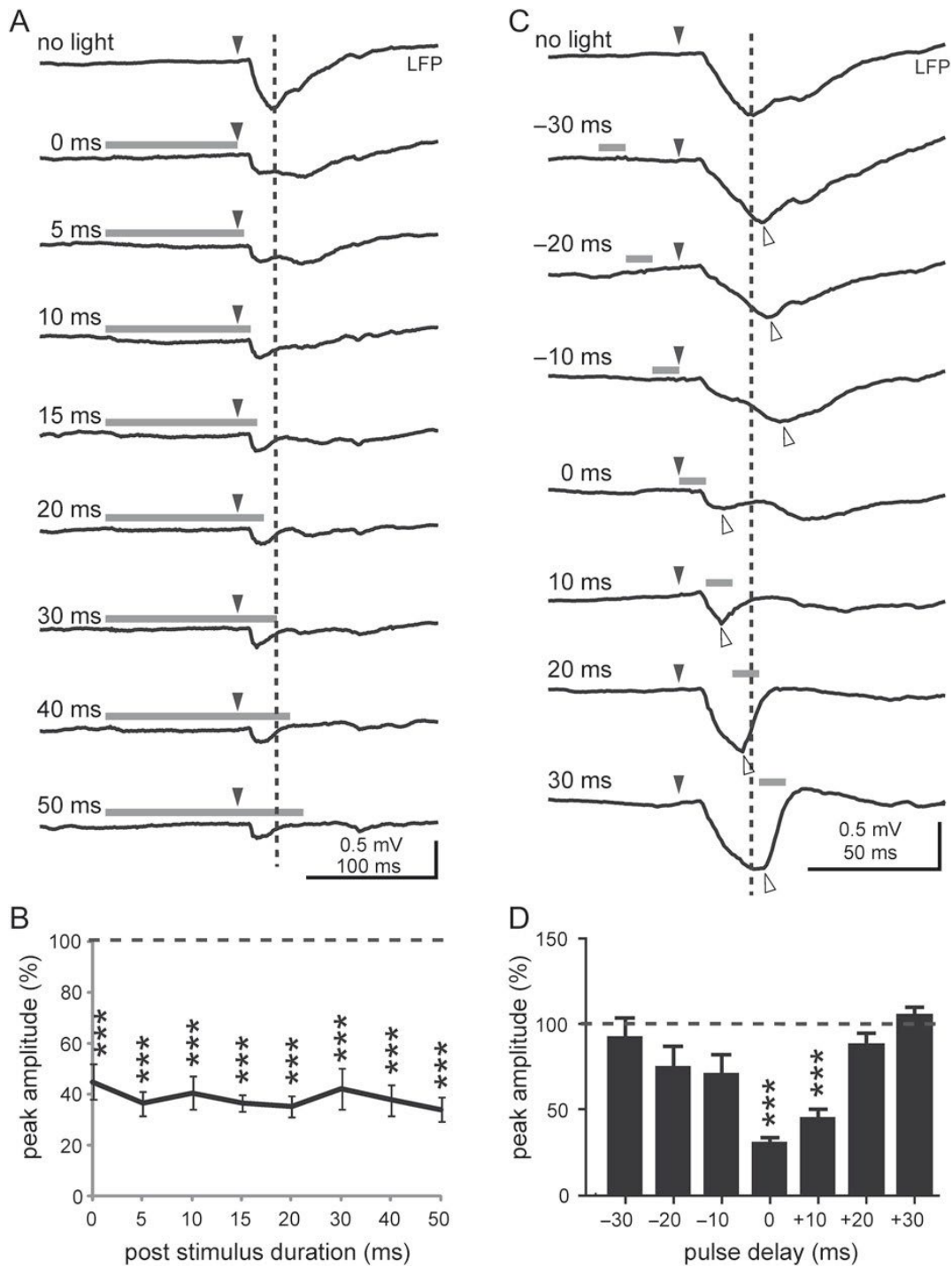


*Figure 4-11: Effect of increasing PV-inhibition duration and influence of different timing of transient PV-inhibition on sensory-evoked cortical responses. (A) Average of 60 evoked LFP responses to single whisker stimulation combined with different durations of activating PV interneurons ($n = 6$ mice). (B) Normalized peak amplitude of LFP response at increasing PVinhibition intervals. (C) Timing of 10 ms PV-inhibition and effect on evoked LFP response (average of 60 evoked LFP responses from 6 mice). (D) Normalized first peak amplitude indicated by empty arrows of LFP response at different PV-inhibition time points. Statistically significant differences (Paired t test) versus the control (no light) condition are indicated by $***P < 0.001$. (Fig. adapted from J.-W. Yang et al., 2017 by permission with Oxford university press)*

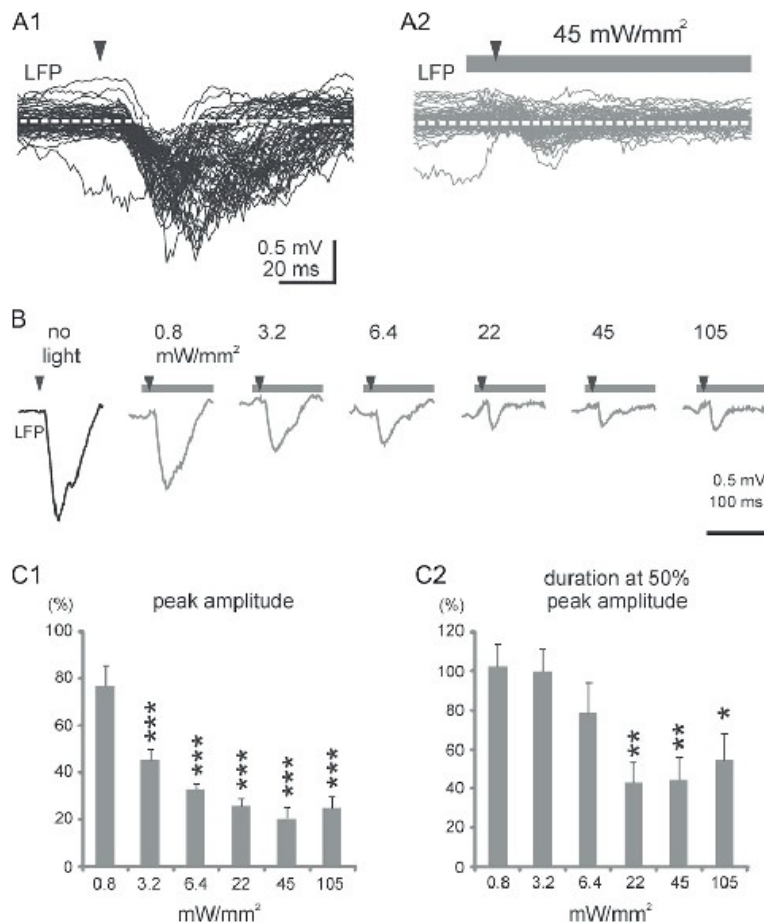


Figure 4-12: Optogenetic activation of PV interneurons causes amplitude decreases in stimulus-evoked cortical responses. (A) 60 superimposed raw traces ($n = 6$ animals) of evoked LFP activity recorded in deep layer II/III of the principal barrel column to single whisker stimulation under control condition (A1, no light) and during optogenetic activation of PV interneurons (A2, light on, 45mW/mm^2). (B) Decrease of sensory-evoked response in layer II/III to increasing laser intensities (average of 60 evoked LFP responses from 6 mice). Note: the traces in A2 and B with illumination were calculated by subtracting the LFP response during illumination without sensory stimulation from the sensory-evoked LFP response during the same intensity of illumination (see the details in Materials and Methods). (C) Normalized decrease in response peak amplitude (left) and decrease in response duration at half maximal amplitude (right) with increasing laser intensities ($n = 6$ mice). Responses were normalized and compared with control (no light). Paired t test, $*P < 0.05$, $**P < 0.01$, and $***P < 0.001$.

(Fig. adapted from J.-W. Yang et al., 2017 by permission with Oxford university press)

Modelization of efficient optogenetic modulation

To evaluate the number of neurons affected by the optogenetic stimulation we used the Kubelka-Munk approximation for diffuse refraction in heterogeneous media. Our approach consisted in assuming two extremes, a spherical spread and a conical spread from the fiber tip, the truth being probably between both. To broadly visualize the light propagation in brain tissue we devised a simple protocol. We embedded a whole unfixed brain into a bloc of agarose leaving only the very surface of the cortex exposed. We then placed this surface against a fluorescent

plate on top of our inverted microscope. We inserted a 200 μm fiber vertically from the top of our preparation using a micromanipulator and taking a picture of the fluorescence every 50 μm . The result in Fig. 4-13 is only qualitative but shows us that the spread of light is broadly conical but not doesn't have sharp edges. Imaging at these different depths requires scaling the detection and as such this image probably underestimates the spread closer to the fiber tip. Another important factor contributing to the "fuzziness" of the excitation is the expression itself (Stroh et al., 2013). Opsins are expressed in neuronal bodies but also across neurites, while illumination of the cell body affects a neuron more strongly (like basket cell synapses) activating opsins on a neurite does affect neuronal activity. As a result, cells projecting within the illuminated region but whose cell bodies are situated outside are indeed affected by optogenetic modulation. This is why we have to consider two extremes in our evaluation of the effect of light in our samples.

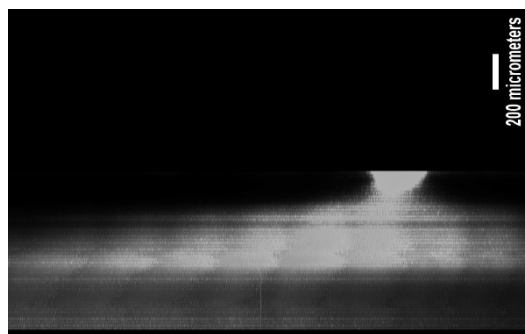


Figure 4-13 light propagation in fresh mouse brain tissue at 488nm (Fig PH. Prouvot)

Our model consists in using available tools to evaluate the power density in the depth of the tissue and to then use this curve to define a threshold below which cells are no longer effectively affected. The calculations are in essence quite simple. We used known values for thickness of each cortical layer and considered that the fiber was touching the surface of layer I. We then calculated the top radius and bottom radius of a frustum corresponding to each layer using Pythagoras's relationship. We then calculated the volume of each frustum and multiplied it to the average cell density in said layer.

This simple approach proved surprisingly precise when comparing it to the effective activation depth in figure 4-14. Our calculations gave us an effective depth of 650 μm to reach action potential threshold in parvalbumin interneurons and the effective depth at which we stopped evoking action potentials directly with 488nm light was indeed 650 μm .

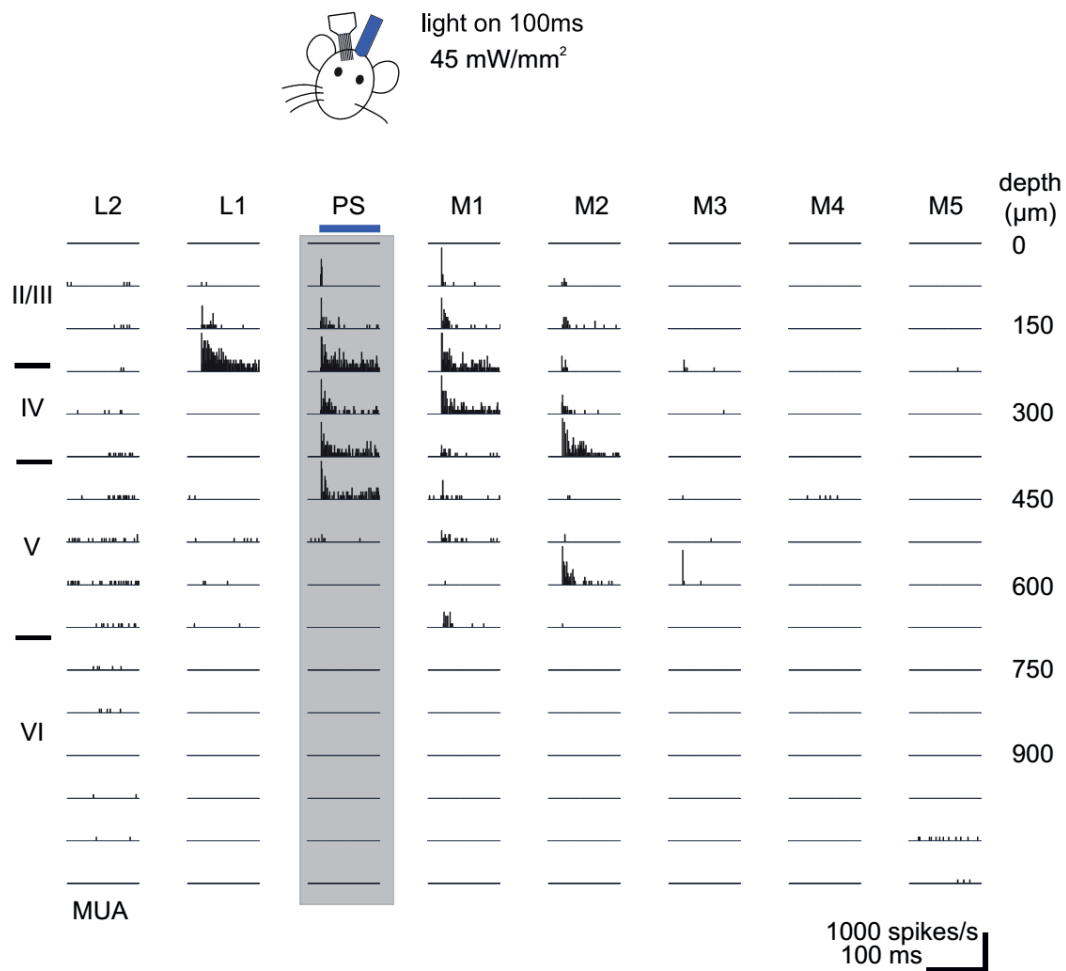


Figure 4-14: Spatial distribution of MUA activity induced by optogenetic activation of PV interneurons. A 488 nm blue light pulse (45 mW/mm², 100 ms) was applied in the immediate vicinity of the principal shank in one P133 mouse. Note that induced activity spanned layers II/III to V and shanks L1 to M3. Action potentials are observed down to 650μm. Lateral spread proves to be more ovoid than purely conical. (Fig. adapted from J.-W. Yang et al., 2017 by permission with Oxford university press)

A Small Number of Inhibited Interneurons Exert Significant Influence on the Cortical Representation of Sensory Stimuli

Estimating the number of effectively inhibited neurons in the local network requires 3 steps: (1) assessing the density of ArchT positive neurons, (2) estimating the photocurrent needed for effective inhibition of action potential firing, and (3) estimating the light attenuation in tissue upon illumination with an optical fiber (Schmid et al., 2016). Firstly, the density of ArchT-tdTomato positive neurons in layer II/III and V was assessed in coronal brain slices using a dedicated epifluorescence microscope equipped with stereology software. We found that in layer II/III 2580 ± 250 cells/mm³, and in layer V 2380 ± 890 cells/mm³ (n = 5 mice) exhibit strong, membrane-bound expression of ArchT, about 2% of the neuronal population of the

cortical column ($78\,986 \pm 60\,466$ neurons/mm³, based on (Lefort et al., 2009). Given that 10–20% of the neuronal population are interneurons (based on Gentet et al., 2012; Lefort et al., 2009; Schüz & Palm, 1989), 10–20% of the interneuron population strongly express ArchT. Secondly, we assumed a minimal inhibitory current to be required for interneuron inhibition ranging at 200–250pA (Galarreta & Hestrin, 2002). To reach this current by ArchT activation, a local light density of approximately 1.5mW/mm² is required (Han et al., 2011). Thirdly, we estimated the area in which the light density exceeds this threshold under our light delivery conditions using a 200 μm fiber with an NA of 0.39 and a light density of 150mW/mm² at the tip of the fiber and a wavelength of 552 nm. The attenuation of light in brain tissue is dependent on species, wavelength, microarchitecture of the brain tissue, and vascularization. Implementing all these parameters in a comprehensive model has not been accomplished yet, the most common approach for modeling light attenuation is the Kubelka–Munk model, postulating a conical geometry (Aravanis et al., 2007). However, existing experimental data strongly suggest that this model underestimates lateral scattering proximal to the fiber tip (Stroh et al., 2013; Yizhar et al., 2011). This deviation from the conical model is less prominent for deeper structures, therefore, for layer V we used only the Kubelka–Munk model, for layers II/III we considered a spherical model in addition, representing an extreme scenario of lateral scattering (Fig. 4-14A) (Schmid et al., 2016). The fiber being placed on top of the cortical surface, using the Kubelka–Munk model and applying a power density of 150mW/mm² at the fiber tip, the inhibition threshold of 1.5mW/mm² is reached at a distance of 0.8mm, exceeding the extent of expression in dorsoventral direction. For the lateral extent, assuming the extreme case of the spherical model, the entire layer II/III expressing region would be within above-threshold illumination (Fig. 4-15A). Taken together with the cell density measures, 250 ± 24 (n = 5 mice) PV positive interneurons were inhibited in layer II/III according to the spherical model. Assuming the Kubelka–Munk model, in layer II/III, a volume of 0.0376mm³ would be illuminated, smaller than the volume of expression, resulting in 97 ± 10 inhibited neurons. In layer V, due to the conical spread assumed by the model, the entire expression is illuminated above threshold, thus 162 ± 18 neurons are estimated to be affected under our illumination conditions.

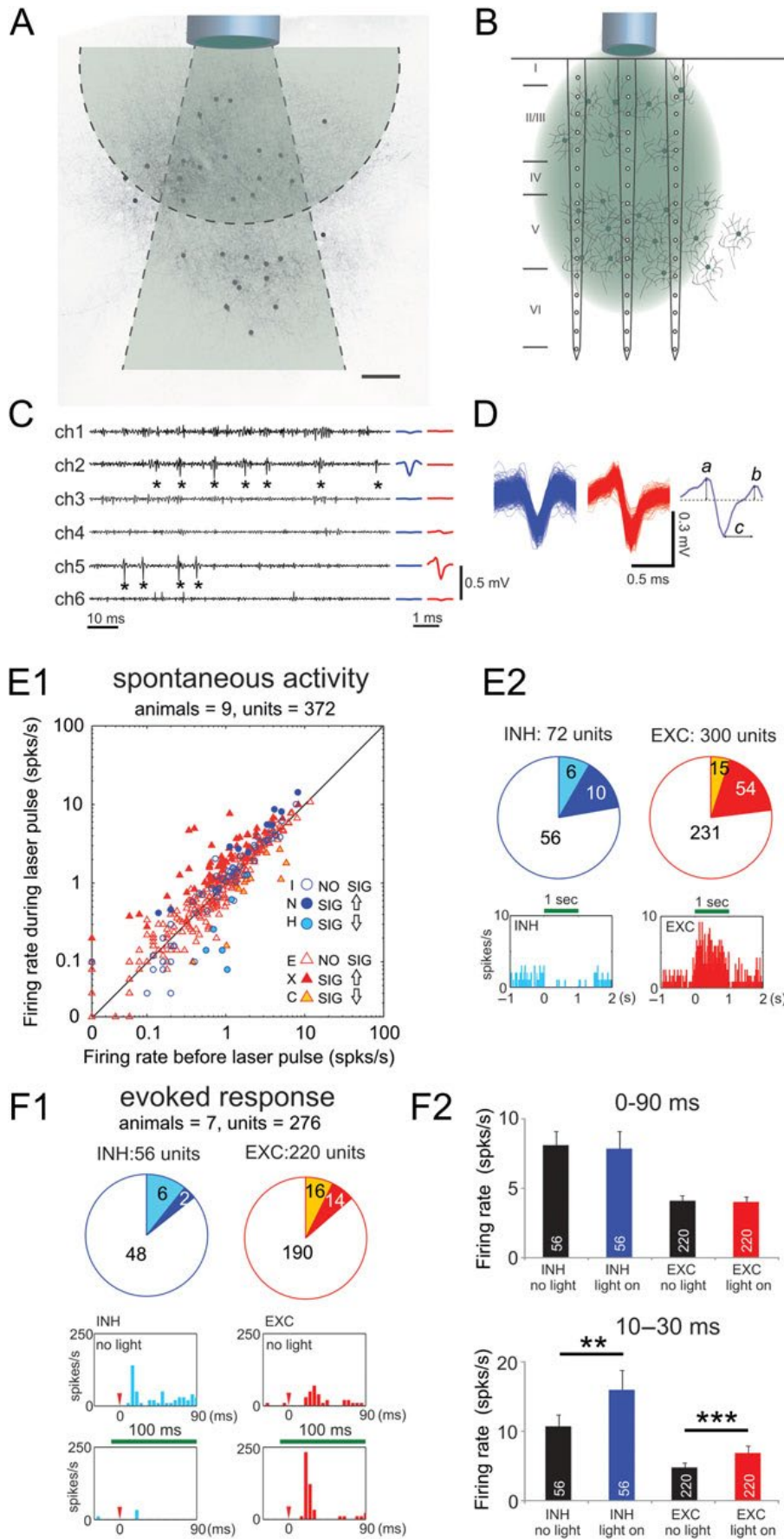


Figure 4-15: Optogenetic inactivation of a small number of PV interneurons exerts a global increase in neocortical activity. (A) Representation of light propagation

relative to ArchT expression in mouse barrel cortex, overlaid with confocal micrograph of a coronal brain slice at the level of ArchT expression. Circle: representation of the spherical spread. Frustum: Representation of the Kubelka–Munk model. Scale bar: 100 μm . (B) Representation of average cell densities relative to the recording electrodes and cortex layers, overlaid with the area of above-threshold illumination based on a combination of modeling and experimental data. (C) High-pass filtered signals (0.8–5 kHz) from 6 channels recorded simultaneously with an 8-shank 128-channel probe showing single unit spontaneous activity in a 100 ms long interval. Stars mark detected single unit events that were sorted as inhibitory (INH) and excitatory (EXC) neurons. Their average spike waveform profiles are shown in right panel (blue for INH and red for EXC). (D) Spike waveforms extracted from the INH and EXC neurons marked in C. The 3 features extracted from the spike waveforms to perform cell classification: a and b, early and late baseline-to-peak amplitude; c, trough to late peak latency (right panel). (E1) Comparing spontaneous mean firing rate of sorted units before versus during green light pulse (150mW/mm²). Circle symbols represent INHs and triangle symbols represent EXCs. Empty symbols represent neurons showing no significantly (NO SIG) different firing rates in both periods and filled symbols represent neurons showing significantly (SIG) different firing rates ($P < 0.05$, Wilcoxon signed-rank test). Dark and light blue circles represent INHs with significantly increasing (upward arrow) or decreasing firing rates (downward arrow), respectively. Red and yellow triangles represent EXCs with significantly increasing or decreasing firing rate, respectively. (E2) Pie charts showing the numbers of INHs and EXCs with no significantly different, significantly increasing and decreasing firing rates. Lower row shows examples of green light pulse inducing decrease in firing rate in 1 INH, and increase in firing rate in an EXC. (F1) Comparing evoked mean firing rate (0–90 ms after single whisker stimulation) of sorted units between no light versus green light pulse (150mW/mm²). Pie charts highlight the numbers of INHs and EXCs exhibiting significant increases or decreases (Mann–Whitney–Wilcoxon test). Examples of green light pulse decreasing evoked firing rate in 1 INH and increasing firing rate in another EXC. (F2) Upper panel shows the mean firing rate of INHs and EXCs in the time window of 90 ms after whisker deflection (number marked with bar diagram represent the number of units). Lower panel shows the mean firing rate of INHs and EXCs in the time window of 10–30 ms after whisker deflection. Note: data in E for spontaneous activity was in total 372 units from 9 mice and data in F for evoked response was in total 276 units from 7 mice. (Fig. adapted from J.-W. Yang et al., 2017 by permission with Oxford university press)

Therefore, we conclude, that a typical light pulse optogenetically inhibits between 260 and 410 cells, covering 3 electrode shanks, assuming an ellipsoid shape (Fig. 4-15B) based on model and experimental data (Yizhar et al., 2011). In the case of ChR2 stimulation, using similar volume calculations (see Materials and Methods for detail), resulted in 74 ± 9 to 116 ± 14 cells in layer II/III depending on the model of light propagation and 67 ± 8 cells in layer V. In total between 140 and 180 cells were excited in these experiments. To relate these cell numbers to functional data in our experimental setting, we conducted a single-unit analysis of the MEA data for the ArchT mediated disinhibition. This method allowed the simultaneous recording of numerous single units, which were classified as putative INH and EXC neurons (Fig. 4-15C, D, Fig. 4-15; for details (Reyes-Puerta, Kim, et al., 2015; Reyes-Puerta, Sun, et al., 2015)). In

total, 526 single units were detected ($n = 13$ mice), 79% (415) of these units were identified as EXC neurons, 21% (111) were identified as INH neurons (Fig. 8-4), in line with the aforementioned histology data. The putative inhibitory neurons include both PV and SOM cells (Ascoli et al., 2008; Rudy et al., 2011), but is not limited to them. In this regard, all subtypes of fusiform neocortical interneurons have shorter spike duration than pyramidal cells (Cauli et al. 2000). In the lateral amygdala, cluster analysis of interneurons identified only one major subtype (burst-firing adapting, 15% of the total population of GABAergic cells) which present broad spikes comparable to pyramidal cells (Sosulina et al., 2010). Considering these studies, we estimate that in our data the sorted putative interneurons represent not only PV and SOM cells, but also other interneuron types with narrow spike waveforms, thus accounting for ~80% of the total population of inhibitory cells. A small proportion of GABAergic neurons were possibly misclassified as putative EXC neurons—but this accounts for about 5% of the total population of EXC cells, due to the larger size of this group. Upon illumination during spontaneous activity recordings ($n = 10$ mice), 8.3% (6 of 72 INH units) of the putative INH neurons significantly decreased their firing rate (Fig. 4-15E), well matching our histological quantifications given the variability of the parameters involved. Notably, 10 inhibitory neurons increased their firing activity, yet it has to be noted, that our recordings cannot differentiate between PV and other interneurons, and secondary network effects may occur. While about 18% of excitatory neurons exhibited a significant increase, 5% showed a decrease in firing rate. Studying the single unit responses after whisker stimulation during illumination, about 11% of the inhibitory neurons (6 of 56 INH units) significantly decreased their firing rate (Fig. 4-15F), very similar compared with spontaneous activity, and a small proportion of 4% increased firing activity. The excitatory units exhibited an equal proportion of significantly increased and decreased firing rate (6% increase, 7% decrease). Interestingly, averaging the firing rate in the time window of 90ms after whisker deflection resulted in no effect on both excitatory and inhibitory firing rate. However, when limiting the analysis to a 20ms time window, covering the peak response (Fig. 4-6B, D), we notably detected a significant increase of excitatory and inhibitory firing rate ($P = 0.0002$ for EXC, $P = 0.0072$ for INH) (Fig. 10F2). In summary, our results indicate that modifying locally a very small subset of PV interneurons exerts a prominent global effect on excitatory and inhibitory neurons, both during spontaneous as well as stimulus-evoked activity, and that this effect exhibits a high degree of temporal specificity.

Study 3: Efficient optogenetic inhibition of spiking activity of ArchT-expressing newborn granule neurons in the olfactory bulb

Within the context of the development of all optical physiology approaches in the laboratory another project utilized fiber based optogenetics *in vivo*. This time in combination with twophoton calcium imaging in the olfactory bulb. The objective of this study was to evaluate the impact of adult born neurons on sensory processing in the olfactory bulb. My contribution consisted in helping design a protocol for *in vitro* controls to measure the responsiveness of newborn neurons to optogenetic stimulation. These measurements then informed the model I previously described in the methods section and in study two to evaluate the effective optogenetic stimulation *in vivo*.

To test for effective inhibition of newborn granule cells in the depth of brain tissue, together with minimizing potential non-specific light effects such as tissue heating (Rungta et al., 2017), we analyzed the electrophysiological response of ArchT- expressing newborn granule cells to light stimulation (552 nm) using whole cell patch- clamp recordings in acute OB slices of animals injected with ArchT-encoding viruses in the SVZ. The *in vivo* all-optical setup comprises an optic fiber (200 μm of diameter) placed on top of a glass coverslip covering the OB (Fig. 5-1 a), with the newborn neurons located deep in the granule cell layer. For *in vitro* electrophysiology, we mimicked this *in vivo* configuration by placing the acute OB slice on top of a glass coverslip and positioned the optic fiber below (Fig. 5-1 b). This ensured we did not underestimate scattering through the glass coverslip. The ArchT-expressing newborn neurons were visualized by their tdTomato fluorescence and were patched and filled with an internal solution containing the fluorescent dye Alexa Fluor 488 (Fig. 5-2 d). Applying increasing light intensities resulted in increasing inhibitory currents (Fig. 5-2 e; 6 neurons) displaying a roughly linear correlation for light intensities below $120\text{mW}/\text{mm}^2$ and reaching saturation at levels between 120 and $140\text{mW}/\text{mm}^2$, in line with the typical dose-response curve dynamics for opsins (Fois et al., 2014). Indeed, light- induced hyperpolarizations generated a complete inhibition of action potential firing induced by a depolarizing current pulse (Fig. 5-2 f), throughout repeated trials of optogenetic silencing (Fig. 5-2c.). We next calculated the power intensity at the level of the recorded neuron in the depth of the tissue, using the Kubelka Munk model for light distribution and attenuation in brain tissue (Aravanis et al., 2007; Diester et al., 2011; Schmid et al., 2016) (Suppl. Fig. 5-2d). For the subsequent experiments, we chose a light intensity of $10\text{ mW}/\text{mm}^2$ at the level of the neuron (corresponding to ca. $95\text{mW}/\text{mm}^2$ at the fiber tip), still

well within the linear range, and similar to previous studies (Schmid et al., 2016; Stroh et al., 2013).

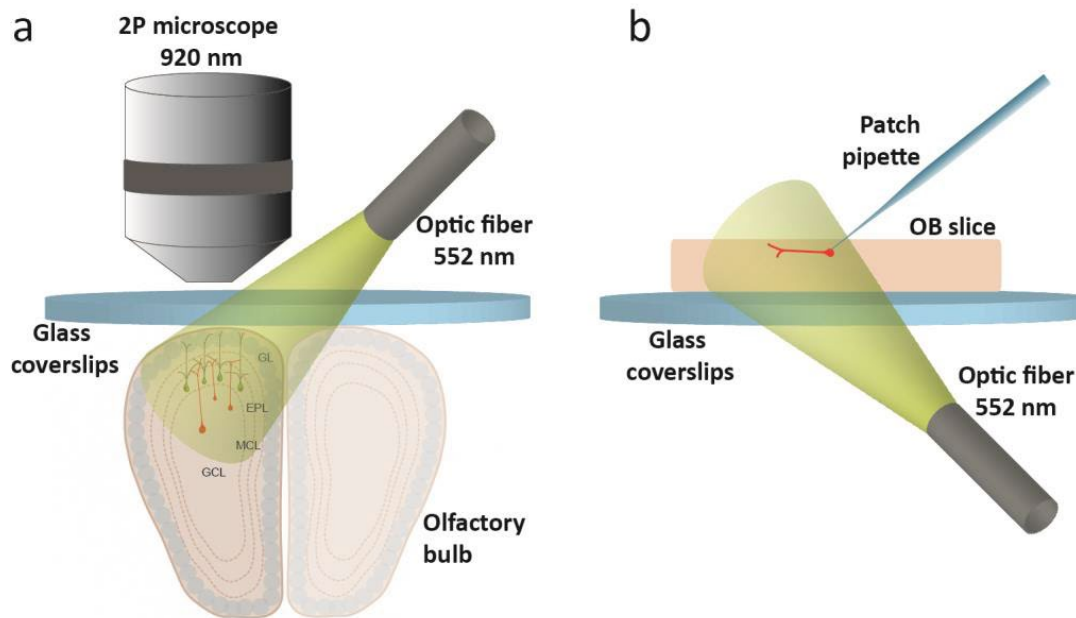


Figure 5-1: Schematic representations of the in vivo and in vitro setups. (a) In vivo experimental setup. The glass window covers the dorsal OB allowing for simultaneous imaging of the GCaMP6f-expressing M/T cells and optogenetic inhibition of the ArchT-expressing newborn granule cells with an optic fiber (200 μ m diameter, 552 nm). (b) Electrophysiology setup for the in vitro experiments mimicking the in vivo condition. The optic fiber is located below the coverslip to provide optogenetic inhibition of the newborn granule cells during the patch-clamp experiments. (Fig. by C. Fois)

Evaluation of the number of inhibited newborn neurons

We combined electrophysiological results, quantification of ArchT-expressing newborn neurons and already established modeling of light distributions to evaluate the number of inhibited newborn neurons in the in vivo experiments (Rungta et al., 2017). For the calculations of light penetration, we used the online tool provided by the Deisseroth lab (<http://web.stanford.edu/group/dlab/cgi-bin/graph/chart.php>). We used a 200 μ m fiber with a numerical aperture of 0.39, an initial power density of 95mW/mm² and a wavelength of 552nm. ArchT-positive cell density was evaluated in equally spaced sections (every 300 μ m; 7 animals) resulting in a density of 410 ± 8 cells/mm³. Using the previously described model for light propagation in tissue, we concluded, that the light density falls below this value at a depth of 600 μ m. We then calculated the illuminated volume as a frustum with a 0.1 mm radius top

section, and multiplied this value by our cell density, to get the final number of cells that are inhibited on average in the in vivo experiments (see methods).

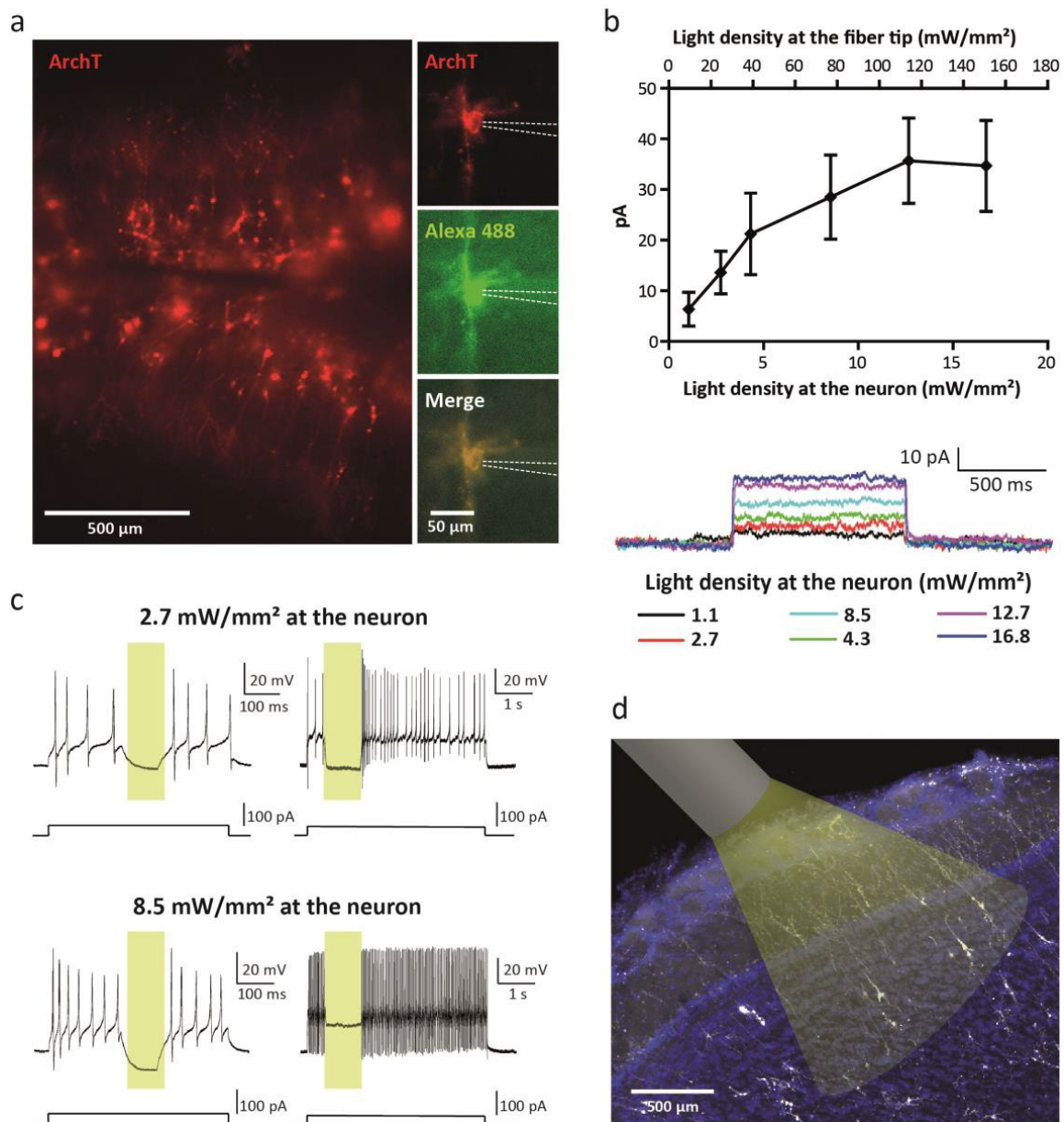


Figure 5-2: Assessing the number of optogenetically inhibited newborn neurons. (a) Left: ArchT-positive neurons in an acute living OB slice. Right: higher magnification of an ArchT-positive recorded newborn granule cell filled with Alexa 488 during the whole-cell patch-clamp recording and overlay with the ArchT-tdTomato fluorescence. (b) Top: average dose-response curve of the inhibitory current to light density. Upper axis is light power density measured at the fiber tip; bottom axis is light power density at the neuron corrected for attenuation through the 300 μm thickness of the acute slice (6 neurons). Bottom: Voltage clamp recordings demonstrating photocurrents induced by different 552 nm laser light power (1 s duration). (c) Current clamp mode recordings of ArchT-positive newborn granule cells showing a robust silencing of firing in response to 552 nm light stimulation (left panels = 100 ms, right panels = 1 s) during a current-injected (left panels = 500 ms, right panels = 5 s) depolarization pulse. (d) Representation of light penetration in the tissue according to an application to the

KubelkaMunk model (penetration depth = 600 μm). (Fig by C. Fois, N. Marichal and PH. Prouvot)

Estimating the number of optogenetically silenced newborn neurons

The patch-clamp experiments demonstrated that effective inhibition is achieved at light intensities of $2.7\text{mW}/\text{mm}^2$ at the level of the neuron in the depth of the tissue. Assuming an initial light intensity at the fiber tip used for the *in vivo* experiments of $95\text{mW}/\text{mm}^2$ and using the Kubelka Munk model (Fig 5-2d) this light intensity would be reached at a depth of $600\mu\text{m}$, thus encompassing the granule cell layer populated by ArchT-expressing neurons. We then conducted quantifications of the density of ArchT-expressing neurons in brain slices, resulting in a density of 410 ± 8 cells/ mm^3 . Combining the relative density measures with the dimensions of the frustrum effectively illuminated following the Kubelka Munk model, yields a number of 44 ± 8 (7 animals) newborn neurons being optogenetically inhibited. This relatively low number of neurons could then be related to a detectable change in activity in mitral cells in the following part of this work (not shown here). This methodology for evaluation of optogenetically modulated cells could be put in place with as good controls as possible in a short time span. It provides a simple *ex vivo* framework for better understanding of future optogenetics studies *in vivo*.

Study 4: Mesoscale imaging of the whisker field

Identifying which cortical region corresponds to which whisker is an essential element of recording sensory evoked activity in the barrel cortex. The typical method used by electrophysiologists is Imaging of Intrinsic signals. This technique consists in imaging the brain surface illuminated at 625nm while focusing slightly below the pial surface in order to measure the change in reflectance due to blood flow and blood oxygenation. This method requires very little materials (a camera and a stable light source) but the signal is very low, requiring averaging over a numerous (10-30) trials to identify an active region. The oxygenation level and consequently the anesthesia of the animal is also important as it strongly impacts the observed effects. We used this technique in the barrel cortex in PRG-1 KO and wild type mice during acute experiments. These mice were readily available, and we decided to combine testing the feasibility of this technique with measurements to compare KO mice with controls. We could identify barrels using high trial repetition (10 baseline and 30 stimulation trials) and averaging the responses over those repetitions (Fig. 6-1 top panels). We found that PRG-2^{-/-} mice revealed a significantly broader hemodynamic response (Mann-Whitney test; $n = 7$ mice per group). $*p < 0.05$ at 5% threshold (Fig. 6-1 left three panels). This was suspected because the deficiency in PRG-1 receptors impairs the proper targeting of thalamic projections to individual barrels. While this method could be used routinely by our collaborators on a dedicated recording system in our hands it was less reliable. We used the body and filter set of one of our two-photon system with a $\sim 45^\circ$ angled illumination and an ANDOR sCmos camera controlled by micromanager. The system was not particularly dedicated for that and had to be adjusted every recording session. The signal was so low that identifying barrels required over 30 repetitions making the stimulation of a single whisker last 15-20min upon which one should add the same time for analysis. This time can be spent without issue when Intrinsic imaging is the goal of the experiment but it is excessive as a preliminary experiment. It would mean spending an hour or more before performing the actual recordings with all the implication for the physiological state of the animal that an extra hour of anesthesia entails. Alternatively, one solution would be to identify the barrel of interest before virus injection.

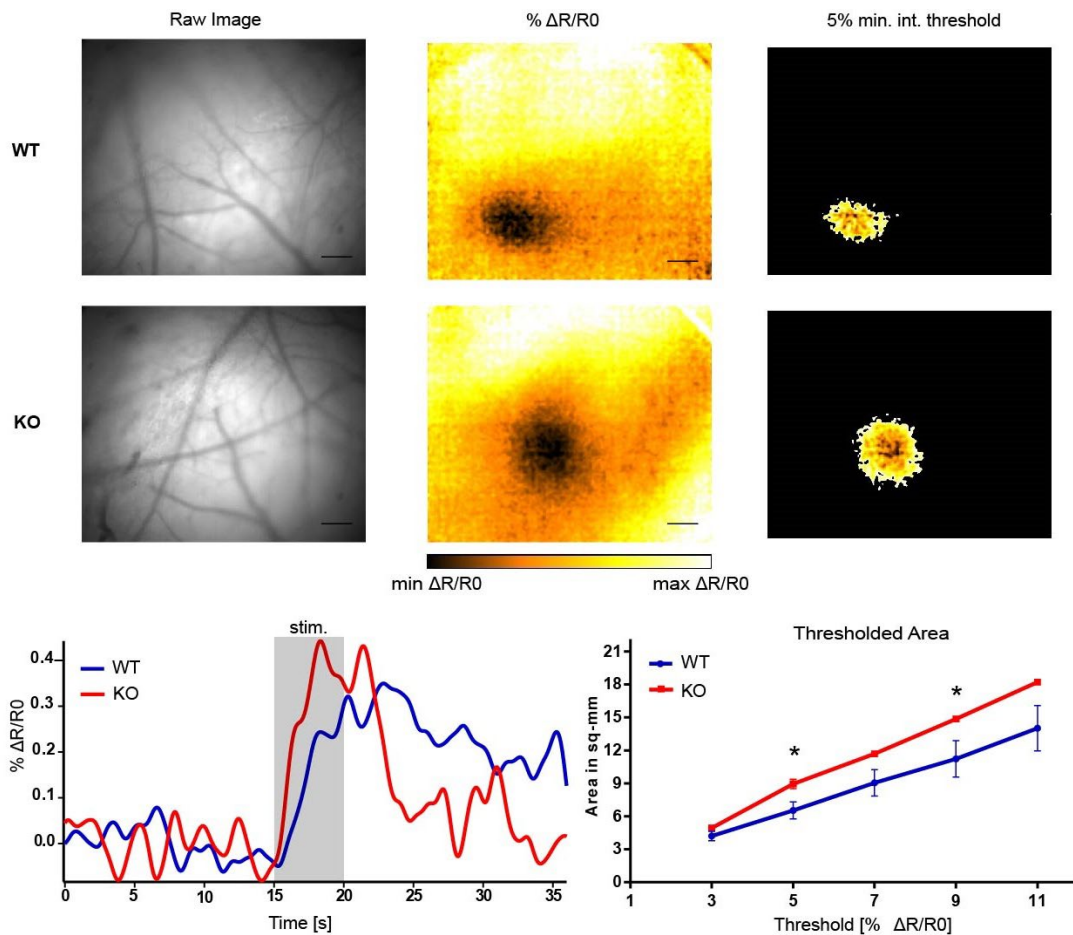


Figure 6-1: Intrinsic optical imaging of PRG-1 KO mice. Representative Color-coded images representing changes of hemodynamic response (DR/R0) after single-whisker stimulation using of intrinsic optical imaging in WT (top row) and PRG1^{-/-} (middle row) mice. From left to right: Blood vessel map acquired under 560nm illumination, Blood oxygenation variability image obtained by averaging single whisker response 10s post stimulation over 30 trials. Threshold set at 5% DR/R0 reflecting steepest drop of hemodynamic response is delineated. Bottom row left: average intensity over time from the 0,5mm at the center of the responding region. Bottom row right: Surface of the thresholded area at different threshold values. Values are significant at 5 and 9% (Fig by PH. Prouvot data acquisition PH. Prouvot and S. Sahani adapted from Cheng et al., 2016)

Using Intrinsic Optical Imaging to target virus expression to a single barrel

In a pilot experiment in our collaborating laboratory () we tried using IOI to target the virus injection. The rationale was that if we center the expression on an identified barrel, we could target it for OGB-1 injection using epifluorescence on our two-photon microscope. While it proved unpractical ultimately this pilot was successful in three out of three mice and shows it is possible to express opsins in superficial layers of a single barrel. We used the drug cocktail medetomidine/midazolam/fentanyl to perform IOI in a custom system. After identifying Barrels B1 and B2 we carefully injected 200nl of the same virus solution as earlier at an angle of 60° inserting the pipette only superficially to 400μm. The mouse was headfixed temporarily during

the procedure using very small amounts of spray adhesive (super 77 3M) easily removable after the surgery (Fig. 2-1). The exposed surface of the skull was kept covered in 2% agarose to improve optics and post-op recovery. The skull was not opened or thinned as in juvenile mice the bone is still transparent enough to perform these experiments through it.

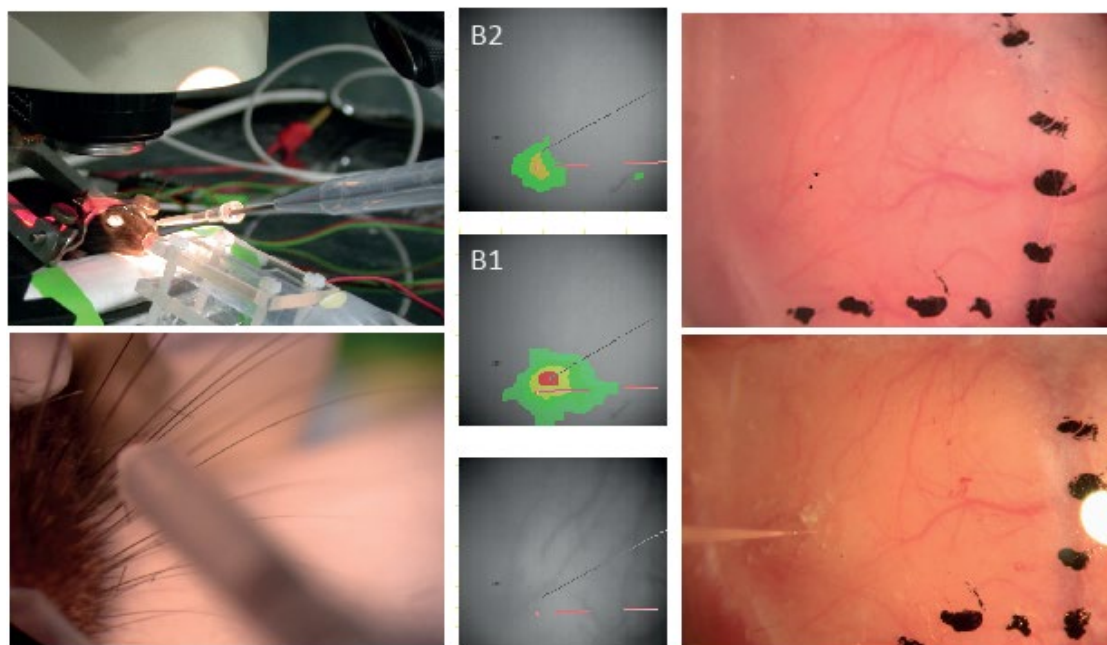


Figure 6-2: Intrinsic optical imaging identification of whiskers. A1 Intrinsic optical imaging setup A2 close up of the positioning of the whisker stimulator positioned on a single whisker, care was taken not to stimulate multiple whiskers. B false color identification images for B1 and B2 overlaid on a raw image of the blood vessels. C positioning of the identified barrels on a color image of the surface of the skull. Black dots are spaces 1mm apart with the angle on bregma. The lower picture was taken during the injection using a glass pipette inserted in a minimal craniotomy (Fig. by JW. Yang and PH. Prouvot).

The virus expressing region was identified using an epifluorescence microscope on the open craniotomy to target insertion of the DiI coated microelectrodes. After the recordings the brains were fixed in 4% PFA and sliced at 200 μ m thickness tangentially to the cortical surface. Slices in layer IV were stained with cytochrome oxydase to reveal the shape of the barrels. The expression of ArchT can be seen to overlap with the center electrodes of the array (Fig 6-3 left and center panel). The confine of the expression overlapped with the confines of the targeted C1 barrel (Fig. 6-3 right panel) with a maximum overlap on half one neighboring barrel. Here the targeted barrel was C1 and overlap was with with C2.

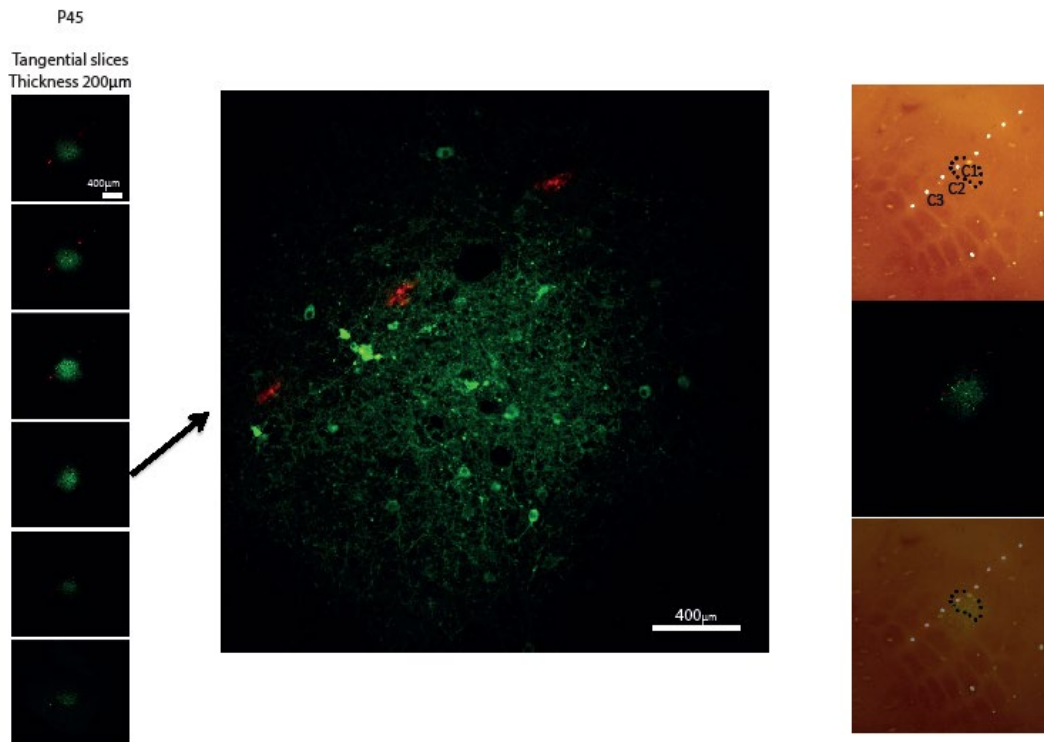


Figure 6-3: Single barrel expression of ArchT. Left: Confocal micrographs of tangential slices of the expressing barrel three weeks after injection and taken after recording. Expression was limited to the first 700µm and was approximately 400µm across. Center: confocal micrograph of the expression around 600µm (green) overlaid with DiI staining left by the recording electrodes (red). The electrodes were placed using the position of blood vessels and fluorescence as seen from the surface. Right: Expression overlaid over the cytochrome oxidase staining revealing the barrel map. (Figure PH Prouvot and JW. Yang)

We achieved ArchT-GFP limited within the confines of a single barrel (Fig 6-3) mostly in layer II/III. This method could prove interesting for future studies investigating the connectivity between directly neighboring barrels. In our particular case however, this was not realistically usable. The principal reason was that the imaging system was out of the animal house whereas the S2 was in and shuffling animals in and out was frowned upon. The whole procedure including IOI, data analysis and virus injection lasted three hours, required two persons and the booking of two common systems, as a result it was unfortunately not realistic to make it routine for this particular project.

The reverse would have consisted in injecting the virus semi-blind and identify the barrel on the day of imaging. The expression of our calcium indicator and opsin is limited to 1-3 barrels that one would need to be lucky to identify in a few trials. For all these reasons and because we later decided to move from acute to chronic experiments using GECIs we decided to try using

surface recordings of the GCaMP signal to identify which whisker corresponds to the expressing region.

Two-photon calcium imaging under anesthesia

Implementation of two-photon calcium imaging

Our first endeavor was running two-photon calcium imaging experiments. We used a bare bones Lavisision biotec trimscope III to perform the first recordings the configuration of the microscope and the mouse holder are detailed in the section the improvements to the recording system. These primary recordings were performed using a classical galvanometric scanner to move the focal point of the laser so in order to attain a usable minimal imaging frequency of 10Hz we had to decrease the number of lines scanned drastically (Fig. 6-6), limiting the field of view and the number of cells imaged at once. The next steps towards imaging whisker evoked activity consisted in identifying which whisker corresponds to the imaging region and imaging larger fields of view to increase our odds of detecting activity.

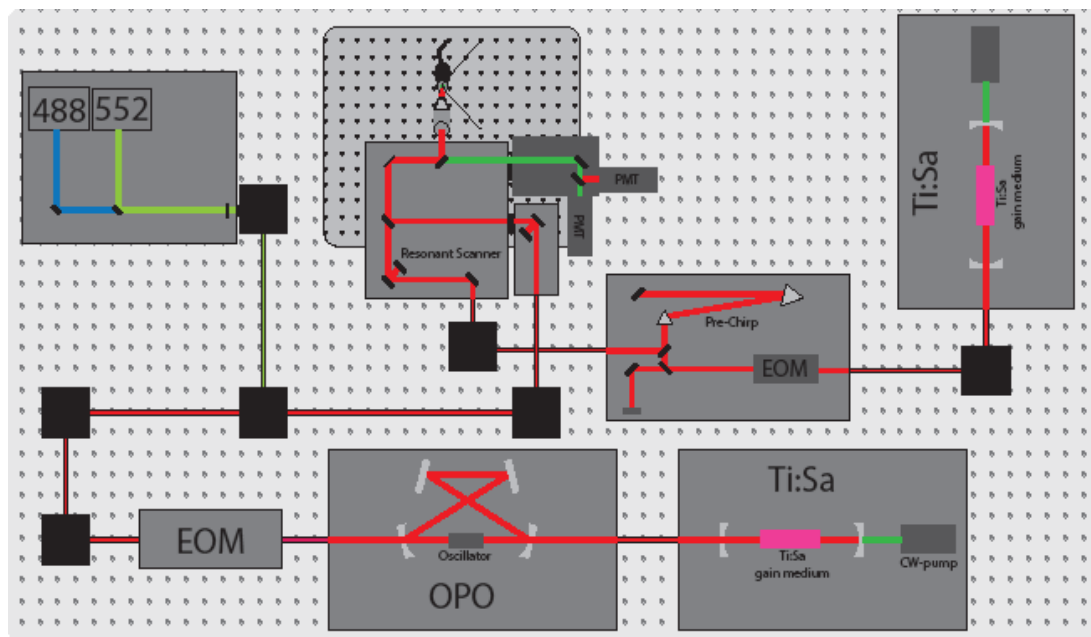


Figure 6-4: General schematic of the Trimscope II.

This system was composed of two light paths with two chameleon ultra 2 laser heads. One for excitation between 700 and 1000nm and the other pumping an optical parametric oscillator (basically a laser head without its own pumping laser) to achieve excitation wavelength between 1000 and 1600 necessary of two-photon optogenetics. Note the pre-chirp module combined with the electro optical modulator controlling laser power. The OPO light path was not pre-chirped. Also note the supplementary excitation wavelength at 488 and 552nm provided by two OBIS lasers. These extra lasers were used for single photon optogenetics. (Fig PH. Prouvot)

To increase our field of view we acquired a resonant scanner to replace the classic galvanometric previously installed. The main difference being that a galvanometric scanner needs time to get up to imaging speed and needs to decelerate and accelerate at each change of direction at the end of each scanning line whereas the resonant scanner moves at its resonant frequency, meaning the framerate at a given field of view cannot be adjusted directly but the set framerate is much higher than normal (here 30.5Hz). Notably the frequent change in direction at maximum speed can damage the galvanometric scanners up to complete failure which we experienced after about 6 month of daily use. On the contrary resonant scanners are much more resilient being able to function daily for years without failure. We also changed the situation of the mouse on the table to avoid movement artifacts due to breathing, we moved to isoflurane induced anesthesia at first for better control of anesthetic depth but soon realized that the mask prevented access to the whiskers for stimulation, so we changed to urethane anesthesia for consistency with our collaborators. We also installed a heating element for the perfusion fluid since temperature can have a strong impact on global and local neuronal activity (Schwalm & Easton, 2016).

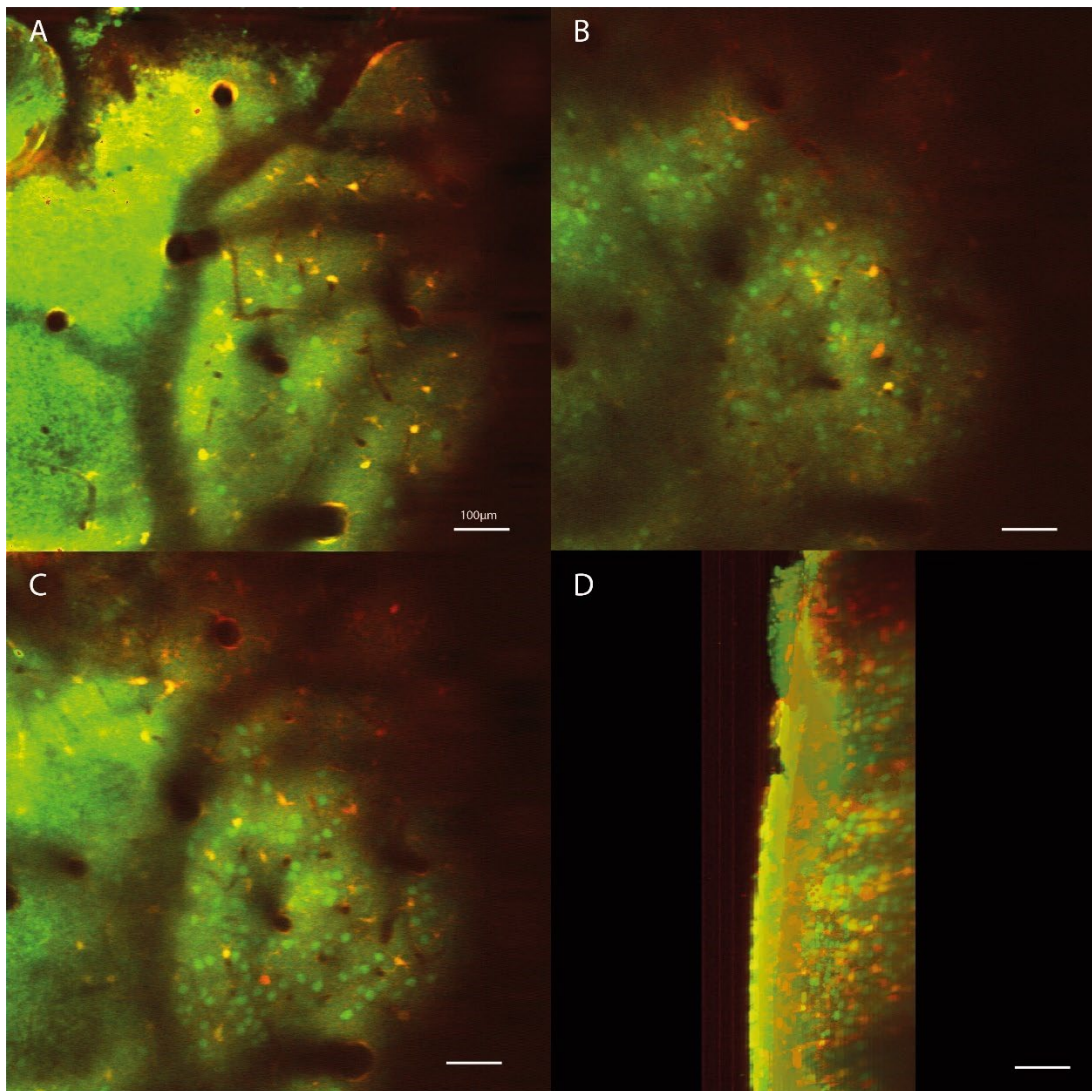
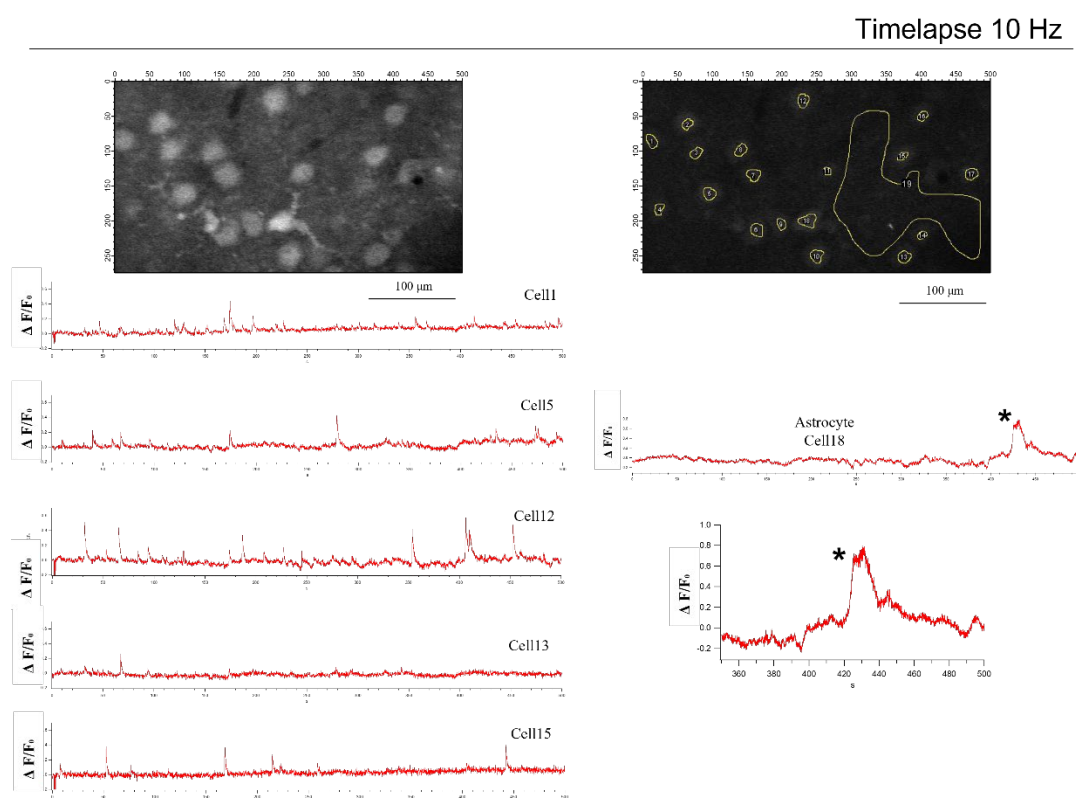


Figure 6-5: Typical OGB1 staining in the barrel cortex combined with SR101 astrocytic staining. A In layer I (50µm from the dura) showing mostly astrocytes and their particular high uptake of the sensor. Blood vessels shadows can be seen horizontal across the surface. Note that most cells are co-stained with SR101 indicating they are astrocytes. B-C Typical layer in putative layer III (300µm from the dura) showing neurons and astrocytes. Note the vertically penetrating blood vessels D transversal image of the same staining. Scale bars are 100µm (Fig PH. Prouvot)

Spontaneous activity at single cell level

To test our two-photon setup, we first performed recordings of spontaneous activity under Ket/Xyl anesthesia using OGB-1 AM as a Ca^{2+} reporter. We chose potentially active cells using the live feed and centered a reduced field of view around them. The number of pixels in a line is not relevant to speed since the longest time taken by the scanner is to slow down and reverse direction outside of the imaging frame. Ignoring regions not containing cells does decrease data size, which can be an useful. To achieve 10Hz the frame had to be limited to approximately 275 lines scanned (~235µm) for 15Hz ~160 lines (~137µm) and for 30Hz ~110 lines (~94µm). Note

that these numbers are dependent on this particular system and can change with age of the scanner. The primary recordings under ketamine xylazine anesthesia are depicted in Fig. 6-6. The cells are clearly visible and distinguishable from each other and the signal to noise ratio is reasonable. The dye SR101 can be used to identify astrocytes since OGB-1 also stains them (Fig. 1-9) but their calcium kinetics makes them simple to manually discriminate from neurons. Typically, 1-10 cells were recorded simultaneously. To control for activity, we extracted the mean grey value of manually drawn ROIs over each individual neuron and astrocyte and over the whole frame. Astrocytes present very high fluorescence relative to neurons due to their higher uptake of OGB1-AM and they present a smaller cell body size and larger more visible projections, whereas neurons are more circular with rarely visible projections and present lower average fluorescence. Astrocytic activity presents different dynamics with slower rising events on the second timescale typically presenting a short plateau whereas neurons present a typical fast rise time with exponential decay and a sharp peak (Fig 6-6 top panel right).



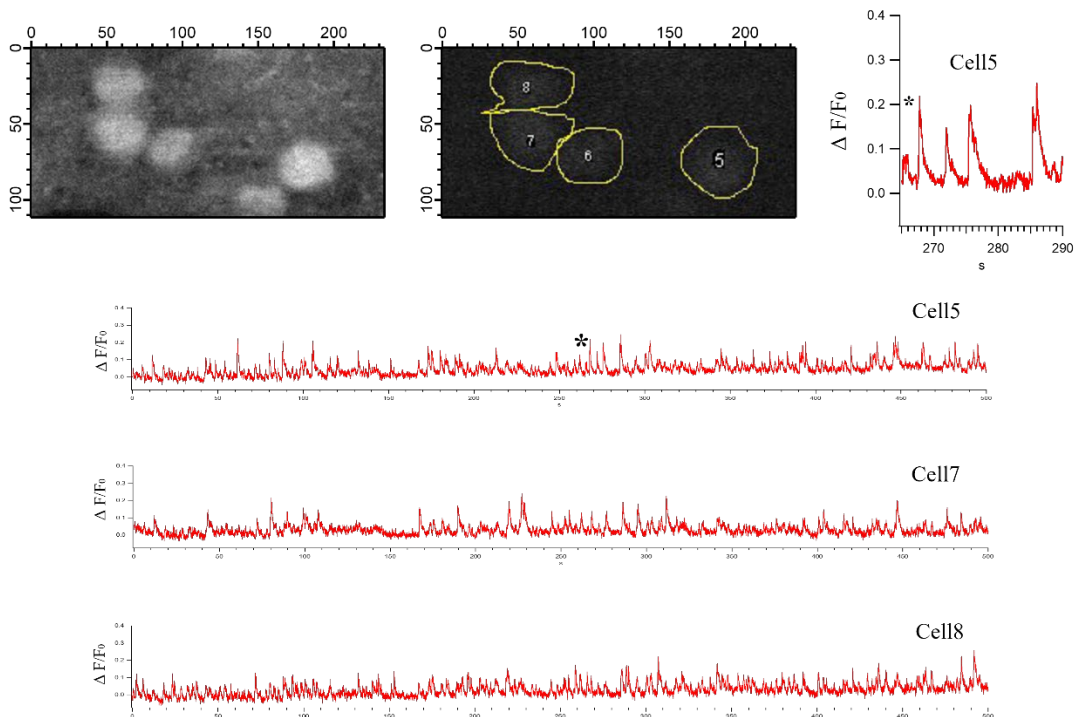
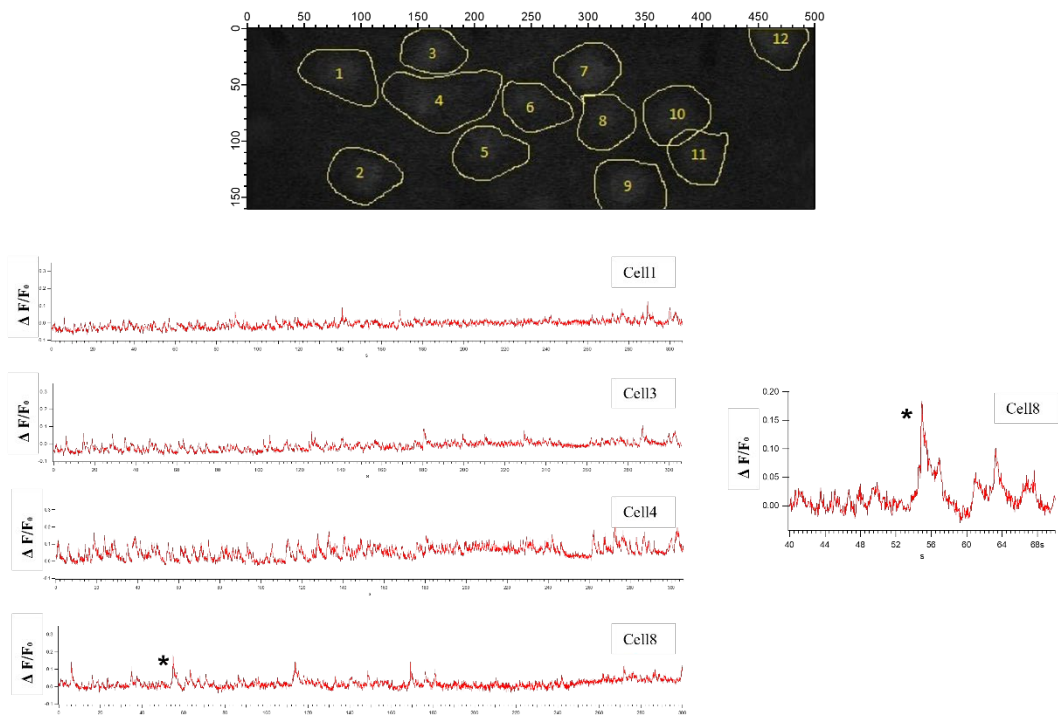


Figure 6-6: Recording of spontaneous activity using a galvanometric scanner. A: Recordings of spontaneous activity in the barrel cortex under 1.5% isoflurane recorded at 10Hz, traces in red display activity of select active cells during the recording period. The bottom trace represents slower activity typical of an astrocyte. B: similar recording at a lower anesthesia level of 1% isoflurane recorded at 15Hz hence the smaller field of view. Lower trace is an example of a burst of activity in neuron x C: example of the size of the field of view necessary to achieve 20Hz

with a galvanometric scanner. Only a few cells can be recorded at a time. Particularly active cells at 1% isoflurane are displayed here. (Figure PH. Prouvot)

In subsequent recordings we used a resonant scanner and recorded at 30fps full frame under 1% isoflurane anesthesia. We used either a 40X or a 20X magnification objective depending on the experiment and the size of the staining. The cell density was consistent with previous measurements at around 1470 ± 80 cells/mm² (Arnoux et al., 2018) (Fig. 6-5). We stimulated individual whiskers using the same method as in study 2 (Fig. 6-2). We used the layout of surface blood vessels and stereotactic coordinates to target the C1-2 and D1-2. We began by testing stimulation of individual whiskers to find the principal whisker of our recording region. We did not observe responding cells in those recordings. We then stimulated the whole whisker field in an attempt to detect any whisker evoked activity (Fig 6-7). Unfortunately we never detected reliably responding cells in those recordings. This is probably due to the compounding effect of long anesthesia. The surgery for these experiments being very long we performed them under 15-2% anesthesia for 1.5-2 hours. This could be a reason why spontaneous activity appears low. Other reasons could be a bad identification on our part and as we will see later the accumulating desynchronization in those recordings making timelocking impossible. Additionally the proportion of cells responding directly to unidirectional stimulation of a single whisker is low especially in layer II/III and the response themselves can as low as 0.1Hz in awake to 1-4Hz under urethane anesthesia (Vijayan et al., 2010). It might be that calcium imaging is not sensitive enough to detect such minor activity.

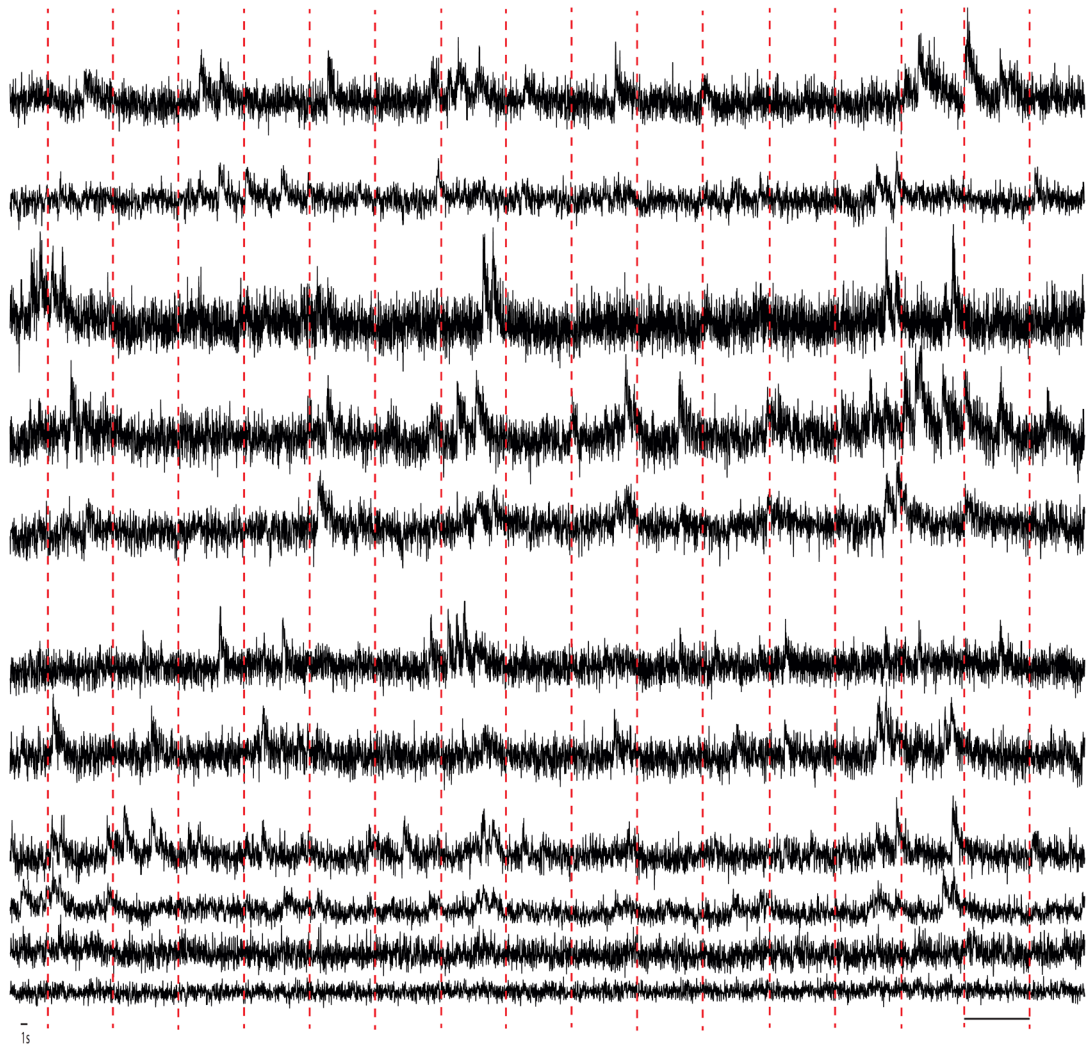


Figure 6-7: Anesthetized recordings upon single whisker deflection
Individual traces represent individual cells, bottom two traces represent neuropil signal. Red dashed bars are whisker deflection events in the principal whisker. Note the quasi-absence of time-locked response in individual cells. Scale bar: 10s (Figure PH. Prouvot)

Neuropil signal is an indicator of global brain state

Neuropil signal in our recordings is defined as the signal extracted from the whole field of view excluding cell bodies. In the case of ogb1 all cellular structures in the injected region get stained, this includes cell bodies, passing fibers and astrocytes. The average activity of the neuropil portion of the field of view can be likened to the signal recorded using optical fiber in that it represents a grand average of activity in the region. The neuropil signal in layer II/III of OGB1AM stained recordings has previously been investigated by (Kerr et al., 2005). They discovered that using classical injection methods very similar to the one used here the pure neuropil signal in Layer II/III is representative of global layer V activity and that it also strongly correlated to the electrocorticogram signal. By performing layer V exclusive staining they also showed no change in the correlation with ECoG signal indicating these fluctuations in classical

OGB-1 recordings originate from layer V. Interestingly multiple studies investigating global slow wave activity in the cortex showed that these waves can be initiated in multiple places in the cortex but that they are mostly initiated in deeper layers then propagating across the cortex and eventually to the thalamus and hippocampus (Destexhe et al., 2007). Earlier we investigated slow wave activity in the somatosensory cortex using fiber photometry and it would be interesting to situate the brain state we are recording at in layer II/III without the need for supplementary readouts. This could also prove valuable in the context of reanalysis of two-photon calcium imaging datasets. To be more specific the network dynamics and response to stimuli locally are closely linked to arousal levels in the whole network. In burst suppression or slow wave state, the network is expected to respond by an all or none multi-cell burst of activity while in persistent up state or active wake the activity is expected to be sparse. In studies using any kind of stimuli, be it sensory or optogenetic this could explain part of the result variability.

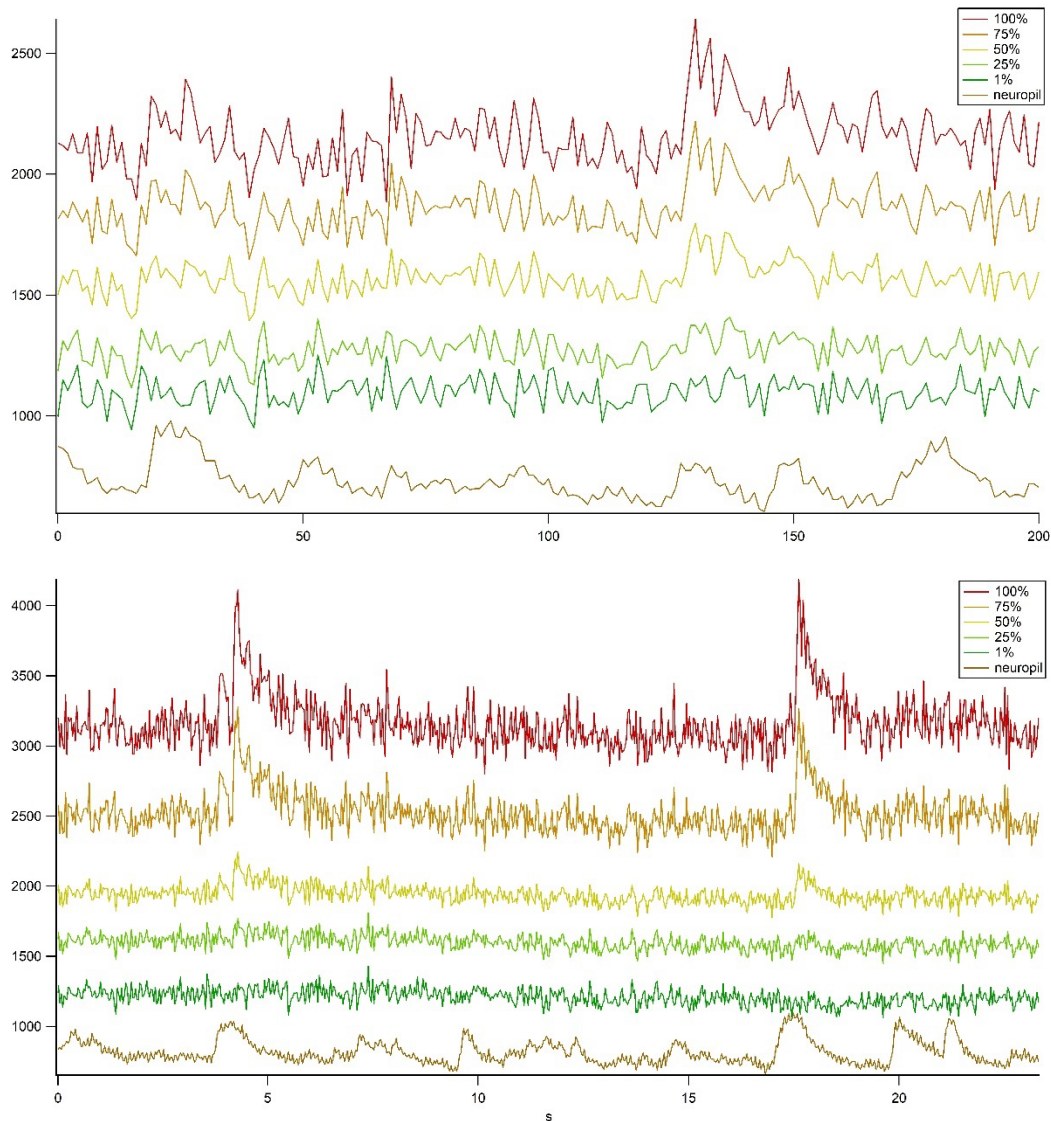


Figure 6-8: Single cell participation to neuropil signal.

*Top: example of participation of a single cell stained with OGB-1 to the neuropil signal depending on the proportion of the field of view it represents. Bottom: similar example with Gcamp6f. A typical cell represents on average ~30*30 pixels at 40x, around 1% of the field of view. Single cell's signals become undetectable at 25% with OGB-1 signal and at 1% with Gcamp6f signal. (Figure PH. Prouvot)*

The difficulty of online analysis of two-photon microscopy resides in the ROI based analysis. Two solutions are available for that, either drawing the ROIs before the recording (or doing line scanning) or using computer algorithms to detect cells and extract their signal online. Resolving this challenge opens the door to closed loops recordings and potentially closed loop all optical physiology. The interesting advantage given by the neuropil signal then is that it doesn't require drawing of an ROI and can be read online with little adjustment to the recording software and doesn't necessitate high processing power. It also can compensate for the need of a secondary readout (ECoG, lfp or optic fiber) of brain state. We extracted signal from a sample cell, a background region of similar fluorescence level and average fluorescence from the full frame. We mixed the signals by assigning a weight of 100, 75, 50, 25 or 1% to the single cell relative to the noise. In the most common recordings using a 40x objective our field of view was 512*512 pixels over 440*440 μ m. At this magnification a single cell represents 900 square pixels, approximately 1% of the field of view. A single event tends to disappear in the noise band already at 50% for OGB-1 and 25% for Gcamp6f recordings (Fig: 6-8). This suggests that it is possible to measure the neuropil signal from the full frame average fluorescence change without the need to exclude cell bodies. We also compared neuropil signal gcamp6f in twophoton imaging and surface recordings at deeper anesthesia. In most two-photon recordings the brain state is considered to be persistent up state because of the anesthesia used without using supplementary controls. The change in arousal state due to anesthesia is not instantaneous and depends on the type and administration, following it online would improve experimental control. It would be interesting to classify older recordings into different brain states using neuropil signal as a marker and to investigate how that affects results such as sensory activity or spontaneous activity in pathological conditions. Full frame neuropil signals resemble fiber photometry and epifluorescence signals. Interestingly neuropil signal recorded using gCamp6f under the CamKII promoter under the same 1.5% isoflurane anesthesia appears more complex and sparser. This could be due to a larger participation in subthreshold dendritic calcium events because of the much larger sensitivity of Gcamp6f compared to OGB-1 and the averaging over a smaller region compared to fiber photometry and epifluorescence.

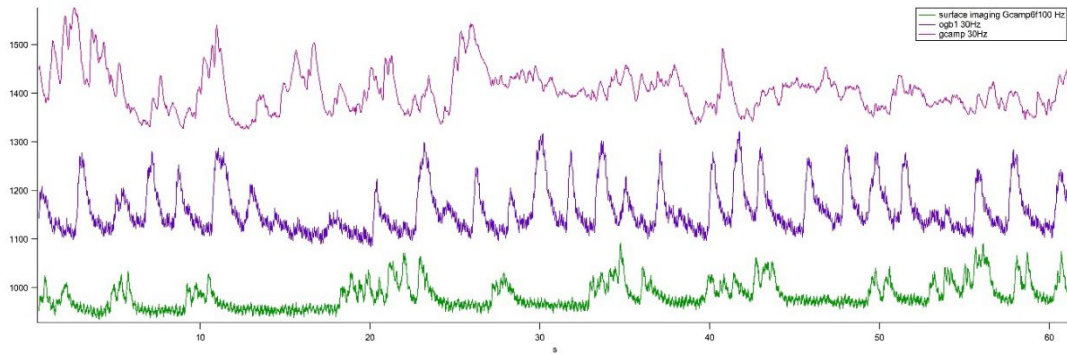


Figure 6-9: Similar patterns of activity in the neuropil signal using OGB1 and GCamp6f. All three signals recorded under 1.5% isoflurane anesthesia. Note the qualitative difference between the GCamp6f neuropil signal and the one from surface imaging. This is probably due to the stronger participation of large amplitude events in neurites and cell bodies in the full frame neuropil signal using gcamp giving the appearance of sparser activity because the detection threshold is lower. When the signal is more averaged in surface imaging it resembles more the OGB1 neuropil signal or the fiber photometry signal. (Figure PH. Prouvot)

Visually evoked activity in awake recordings

Considering the lack of whisker-evoked activity we observed using two-photon microscopy under different modes of anesthesia we decided to explore recording in awake head restrained animals. This implied two changes. A holder capable of preventing movement artifacts and habituating the mice to stay calm when headfixed on the trackball. It would have been possible to restrain the animals, but the habituating period is longer and other projects in the laboratory required the investigation of locomotion in conjunction with two-photon calcium recordings.

The recording system

This drastic modification of our recording system required a large time investment. We used a bare bones version of the Trimscope II similar to our other systems, on it we adapted at first a complete virtual reality system from Phenosys including proprietary holder, implant, trackball, screen setup and software. This system presented two issues. First and foremost, the software being proprietary no option to stream the state of the virtual reality to an external synchronization tool was available. As we discussed multiple times here synchronization of recording and stimulation modalities is key to any type of recording and we required an update to the software and hardware to output at minimum timing of the drifting grating stimuli and the x y movements of the trackball. We used an analog/digital (A/D) converter to convert signal from the VR system to analog and then digitized them again using the same kind of A/D converter as before (CED 1401) to synchronize the VR system with the two-photon and the

eventual extra sensory stimulation. The parameters extracted from the VR system are all separated into individual channels. Two channels for the x and y axis velocities from the trackball and 8 individual channels for every orientation of the drifting grating visual stimuli. The two-photon system we used is a basic Trimscope II with a Chameleon modelocked laser, pockels cells, a secondary pre-chirper, a resonant scanner and one PMT for single color detection. A secondary light path consisted in two CW laser diodes coupled through a mechanical shutter into a single optic fiber, redirecting the light to a set of galvanometric scanners for simultaneous imaging and optogenetic stimulation. The trackball system from phenosys consists in a machined aluminium block in which the styrofoam ball rests, holes at the bottom of the depression allow for pressurized air to let the ball glide without friction (Fig. 6-12). On it are mounted mechanical brakes, two optical sensors for X and Y direction and two retractable spouts for liquid administration and air puffs. The holding arm provided by Phenosys is very adjustable in pitch and roll but is designed to come from the back of the animal facing the screen. In our case the microscope turret prevented this positioning of the arm. As a result, we modified it to come from the side and angle twice to reach the animal from the back (Fig. 6-12).

The orientation had to be conserved because of the linear design of the implant, it is supposed to be glued along the skull for maximum contact surface. This new arm unfortunately was too flexible for two-photon microscopy and resulted in large movement artifacts whenever the mouse attempted to move its head. We designed our own holder.

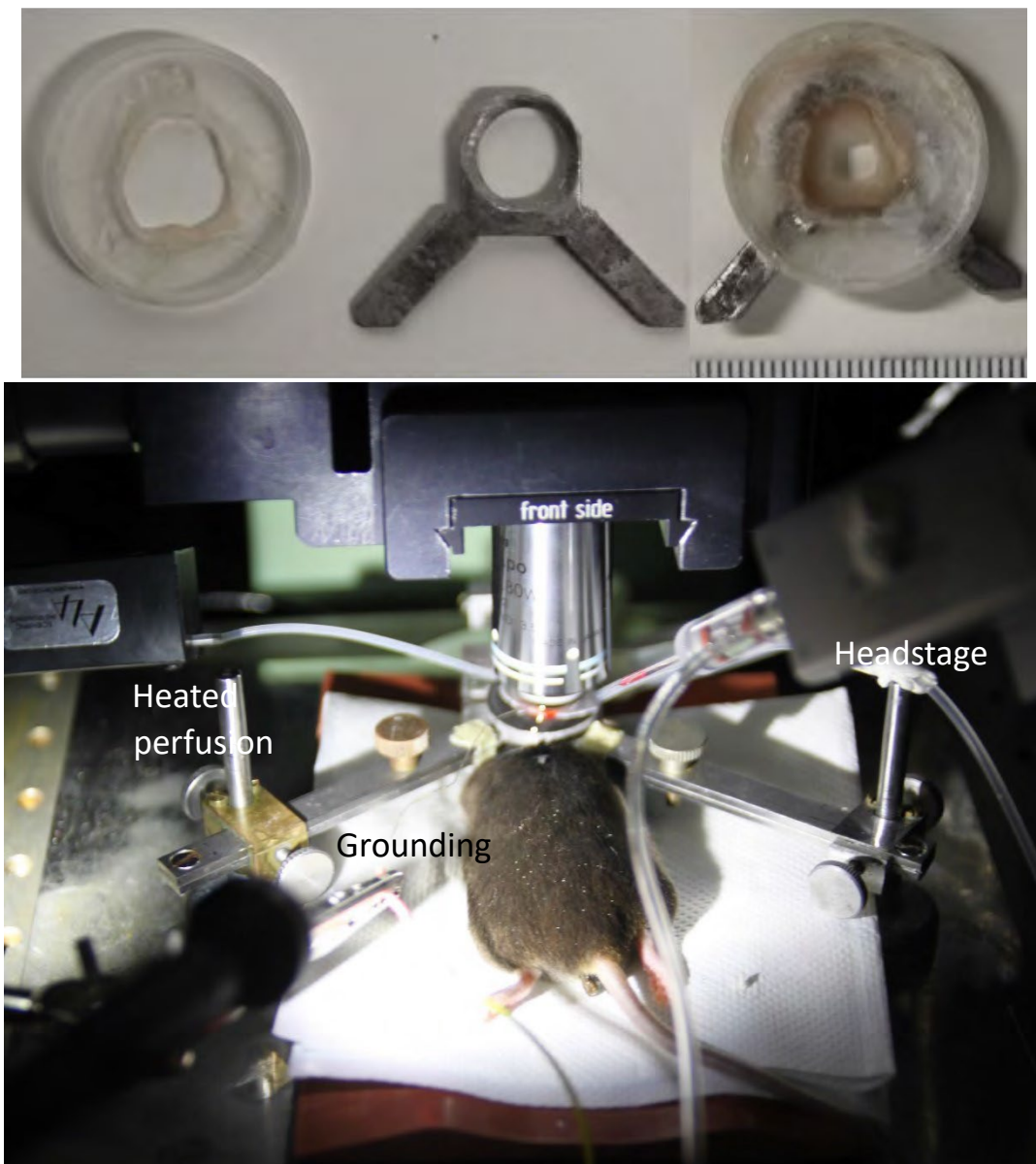


Figure 6-10: anesthetized recording mouse installation. Top row: The modular design of our initial chamber. The two arms attached to the circular chamber are angled towards the back to allow for an easier manual fixation. The metal was scored with a dental drill to facilitate adhesion of the cyanoacrylate. The ventral part not displayed here curves to espouse the shape of the skull. The plastic chamber that is glued on top is disposable and the size of the opening was adapted manually to each experiment. The right picture shows an example after use, dental cement was used to fill up around the craniotomy to provide better adhesion to the skull. Scale in mm Bottom row: the chamber in use under the microscope. The large opening allows for multiple devices to fit for injection and electrophysiology as well as for perfusion of warm PBS. (Figure PH. Prouvot)

Implantation surgery for chronic imaging

Because the animals need to be habituated to the recording setup for awake recordings the time investment per animal increases significantly in awake recordings. When adding the surgery duration, the waiting time for virus expression, the animal training and the time necessary to

identify the transfected barrel between 4 and 6h are spent per animal over a period of two weeks. The success rate of all these steps also implies that successfully implanted and trained mice should be kept for more than one recording session. Scientifically it also makes sense to record the same region for a longer time that a single recording session allows for. We tested two possible implants for awake chronic imaging.

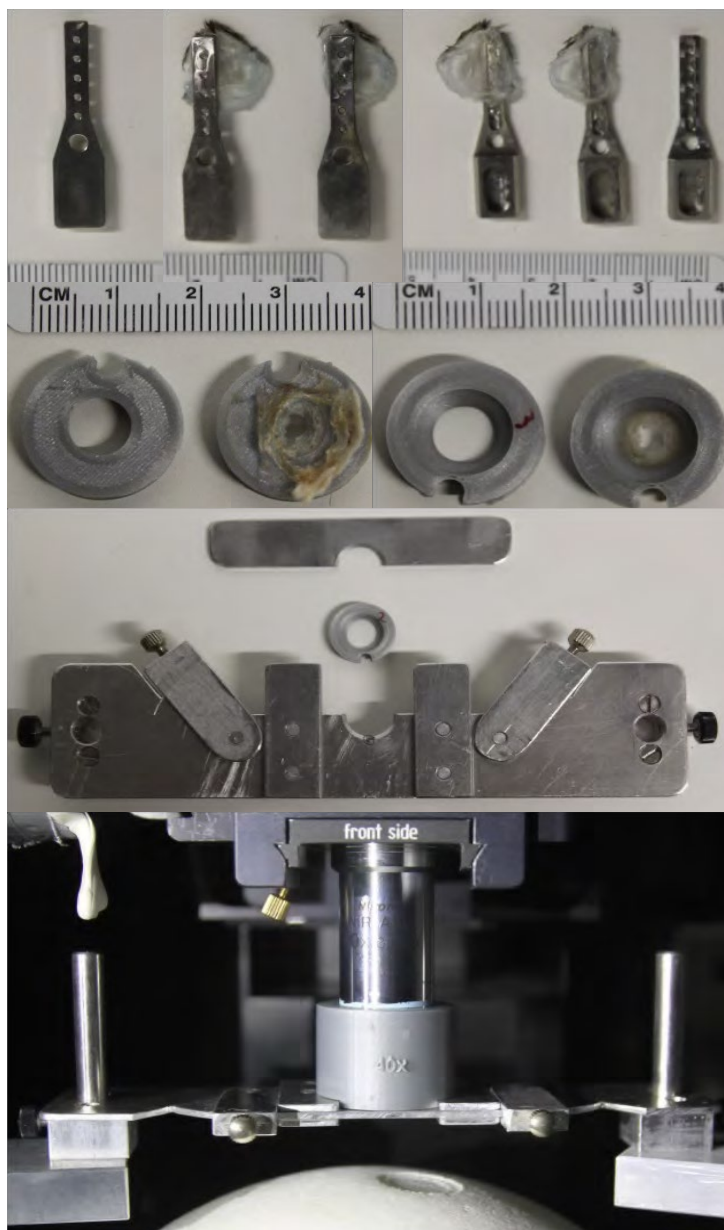


Figure 6-11: Head fixation system for awake recordings. Top row: the initial design of the holder for in awake recordings provided by phenosys. Unused and after sacrifice of the animal. The chamber glass window still embedded in resin shows the relatively small surface area of fixation. The resin had to be shaped in a small pool to hold enough water to immerse the lens of the objective Second row: the round holder designed by the Cambridge team. The sample shown here was 3D printed and proved perfect for longitudinal recordings. The circular shape helped mitigate any flexibility of the skull. The pool formed contained enough liquid for water immersion of the objective. Third row the clamping hold used. The removable bar was used to slide the mouse more easily into the clamp. The whole device could be removed and used in the

housing cage to habituate the mouse. Bottom row: the assembly under the microscope, a 3D printed sleeve mitigated any light from the visual stimulation. (Figure by PH. Prouvot)

The second adaptation was to the holding system. The original implant see (Fig. 6-11 top) is very simple to implant on the skull and hold very well long term (we tested as long as 4 months with almost no issues). The fact it protrudes a lot at the back of the head makes it very easy to manually catch and install in the holder making mice installation fast and less stressful for the mice and the experimenter. When recording calcium imaging with the two-photon in behaving mice however we noticed large vertical movements when the mouse attempted to turn or lift its head. The movement when the mouse ran was minimal but enough to warrant correction and to move non equatorial cells out of the imaging plane. We tried using a thicker arm for the holder and strongly securing the implant in the holder with a thumbscrew, but it didn't improve the recording quality (Fig 6-12 top). This is probably due to the length and thinness of the implant itself, combined with the slight flexibility of the mouse skull.

Consequently, we changed our protocol to use a round chamber and holder provided by the team of Sidney [REDACTED] (Uni Heidelberg). Being attached to the skull all around the imaging window this holder compensates for the flexibility of the murine skull. The attachment of the implant into the holder also allows for more contact area (Fig. 6-11). This holder allowed us to get rid of the movement artifacts even when the mouse was running (Fig. 6-13). The whole trackball and holder are installed on a moving table to provide xy movement while z movement of the imaging plane is handled by moving the objective. We mostly used a metal version of this holder with a small drop of UV-curable resin in the groove to absorb any movement due to tolerance discrepancy. We also tested a 3d printed version of that holder (printed using an ultimaker 3) and it proved usable as a single use solution

(Fig. 6-11 middle and Bottom). To avoid any contamination of the signal by the light of the screens used for visual stimulation or virtual reality navigation we 3D printed an adaptor fitting the holder and the objective (Fig. 6-12).



Figure 6-12: Overview of the awake visual stimulation system.

Top three images: A mouse implanted using the original phenosys system navigating a simple corridor in virtual reality during habituation. Bottom image: A mouse in the process of being recorded using the final setup. Note thickness of the fixation arms and their position to minimize the obstruction of the mouse field of view. The ball was adjusted to the optimal height for the mouse to walk easily without pushing on it and without hanging from the holder. Thanks to the shielding around the objective mice could be imaged even under the bright light of the screens. (Figure by PH. Prouvot)

Recording activity in awake mice on a treadmill entail knowing the activity status of the mice. The phenosys trackball we used recorded x and y movement as a .csv file that could be synchronized post-hoc. Given the precise timing of neuronal activity relying on timestamps from the internal clock of this computer was insufficient. Moreover, precisely synchronizing the internal clocks of two separate computers not connected to the internet would prove

difficult. Our solution was to derive a copy of the x and y datastream directly from the phenosys acquisition board and to feed it into our usual CED1401 acquisition board for it to be recorded and displayed at the same time as all synchronization streams from the two-photon microscope. This required negotiations with phenosys but proved an excellent solution. The final step for a complete behavioral system would be to use a camera to monitor the behavior of the mouse, but it was not necessary at this step in the project.

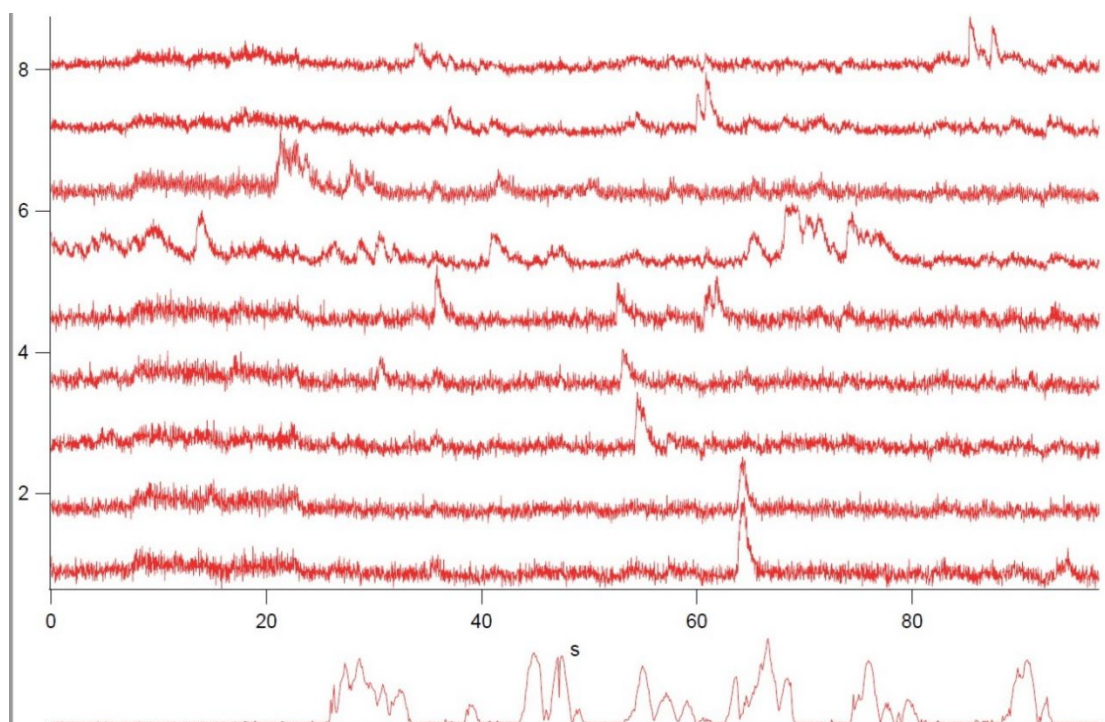


Figure 6-13: Example fluorescent traces of Gcamp fluorescence in the visual cortex combined with measurement of mouse velocity (lower trace). The increase in noise from 5 to 20s is due to movement artifacts caused by the mouse exerting force vertically. Note the absence of movement artifacts during locomotion. (Fig PH. Prouvot and H. Backhaus)

We successfully recorded spontaneous activity in chronically implanted mice. As visible in the previous figure it was possible to record activity of individual neurons in awake conditions without suffering from movement artifacts during locomotion. The only slight movement artifacts were due to the mouse applying force in the vertical direction when trying to look up and pushing on the trackball. Having proven that these recordings were conceptually possible we moved back to the barrel cortex to record whisker evoked activity.

Recording of whisker evoked activity in the primary barrel field

We slightly modified our virus injection parameters to achieve larger fields of expression of Gcamp6f. While injecting at an angle of 60° we performed an injection of 100nl every 100µm

starting 800 μ m from the surface and ending at 300 μ m. This allowed us to achieve larger fields of expression.

We then took advantage of this larger expression to test if it was possible to identify individual barrels using epifluorescence. We used the same system as for intrinsic optical imaging with an excitation light of 488nm through the objective. We performed the same stimulation paradigm as for IOI. Analysis showed us that it is indeed possible to identify single barrels but from single trials instead of requiring averaging over multiple. The fluorescence change was large enough to be identified visually during the recording greatly enhancing the speed at which we could test individual whiskers.

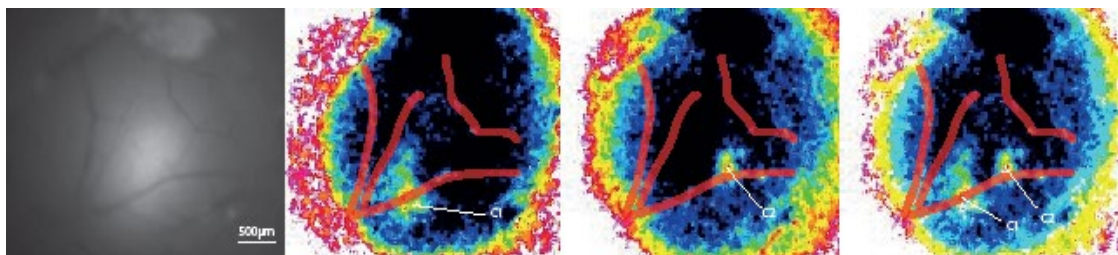


Figure 6-14: Surface calcium imaging identification of barrels. Epifluorescence still image from the expressing region of a mouse injected with Gcamp6f the expression approximates 2.5mm in diameter. B false color image of the identified barrel C1 after DF/F0 and post stimulus averaging of the first 100 frames during a single trial. Arrow indicates the center of the responding region C identification of C2 D overlay of images resulting from C1 and C2 (Fig PH. Prouvot)

After having used surface calcium imaging in mice injected with gcamp6f to identify the whiskers within our field of expression we trimmed all whiskers on that side except the principal one in which field we would record. We then applied mechanical deflections as described earlier and recorded the response in the primary contralateral barrel field (Fig. 6-16). Responses of individual cells could not be detected while an event could be detected in the neuropil for every trial. Interestingly cells seemed to be more active during locomotion. We performed these final recordings only in a small set of 3 female mice as a proof of concept because the time and budget allowed for the project was running out.

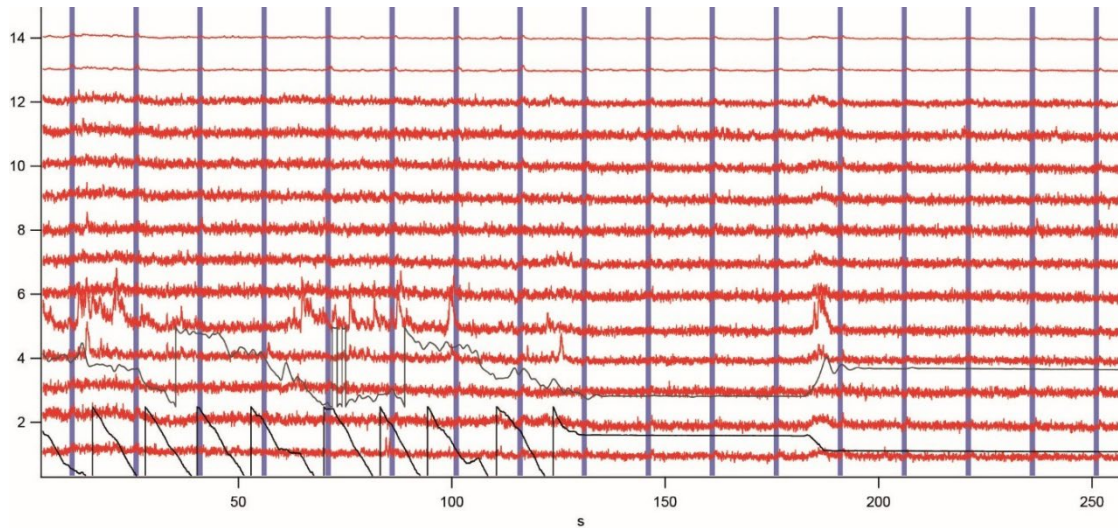


Figure 6-15: Whisker evoked activity in the primary identified barrel field. Red traces represent calcium traces from neurons (bottom 12) and neuropil (top 2). The black trace represents x and y velocity (respectively top and bottom). There seems to be more activity during locomotion but whisker evoked activity could not be detected in individual cells (Fig PH. Prouvot).

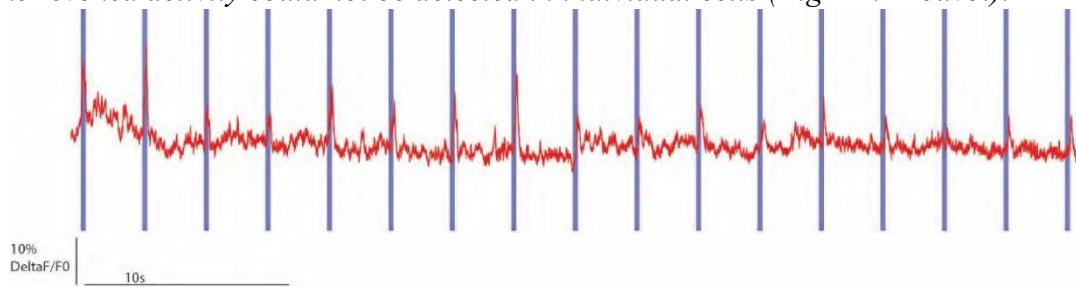


Figure 6-16: Whisker evoked activity in the neuropil upon whisker deflection in the barrel cortex. Note the response to every individual event with varying amplitude. Also note the sparse spontaneous activity. (Fig. PH. Prouvot)

Even in the absence of individual cells responding, sensory evoked activity could be detected in the neuropil, indicating the presence of an input from layer V. Note that the response appears slightly later with each stimulus train. We found out that this was due to a bottleneck in our computer hardware. Our hard drive was not able to store the data fast enough and as a result frames were lost. The recording software was however designed to acquire a set amount of frames and padded the recordings at the end to reach that amount. The recordings then appear normal but are missing random frames and present an accumulating delay. This delay is cumulative, the longer the recording, the longer the delay.

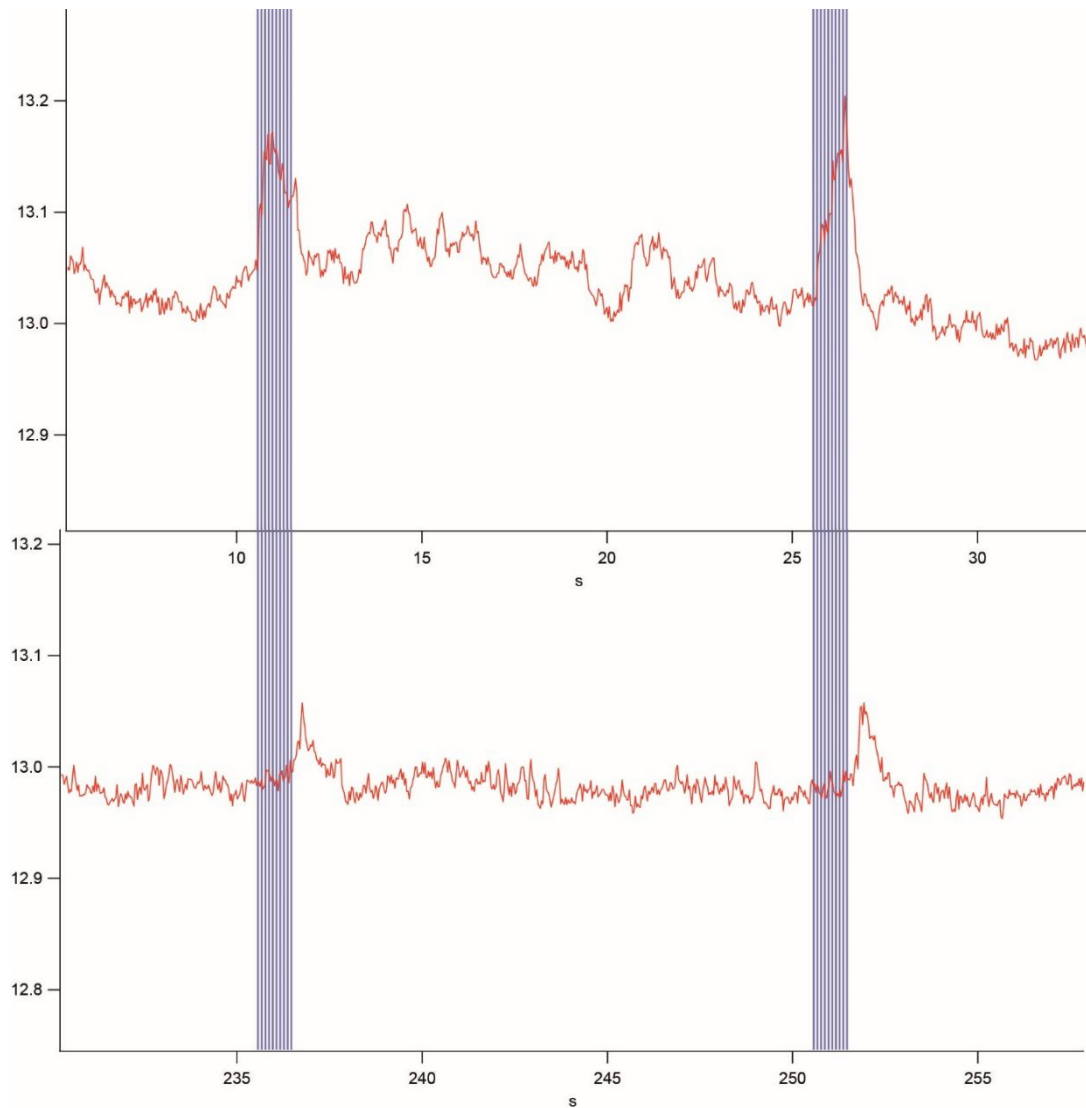


Figure 6-17: Cumulative delay between imaging and stimulation. Red trace represents the neuropil signal from the whole field of view, blue trace represents the 10 pulses of whisker stimulation. Top panel first thirty seconds of recording showing good timing. Bottom panel same recording after four minutes of recording showing a delay of approx. one second between recording and stimulation. (Fig. PH. Prouvot)

We additionally recorded in the visual cortex in an effort to transfer the methods to the project of Hendrick Backhaus. We applied visual drifting grating stimuli with random orientation in 45° intervals. Here visually evoked events could be detected, different cells responded to different orientations as expected.

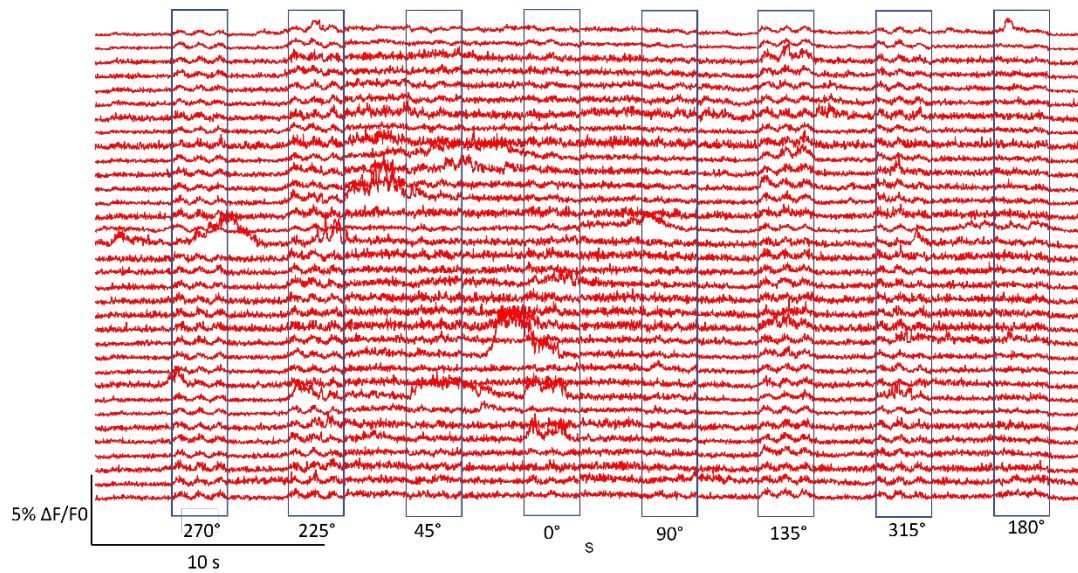


Figure 6-18: Visually evoked activity in awake mice submitted to drifting grating stimuli. Each trace was extracted from an individual cell. Blue boxes indicate the duration of a drifting grating stimuli. The angle of the stimuli is indicated under the box. Orientation was randomized (Fig. PH. Prouvot, Acquisition with H. Backhaus).

Discussion

Technical implementation of two-photon microscopy

Minimizing movement artifacts through chamber and holder design

As we saw using a proper fixation system is a crucial step in performing successful in vivo experiments, particularly in the case of two-photon recordings where movements as small as 510 μ m can affect recording quality greatly. We tested three different fixation systems in this work. A supplementary one consisting in a 2x5mm S bracket (not shown here) was used in the lab successfully for chronic anesthetized recordings in study 3.

Acute recordings during terminal experiments can be done a variety of ways as stability is less of an issue and having a pool of heated ACSF or PBS on top of the exposed brain is the most crucial part. As such two options worked for us, a round plastic petri dish glued directly on top of the skull with the mouse placed under the table and a metal bracket glued to the skull on which a plastic or metal round chamber was glued. The first option was used successfully in the [REDACTED] labs (Chongqing tmmu; TUM Munich) but with a modified table to access the mouse more easily. We could not modify the configuration of our table, consequently the mouse was hard to access, requiring lifting of the objective for any observation or procedure.

We mainly used the chamber designed in collaboration with our fine mechanical workshop (Mr [REDACTED] in particular). This two-piece apparatus required fixation in two steps with cyanoacrylate and dental cement but presented less leakage. Because the mouse was placed in a clamping mechanism on top of the table it was much more accessible and allowed us to monitor it visually and electronically much more efficiently. The smaller size of the chamber also meant faster turnover rate of the liquid, meaning easier overflow but also making it easier to keep at physiological temperature. We slightly struggled to find the right chamber size to accommodate enough space for a patch pipette. Too small and the angle left between the objective and the border of the chamber is too narrow, too big and the chamber would make access to the eyes and the snout complicated. Almost all experimenters in the lab used the same chamber successfully for recording in different cortical regions (S1, Barrel cortex, Visual cortex). The two-piece design meant the metal part was reused from one experiment to the next after cleaning it from glue and cement in acetone and the plastic element was discarded. The metal piece provided the necessary rigidity while the plastic part could be hand drilled to fit each experiment. We sometimes used a metal replacement for the holed petri dish but cyanoacrylate doesn't always bond properly to metal if not perfectly cleaned, scored or etched

properly. Using one plastic and one metal part increased the chances of success. All in all, this chamber design is easy to use and to adapt making it convenient for repeated cortical recordings. For awake experiments we began by using the straight holders provided by Phenosys, as discussed earlier these were not rigid enough for two-photon awake recordings. We used them for Intrinsic imaging experiments and some surface *gcamp6f* recordings to test them and found them sufficient for anesthetized imaging but never for awake. The best part of this holder is probably the clamping mechanism, the forward angle can be easily adjusted, and it can be rotated for better access to lateral regions like the auditory tract. The movement we observed was in part due to the modification we added to the holding arm to position it on the side of the trackball. We had no choice but to put it there because of the foot of the microscope being in the way of the position intended by phenosys. The other movement inducing flaw in this design comes from the implant itself. The straight design has advantages namely a large surface for bonding to the glue and it is extremely easy to catch even on a moving mouse. The main flaw comes from the straightness of it, because it needs to be glued on the unused hemisphere it leaves the other hemisphere completely free which in itself is a positive, it just needs to be covered in a cap of glue or cement. The issue resides in the flexibility of the mouse skull, because the free side is not held by the metal holder it is free to slightly flex and this is enough freedom of movement to make recordings unusable. A relatively easy fix would be to change the straight bar to a donut shaped element that would hold the skull in place all around the imaging field. This chamber has however been successfully used for awake fiber photometry where skull flexing is less of an issue because the fibers are fixed to the skull and move with it. The final design we used for awake two-photon recordings was provided to us by the lab of [REDACTED] in Heidelberg reproduced and adapted at our workshop following our specifications. It partially reproduces the round design we proposed earlier but with a circular clamping mechanism. It would not be ideal for recordings lateral areas of the brain because of its size and the surface area necessary for adhesion, but it proved perfect for our use in the barrel and visual cortices. The size of the chamber made it lighter and more comfortable for the mice and improved durability slightly since the bonding surface was larger. But this small size and low protrusion also presented the only issue with this system, it is difficult to catch with fingers (especially gloved) and awkward to install in the clamping mechanism. The solution was to train the animals longer so they remained calmer when being installed in the clamping system as the procedure can be stressful for the animal and the experimenter. Having the mice stressed during the procedure also means more resistance, more force applied and more chances

for the implant to detach during the procedure. The alternative solution was to shortly anesthetize the mice with isoflurane and let them recover once fixed. This is what was used in the lab in the case where training was undesirable or unnecessary. All the recordings presented here however were made after habituation and without anesthesia.

Animal consciousness

Part of the experiments in this work were performed in anesthetized animals while others were performed in awake animals; here, we shall discuss the advantages and disadvantages of both possibilities.

anesthesia and brain states

We discussed earlier the variety of rhythms in the brain during wake and sleep. Anesthesia is in some ways comparable to sleep as in some activity patterns and rhythms present in sleep are reproduced (M. Steriade, Nunez, and Amzica 1993b). The chemical nature of the alteration of activity however creates some differences. Depending on the chemical nature of the anesthetic activity in the brain is altered differently. We already detailed the different anesthetics we used for different recordings. Here we will discuss the brain rhythms found when using these anesthetics.

We performed recordings with Ketamine/Xylazine very early on, we could record spontaneous activity in individual cells in this condition and the animals could be kept stable for about an hour at a time. However, a new dose of anesthetic had to be re-injected every hour intraperitoneally. This meant having access to the mouse body and potentially moving the field of view and occurring lost time finding the same cells of interest. It also represents a risk of accidentally killing the mouse with each new injection. Moreover, while the surgical plane could be considered stable the level of activity would vary slightly from the initial injection up until the next one was necessary.

We only used medetomidine in the fMRI study presented early on for its capacity to produce anesthesia while presenting persistent up state. Because it needs to be perfused at a constant rate to maintain the desired level of anesthesia, we installed a catheter to the peritoneal cavity of the rats. This solution could be used for Ket/Xyl anesthesia for a more constant rate of perfusion.

Isoflurane is the most versatile anesthetic we used, the dosage can be controlled fast and precisely during an experiment. It is a very general anesthetic, GABA receptor agonist, and NMDA antagonist and reducing Potassium conductances in activated channels. At low dosage (0.5-1%) the animals are lightly asleep and general activity levels can be classified in a persistent up state, while at higher concentrations (>1.5 %) the general activity drastically decreases to enter up-down state, the frequency of up states decreasing the further you increase the concentration. Because it is a potent general inhibitor of neuronal activity, which reduced our chances of observing active cells, we finally phased out of using it in favor of awake experiments. It is an interesting product to study slow waves states from a mechanistic point of view, or to manipulate a microcircuit while suppressing general activity. As we found out it is however not so great to study sensory evoked activity in the cortex as the general suppression of activity greatly reduces any activity to be observed.

Urethane was used in large part during this work because it is very convenient for terminal experiments. The anesthesia is relatively light and long lasting, but it varies across time between periods of slow waves resembling NREM sleep and periods resembling REM or light wake with a period of about 8-11minutes (Clement et al., 2008; Pagliardini et al., 2013). Chemically altering the acetylcholine balance does affect this cycle in a similar way as it does natural sleep. Disruption of the PPT using conotoxin also altered this cycle in a similar way as it does natural sleep (Pagliardini et al., 2013). Recent data however suggests that activity under urethane anesthesia is distinct from natural sleep in some key parameters an the major one being the absence of response to a noxious stimulus under urethane anesthesia (Mondino et al., 2021). This is another argument in favor of a reanalysis of this dataset classifying epochs into brain states more precisely. An in-depth analysis of the properties of each state, transition rates and how they are affected by optogenetic modulation of PV interneurons would help us better understand the phenotypical differences with natural sleep.

Awake recordings

To avoid at least partially the controversies brought by anesthesia we, like several laboratories in the field, recently decided to perform our recordings in awake animals. This entails large changes in the experimental protocol but has multiple advantages. First and foremost, no anesthesia is used during the recordings themselves, so no artificial modification of the

Excitation/Inhibition balance, no need to control for brain state or anesthesia depth and no chemical modulation of neurotransmitter activity. As we already detailed this also means more movement artifacts and we spent a significant amount of time finding a solution to this problem but once the groundwork has been done all optical physiology in awake animals can reasonably become routine. The time necessary to prepare each animal is only slightly higher (2-4hours over three weeks for awake versus 1-2 hours over two weeks per mouse for acute experiments) than for acute experiments and each mouse can be recorded from for up to three months (potentially 6 months) drastically reducing the number of mice necessary for each study. Chronic recordings also enable new questions since it is possible to record the same cells across long periods of time and to train the animal in a behavioral task. The main drawback is that because the animal is awake the experimental conditions are less controlled and interrogating simple networks can become more complex when taking into account the behavioral state of the animal (resting, running, exploring the virtual environment, etc.). Because it is then not possible to chemically control the arousal state of the animal in the future awake recordings should include a modality to control for it. Locomotion is already available in our recordings, but video monitoring of pupil dilation and whisking would provide an excellent addition and would allow us to classify responses further into attention states and to push the explanation of response variability further.

Technical considerations into the design of a two-photon microscope

Open-source vs proprietary

Nowadays multiple companies offer out of the box two-photon microscopy systems with options for structural or functional imaging. As such a team looking for a two-photon imaging system might find a solution corresponding to its needs relatively easily and at a good price. In the past numerous teams have however built their own systems as the basic components are easy to source and the software principles are relatively simple. We will detail the basic components in the next sections. For most applications the commercial systems on offer nowadays suffice. It is possible to push the boundaries by building a custom imaging system. The main routes explored at the moment of writing have been 3D live imaging, enlargement of the field of view, two-photon optogenetics, random access microscopy and three photon microscopy.

Essential tools and accessories

The basic structure of a two-photon microscope can be explained fairly simply but the technology within each part is complex. The basic structure as in Fig. 1-9 is a light source a scanner a microscope and a detector. Most systems nowadays use extra tools in the treatment of excitation light to provide better speed or resolution. Pre-chirping was already standard with the two main suppliers for femtosecond pulsed lasers to compensate for the optical elements within the laser system. Most companies building two-photon microscopes now also include chirp compensation for the optical path from the laser head to the sample. More recently the use of adaptive optics from the world of telescopes has started to see use to compensate for distortion of the beam due to traversing biological tissue. We could not detect difference in image quality for live imaging, but I believe it could improve high resolution imaging.

Light source

At the core of any laser scanning microscope lies the laser. For two-photon microscopy in particular it needs to be powerful (1-4 Watts accounting for power loss in the system), femtosecond pulsed and tunable between 800-950nm in wavelength in order to achieve the twophoton effect discussed earlier. These criteria are met in Titanium Sapphire ultrafast lasers most commonly used like the Mai-Tai or InSight (spectra-physics), the chameleon (coherent), the Tiberius (Thorlabs) and the M squared (Sprite XT). These lasers are bulky, require watercooling, complex controllers and run in the range of 100 000 euros although the price tends to decrease. There also exists a range of non-tunable femtosecond pulsed lasers emitting usually around 900nm. Depending on the factory specified power output of one of these lasers it can sometimes be split between two imaging setups to reduce costs. Typically given the pulsating nature of these lasers one is looking for short pulses with high power and low frequency to facilitate fast imaging and limit photodamage. Photodamage is caused by photobleaching and heating which is dependent on the average power over time deposited in the tissue, having shorter pulses less frequently doesn't reduce excitation quality but reduces the necessary pixel dwell time and as such heating. On top of the short pulses provided by modelocking the laser itself most systems include a pre-chirping module that further shortens beam duration. It is for us in this same module that a pockel cell for power control is included.

Scanning

Two-photon microscopy is a laser scanning imaging method, the focused beam from the laser is moved across the sample typically by using a set of galvanometric mirrors oriented orthogonally to each other. There are other methods to move the laser beam such as digital micromirror devices or SLMs (spatial light modulators). In our setup we used galvanometric mirrors, at first these mirrors were driven at a speed chosen by the user (usually 15-30Hz) but the rapid movements and changes in movement direction (especially in the x direction) caused too much mechanical stress and a rapid deterioration leading to of the x-direction motor breaking after about a year of daily usage. We replaced them with resonant scanners where the x-direction mirror oscillates at a set resonant frequency (6000-12000Hz) which prevents modulation of the recording frequency but lasts much longer (5 years daily use and counting). It also enables full frame recordings at 30 frames per second with higher framerates available when reducing the number of lines scanned in each frame. It however prevents slow scanning and line scanning, for respectively high SNR anatomical imaging and ultrafast low-resolution calcium or VSDI imaging. Since most applications of this laboratory are about calcium imaging however it represents an excellent trade-off. In System I two configurations are available, one with a resonant scanner and one with a classic galvo scanner for slow imaging. An alternative scanning solution uses AOD (acousto-optic-deflectors) allows for ultra-fast imaging with a possibility to scan in 3D. It has only become available commercially since 2020 (Karthala AODscope). This kind of system is the only real solution for VSDI full frame imaging in vivo (Kremer et al., 2008; Salomé et al., 2006).

Microscope

In this section we will discuss the final parts of the optical path dedicated to focusing the beam into the sample. In our systems an out of the box upright microscope body from Olympus is used. It is supplemented with an add on containing the scanners and the tube lens on top, once the light is collimated and oriented it enters from the top, crosses the empty filter tower, and a dichroic filter before entering the objective. Objectives need to meet a few parameters to be compatible with two-photon microscopy. They need a large enough numerical aperture to detect light and to be optimized for excitation and emission lights used in two-photon to provide comparable focalization and transmission efficiency from 450nm up to 1400nm. Nikon and Olympus are the main providers of such specialized objectives and 40x, 20x and 16x magnifications are available with differing numerical apertures. The 25x objective

(XLPLN25XWMP2) we used, proved to be the best tradeoff in terms of NA and field of view but being very broad it could not be combined with any other injection or electrical modality. We used it mainly for awake recordings. For anesthetized recordings we used our 40x (Nikon RMS40XPF) and our 16X (CFI75LWD16XW) presented acute enough angles to insert a pipette for bolus injection or LFP recordings.

Detectors

Even though peak excitation power is very high in two-photon microscopy the light emitted from the excitation spot is comparatively very weak but opposite to confocal microscopy all light emitted comes only from the imaging plane and the excited voxel, as a result there is no need for a pinhole to filter out of plane light and as many photons as possible should be collected. The counterpart to this is the need for extremely sensitive detectors, ideally single photon sensitive photomultiplier tubes (PMTs) are used. These detectors use serial couples of dynodes to greatly amplify the signal from detected photons. In our case these PMTs are from Hamamatsu and possess single photon sensitivity. The objective should have a numerical aperture as large as possible since all light coming from the sample comes from the excited voxel as much as possible of it should be collected. For calcium imaging it does not particularly to be apochromatic across the whole visible light spectrum, transmission in IR and green and numerical aperture take precedence over everything else. The counterpart to this is the extremely high sensitivity of the image quality to parasitic light, as such the sample should be well isolated from light. The final important part of the detection system is the dichroic filter separating the excitation light from the emitted light. Briefly the main filter above the objective should transmit 700nm and over to allow excitation light to pass while reflecting the visible light (700nm) produced by the sample towards the PMTs. In the filter block before the PMTs an extra security high pass filter should block over 700nm to reflect any light from the laser. Then the light is separated into red and green paths into two different PMTs. PMTs and speed are inherently faster and more sensitive than cameras at the cost of recording only a single point, in that they are perfectly suited for laser scanning microscopy. We used two generations of PMTs all provided by Hamamatsu, the first were optimized for sensitivity at the cost of speed and were used for normal galvanometric scanning, the second were optimized for speed and were used for resonant scanning.

Accessories

In the case of our experimental system 1 we also tested in collaboration with LaVision Biotec a few tools to either improve the system or provide extra options. The first improvement brought to our system 1 was the change from a set of galvanometric scanners to a resonant scanner. This change was pushed by the fact our original set of scanning mirrors broke from mechanical stress of being driven at speeds higher than specifications. To accommodate the faster sampling rate the PMTs were also changed to faster models. Because we did not want to lose the possibility of slower high-resolution imaging only the X scanner was changed to a set of automated interchangeable mirrors. This piece of equipment performed extremely well, and the resonant scanners were eventually good enough that the galvo scanner became almost redundant, instead we preferred using frame averaging to increase SNR for quick structural imaging. The only issue we noted was the resetting of the mirrors to the galvo setting at each restart, taking a few seconds to switch back every time. Normally not an issue but because of numerous informatic bugs forcing frequent restarts of the system we avoided any unnecessary manipulation.

Optogenetics

The main customization to our needs has been the addition of an extra light path to each system for optogenetic stimulation to move towards all optical imaging. For single photon optogenetics the added system itself is quite simple and almost identical to the excitation light path of a confocal microscope. One or in our case two CW lasers are coupled through a shutter into an optics fiber directing them to a set of galvanometric mirrors. This was used in study 3 in the olfactory bulb, it proved efficient at providing sufficient light precisely in the field of view but presented some issues. First and foremost are the artifacts, even when using precisely designed filters to separate the recording wavelength (under 515nm) from the one used for optogenetics (552nm), the excitation light is strong enough to be detected by the ultrasensitive PMTs and to produce large optical artifacts. This will always be a hindrance to all optical physiology but could be worked around by using two-photon optogenetics in the future as it does not produce any optical artifacts.

Possible improvements to two-photon microscopy systems

Computer interface to a two-photon microscope

Initially most new microscope technology are first applied to structural imaging, be it in biology or other domains. Functional imaging since it usually requires higher recording speeds appears

later when the technology becomes sufficiently advanced to provide usable framerates. This was the case with fluorescence microscopy, confocal microscopy and two-photon microscopy. When physiologists finally get their hands on new imaging technologies the framework is already geared towards high resolution imaging. Since most laboratories use the technique for high resolution imaging with less time consideration companies wanting to sell their products orient their production and research and development in this direction. The issues we suffered from at the beginning of this were first that a few technologies like resonant scanning, fast PMTs and others were still in development and would become standardized after a few years. Second a lot of the physical design of the microscope was geared towards imaging glass slides and at most cell cultures, a lot of legwork was needed to modify the equipment and adapt animal holding solutions to microscopes that were not designed for it. Finally, the software and computer hardware were not properly designed to handle the data flows provided by live imaging.

Upstream labelling of data and mechanical states

A big part of progressing towards successful experiments is keeping track of experimental parameters. Easily accessing all parameters of an experiment during analysis allows the analyst to efficiently classify the data. This becomes particularly apparent when data acquisition and analysis is divided in between two scientists as tends to be the case more and more. Evidently taking manual notes in a traditional lab book will always be the most stable way to keep track of information and should be kept a habit and as a failsafe. However experimental design should move in the direction of direct online labeling of data. In our case the obvious main modality is the calcium imaging, but a variety of parameters are also recorded in parallel. On the side of the imaging computer the experimenter needs to adjust, the framerate of a recording, the intensity of the laser power (for imaging as well as for stimulation), the depth of recording and the position of the recording site. Outside of the imaging the experimenter also needs to account for: the physiological state of the animal (breathing rate, heart rate, oxygen saturation and eventually temperatures of the bath and the animal), the stimulation parameters (intensity, frequency and position or quality) and sometimes a secondary recording modality (electrophysiology or behavioral state). If the animal is awake and behaving these parameters change, the physiological parameters are replaced by one or multiple cameras monitoring the behavioral task of the animals, stimulations are still possible and should be accounted for and the state of the eventual virtual reality should be recorded. Synchronizing all these modalities

is no simple task, an already relatively complex microscope becomes part of a larger system that bloats up very quickly. In this situation it seems logical to arrange everything around the most complex piece of equipment, in our case the two-photon microscopes. Another argument in favor of that is that imaging software are very complex and hardware demanding so it is simpler to infeudate other systems to it. In our case we used spike2 and the CED 1401 AD converter to record copies of the internal signals of the microscope and arrange everything around it. However, this complicates the data analysis downstream as part of the information about a recording is in the recording file (not much other than the images themselves), part in the spike2 file, and the final part in the lab book of the experimenter. The largest file here is the imaging file by a factor of more than 1000x. As such including all the rest of the data stream into the metadata of the imaging file would not increase the size by much but would make analysis significantly easier. To begin with all parameters of the recordings should be labeled since up until now not even the laser intensity is in there. In the future given the large part of the two-photon microscopy market taken by live imaging setups it would be interesting to see systems integrating physiological parameters, stimulation trigger and eventually simple electrophysiology into two-photon microscope design. An excellent example of data uniformization can be found in the field of electro-encephalographic recordings. Because that technique became routinely used in human medicine the data format had to be collegially made uniform. This was done in 1992 and updated in 2003 (Kemp et al., 1992; Kemp & Olivan, 2003) The resulting European Data Format or .edf file format can be used for any time series and is designed to contain supplementary information natively. There have been similar attempts in the imaging field with mitigated results, the main file format: tagged image file format or .tiff lacks the capacity for complex metadata and the alternative ome.tif allows for storing of complex metadata but the contents and structure of that metadata need to be uniformized to allow for easier transfer for analysis. This is also an important point in the move towards a more open science. In part due cases of scientific fraud an important push has been made by scientists and publishers to render raw datasets publicly available post publication. In the case of imaging data, the sheer size of the datasets is a limitation but also the variety of file formats some of them being proprietary and could potentially be unusable in the future when the right software will not be available anymore. Uniformization of data formats should be an important step towards more open science.

Future proofing computer interfaces

Identifying bottlenecks and removing them. A sometimes-overlooked parameter limiting the quality of data acquisition and the comfortability of software usage is the hardware of the recording computer. Our first recording computer was running on windows XP 32 bits and using an HDD for data storage, one of the first problems we encountered was that our recordings were too large to be stored in the limited (8go) of RAM and had to be dumped online to the hard drive. This can create a problem if at any point lag happens in the software (and it does) and the RAM fills up, producing either a crash or causing one or multiple frames not to be recorded. In our case the computer tended to crash and need a reboot, causing heavy delays in the experiments. This happened early on, and we had to deal with it by reducing the field of view we were recording since less pixels=less data. This illustrated the importance of such a bottleneck. Our system was perfectly able to record large fields of view at high frequencies, but the computer could not save the frames fast enough. After two years we switched to a Windows 7 64bits computer with 16gb of RAM and a slightly faster HDD, the larger amount of RAM made the crashes less frequent and allowed us to increase the recording field of view enough to match the capabilities of the microscope hardware. The next bottleneck that we discovered happened at the Hard drive level, since our datasets were still much larger than what the RAM could handle (and using more RAM would have required changing the motherboard) we were still dumping the recorded frames to the hard drive during the recording. We discovered while doing control experiments to test synchronization with a third-party computer that the recordings were irregular (Fig. 6-18) further investigation showed us that whenever there was a delay in writing of the data to the hard drive (we still are not entirely sure what caused these delays) the new frames were dropped and not written to the hard drive and therefore lost. The company producing the microscope and software refused to communicate on the subject and we can only suppose that this was implemented in software to prevent crashes. It would have been simple to just timestamp the dropped frames, allowing us to properly synchronize posthoc but that would have been an admission of failure. The simple solution to this was to switch the HDD with an SSD with less storage space but orders of magnitude higher writing speeds. The wide commercial availability of nvme SSDs will allow for even faster data handling and will move the next bottleneck to the microscope hardware side. An interesting improvement that would be allowed by faster processors and write speed would also be to synchronize all extra modules of the microscope on the same computer instead of using a second computer. In

conclusion when building a microscope costing in the hundreds of thousands of euros it is wise and often neglected to invest in matching computer hardware.

Slow wave activity in the context of largescale networks

Our results from the study 1 using fiber photometry provide evidence for large-scale recruitment of cortical networks upon a specific type of neural activity – slow waves – which have previously been shown to be present under different types of anesthesia (Busche et al., 2015; Chauvette et al., 2011; Mukovski et al., 2007; Poulet & Petersen, 2008; Seamari et al., 2007; Zucca et al., 2017) and in natural slow wave sleep (Chauvette et al., 2011; Massimini et al., 2004; Mukovski et al., 2007; Steriade et al., 1993; Steriade & Amzica, 1998). Although the main features appear similar to those of the NREM delta oscillation (Mukovski et al., 2007; Reig & Sanchez-Vives, 2007), under anesthesia, slow waves appear more rhythmic and more synchronous across the cortex and also show longer silence periods (Busche et al., 2015; Chauvette et al., 2011) with, as we showed, a relationship with anesthesia depth. During natural sleep, spindle activity - which is related to memory consolidation (Oesch et al. 2020) - is grouped by slow waves (Eschenko et al., 2006; Marshall et al., 2006; Ngo et al., 2013; Oesch et al., 2020) but this is not the case for anesthesia induced slow waves (Boly et al., 2012; Murphy et al., 2011). On the contrary general anesthesia has been shown to potentially impair cognitive function and in particular memory (Amiri et al., 2020; Davis et al., 2014). Potentially through GABA receptor (Zurek et al., 2014) or cholinergic impairment (Beninger et al., 1986). Nevertheless sleep slow waves and anesthesia slow waves may recruit the same cortical and subcortical structures (Murphy et al., 2011). Although cortically generated (Steriade et al., 1993; Timofeev et al., 2000) slow waves also engage the thalamus (Sheroziya & Timofeev, 2014; Steriade et al., 1993; Stroh et al., 2013) and hippocampus (Ji & Wilson, 2007; Karalis & Sirota, 2022; MA Busche, 2015; Sirota et al., 2003) suggesting that slow wave associated excitation plays a synchronizing role in functional coupling of remote brain regions (Hahn et al., 2006). Although this is unlikely the case for anesthesia related slow waves (Murphy et al., 2011) they might recruit the same structures and thereby provide a spatiotemporal mechanism for such plasticity-relevant cortico-hippocampal functions (Logothetis et al., 2012). Intracortically, slow waves can propagate as a travelling wave (Busche et al., 2015; Matsui et al., 2016; Stroh et al., 2013), likely by relays of local populations of cells (Destexhe et al., 2007). Depending on excitability state of the network, a slow wave event could either remain local (Nir et al., 2011; Vyazovskiy et al., 2011) or could spread

‘smoothly like an oil-spot’ (Huber et al., 2004; Sanchez-Vives et al., 2017). The recruitment of sub-cortical regions is discussed to rather involve longrange excitatory projections (Leong et al., 2016). Although slow wave activity is a multiscale phenomenon (Jercog et al., 2017; Sanchez-Vives et al., 2017), previous work has focused either on local and cellular (X. Chen et al., 2013; Grienberger et al., 2012; Kerr et al., 2005; Sanchez-Vives & McCormick, 2000; Stroh et al., 2013) or on largescale characteristics (Massimini et al., 2003) of slow waves. Here, we tried to bridge different levels of observation, the mesoscopic representation of slow waves in a defined cortical population and the microscopic using two-photon microscopy and electrophysiology.

Advantages and drawbacks of awake experiments

Physiological state

While during awake recordings there is no exogenous chemical modulation of activity of the brain through anesthetics the attention state of the animal can still vary. The animal can be under stress, attentive, relaxed and with sufficient habituation it can even naturally go to sleep (Aime et al., 2022). For the recordings to be under a uniform state of attention the experimental parameters need to be under strict control. To avoid unnecessarily stressed animals they need to be habituated to the experimenter and the manipulation (Juczewski et al., 2020). The habituation can begin properly after 2-3 weeks recovery from the implantation surgery. This recovery delay can be as short as a week for if viral expression is not necessary but, in our case, this was also the delay for viral expression. After the first week of recovery, when checking on the animals the experimenter should habituate them to manual handling beginning by just placing their hand in the cage and letting them move around it, then gently stroking the animals and finally picking them up gently in a cupped hand and letting them move from one hand to another and explore this new environment. This initial habituation can be as short as 5min per day but greatly facilitates the next step. If the animal is recovering well the experimenter can start to touch the recording implant and try to hold it for a few seconds. After two training sessions the animals should already start to calm down when handled in such a way. This has the advantage of testing the resistance of the implantation and selecting the animals with a properly attached implant. Animals with implants detaching at this step were sacrificed immediately. Then once the animals are fully recovered from surgery (2-3 weeks) the experimenter should bring them to the recording setup and start by picking them up and placing them on it letting them explore while keeping their tail secured between two fingers as a safety.

If the animals are already used to manual headfixation the experimenter should already start to affix the animal in the clamping system for a few seconds to a few minutes depending on the reaction of the animal. After repeating this daily for 3-5 days the animals should be capable of staying calm on the system for up to 30min, enough for a recording session. We did not train the animals in a particular behavioral paradigm, but this could reasonably be started after 3 days of habituation. This protocol can be slightly shortened to 2-3 days post recovery by performing all the habituation steps twice daily instead of once. The habituation sessions should all be performed at the same time of the day for optimal results. Especially considering that these experiments are performed during the light period, mice normally sleep during that period, keeping the experiments to the same time minimizes the impact on the circadian rhythm. The gentleness of animal handlers in their routine tasks while usually unimportant has an impact in this type of habituation, it makes sense to ask the animal caretakers for particular care with the few cages of implanted animals.

Movement artifacts

Movement artifacts are a major obstacle to all awake recordings but in two-photon microscopy movements as low as 10 μ m in the tangential direction (perpendicular to the imaging plane) are enough to move all cell bodies out of the imaging plane. Respiration artifacts can sometimes be an issue in anesthetized recordings but are often caused by either hypoxia or improper fixation. Brain swelling and movement related to blood pressure in the brain can also happen and are suppressed here by the long-term implantation of the glass window. Slow drifting movement artifacts can appear for multiple reasons (including brain swelling) but can often be corrected post hoc. During awake behaving recordings however, the animal can move its body while having only the head fixed. To prevent tangential movements in this case we found a few important parameters. These movements appear either when the mouse is struggling against the fixation and tries to move its head vertically or when the mouse is running on the trackball. Interestingly the beginning of a running period and its end are the moments where the largest movements appear. These two situations are the moments when the animal is exerting the most force vertically, the direction where the mouse can exert the most force is up, since it can push against the running surface. The force a mouse can exert down is limited by its weight. The easiest parameter to adjust then is the distance between the ball and the holder, the mouse should not be able to rest flat on the surface of the ball but should also not be hanging by its implant with its legs extended. Having the correct distance prevents the mouse from being able to exert

too much force by pushing against the ball or other running surface. Finally choosing the proper fixation system for the type of recording is primordial. For two-photon microscopy this means a stiff holder ideally with multiple points of attachment. In our case we tested straight implants provided by Phenosys and custom circular implants from the lab of (██████████ Heidelberg University). The straight implants proved too flexible with a single arm sticking out from the table and to the mouse. The movement artifacts were often larger than approx. 30µm, enough to move the recorded cells out of focus. Such large movement artifacts are too big to be corrected post hoc. Even stiffening of the arm by using thicker material proved unsuccessful. Observation at low magnification showed us that this implantation system also brings its own issues, since the holder is straight the glass window is glued on one side of it and the rest of the exposed skull is covered in a chamber made from resin. Because the skull of even an adult mouse remains flexible especially at the junction of cranial plates (Moazen et al., 2015) and the resin needs to strike a good balance of stiffness and flexibility so as not to brake, there remains a certain level of flexibility in the system. Enough flexibility to move the imaging field of view when the mouse exerts vertical force. The implant we settled on, prevents flexibility by being circular and going all around the imaging window, preventing the natural flexibility of the skull. Moreover, the clamp in which this implant is fixed is also circular further preventing any deformation, it is also held on two sides so while it is approximately 1mm thin the clamp itself does not deform.

Ethical considerations

Additionally, to the usual ethical consideration of animal experiments performing recordings in awake animals poses supplementary questions. How is the implant affecting the animals in terms of pain, discomfort, and risk of infection? Are the recordings themselves painful or too stressful? The implantation surgery is quite invasive and naturally induces more pain than a simple virus injection surgery. Using painkillers during the recovery reduces the discomfort and pain it causes, the behavior of the animals tends to normalize completely one week postsurgery and they show no particular signs of pain when visually assessed using for bodily signs and the rodent grimace scale as early as 4 days post-surgery (Akintola et al., 2017). Once the cicatrization is complete the animals stop scratching after the implant and appear used to it. Concerning habituation and recording, the animals show some signs of stress and discomfort at first when the experimenter holds the implant manually (light struggling, vocalizations), but once the animal stops trying to escape after 1-2 sessions the signs of stress disappear and they

relax (Jordan, 2021). The behavior shown by the animals during this habituation is very similar to the behavior shown during classical restraining holding the animals by the neck and the pattern of habituation was, in our hands, similar. The habituation on the recording system shows the same pattern and once the animals are habituated, they stop trying to move their heads vertically and start trying to explore their new environments. While these experiments are more stressful for animals than anesthetized recordings due to the consciousness of the animals, they make sense in the context of reduction and refinement of animal experiments. We certainly keep animals in a situation of potential suffering for longer than with acute experiments and it should be taken into consideration when deciding on such experiments and especially when deciding how long the longitudinal recordings should be. However, sampling the same animals' multiple times has two effects.

One: the number of animals necessary to obtain good data is drastically reduced, if one imaging session fails it is possible to try again using the same animals. The number animals necessary to establish a good experimental protocol might be similar but once it has been established, chronic experiments remove the risk of surgical failure at each experiment and increase the chance of acquiring a significant dataset in each animal.

Two: Chronically implanted animals can be sampled across time and the quality of data obtained from them is drastically improved as it can be put in a long-term context. For example, the evolution of a pathology, learning or adaptation to stress. Moreover, repetitive sampling of the same region can drastically improve the statistical value of each cell. Recording 100 cells from 3 animals does not yield the same interest as characterizing 30 cells from one animal in depth and understanding the relationship between their timing of activity, interactions, response parameters and evolution across time. Chronic sampling of animals has the possibility of greatly improving our understanding of neural circuits by enabling a better depth of analysis. Multiple imaging techniques can also be applied to each animal to gain a more holistic view of the system.

All in all, using a chronic preparation could reduce the number of used animals by a factor yet to be quantified, especially when reusing the same animals for multiple experimental modalities.

Parvalbumin interneurons show unexpected effects on local networks

In study 3, we found that inhibiting PV interneurons causes a broad spectrum increase in spontaneous activity in mouse barrel cortex in vivo. Oppositely, activating PV interneurons

strongly reduced the power spectrum of spontaneous activity. Furthermore, PV-mediated disinhibition upon single whisker stimulation induces a widespread increase in synaptic excitation, but an increase in suprathreshold spiking activity only in neighboring columns. In contrast, activating PV interneurons decreased synaptic excitation and spiking activity both in principal and neighboring barrel columns. These effects are short-lasting and are critically dependent on the timing of optogenetic modulation, with the strongest impact on cortical excitability during the first 20ms after onset of whisker stimulation. Notably, this drastic effect is mediated by a rather small number of PV interneurons, constituting only around 10% of the local PV population, around a few hundred neurons.

Lateral effects

PV interneurons, anatomically, as chandelier and basket cells seem to project mostly locally. An explanation to our results other than a subpopulation of further projecting interneurons could be due to the strong electrical coupling within the PV interneuron population. PV interneurons express connexins and seem to be extremely well connected to each other, interestingly this is the case in the cortex but also in the cerebellar molecular layer. This property could be the source of far spreading inhibition of action potentials and field potentials in our results. It does not entirely explain why the inhibition of action potentials is more intense in lateral barrels compared to the principal one. This effect could be dependent on a local inhibitory loop from VIP interneurons that only affects one barrel at a time. Studying the interaction between these two populations on a mesoscale level like here could be an interesting further investigation into the inhibitory interaction between barrels.

Sensory modulation

One effect we could not explain in our results upon inhibition of the local PV population is the secondary sensory excitation when the inhibition is maintained for more than 20ms. Because we do not induce any excitation of the network after the 2ms stimulation this second peak can only be due to another source of excitatory activity in the network. A recent study showed that PV neurons in layer V do sharpen the timing of the sensory response this study shows something resembling this secondary peak upon PV inhibition albeit with less precise timing in awake mice (Vecchia et al. 2020). An explanation could be that an excitatory feedback loop going through the network reaches the cortex again around that time but is normally suppressed by PV interneurons.

Implementing an optogenetic approach to silence or activate interneurons in combination with MEA recordings

One of the inherent pitfalls of genetic targeting of opsin expression to a defined neuronal subpopulation is the specificity of the promoter. This is of particular relevance for approaches employing a direct control of opsin expression by a cell-type specific promoter encoded in 1 viral plasmid. In this case, 2 conditions must be met: firstly, the expression needs to be rendered specific, and secondly, a high expression level has to be realized, as the photocurrent brought about by individual pumps is rather small and therefore a large number of opsins need to be expressed (Fois et al., 2014; Sohal et al., 2009). Typically, promoters specific for interneuron populations are rather weak, so a direct control of ArchT or ChR2 expression by the PV promoter will not lead to sufficient opsin expression. Here, we circumvent this problem by employing a transgenic mouse expressing the enzyme cre-recombinase 4 in PV interneurons only (Sohal et al., 2009). Upon injection of a viral construct driving expression of ArchT or ChR2 by a strong ubiquitous promoter but flanked by 2 flox cassettes, expression will be limited to cre-expressing interneurons, but at the same time driven by a strong promoter (Cardin et al., 2009, 2010; Sohal et al., 2009). However, we still could not confirm that 100% of the expressing cells were PV-positive. Indeed, while PV is exclusively expressed by GABAergic interneurons and mainly by the so-called basket cell class, it is also expressed at lower levels by other types of interneurons (Gentet, 2012). Our results are well in line with these reports, and we could rule out expression in excitatory neurons.

Other types of interneurons

The three main types of cortical interneurons differ greatly in their connectivity and their function in sensory processing. Their effect on sensory processing has been studied in other sensory areas but these studies concentrate on processing within a single cortical column mostly in the visual cortex. PV interneurons have been shown to linearly transform the sensory response and to be dependent on activity from VIP interneurons (Atallah et al., 2012; Kerr et al., 2007; Sachidhanandam et al., 2016; Zhu et al., 2015).

Excitation-inhibition balance

PV interneurons exert strong somatic inhibition at multiple layers in the cortex and are a key component of the cortical microcircuitry. Their key position in the cortical flowchart makes

them an important component of the E/I balance in the cortex. In this work we mostly studied cortical circuitry, but PV positive interneurons are quite ubiquitous in the brain with different final functions but similar positions in the circuits. They do have an impact but first how limited in time second how is PV interneuron activity modulated?

Schizophrenia

Schizophrenia is more and more believed to be a pathology linked to a deficient excitation inhibition balance. Multiple studies have shown an impairment in parvalbumin interneuron number in patients affected by schizophrenia. The supposed explanation is that without the tight control they exert pyramidal neuron can depolarize and fire action potentials in an uncontrolled manner, introducing noise in a system where a single action potential can carry significant information (Arce et al., 2006; Kaar et al., 2019; Nakazawa et al., 2012). In fact studies showed that induced cortical noise can affect sensorimotor control, a function that is affected in schizophrenic patients (Carment et al., 2019, 2020; Lindberg et al., 2016).

PV interneurons and slow waves

In these experiments we showed the strong E/I change provided by PV interneurons and how this affects slow wave patterns under anesthesia. Do cortical PV interneurons directly control slow waves patterns in the brain? It seems highly improbable given the importance of subcortical structures in initiation and modulation of these events. However slow waves occurrence and frequency do seem to be highly related with PV activity and probably with the state of E/I balance. We showed here that PV interneurons can reduce the occurrence and amplitude of slow waves when activated and that reducing their activity does allow for higher amplitude events.

It has also been shown recently that slow waves can occur during wake locally within superficial layers of the somatosensory cortex during REM sleep (Funk et al., 2016). While this might be due to local cholinergic neuromodulation the local network of inhibitory neurons certainly plays a large role, we have shown here the locality of efficient parvalbumin inhibition and the efficiency of a small population in superficial layers of the cortex. While probably not sufficient by themselves it would be interesting to investigate how parvalbumin interneurons regulate slow wave activity during spontaneous events and if their inhibition is due to another GABAergic population or through neuromodulators.

Towards a better understanding of optogenetic modulation

The Kubelka-Munk approach

The Kubelka-Munk equation to characterize light penetration in biological tissue is very crude, it depends only on a few parameters. The absorption coefficient of the tissue S_z , which itself is dependent on the wavelength. On this basis we add the diminution in power density due to the geometric spread of light. This approach is crude in that it doesn't account for diffraction inside the tissue. It also considers the tissue homogeneous and doesn't account for the presence of blood vessels or for different absorption coefficients of different tissue structures like layer I or layer IV for example. Some publications have used more realistic Monte-Carlo based models to get a better understanding of geometrical light spread (Fenno et al., 2011; Maglie et al., 2019; Yizhar et al., 2011) but we haven't used those yet. For the sake of simplicity to be able to compare multiple parameters a bit faster we used the simplified geometric model presented here. Now that we established that it predicts modulation volume relatively accurately, we plan to use it in future studies in conjunction with establishing a dose-response curve to choose the appropriate stimulation parameters. This can prove particularly useful when targeting small subcortical nuclei.

Assessing the Scope of Optogenetic Network Modulation

Multiple experimental parameters influence the scope of optogenetic network activation: Firstly, AA-virus injections inherently result in varying infection rates per neuron due to multiplicity of infection, leading to heterogeneity of opsin expression (Aschauer et al., 2013; Blits et al., 2010; Burger et al., 2004; Markakis et al., 2010), this in turn affecting inhibitory photocurrents. However, while this induces jitter, it might create a less artificial pattern of inhibition. Secondly, while light penetration can be estimated by established models, the highly heterogeneous brain tissue, in particular the high-light scattering and absorbent microvasculature, can only be modeled to a certain extent. Finally, for optical inhibition even more so than for excitation, efficient inhibition of action potential firing depends on many physiological parameters like neuromodulation, state of the animal, membrane resistance, and synaptic inputs (Lee et al. 2014). This inherently limits the accuracy of any approach assessing the scope of optogenetic network modulation. While initial studies employed the Kubelka-Munk model (Aravanis et al., 2007), assuming a conical spread, experimental data revealed that this approach underestimates the lateral spread (Stroh et al., 2013; Yizhar et al., 2011). There are different hypotheses about this underestimation. The scattering in tissue could lead to

sufficient light reaching cells outside of the theoretical light spread, this scattering would lead to an exponential decrease in intensity with distance which resembles experimental data (Fenno et al., 2011; Stroh et al., 2013). Another possibility that would explain data from (Stroh et al., 2013) would be that when illuminating a sufficient part of the dendritic tree of a cell, action potentials can be evoked and in any case some level of excitation is produced. This would fit within experimental data but would be very complex to model. More complex modeling approaches based on Monte Carlo simulations led to rather ellipsoid geometries (Yizhar et al., 2011; Yona et al., 2016). In our present study, the correlation of histology/modeling data using the combination of 2 geometrical models with actual single unit recordings resulted in a striking convergence of optogenetically modulated cell numbers, mutually supporting the validity of our estimates.

More comprehensive modelizations

In recent years a few more informatically inclined laboratories have investigated light spread in biological tissue and provided simulation tools to calculate light spread more realistically. These models mostly use Monte-Carlo simulations to evaluate diffraction. A final parameter to account for in these tools would be blood vessels. Blood vessels can account for a large surface of the illuminated brain tissue, most of the time the experimenter consciously avoids placing the fiber close to a surface blood vessel, but they can still produce shadows in the illuminated volume. One could use an image of the brain surface to evaluate the presence of blood vessels in the area in order to evaluate shadows in the illuminated volume. Luckily blood vessels tend to be horizontal only on the surface and penetrate the cortex vertically in layer I which could facilitate taking them into account. In the end however a precise estimation of the number of cells stimulated is very important when using broad field stimulations. By controlling the size and delimitation of the expression area upstream like we showed here and checking for the surface expression before the experiment one can get an order of magnitude estimation of the number of cells quite easily. Moreover, the genetic targeting nature of optogenetics already allows a good degree of precision in the targeting of cellular population. A skilled experimenter combined with a well-chosen genetic targeting strategy are enough most of the time. Putting large efforts and time into refining these tools would only be useful when using very specific techniques and in a laboratory using optogenetics only as a secondary tool, the same efforts can be put to much better use analyzing the data more in depth.

It must be noted that anyhow due to the aforementioned experimental variables, any assessment can only provide order-of-magnitude estimations. Using the Kubelka-Munk model of scattering in combination with a geometrical model and a histological assessment of cell densities represents a very straightforward way to estimate the number of cells potentially activated (or in our example inhibited) by optogenetics. In the near future, the field of optogenetic interrogation of circuits has to move from rather mechanistic connectivity studies to approaches taking into account the scope of optogenetic network modulation. Therefore, a generalization of this practice in the field would be advisable, even more as network effects drastically depend on the architecture of the respective cortical circuits.

The best approach to precisely know how many cells are modulated is quite simple in the end. By taking care of producing only a small expressing region corresponding as exactly as possible to the region of interest like we did using intrinsic optical imaging and by using a slightly larger illumination method. One can be sure to excite all cells expressing the opsin, those can then be counted, and the modulation precisely known. This would be interesting to verify using optetrodes recordings.

Prospective re-analysis the data

The data we acquired in study 3 in particular is extremely rich. The analysis we performed here concentrated on the direct effect of PV modulation on sensory activity. Like multiple electrophysiological studies from the same laboratory there are multiple avenues for re-analysis of the data, considering spontaneous activity, state modulations within urethane anesthesia and more in-depth spike sorting. We did not explore these avenues because we lacked time, but the possibility remains.

Effect of brain state on sensory activity

In this project we discovered an effect on PV interneurons modulation on brain states recorded in the cortex under anesthesia. We showed that PV interneuron activation decreases the occurrence of brain states and that their inhibition increases it. However, this analysis was performed at the very end of the project and surprised us by its results. As we expected direct evocation or suppression of up states. Urethane anesthesia resembles natural sleep in that recordings display different phases displaying different dominant frequencies (Clement et al., 2008; Pagliardini et al., 2013; Sharma et al., 2010). In some of our recordings we observed slow waves states occurring during stimulation periods and we did exclude these trials from analysis.

An interesting possibility would be to reclassify all data sets according to the brain state displayed in them and then look at the effect of each state on sensory stimulation. Is sensory stimulation affecting the occurrence and frequency of slow waves? We would expect whisker stimulation to directly evoke up states like in the hind paw of rats (Schmid et al., 2016) Wachsmuth, Schwalm, P. H. Prouvot, et al. 2016) or in the visual cortex (Stroh et al., 2013). We would then expect local optogenetic modulation of PV interneurons to reduce the success rate of sensory up-state evocation. How does sensory response change when the brain is in a slow wave state or in a persistent up state? It would also be interesting to explore the modulation of sensory response across the continuum between persistent up-state and up-down state and if PV interneurons play a larger modulatory role in one state or the other.

Impact on power spectra of spontaneous and evoked activity

We found that transient inhibition of a small number of PV interneurons causes a significant broad spectrum increase both in spontaneous and evoked network activity, ranging from theta to gamma frequency bands (Figs. 3 and 4). Activation of PV interneurons during spontaneous activity significantly reduces spectral LFP power over wide range of frequencies (Suppl. Fig. 4). An earlier study in the prefrontal cortex found that optogenetic inhibition of PV interneurons reduces power in the gamma frequency band evoked by light activation of excitatory pyramidal neurons (Sohal et al., 2009). Different experimental designs between this earlier study and our present work may explain this discrepancy. Firstly, rodent prefrontal and barrel cortex exhibit prominent differences in cytoarchitecture, with the prefrontal cortex being largely devoid of granular layer IV (Shepherd, 2009; Van De Werd et al., 2010). Secondly, Sohal et al. optically activated ChR2- expressing excitatory neurons, while here we deflected single whiskers, directly activating both excitatory and inhibitory neural networks in barrel cortex. In the visual cortex of the mouse, lacking layer IV barrels but exhibiting a similar organization of horizontal layers, the optogenetic inhibition of PV interneurons led to an increase in the spiking rate of pyramidal cells (Atallah et al., 2012), in agreement to our data. It should be noted, that LFP and MUA represent qualitatively different readouts of neuronal activity. LFP majorly reflects the subthreshold membrane potential changes of a rather large population of neurons surrounding the recording site, potentially still being impacted by activity from more than 1cm from its origin (Kajikawa et al., 2011). Conversely, MUA reveals the suprathreshold activation of neurons within a radius of only about 140 μ m from the recording site (Buzsáki, 2004). Consequently, when placed in the PS, only MUA recordings will be able to unambiguously

reflect activity within this shank, while LFP, which also dominated by local activity, will also be impacted by activity outside of the PS, and integrate nonlinearly both spiking and synaptic activity (Buzsáki et al., 2012). Therefore, local spiking specific readouts are better suitable assessing the lateral spread of evoked cortical activity.

Impact of PV Modulation on Slow Oscillations

During quiet wakefulness, NREM sleep and some forms of anesthesia (e.g., urethane or ketamine-xylazine), cortical dynamics show prominent slow oscillations (1Hz Up and Down states) (Reyes-Puerta et al., 2016; Steriade et al., 1993; Stroh et al., 2013). In the present study we indeed observed spontaneous Up–Down state transitions. We demonstrated that under urethane anesthesia, inhibiting PV interneurons reliably induced transitions from Down to Up states and extended the duration of Up state accompanied with an increase in high frequency oscillations nested within Up state, as previously proposed by (Compte et al., 2008). Another recent study found an increase in activity of PV interneurons during NREM episodes relative to REM episode suggesting that their inhibition is participating in the inhibitory dynamics of this state, the same team also showed that PV interneurons are active particularly during spindles nested within slow waves when SOM interneurons are active immediately before which could be in line with our results. PV interneurons might not evoke up states directly but have an implication in their modulation (Niethard et al., 2018, 2021). In contrast, activating PV interneurons reduced the occurrence of slow oscillation as well as the high frequency oscillations occurring during an Up state. These results are well in line with a recent study showing that PV interneurons play a role in modulating the slow oscillation (Zucca et al. 2017). They are not in line with (Niethard et al., 2018) however but this could be due to layer specific effects. The Niethard study only observed neurons residing within the superficial layers of the cortex and it seems probable that PV interneurons play very different roles in different layers of the cortex during slow waves events like they do for sensory processing. Note, that activating PV interneurons did not completely abolish the occurrence of up states. Indeed, it has been shown that modulating SST interneurons (Zucca et al., 2017) and excitatory neurons (Stroh et al., 2013) also impact Up–Down state transitions. In the future, it will be interesting to perform optogenetic modulation of all relevant cortical cell types to explore their specific role in those state transitions. While they are barely accessible to two-photon imaging it would be interesting to record interneurons in different layers during slow wave events to determine

if they present different activity patterns across sleep stages. This could be done using microprisms or GRIN lenses to record simultaneously across all layers of the cortex.

Impact on Spatiotemporal Representation of Sensory-Evoked Activity

Each PV interneuron innervates 200–1000 pyramidal neurons, thereby controlling the synchrony of cortical network activity (Kubota, 2014). However, PV interneurons not only target pyramidal cells, but also connect to each other by electrical synapses and by reciprocal GABAergic chemical synapses (Galarreta & Hestrin, 1999, 2002; Gibson et al., 1999). These synapses allow for electrical coupling of the interneuron network, spreading inhibition or excitation potentially further than we expect without individual neurons projecting directly. Such a mechanism could explain our results showing PV interneuron modulation across barrels further strengthening lateral inhibition. In addition, a high degree of connectivity between PV and somatostatin expressing (SOM) interneurons by inhibitory chemical synapses has been reported (Gibson et al., 1999). Along this line, here we did not only observe an optogenetically modulated reduction, but also an increase of interneuron activity, suggesting secondary network effects. In vitro experimental evidence demonstrates a small, functionally defined subpopulation of fast-spiking neurons in layer IV, which mediates thalamocortical feedforward inhibition in excitatory neurons, therefore directly affecting spiking output of the excitatory network in barrel cortex (Q. Q. Sun et al., 2006). This powerful feedforward inhibition, presumably provided by PV interneurons, shortens the coincidence detection window in pyramidal neurons (Pouille & Scanziani, 2001). Our data shows that inhibiting a small number of PV interneurons in layers II/III and V impacts cortical excitability most strongly during the first 20ms after onset of whisker stimulation, supporting the “window of opportunity” concept (Pritchett et al., 2015). Besides feedforward inhibition, PV interneurons also have been proposed to play an important role in controlling lateral inhibition. Chagnac-Amitai et al., 1989 reported that a 10–20% reduction in GABAergic inhibition causes a prominent increase in the horizontal spread of excitation. Anatomical evidence in rat barrel cortex shows large basket interneurons, presumably PV interneurons in layer II/II, extend their terminals several hundred micrometers away (Helmstaedter et al., 2009), allowing long-range lateral inhibition. Indeed, we found that inhibiting a small portion of PV interneurons causes a widespread increase of sensory-evoked LFP response reaching at least 1.2mm in diameter from the principal column, which correlated with the stronger increase in spiking activity in neighboring columns. These results confirm the important role of PV interneurons in cortical lateral inhibition. Strikingly, in

multiunit recordings, representing spatially well-defined neuronal firing rates, no change was observed in the PS, situated well within the transfected barrel, but an increase of MUA was observed at 200–600 μm laterally in each direction. Moreover, within the PS, no measurable effect on neuronal spiking was found even in the very layers exhibiting robust expression of ArchT (Fig. 4-9F, Fig. 8-3). This supports the notion of PV interneurons playing a highly specific role in cross- columnar (as opposed to intracolumnar) inhibition (Fig. 7-1).

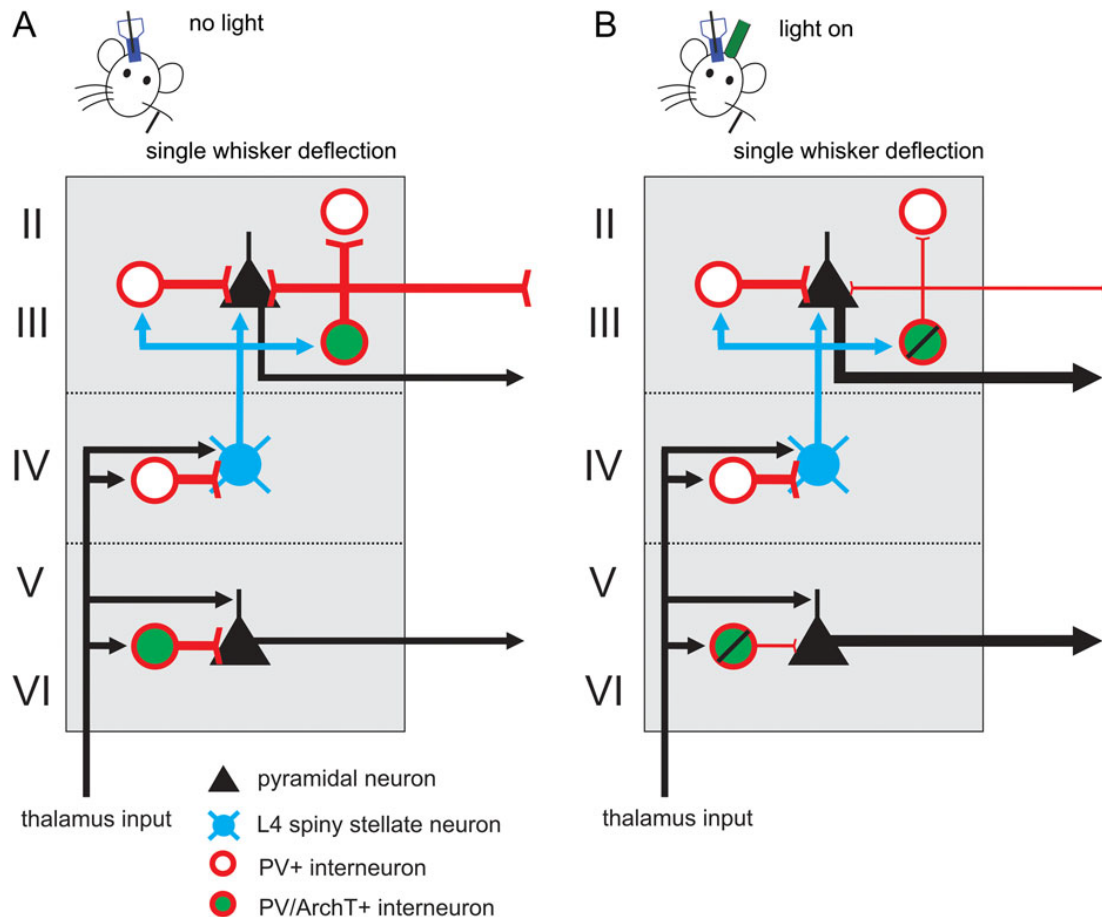


Figure 7-1: The influence of the PV-mediated disinhibition on the signal processing of the response evoked by single whisker stimulation. (A) Under normal condition, the evoked information by single whisker stimulation is transferred by thalamus into corresponding principal barrel column. The thalamic input targets layer IV spiny stellate neurons (blue), PV interneurons (red circle) and deep layer pyramidal neurons (black triangle). PV interneurons provide feedforward and lateral inhibition on pyramidal neurons and other PV interneurons. In this study, the ArchT/PV interneurons (red circle filled with green color) are located in layer II/III and deep layers. (B) During optogenetic inhibition of ArchT/PV interneurons, the output strength of PV/ArchT interneurons decreases and the output strength of pyramidal neurons in layer II/III and deep layers to neighboring columns increases. (Fig. from J.-W. Yang et al., 2017 by permission with Oxford university press)

Outlook

All optical physiology

Optogenetics

There is no question that optogenetics marked a step in experimental neuroscience. Being able to stimulate a genetically defined cell population unambiguously opened the field up to much more precise dissection of neuronal networks. It particularly improved to possibilities of in vivo experiments and democratized experiments that required years of training before.

Two-photon optogenetics

Optogenetics spatial resolution is still significantly limited by light diffraction in the tissue and the illumination techniques. The problem of limiting the field of excitation in diffracting media is the same as for imaging, even if the focal spot is extremely small there will always be excitation within the beam above and below the focal spot. Naturally researchers have started to explore (V. Emiliani, E. Boyden and K. Deisseroth) techniques to perform two-photon excitation of opsins. The first limiting factor has been the small two-photon cross section of ChR2 until the development of red shifted opsins with larger two-photon cross sections like c1v1 (Diester et al., 2011; Fenno et al., 2011). The next obstacle has been to deposit sufficient power on the cell membrane to reliably evoke a photocurrent. This has been achieved through different approaches. Spiral scanning (Rickgauer & Tank, 2009) of the focal spot while focusing on the cell membrane has helped alleviate that issue while reducing photodamage, it however requires an extremely fast scanner and produces some lag between stimulation of multiple cells. We did test it in vivo in the lab with moderate success. The approach that seems to have stuck in the field is the one developed by E. Papagiakomou and V. Emiliani in 2010 who pioneered the use of spatial light modulators for scanless excitation of opsins (Papagiakomou et al., 2010). Since then multiple teams have adopted that method and sometimes refined it to achieve multi-plane excitation of opsins in vivo (Packer et al., 2015; Z. Zhang et al., 2018).

Another approach worth mentioning is random access two-photon microscopy using a series of acousto-optic modulators that could be used for fast scanning excitation across imaging planes (Xue et al., 2022).

Finally, micromirror devices are sometimes still being used to achieve scanless excitation of opsins. Mostly used in vitro because of the relative lack of flexibility of the spatial modulation

they present and the absence of vertical control of the beam the advantage of being simpler to program (Husson et al., 2012).

Optrodes

An interesting combination that has been developed is to use the cell specificity of optogenetics to inform more classical electrical recordings. The first solution commercialized by ALA instruments consists in a light guide within a glass patch pipette, this has been used to blind patch genetically identified cells (Ding et al., 2022; Miranda et al., 2021). This is already a very powerful solution that could even improve the efficiency of automated patch clamp systems (Kodandaramaiah et al., 2012).

By inserting tetrodes and optical fiber in the close vicinity of each other (often by physically gluing them together) one can pulse the excitation light and identify responding neurons. Once the responding neuron's identity has been established using spike sorting one can study the patterns of activity of a genetically defined subpopulation of neurons (Anikeeva et al., 2011). This still remains a niche method mostly for technical reasons as very few commercial solutions are available yet, but it could provide tremendous new specificity to tetrode and multi electrode array recordings. The technical approaches to optrodes are still being refined to make them provide enough power without sacrificing the quality of recording and being small enough not to induce too much damage. Some devices developed by the Yoon lab have produced some based on the architecture of Michigan probes (Buzsáki et al., 2015; Wu et al., 2013). Given the technical challenge of integrating light guides or micro-LEDs within these extremely small devices the result is prohibitively expensive but could decrease in price with technological improvements. The approach taken by the groups of Deisseroth and Anikeeva of combining tetrodes with optical fibers by gluing them together represents an interesting middle ground. The improvements in optic fiber and hydrogel (Karami et al., 2021; Wyss et al., 2021) fabrication (Frank et al., 2020; Y. Lee et al., 2020; Maglie et al., 2019; Park et al., 2017; Sileo et al., 2018) are starting to allow the fabrication of integrated devices with even smaller footprints and easier to use routinely.

Two-photon calcium imaging

Two-photon calcium imaging is still a recent technique, it reached usefulness in the 2010s and now a decade later it is starting to become more commonplace. When we began this work multiple bottlenecks made it a challenging technique requiring a lot of time and monetary

investment. The financial aspect has decreased slightly thanks to the improvement in technology (laser, computer hardware and software). The time aspect has also decreased largely thanks to the much larger literature now available on the subject and the standardization of a few methods. It is now much easier to find a researcher with significant experience in twophoton calcium imaging capable of establishing a setup and training a team.

Naturally the technology keeps on improving and the cutting edge of the field presents good promise. A few teams are pushing the boundaries of optical physiology and a lot of them are moving towards improving and standardizing all optical physiology in increasingly large field of views. Multiple possibilities are being explored to increase the field of view in two-photon microscopy. One path aims at imaging multiple positions in the z axis and another one to increase the field of view while conserving proper temporal resolution.

To achieve high (over 100Hz) imaging speeds the other technical option resides in using non scanning techniques to avoid the mechanical limitations of the scanning mirror themselves. To orient a beam without moving parts one can use Spatial Light Modulators (SLM), ElectroOptical Modulators (EOM) or Acousto-Optical Modulators (AOM). SLMs are made of a liquid crystal typically on a reflective surface, by modulating the shape of it electrically one can affect the intensity and phase of the beam, allowing for maskless masking. This method is ill suited for imaging as the reshaping of the SLM cannot reach the speeds needed to achieve high framerates. It is very useful for scanless optogenetics, however.

AOM and EOM operate in a similar way, by applying either a electrical current or an acoustic waveform one can modulate the refractive properties of the device's lens. This can be used to deflect the beam, by using multiple such devices in a row, one can move the focal spot in three dimensions (Kremer et al., 2008; Otsu et al., 2008; Salomé et al., 2006; Villette et al., 2019). The advantage being that the speed at which the beam can be moved is orders of magnitude faster than using mechanical scanners. It also allows for the fast scanning of larger field of views at high magnification as well as scanning multiples planes sequentially in three dimensions. The only disadvantage of the technique is the limitation in wavelength ranges available. Because the scanning is done by adjusting the diffraction parameters of the AOD changing the wavelength requires changing the deflection parameters. Currently this technique is limited in wavelength range but in the future, this might be corrected for by pre-programming all necessary wavelengths. Ultimately the limiting factor for imaging speed will be the pixel dwell

time necessary for sufficient excitation to detect emitted light. It will be mitigated by better sensors and cloud scanning but only up to a certain point.

About line scanning

Line scanning is a possible alternative to resonant scanners to achieve framerates over 30Hz. In line scanning instead of scanning the whole frame line by line from top to bottom each cycle, the user defines lines across region of interests and the software designs a scanning path scanning only these lines sequentially (Buehler et al., 1999). Because the number of pixels scanned each frame is much lower, significantly higher speeds can be achieved easily above 100Hz per cycle without the pixel dwell time suffering (Chaigneau et al., 2003). It is also less damaging to the scanners as the speed is achieved not by pushing the linear speed of one of the scanners to the maximum but through a better balance of x and y movements (although short paths with sharp turns done repetitively would certainly damage the motors over time). It also produces much smaller datasets which is an advantage for streaming, storing and analyzing the data. Another clear advantage is the diminution of photobleaching, since only a thin line is scanned across the sample photobleaching occurs only along the scan path and the rest is preserved (Patterson & Piston, 2000). We did not use this approach for a few reasons. In classical line scanning the user needs to define lines of interest across dendrites or cell bodies they want to record from. This step does make later analysis faster, but the time gained there is lost during the experiment drawing the lines, this is an important disadvantage as time is precious when working with an anesthetized animal, longer times under anesthesia means a slow deterioration of the physiological state of the animal. This consideration is more so valid for awake experiments where the animal should spend as little time as possible fixated in the recording system. The fluorescent staining also degrades over time in the case of acute stainings like OGB-1. Furthermore, that unexpected movements are not uncommon and any z movement would mean having to redraw the scan path every time. In terms of analysis, because the amount of data recorded is streamlined most spatial information is lost and while temporal resolution is much better providing a better view of the dynamics of the marker, the fluorescence level from each cell is averaged over a smaller number of pixels meaning potentially noisier data. Recording the whole frame, while it means a certain amount of useless data points also leaves the possibility for unexpected discoveries and data mining, like in our case the signal from the neuropil. Finally, while faster speeds allow for the study of indicator dynamics in more detail we used well described markers with relatively slow dynamics. We had the choice between both

options but recording full frame seemed better suited for our projects. Line scanning is only advantageous when high imaging speed are absolutely necessary like in the case of voltage indicators.

Brain states in new and old datasets

The study of rhythms in the brain is as old as electrophysiology which is to say relatively recent in the history of biology. The detailed study of brain rhythms during sleep and anesthesia has expanded greatly in the last decade and in particular the study of slow oscillations and their interactions with sensory evoked activity. While these studies are recent electrophysiologists have been recording animals under anesthesia and natural sleep for decades often studying local activity on the cellular or microcircuit scale while not always caring for activity on a more global scale. We discussed already the importance of including a relatively global recording modality in studies of neuronal networks in vivo in order to put local activity on the cellular or microcircuit level in a broader context and enrich the analysis. Looking through at the literature there is an enormous amount of data under a variety of anesthesia and physiological conditions that could be reanalyzed under a new scope. In fact multiple teams upload their published data to public repositories on for example the repository of the Svoboda lab at Janelia (janelia.org/lab/svoboda-lab/data), data from the Allen institute (Anon n.d.-b) or more generally neurodata without borders (nwb.org). Indeed, this argument could apply to any frequency band but the easily detectable and classifiable nature of slow waves it makes the process more realistically feasible.

Supplementary analysis of imaging datasets

Even though one of the subject matters of the Stroh lab is slow waves the time-consuming nature of data analysis forces always forces researchers to make choices on the modalities they want to analyze. Three projects of the lab have concentrated on different neurodegenerative diseases (Huntington, Multiple Sclerosis and Alzheimer) (Arnoux et al., 2018; Ellwardt et al., 2018; Rosales Jubal et al., 2021) using a similar two-photon imaging approach. These studies evaluated changes in microcircuit activity at different steps in the evolution of the condition, concentrating on activity levels in individual cells and at the microcircuit level. Because the brain state was not directly the subject matter here, these studies were conducted without supplementary electrical readout of activity (Ecog or LFP). The physiological state of the animals were carefully monitored through concentration of isoflurane, breathing rate and

oxygen saturation, based on previous data (Adelsberger et al., 2014; Schmid et al., 2016; Stroh et al., 2013) relating the conditions necessary to attain persistent up state. Since then it has become more evident that neuropil calcium activity within Layer II/III of the cortex represents an average of input from lower layers, in particular layer V (Kerr et al., 2005). In the case of these studies, we could screen the data relatively easily to determine if any of the recordings were done in slow wave state or if they were all performed in persistent up state as supposed.

A few parameters would be necessary to properly reanalyze datasets under the scope of slow waves or persistent up state.

The study should be in vivo. While there is information to be gained studying network bistability in vitro, in vivo datasets tend to be larger and include more physiological parameters to control for the anesthesia level itself for example. Ideally the study should include a type of mesoscale readout, this can be electrical LFP, EcoG, EEG or MEA. Or it can be optical like neuropil in the case of 2P recordings or using fiber photometry. Alternatively the activity state can be inferred from other parameters like pupillometry (Schwalm & Jubal, 2017), cortical temperature (Schwalm & Easton, 2016), breathing rate or anesthesia type and dosage. While those methods can be chosen when designing a study, they are less useful here given the large choice of better datasets available. The study should finally have datasets available, this final point is probably the most difficult since making published datasets freely available online when publishing is very recent and certainly not widespread enough. Only a few journals require authors to make the datasets available directly on the publisher's servers upon publication and most authors prefer simply adding a mention "datasets available upon request".

Parvalbumin interneurons show unexpected effects on local networks

Percept sharpening

Earlier studies of sensory activity using electrical recordings suggested that a certain basal level of activity could influence the detection of an input by drowning it in the ambient noise ((Isaacson & Scanziani, 2011). One of the roles of inhibition would then be to reduce the level of ambient activity to favorize the detection of an input. The balance between excitatory and inhibitory activity would then be an essential element of sensory processing in a noisy environment. This idea certainly holds some truth on a general cognitive level but suffers some criticisms on a neuronal level. The connectivity of a neuron is not random and long-term adaptation and learning has already pruned the unused pathways in an adult brain, as a result

each neuron should only receive relevant input. Single cell stimulation has shown that rats can consciously respond to stimulation of a single cortical neuron (Houweling & Brecht, 2008). If an extremely low level of signal is detectable would a coordinated sensory input be drowned in the same level of activity? Our data shows that PV interneurons tend to have the effect of inhibiting lateral barrels more than the principal one. This kind of lateral inhibition would be in theory useful to facilitate discrimination between neighboring whiskers. But if the thalamic input is coordinated one to one between individual whiskers and individual barrels, would it really be necessary? Another idea then would be that the processing provided by PV interneurons could provide coordinated reinforcement to strengthen synaptic weight in a coordinated manner, much like the climbing fibers of the cerebellum on Purkinje cells (Bosman et al., 2008). Reusing the same expression system during a discrimination learning task would provide an interesting answer to that question.

Other Interneuron populations

We saw in the introduction that there are a variety of interneurons in the cortex and that the morphology of the same genetically defined population can even vary depending on their position within the layered organization of the cortex. If we only concentrate on the upper layers of the sensory cortex VIP and SOM interneurons also have a role to play. They have been studied using similar approaches in the visual cortex (S. H. Lee et al., 2012). Those experiments showed that PV interneurons strongly affect the response amplitude while not affecting the direction selectivity of layer 2/3 pyramidal neurons. VIP and SOM interneurons did not affect the sharpness of the response. Given their connections on the dendritic tree these neurons might affect synaptic strength more than response selectivity. A recent study showed that during REM sleep these neuronal populations can decouple activity in the dendritic tree from somatic activity this finding could be one of the reasons for sensory-motor decoupling during sleep and potentially under anesthesia (Aime et al., 2022). This happens through central medial thalamic modulation of the fine balance between VIP and PV interneurons showing an implication in learning of aversive behavior. It would be extremely interesting to know if this dendritic decoupling appears under urethane anesthesia and more generally if our stimulation of PV interneurons induced a form of artificial decoupling that could alter sensory processing or memory.

Pathophysiological considerations epilepsy and schizophrenia

One situation where neuronal noise enters in consideration is in the case of schizophrenia. Schizophrenic patients have been showed to present unusually high levels of activity in their sensory and motor areas (Carment et al., 2020; Lindberg et al., 2016). This high activity seems to result in altered sensory processing with patients being less able to discriminate tactile stimuli for example. They have also been shown to present deficiencies in populations of parvalbumin interneurons (Beasley & Reynolds, 1997; Kaar et al., 2019). We disagreed earlier with the idea that a large field of inhibition like the one provided by parvalbumin interneurons would serve to sharpen sensory perception in healthy individuals. But the deficiency shown in schizophrenia indicates that a deficiency in this sort of blanket inhibition could alter sensory perception (Beasley & Reynolds, 1997; Kaar et al., 2019). This could in fact be a further indication that PV interneurons in the sensory Cortex are essential for percept discrimination. It would be interesting to know if lateral discrimination of stimuli in strongly somatotopic sensory regions like the sensory cortex of the fingers is affected in schizophrenic patients.

PV neurons and slow waves

In these experiments we showed the strong E/I change provided by PV interneurons and how this affects slow wave patterns under anesthesia. Do cortical PV interneurons directly control slow waves patterns in the brain? It seems highly improbable given the very strong effects shown by other regions. And the mostly non cortical origin of slow waves. However slow waves occurrence and frequency do seem to be highly related with PV activity and probably with the state of E/I balance. Our data shows that while they do not affect the occurrence of slow waves, they do affect the higher frequency components nested within. This decrease in high frequency component, because our recordings were within the cortex could be simply due to the strong decrease of action potentials evoked. Our collaborators in the Luhmann lab already studied the intracortical propagation of sensory evoked slow events under urethane anesthesia (Reyes-Puerta et al., 2016). This study showed a rapid and short activation of excitatory neurons in layer V of the principal column while the activity of excitatory neurons in the following columns and in layer IV of the principal one is more spread out. Interestingly the activity of inhibitory neurons is much more largely spread out in layer II/III and IV, it also appears only after a delay of about 20ms in the secondary barrels. This indicates that inhibitory neurons do not receive direct cross columnar thalamic input in slow wave state but mostly intracortical signal. Spike sequences are also led at 80% by excitatory neurons as expected from the

connectivity. These slow waves then tended to propagate vertically within a column before propagating from layer V to neighboring barrels. When applying our optogenetic stimulation of PV neurons given this information we would expect slow wave propagation to be only minimally affected since layer V excitatory neurons appear to be the main cross columnar propagators. Using our proposed protocol of limiting expression to layer II/III we would expect the initiation and propagation not to be affected. Reapplying this method of spatio-temporal spike sorting to our data could yield interesting information about the mechanisms of intracortical propagation of slow waves.

General modulation of slow waves

In natural sleep slow waves are a hallmark feature of NREM sleep and this is where they have been historically studied the most (Jaggard et al., 2021). It is already interesting that the slow wave state appears when under different kinds of anesthesia with potentially different mechanisms. NREM sleep is modulated through interactions between orexin neurons in the hypothalamus and sleep regulatory regions in the pons and midbrain. A major element of change in cortical state at the cortical level directly seems to be acetylcholine release from the basal forebrain diffusely throughout the cortex at the transition between NREM and REM or wake. This under the control of dorsal pontine cholinergic and glutamatergic regions such as the PPT/LDT, and the midbrain dopaminergic VTA.

Towards a better understanding of optogenetic modulation

The Kubelka-Munk equation to characterize light penetration in biological tissue is very crude, it depends only on a few parameters. The absorption coefficient of the tissue S_z , which itself is dependent on the wavelength. On this basis we add the diminution in power density due to the geometric spread of light. This approach is crude in that it doesn't account for diffraction inside the tissue. It also considers the tissue homogeneous and doesn't account for the presence of blood vessels or for different absorption coefficients of different tissue structures like layer I or layer IV for example. Studies of fiber photometry for biological applications show the collection field as rounded frustum (Maglie et al., 2019; Pisanello et al., 2019). The less well-defined shape of efficient optogenetic stimulation that we showed here and appeared in (Stroh et al., 2013) is probably due to the possibility of exciting passing axons and dendrites, potentially evoking action potentials in cells slightly outside the suprathreshold zone. This is still better than electrical stimulation as it is still limited by the expression pattern.

Our model proved reliable even when using an extremely basic model of light attenuation in biological tissue. Since then, some different approaches have been published.

Quantification of optogenetic stimulation in the olfactory bulb

While there is an emerging picture on the connectivity of newborn neurons in the OB (Bardy et al., 2010; Deshpande et al., 2013), the functional net impact of these connections on Mitral/Tufted (M/T) circuitry is not clear. An individual M/T cell receives inhibitory input from around 2000 granule cells (Lepousez & Lledo, 2013). Consequently, the removal of input from a few newborn GC to the M/T cells alone should rather results in a net disinhibition. The results of modulation (not shown here), however, showed a strong and consistent shortening of M/T response duration, and a reduction of the response magnitude. This suggests an indirect functional pathway. Moreover, despite the very low number of silenced neurons, almost the entire local microcircuit seems to be impacted. A previous elegant study using optogenetic activation of newborn neurons combined with electrophysiology (Bardy et al., 2010), suggests a functional inhibitory connection of newborn neurons with local interneurons such as short axon cells and external tufted cells. Together, the dominant functional impact of few newborn granule cells to local circuitry seems not to gain-control individual M/T cells, but rather to modulate the entire local microcircuit presumably via indirect pathways.

More comprehensive approaches

In recent years a few more physically inclined laboratories have investigated light spread in biological tissue and provided simulation tools to calculate light spread more realistically. These models mostly use monte-carlo simulations to evaluate diffraction. A final parameter to account for in these tools would be blood vessels. Blood vessels can account for a large surface of the illuminated brain tissue, most of the time the experimenter consciously avoids placing the fiber close to a surface blood vessel, but they can still produce shadows in the illuminated volume. One could use an image of the brain surface to evaluate the presence of blood vessels in the area in order to evaluate shadows in the illuminated volume. In the end however is a precise estimation of the number of cells stimulated very important when using broad field stimulations. By controlling the size and delimitation of the expression area upstream and checking for the surface expression before the experiment one can get an order of magnitude estimation of the number of cells quite easily. Moreover, the genetic targeting nature of optogenetics already allows a good degree of precision in the targeting of cellular population. A skilled experimenter

combined with a well-chosen genetic targeting strategy are enough most of the time. Putting large efforts and time into refining these tools would only be useful when using very specific techniques and in a laboratory using optogenetics only as a secondary tool, the same efforts can be put to much better use analyzing the data more in depth.

AAV virus and opsin delivery. Multiple experimental parameters impact the scope of optogenetic network activation: First AAV virus injections inherently result in varying infection rates per neuron due to a multiplicity of infection, leading to heterogeneity of opsin expression (Aschauer et al., 2013), this in turn affecting inhibitory photocurrents. However, while this adds jitter, it might create a less artificial pattern of inhibition. Approaches encoding regulatory elements resulting in more homogenous expression levels are currently not feasible due to the limited capacity of AAVs and furthermore require integration to a single site of the genome, in contrast to the episomal or extrachromosomal persistence of the AAVs used in this study. Second, the position of the fiber in relation to the opsin-expressing region will impact the area of above threshold illumination.

Third, while light penetration can be estimated by established models, the highly heterogeneous brain tissue specifically the highly light scattering and absorbent microvasculature can only be modeled up to a certain extent. Finally, for optical inhibition even more so than for excitation, efficient inhibition of action potentials depends on many physiological parameters like neuromodulation, the state of the animal, membrane resistance, and synaptic inputs. This inherently limits the accuracy of any approach assessing the scope of optogenetic network modulation.

Modeling of the optogenetic stimulation. From early on the optogenetic community explored and debated the spatial specificity of optogenetics (Aravanis et al., 2007). While initial studies employed the Kubelka-Munk model, assuming a conical spread, experimental data revealed that this approach largely underestimates the lateral spread (Stroh et al., 2013; Yizhar et al., 2011). Applying more complex modeling approaches based on Monte Carlo simulations led to rather ellipsoid geometries, better matching experimental data (Yizhar et al., 2011; Yona et al., 2016). It has to be noted that anyhow due to the aforementioned experimental variables, any assessment can only provide order-of-magnitude estimations. Using the Kubelka-Munk model of scattering in combination with a geometrical model and a histological assessment of cell densities represents a very straightforward way to estimate the number of cells potentially activated or inhibited by optogenetics. In the near future, the field of optogenetic interrogation of circuits has to move from rather mechanistic connectivity studies to approaches taking into

account the scope of optogenetic network modulation. A generalization of this practice in the field would be advisable, even more as network effects drastically depend on the architecture of the respective cortical circuits. A basic approach like this one could also be used before experiments in when targeting small regions to design a stimulation adapted to the question. Is the goal of the experiment a blanket excitation or inhibition on a large region or a more pinpoint effect on a few neurons in a specific layer. In a similar way to this work optetrode approaches might also give us a better insight into the extent of optogenetic manipulation by more clearly identifying single units affected by the light.

Prospective re-analysis of this data set

Effect of brain state on sensory activity

In this project we discovered an effect on PV interneurons modulation on brain states recorded in the cortex under anesthesia. We showed that PV interneuron activation decreases the occurrence of brain states and that their inhibition increases it. However this analysis was performed at the very end of the project and surprised us by its results. Urethane anesthesia resembles natural sleep in that recordings display different phases displaying different dominant frequencies (Reyes-Puerta et al., 2016; Reyes-Puerta, Sun, et al., 2015). In some of our recordings we observed slow waves states occurring during stimulation periods which could explain variability in our and older datasets. An interesting possibility would be to reclassify all data sets according to the brain state displayed in them and then look at the effect of each state on sensory stimulation. Is sensory stimulation affecting the occurrence and frequency of slow waves? How does sensory response change when the brain is in a slow wave state or in a persistent up state?

Impact on Power Spectra of Spontaneous and Evoked Activity

It would be interesting to perform optogenetic modulation of all relevant cortical cell types to explore their specific role in those state transitions. That is, especially in the case of urethane anesthesia in which anesthetic state switches without external intervention.

During NREM sleep high frequency oscillations called spindles are nested within the slow events. Our data seems to suggest that these spindles are partially suppressed by PV neurons. It would be interesting to see the impact of this modulation on cognitive function. Recent literature has also shown that regions of the sensory cortex can enter a local slow wave state (Funk et al., 2016) during REM sleep in layer IV and III allowing, according to the authors, a local sensory

network to disconnect from the cortical and subcortical network facilitating dreaming or memory consolidation (Aime et al., 2022; Oesch et al., 2020). The local excitatory inhibitory balance certainly has an implication in this phenomenon, and we showed here that PV interneurons could affect that local balance significantly enough to produce such an effect.

Direct evocation of up states within a brain state

In this work we used anesthesia to model a specific brain state in order to study the modulation of activity within persistent up state or slow wave state. How this activity relates to natural sleep and REM and NREM states is a complex discussion. The only current arguments other than the appearance of activity are about the effects of anesthesia on the two-process system of sleep debt. Propofol anesthesia reduces sleep debt accrued during sleep deprivation and sevoflurane reduces NREM but not REM sleep debt (Pal et al., 2011; Tung et al., 2004). The mechanisms of induction are however still relatively unknown, even though some common centers between anesthesia and sleep have been identified in the lateral hypothalamus and habenula (Gelegen et al., 2018; Jiang-Xie et al., 2019).

Within up-down states we concentrated on slow wave activity and tried to modulate it through different means. We repeated previous experiments showing that sensory stimulation can evoke slow waves directly. Some make the argument that slow waves are periods allowing for sensory decoupling of the network, but we showed again here that sensory stimuli can directly evoke them. Is it possible that sensory stimulation during NREM sleep evokes slow waves directly. In our study of the modulation provided by PV interneurons we were interested to see if lifting the inhibition provided by these neurons could allow for a direct evocation of up state. It did not, modulating PV interneuron's activity during slow wave state does not lead to a direct increase in slow waves upon lifting the inhibition.

Another study performed around the same time however showed that Parvalbumin interneurons have a clear implication in spindles. They showed an increased activity during spindles to the contrary of VIP interneurons (Niethard et al., 2018) and present two distinct subpopulations active early or late within cortical up states (Puig et al., 2008).

The nature of the fiber photometry signal

In our early studies using fiber photometry we considered it as a readout of suprathreshold neuronal activity while LFP is dominated by subthreshold activity. Considering the filtering parameters we used and the literature we can consider this to be true (Kajikawa et al., 2011).

Concerning the Calcium recordings, the question is slightly more complicated. Multiple papers in the early stages of fiber photometry make the argument that sufficient calcium only enters the cell to be detected when action potentials are evoked (Adelsberger et al., 2014; Grienberger et al., 2012; Stroh et al., 2013). When looking at transients within a cell body this is undeniably true. When looking at a volumetric average of calcium changes this should be discussed and further investigated. Our measurements of the neuropil signal relative to the signal in cell bodies indicates that a single cell body is simply too small and produces too little intensity to participate in the full field neuropil signal. It follows that extrapolating this finding to the volumetric fiber photometry recordings the signal observed must be dominated by an average of neuropil more than cell bodies. The situation could be different between chemical indicators and genetically encoded ones, however.

Chemical indicators like OGB1 or Fura are non-specific, they enter all compartments of most cells in the bolus injected region. Most importantly they enter into non-myelinated neurites passing through the region as has been nicely shown (Kerr et al., 2005), consequently the neuropil signal represents activity of cells whose cell body resides within the region but also activity of passing neurites. Like the previously cited paper shows, in the visual cortex it is then dominated by activity from layer V neurons projecting to layer II/III. This has been shown to also be the case in barrel cortex and we can assume that it is so in sensory cortices in general given their conserved structure. Fiber photometry represents an average of calcium changes in a oblong volume up to 400 μ m in front of the fiber. A single cell would represent quasi-insignificant proportion of such a volume. As a result, the transients we observe could be due to synchronized activity, but it can be locally synchronized activity or synchronized input.

This has been calculated in OGB-1 recordings using glutamate stimulation (Grienberger et al., 2012) showing that a minimum of 20 synchronized neurons are necessary to produce sufficient fluorescence change to be detected using fiber photometry. Because the signal detected from fiber photometry extends approximately 400 μ m in front of the fiber (Pisanello et al., 2019) this would be approximately 0.26 mm³ a volume that would contain approximately 28 000 neurons. The necessary proportion to evoke detectable activity is extremely small, because activity is still sparse in fiber photometry this is an indication that synchronized activity is rare in situations other than anesthesia, quiescence or sensory activation. In the recordings presented here were done under different anesthesia. This hypothesis would explain why single transients are quite hard to distinguish under desynchronized states like low isoflurane anesthesia or medetomidine.

The interpretation of the results must be different when using GECIs first of all the entirety of the signal recorded can be attributed to a genetically defined neuronal population. This is easier or harder to interpret depending on the prominence of the promoter used. In the data presented here we used camKII as a promoter, as a result all our signal comes from excitatory cells. When using classical AAVs 1-2-5 the expression is also limited to cell bodies close to the site of injection, these viruses do not induce expression retrogradely through the axons. These limitations already tell us that any signal we record is coming from the injected region specifically. The intensity of the signal produced by these sensors is also of higher magnitude than even the best chemical sensors so a single cell's signal can be more easily detected. The question remains however that which proportion of the signal is due to action potentials causing calcium entry and which part is due to subthreshold calcium changes in synapses and neurites. We can say that the amplitude of action potential evoked transients is very large compared to neurite transients but the question merits investigation. Optetrodes becoming more readily available might give us some answers by allowing us to correlate calcium signal with action potentials and with local field potentials. An interesting experiment would also be to combine fiber photometry in slices with single cell recordings and to evaluate the participation of single cells to the signal recorded with a fiber in a repetition of (Garaschuk, Milos, Grienberger, et al., 2006). Finally a recent study underlined the participation of the vasculature to the photometry signal (W.-T. Zhang et al., 2022) showed beautifully that hemoglobin does affect the signal from Gcamp by absorbing excitation and emitted light. The result is a negative deflection in the signal concurrent with the hemodynamic response.

Current limitations of GECIs

GECIs are a significant improvement in the specificity of calcium imaging. There is no question that their longevity and specificity are key factors in a longitudinal understanding of subpopulations in neural circuits. Their current limitations lie in the complex genetic makeup of neurons. In this work we considered only the separation between glutamatergic and GABAergic neurons first and then the genetic specificities of interneuron subpopulations. However there are functional differences within cells presenting similar molecular markers parvalbumin expressing interneurons, although all inhibitory and fast spiking can present vastly different patterns of activity upon stimulation (Helm et al., 2013) While this is currently difficult to address with the methods we have it is worth remembering so as not to over interpret the results.

Let us also remember that the relationship between calcium concentration and fluorescence is not linear in the case of GECIs due to the multiple binding sites for calcium. Intensity can be used as a readout of the intensity of activity, but comparisons can only be drawn within the same recording session. The contribution of signals from a variety of cells will make interpretation of results difficult, especially considering the functional heterogeneity of neuronal population when using general promoters like CamkII or Vgat.

A promising method to bypass the functional limitation could be the so-called TRAP method. By using immediate early genes like *cfos* to control the expression of an opsin or a GECI it is possible to express a protein of interest only in a functionally defined population. This technique potentially in combination with optogenetics could help record and manipulate precisely functionally defined subnetworks within a nucleus and on a brain-wide scale (CJ Guenther, K Miyamichi, HH Yang, HC Heller et al., 2013; Koutlas et al., 2022; Tasaka et al., 2018).

Another potentially underutilized possibility is rabies-mediated viral tracing. Normally used for tracing of presynaptic populations this can be used to express a sensor or an opsin in the presynaptic connectome of a nucleus. In the case of the barrel cortex here it could be interesting to trace the presynaptic connectome of PV interneurons in Layer v and II/III separately in a single barrel to investigate inter-layer and inter-barrel connectivity more in depth ((Reyes-Puerta, Kim, et al., 2015; Reyes-Puerta, Sun, et al., 2015)).

Genetically encoded neurotransmitter sensors

Very recently GPCRs modified with a c-terminal GFP have been developed by the team of Yulong Li. These modified receptors present GFP fluorescence upon binding of the endogenous receptor (Feng et al., 2019; Jing et al., 2018; F. Sun et al., 2018, 2020). These sensors have been successfully used in fiber photometry and two-photon imaging (Hasegawa et al., 2022). While presenting a weak SNR currently improvements in their molecular design are already being published, opening a vast array of possibilities to investigate circuits. It would now become possible to time the release of neurotransmitters to activity of the animal or in the studied network. In the context of brain state modulation this would be particularly useful to understand the potential cholinergic modulation of cortical activity under anesthesia, specifically during natural fluctuations of urethane anesthesia.

Closing statement

As I mentioned at the beginning of this work this project started in an empty laboratory with ample funding and a very innovative knowledge of optical techniques from Professor Stroh. We used significant amount of time to establish state of the art methodologies tailored to each individual study we aimed to perform. As with most projects, some experiments took unexpected turns and we discovered more items to improve as the projects progressed. The techniques we established and used remain innovative in the field. The technical knowledge we gained, including some unpublished findings, pushed our understanding of optical physiology a little bit further. Opto-fMRI is slowly leading to new perspectives on the nature of the hemodynamic response and the mechanisms of resting state fMRI. The new insights on the many uses of fiber photometry led us to further the understanding of anesthetic states and slow waves propagation, with possible implications in resting state and sleep studies. We also expanded the understanding of interneuron circuits in the barrel cortex, with general implications on cortical sensory processing. We hope the methodology of combining optogenetics with multichannel recordings will contribute to further the understanding of the function of specific cortical cell types. I hope that myself and others will be able to use this biological and technical knowledge to continue building a more integrated vision of the complex system that is the mammalian brain.

Thank you for your time reading my work.

APPENDIX

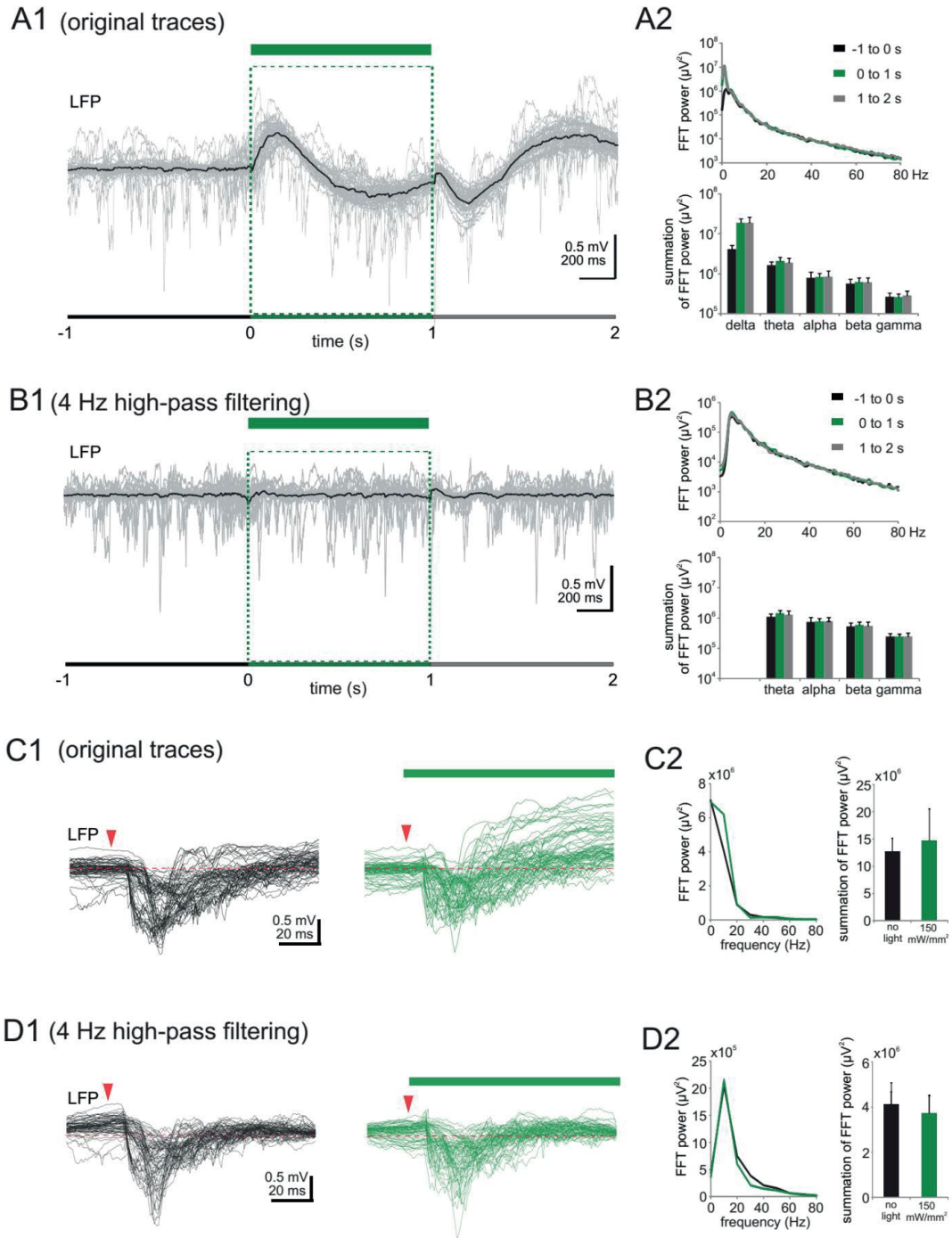


Figure 8-1. 4-Hz high-pass filtering eliminates light-induced artifacts in spontaneous and evoked LFP activity. (A1) Spontaneous LFP activity (original traces) recorded in deep layer II/III of principal shank before, during (green horizontal bar) and after green light pulse illumination. Fifty superimposed traces of 3 s duration were aligned according to the onset time of the light pulse (1 s duration, 150 mW/mm², every 10 s). Three periods were defined: before (-1 to 0 s), during (0 to 1 s) and after illumination (1 to 2 s). (A2) Upper panel: Fast Fourier transformation (FFT) of spontaneous LFP activity during the three periods (average of 5 non-ArchT-expressing PV-Cre mice). Lower panel: Bar diagram illustrating FFT power from delta to gamma band. Note the light-induced increase of FFT power in delta frequency

during and after light illumination. (B) Same data as in A after 4 Hz high-pass filtering applied to reduce the light induced artifact in FFT analysis. (C1) 80 superimposed traces ($n=8$, 3 C57BL/6 and 5 PV-Cre mice) of evoked LFP activity (original traces) recorded in deep layer II/III of the principal barrel column to single whisker stimulation under control condition (left, no light) and during light pulse illumination (right, 150 mW/mm^2). (C2) Left: Bar diagram illustrating slight but nonsignificant increase of FFT power during green light illumination (Wilcoxon signed-rank test, $n=8$ mice). Right: FFT of evoked LFP activity during no light (black line) and light on (green line) conditions (average of 8 mice). Note the increase of FFT power in the delta frequency band during light illumination. (D) Same data as in C after 4 Hz high-pass filtering applied to reduce the light-induced artifact in FFT analysis. (Fig from (J.-W. Yang et al., 2017 by permission with Oxford university press))

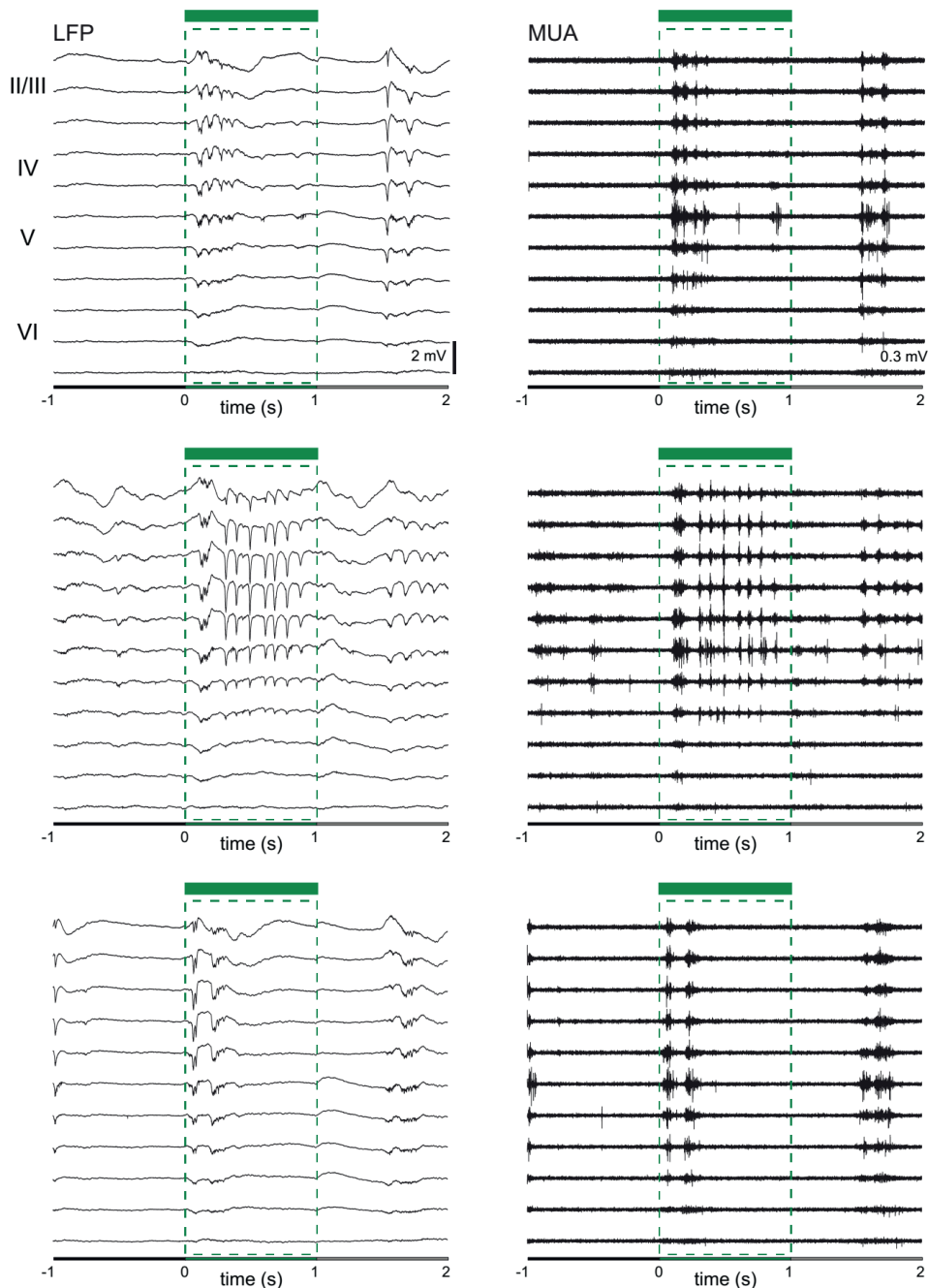


Figure 8-2. Layer representation of Induced slow oscillation during PV inactivation. Three representative induced slow oscillations from Fig. 3D1 show increase in LFP and MUA activity across all layers (Fig. from J.-W. Yang et al., 2017 by permission with Oxford university press)

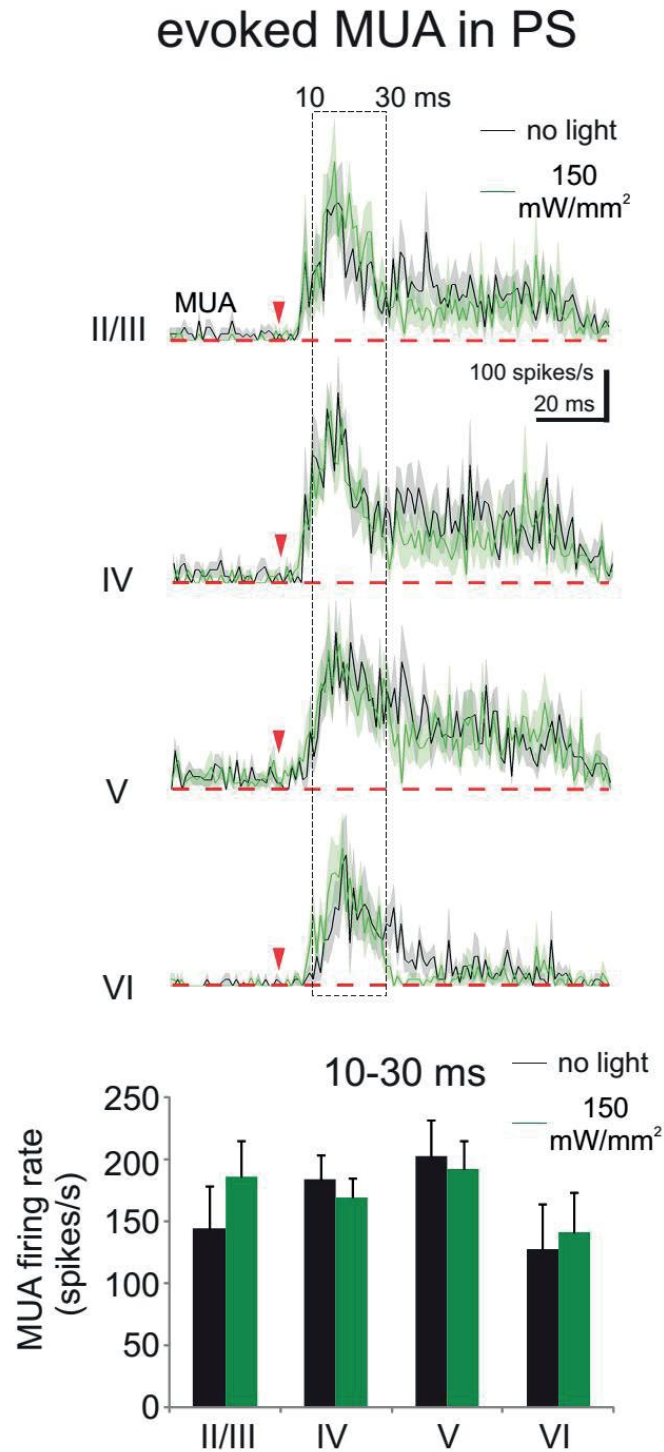


Figure 8-3. MUA activity upon optogenetic inhibition of PV interneurons does not differ between cortical layers in the principal shank. Upper panel: Average of evoked MUA in different layers of principal shank (PS) during control trials (black) and during optogenetic inhibition of PV neurons (green). The gray and light green shaded areas represent standard

errors. Lower panel: In all layers averaged MUA firing rate is not significantly different between control trials and optogenetic inhibition of PV neurons in the time window of 10 to 30 ms after whisker deflection (paired-t test, $n=8$ mice). (Fig from J.-W. Yang et al., 2017 by permission with Oxford university press)

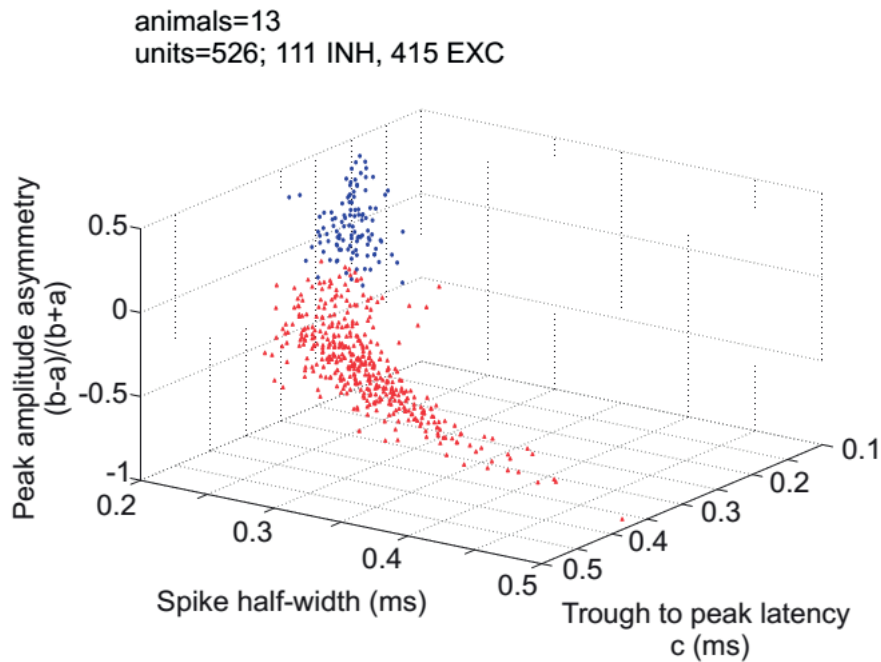


Figure 8-4. Analysis of spike-sorting data to identify putative inhibitory and excitatory neurons. Separation of putative INH ($n=111$) and EXC ($n=415$) neurons based on the three waveform parameters: spike half-width, trough-to-peak latency and peak amplitude asymmetry ($n=13$ mice). (Fig. from J.-W. Yang et al., 2017 by permission with Oxford university press)

References

- Adelsberger, H., Grienberger, C., Stroh, A., & Konnerth, A. (2014). In vivo calcium recordings and channelrhodopsin-2 activation through an optical fiber. *Cold Spring Harbor Protocols*, 2014(10), 1074–1079. <https://doi.org/10.1101/pdb.prot084145>
- Aime, M., Calcini, N., Borsa, M., Campelo, T., Rusterholz, T., Sattin, A., Fellin, T., & Adamantidis, A. (2022). Paradoxical somatodendritic decoupling supports cortical plasticity during REM sleep. *Science (New York, N.Y.)*, 376(6594), 724–730. <https://doi.org/10.1126/SCIENCE.ABK2734>
- Akintola, T., Raver, C., Studlack, P., Uddin, O., Masri, R., & Keller, A. (2017). The grimace scale reliably assesses chronic pain in a rodent model of trigeminal neuropathic pain. *Neurobiology of Pain*, 2, 13–17. <https://doi.org/10.1016/J.YNPAI.2017.10.001>
- Alagesan, K., Nunn, J. F., Feeley, T. W., & Heneghan, C. P. H. (1987). Comparison of the respiratory depressant effects of halothane and isoflurane in routine surgery. *British Journal of Anaesthesia*, 59(9), 1070–1079. <https://doi.org/10.1093/BJA/59.9.1070>
- Alkire, M. T., McReynolds, J. R., Hahn, E. L., & Trivedi, A. N. (2007). Thalamic Microinjection of Nicotine Reverses Sevoflurane-induced Loss of Righting Reflex in the Rat. *Anesthesiology*, 107(2), 264–272. <https://doi.org/10.1097/01.ANES.0000270741.33766.24>
- Alloway, K. D., Lou, L., Nwabueze-Ogbo, F., & Chakrabarti, S. (2006). Topography of cortical projections to the dorsolateral neostriatum in rats: Multiple overlapping sensorimotor pathways. *Journal of Comparative Neurology*, 499(1), 33–48. <https://doi.org/10.1002/CNE.21039>
- Alloway, K. D., Zhang, M., & Chakrabarti, S. (2004). Septal columns in rodent barrel cortex: Functional circuits for modulating whisking behavior. *Journal of Comparative Neurology*, 480(3), 299–309. <https://doi.org/10.1002/CNE.20339>
- Amiri, A., Karvandian, K., Ramezani, N., & Amiri, A. (2020). Short-term memory impairment in patients undergoing general anesthesia and its contributing factors. *Saudi Journal of Anaesthesia*, 14(4), 454. https://doi.org/10.4103/SJA.SJA_651_19

- Andermann, M. L., Gilfoy, N. B., Goldey, G. J., Sachdev, R. N. S., Wölfel, M., McCormick, D. A., Reid, R. C., & Levene, M. J. (2013). Chronic cellular imaging of entire cortical columns in awake mice using microprisms. *Neuron*, *80*(4), 900–913. <https://doi.org/10.1016/J.neuron.2013.07.052>
- Andermann, M. L., & Moore, C. I. (2006). A somatotopic map of vibrissa motion direction within a barrel column. *Nature Neuroscience*, *9*(4), 543–551. <https://doi.org/10.1038/NN1671>
- Anikeeva, P., Andalman, A. S., Witten, I., Warden, M., Goshen, I., Grosenick, L., Gunaydin, L. A., Frank, L. M., & Deisseroth, K. (2011). Optetrode: a multichannel readout for optogenetic control in freely moving mice. *Nature Neuroscience*, *15*(1), 163–170. <https://doi.org/10.1038/NN.2992>
- Aravanis, A. M., Wang, L. P., Zhang, F., Meltzer, L. A., Mogri, M. Z., Schneider, M. B., & Deisseroth, K. (2007). An optical neural interface: in vivo control of rodent motor cortex with integrated fiberoptic and optogenetic technology. *Journal of Neural Engineering*, *4*(3). <https://doi.org/10.1088/1741-2560/4/3/S02>
- Arce, E., Leland, D. S., Miller, D. A., Simmons, A. N., Winternheimer, K. C., & Paulus, M. P. (2006). Individuals with schizophrenia present hypo- and hyperactivation during implicit cueing in an inhibitory task. *NeuroImage*, *32*(2), 704–713. <https://doi.org/10.1016/J.NEUROIMAGE.2006.04.189>
- Arnoux, I., Willam, M., Griesche, N., Krummeich, J., Watari, H., Offermann, N., Weber, S., Dey, P. N., Chen, C., Monteiro, O., Buettner, S., Meyer, K., Bano, D., Radyushkin, K., Langston, R., Lambert, J. J., Wanker, E., Methner, A., Krauss, S., ... Stroh, A. (2018). Metformin reverses early cortical network dysfunction and behavior changes in Huntington's disease. *ELife*, *7*. <https://doi.org/10.7554/ELIFE.38744>
- Aschauer, D. F., Kreuz, S., & Rumpel, S. (2013). Analysis of Transduction Efficiency, Tropism and Axonal Transport of AAV Serotypes 1, 2, 5, 6, 8 and 9 in the Mouse Brain. *PLoS ONE*, *8*(9). <https://doi.org/10.1371/journal.pone.0076310>
- Ascoli, G. A., Alonso-Nanclares, L., Anderson, S. A., Barrionuevo, G., Benavides-Piccione, R., Burkhalter, A., Buzsáki, G., Cauli, B., DeFelipe, J., Fairén, A., Feldmeyer, D., Fishell, G., Fregnac, Y., Freund, T. F., Gardner, D., Gardner,

- E. P., Goldberg, J. H., Helmstaedter, M., Hestrin, S., ... Yuste, R. (2008). Petilla terminology: Nomenclature of features of GABAergic interneurons of the cerebral cortex. In *Nature Reviews Neuroscience* (Vol. 9, Issue 7, pp. 557–568). <https://doi.org/10.1038/nrn2402>
- Atallah, B. V., Bruns, W., Carandini, M., & Scanziani, M. (2012). Parvalbumin-expressing interneurons linearly transform cortical responses to visual stimuli. *Neuron*, 73(1), 159–170. <https://doi.org/10.1016/J.NEURON.2011.12.013>
- Baker, B. J., Kosmidis, E. K., Vucinic, D., Falk, C. X., Cohen, L. B., Djurisic, M., & Zecevic, D. (2005). Imaging brain activity with voltage- and calcium-sensitive dyes. *Cellular and Molecular Neurobiology*, 25(2), 245–282. <https://doi.org/10.1007/S10571-005-3059-6>
- Barbour, B. (2014). *Electronics for electrophysiologists*.
- Bardy, C., Alonso, M., Bouthour, W., & Lledo, P. M. (2010). How, When, and Where New Inhibitory Neurons Release Neurotransmitters in the Adult Olfactory Bulb. *Journal of Neuroscience*, 30(50), 17023–17034. <https://doi.org/10.1523/JNEUROSCI.4543-10.2010>
- Beasley, C. L., & Reynolds, G. P. (1997). Parvalbumin-immunoreactive neurons are reduced in the prefrontal cortex of schizophrenics. *Schizophr Res*, 24(3), 349–355. [https://doi.org/10.1016/s0920-9964\(96\)00122-3](https://doi.org/10.1016/s0920-9964(96)00122-3)
- Beninger, R. J., Wirsching, B. A., Jhamandas, K., Boegman, R. J., & el-Defrawy, S. R. (1986). Effects of altered cholinergic function on working and reference memory in the rat. *Canadian Journal of Physiology and Pharmacology*, 64(3), 376–382. <https://doi.org/10.1139/Y86-061>
- Bernardo, K. L., McCasland, J. S., Woolsey, T. A., & Strominger, R. N. (1990). Local intra- and interlaminar connections in mouse barrel cortex. *Journal of Comparative Neurology*, 291(2), 231–255. <https://doi.org/10.1002/CNE.902910207>
- Berndt, A., & Deisseroth, K. (2015). Expanding the optogenetics toolkit. In *Science* (Vol. 349, Issue 6248, pp. 590–591). American Association for the Advancement of Science. <https://doi.org/10.1126/science.aac7889>
- Berndt, A., Lee, S. Y., Wietek, J., Ramakrishnan, C., Steinberg, E. E., Rashid, A. J., Kim, H., Park, S., Santoro, A., Frankland, P. W., Iyer, S. M., Pak, S., Ährlund-Richter, S., Delp, S. L., Malenka, R. C., Josselyn, S. A., Carlén, M.,

- Hegemann, P., & Deisseroth, K. (2016). Structural foundations of optogenetics: Determinants of channelrhodopsin ion selectivity. *Proceedings of the National Academy of Sciences of the United States of America*, *113*(4), 822–829. <https://doi.org/10.1073/pnas.1523341113>
- Berndt, A., Schoenenberger, P., Mattis, J., Tye, K. M., Deisseroth, K., Hegemann, P., & Oertner, T. G. (2011). High-efficiency channelrhodopsins for fast neuronal stimulation at low light levels. *Proceedings of the National Academy of Sciences*, *108*(18), 7595–7600. <https://doi.org/10.1073/PNAS.1017210108>
- Berridge, M. J., Lipp, P., & Bootman, M. D. (2000). The versatility and universality of calcium signalling. *Nature Reviews Molecular Cell Biology* *2000 1:1*, *1*(1), 11–21. <https://doi.org/10.1038/35036035>
- Bevilacqua, F., Piguet, D., Marquet, P., Gross, J. D., Tromberg, B. J., & Depeursinge, C. (1999). In vivo local determination of tissue optical properties: applications to human brain. *Applied Optics*, *38*(22), 4939–4950. <https://doi.org/10.1364/AO.38.004939>
- Blits, B., Derks, S., Twisk, J., Ehlert, E., Prins, J., & Verhaagen, J. (2010). Adeno-associated viral vector (AAV)-mediated gene transfer in the red nucleus of the adult rat brain: Comparative analysis of the transduction properties of seven AAV serotypes and lentiviral vectors. *Journal of Neuroscience Methods*, *185*(2), 257–263. <https://doi.org/10.1016/j.jneumeth.2009.10.009>
- Boly, M., Moran, R., Murphy, M., Boveroux, P., Bruno, M. A., Noirhomme, Q., Ledoux, D., Bonhomme, V., Brichant, J. F., Tononi, G., Laureys, S., & Friston, K. (2012). Connectivity changes underlying spectral EEG changes during propofol-induced loss of consciousness. *Journal of Neuroscience*, *32*(20), 7082–7090. <https://doi.org/10.1523/JNEUROSCI.3769-11.2012>
- Borrell, V., Yoshimura, Y., & Callaway, E. M. (2005). Targeted gene delivery to telencephalic inhibitory neurons by directional in utero electroporation. *Journal of Neuroscience Methods*, *143*(2), 151–158. <https://doi.org/10.1016/J.JNEUMETH.2004.09.027>
- Bosman, L. W. J., Takechi, H., Hartmann, J., Eilers, J., & Konnerth, A. (2008). Homosynaptic long-term synaptic potentiation of the ‘winner’ climbing fiber synapse in developing Purkinje cells. *Journal of Neuroscience*, *28*(4), 798–807. <https://doi.org/10.1523/JNEUROSCI.4074-07.2008>

- Boyden, E. S., Zhang, F., Bamberg, E., Nagel, G., Deisseroth, K., ES, B., F, Z., E, B., G, N., & K, D. (2005). *Millisecond-timescale, genetically targeted optical control of neural activity*. 8(9), 1263–1268. <https://doi.org/10.1038/nm1525>
- Brown, A., Brown, S., Ellisor, D., Hagan, N., Normand, E., & Zervas, M. (2009). A Practical Approach to Genetic Inducible Fate Mapping: A Visual Guide to Mark and Track Cells In Vivo. *JoVE (Journal of Visualized Experiments)*, 34, e1687. <https://doi.org/10.3791/1687>
- Brown, E. B., Shear, J. B., Adams, S. R., Tsien, R. Y., & Webb, W. W. (1999). Photolysis of caged calcium in femtoliter volumes using two-photon excitation. *Biophysical Journal*, 76(1 I), 489–499. [https://doi.org/10.1016/S0006-3495\(99\)77217-6](https://doi.org/10.1016/S0006-3495(99)77217-6)
- Buehler, C., Kim, K. H., & So, P. T. C. (1999). High-speed, two-photon scanning microscope. *Applied Optics, Vol. 38, Issue 28, Pp. 6004-6009*, 38(28), 6004–6009. <https://doi.org/10.1364/AO.38.006004>
- Burger, C., Gorbatyuk, O. S., Velardo, M. J., Peden, C. S., Williams, P., Zolotukhin, S., Reier, P. J., Mandel, R. J., & Muzyczka, N. (2004). Recombinant AAV viral vectors pseudotyped with viral capsids from serotypes 1, 2, and 5 display differential efficiency and cell tropism after delivery to different regions of the central nervous system. *Molecular Therapy*, 10(2), 302–317. <https://doi.org/10.1016/j.ymthe.2004.05.024>
- Busche, M. A., Kekuš, M., Adelsberger, H., Noda, T., Förstl, H., Nelken, I., & Konnerth, A. (2015). Rescue of long-range circuit dysfunction in Alzheimer’s disease models. *Nature Neuroscience*, 18(11), 1623–1630. <https://doi.org/10.1038/nm.4137>
- Buzsáki, G. (2004). *Large-scale recording of neuronal ensembles*. 7(5), 446–451. <https://doi.org/10.1038/nm1233>
- Buzsáki, G., Anastassiou, C. A., & Koch, C. (2012). The origin of extracellular fields and currents--EEG, ECoG, LFP and spikes. *Nature Reviews. Neuroscience*, 13(6), 407–420. <https://doi.org/10.1038/NRN3241>
- Buzsáki, G., Stark, E., Berényi, A., Khodagholy, D., Kipke, D. R., Yoon, E., & Wise, K. D. (2015). Tools for probing local circuits: high-density silicon probes combined with optogenetics. *Neuron*, 86(1), 92. <https://doi.org/10.1016/J.NEURON.2015.01.028>

- Cardin, J. A., Carlén, M., Meletis, K., Knoblich, U., Zhang, F., Deisseroth, K., Tsai, L. H., & Moore, C. I. (2009). Driving fast-spiking cells induces gamma rhythm and controls sensory responses. *Nature*, *459*(7247), 663–667. <https://doi.org/10.1038/nature08002>
- Cardin, J. A., Carlén, M., Meletis, K., Knoblich, U., Zhang, F., Deisseroth, K., Tsai, L. H., & Moore, C. I. (2010). *Targeted optogenetic stimulation and recording of neurons in vivo using cell-type-specific expression of Channelrhodopsin-2*. *Neuron*, *65*(2), 247–254. <https://doi.org/10.1038/nprot.2009.228>
- Carment, L., Dupin, L., Guedj, L., Térémetz, M., Cuenca, M., Krebs, M. O., Amado, I., Maier, M. A., & Lindberg, P. G. (2020). Neural noise and cortical inhibition in schizophrenia. *Brain Stimulation*, *13*(5), 1298–1304. <https://doi.org/10.1016/J.BRS.2020.06.015>
- Carment, L., Dupin, L., Guedj, L., Térémetz, M., Krebs, M. O., Cuenca, M., Maier, M. A., Amado, I., & Lindberg, P. G. (2019). Impaired attentional modulation of sensorimotor control and cortical excitability in schizophrenia. *Brain*, *142*(7), 2149–2164. <https://doi.org/10.1093/BRAIN/AWZ127>
- Catania, K. C., & Kaas, J. H. (1997). Organization of somatosensory cortex and distribution of corticospinal neurons in the eastern mole (*Scalopus aquaticus*). *The Journal of Comparative Neurology*, *378*(3), 337–353. [https://doi.org/10.1002/\(sici\)1096-9861\(19970217\)378:3<337::aid-cne3>3.0.co;2-4](https://doi.org/10.1002/(sici)1096-9861(19970217)378:3<337::aid-cne3>3.0.co;2-4)
- Cauli, B., Porter, J. T., Tsuzuki, K., Lambolez, B., Rossier, J., Quenet, B., & Audinat, E. (2000). *Classification of fusiform neocortical interneurons based on unsupervised clustering*. *Neuron*, *27*(11), 6144–6149. <https://doi.org/10.1073/pnas.97.11.6144>
- Celio, M. R., & Heizmann, C. W. (1982). Calcium-binding protein parvalbumin is associated with fast contracting muscle fibres. *Nature* *1982* *297*:5866, *297*(5866), 504–506. <https://doi.org/10.1038/297504a0>
- Chagnac-Amitai, Y., & Connors, B. W. (1989). *Horizontal spread of synchronized activity in neocortex and its control by GABA-mediated inhibition*. *Neuron*, *3*(4), 747–758. <https://doi.org/10.1152/jn.1989.61.4.747>
- Chaigneau, E., Oheim, M., Audinat, E., & Charpak, S. (2003). Two-photon imaging of capillary blood flow in olfactory bulb glomeruli. *Proceedings of the National Academy of Sciences*, *100*(12), 7237–7242. <https://doi.org/10.1073/pnas.1200000100>

- the National Academy of Sciences of the United States of America*, 100(22), 13081. <https://doi.org/10.1073/PNAS.2133652100>
- Chakrabarti, S., & Alloway, K. D. (2006). Differential origin of projections from SI barrel cortex to the whisker representations in SII and MI. *Journal of Comparative Neurology*, 498(5), 624–636. <https://doi.org/10.1002/CNE.21052>
- Chang, C., Liu, Z., Chen, M. C., Liu, X., & Duyn, J. H. (2013). EEG correlates of time-varying BOLD functional connectivity. *NeuroImage*, 72, 227–236. <https://doi.org/10.1016/j.neuroimage.2013.01.049>
- Chauvette, S., Crochet, S., Volgushev, M., & Timofeev, I. (2011). Properties of slow oscillation during slow-wave sleep and anesthesia in cats. *Journal of Neuroscience*, 31(42), 14998–15008. <https://doi.org/10.1523/JNEUROSCI.2339-11.2011>
- Chen, J. L., Carta, S., Soldado-Magraner, J., Schneider, B. L., & Helmchen, F. (2013). Behaviour-dependent recruitment of long-range projection neurons in somatosensory cortex. *Nature* 2013 499:7458, 499(7458), 336–340. <https://doi.org/10.1038/nature12236>
- Chen, L., Guo, Q., & Li, J. Y. H. (2009). Transcription factor Gbx2 acts cell-nonautonomously to regulate the formation of lineage-restriction boundaries of the thalamus. *Development (Cambridge, England)*, 136(8), 1317. <https://doi.org/10.1242/DEV.030510>
- Chen, T. W., Wardill, T. J., Sun, Y., Pulver, S. R., Renninger, S. L., Baohan, A., Schreiter, E. R., Kerr, R. A., Orger, M. B., Jayaraman, V., Looger, L. L., Svoboda, K., & Kim, D. S. (2013). Ultrasensitive fluorescent proteins for imaging neuronal activity. *Nature*, 499(7458), 295–300. <https://doi.org/10.1038/nature12354>
- Chen, X., Rochefort, N. L., Sakmann, B., & Konnerth, A. (2013). Reactivation of the Same Synapses during Spontaneous Up States and Sensory Stimuli. *Cell Reports*, 4(1), 31–39. <https://doi.org/10.1016/j.celrep.2013.05.042>
- Cheng, J., Sahani, S., Hausrat, T. J., Yang, J. W., Ji, H., Schmarowski, N., Endle, H., Liu, X., Li, Y., Böttche, R., Radyushkin, K., Maric, H. M., Hoerder-Suabedissen, A., Molnár, Z., Prouvot, P. H., Trimbuch, T., Ninnemann, O., Huai, J., Fan, W., ... Vogt, J. (2016). Precise Somatotopic Thalamocortical

- Axon Guidance Depends on LPA-Mediated PRG-2/Radixin Signaling. *Neuron*, 92(1), 126–142. <https://doi.org/10.1016/J.NEURON.2016.08.035>
- Cho, A., Haruyama, N., & Kulkarni, A. B. (2009). Generation of Transgenic Mice. *Current Protocols in Cell Biology / Editorial Board, Juan S. Bonifacino ... [et Al.]*, CHAPTER(1), Unit. <https://doi.org/10.1002/0471143030.CB1911S42>
- CJ Guenther, K Miyamichi, HH Yang, HC Heller, L. L., Guenther, C. J., Miyamichi, K., Yang, H. H., Heller, H. C., & Luo, L. (2013). Permanent genetic access to transiently active neurons via TRAP: targeted recombination in active populations. *Neuron*, 78(5). <https://doi.org/10.1016/J.NEURON.2013.03.025>
- Clement, E. A., Richard, A., Thwaites, M., Ailon, J., Peters, S., & Dickson, C. T. (2008). Cyclic and Sleep-Like Spontaneous Alternations of Brain State Under Urethane Anaesthesia. *PLOS ONE*, 3(4), e2004. <https://doi.org/10.1371/JOURNAL.PONE.0002004>
- Clements, J. D., & Redman, S. J. (1989). Cable properties of cat spinal motoneurons measured by combining voltage clamp, current clamp and intracellular staining. *The Journal of Physiology*, 409(1), 63–87. <https://doi.org/10.1113/JPHYSIOL.1989.SP017485>
- Compte, A., Reig, R., Descalzo, V. F., Harvey, M. A., Puccini, G. D., & Sanchez-Vives, M. V. (2008). Spontaneous high-frequency (10-80 Hz) oscillations during up states in the cerebral cortex in vitro. *The Journal of Neuroscience : The Official Journal of the Society for Neuroscience*, 28(51), 13828–13844. <https://doi.org/10.1523/JNEUROSCI.2684-08.2008>
- Dale, N. C., Hoyer, D., Jacobson, L. H., Pflieger, K. D. G., & Johnstone, E. K. M. (2022). Orexin Signaling: A Complex, Multifaceted Process. *Frontiers in Cellular Neuroscience*, 16, 142. <https://doi.org/10.3389/FNCEL.2022.812359/XML/NLM>
- Dávid, C., Schleicher, A., Zuschratter, W., & Staiger, J. F. (2007). *The innervation of parvalbumin-containing interneurons by VIP-immunopositive interneurons in the primary somatosensory cortex of the adult rat.* 25(8), 2329–2340. <https://doi.org/10.1111/J.1460-9568.2007.05496.X>
- Davis, N., Lee, M., Lin, A. Y., Lynch, L., Monteleone, M., Falzon, L., Ispahany, N., & Lei, S. (2014). Post-operative cognitive function following general

- versus regional anesthesia, a systematic review. *Journal of Neurosurgical Anesthesiology*, 26(4), 369.
<https://doi.org/10.1097/ANA.0000000000000120>
- De Kock, C. P. J., Bruno, R. M., Spors, H., & Sakmann, B. (2007). Layer- and cell-type-specific suprathreshold stimulus representation in rat primary somatosensory cortex. *Journal of Physiology*, 581(1), 139–154.
<https://doi.org/10.1113/JPHYSIOL.2006.124321>
- Delpire, E., & Staley, K. J. (2014). Novel determinants of the neuronal Cl⁻ concentration. *The Journal of Physiology*, 592(Pt 19), 4099.
<https://doi.org/10.1113/JPHYSIOL.2014.275529>
- Deschênes, M., Timofeeva, E., Lavallée, P., & Dufresne, C. (2005). The vibrissal system as a model of thalamic operations. *Progress in Brain Research*, 149, 31–40. [https://doi.org/10.1016/S0079-6123\(05\)49003-2](https://doi.org/10.1016/S0079-6123(05)49003-2)
- Deshpande, A., Bergami, M., Ghanem, A., Conzelmann, K. K., Lepier, A., Götz, M., & Berninger, B. (2013). Retrograde monosynaptic tracing reveals the temporal evolution of inputs onto new neurons in the adult dentate gyrus and olfactory bulb. *Proceedings of the National Academy of Sciences of the United States of America*, 110(12). <https://doi.org/10.1073/PNAS.1218991110>
- Destexhe, A., Hughes, S. W., Rudolph, M., & Crunelli, V. (2007). Are corticothalamic ‘up’ states fragments of wakefulness? *Trends in Neurosciences*, 30(7), 334–342. <https://doi.org/10.1016/j.tins.2007.04.006>
- Devor, M., Zalkind, V., Fishman, Y., & Minert, A. (2016). Model of anaesthetic induction by unilateral intracerebral microinjection of GABAergic agonists. *European Journal of Neuroscience*, 43(6), 846–858.
<https://doi.org/10.1111/ejn.13186>
- Diester, I., Kaufman, M. T., Mogri, M., Pashaie, R., Goo, W., Yizhar, O., Ramakrishnan, C., Deisseroth, K., & Shenoy, K. V. (2011). An optogenetic toolbox designed for primates. *Nature Neuroscience*, 14(3), 387–397.
<https://doi.org/10.1038/nn.2749>
- Ding, L., Balsamo, G., Chen, H., Blanco-Hernandez, E., Zouridis, I. S., Naumann, R., Preston-Ferrer, P., & Burgalossi, A. (2022). Juxtacellular opto-tagging of hippocampal CA1 neurons in freely moving mice. *ELife*, 11.
<https://doi.org/10.7554/ELIFE.71720>

- Douglas, R. J., & Martin, K. A. (1991). A functional microcircuit for cat visual cortex. *The Journal of Physiology*, *440*(1), 735–769. <https://doi.org/10.1113/JPHYSIOL.1991.SP018733>
- Douglas, R. J., & Martin, K. A. C. (2004). Neuronal circuits of the neocortex. *Annual Review of Neuroscience*, *27*, 419–451. <https://doi.org/10.1146/ANNUREV.NEURO.27.070203.144152>
- Dumitriu, D., Cossart, R., Huang, J., & Yuste, R. (2007). Correlation between axonal morphologies and synaptic input kinetics of interneurons from mouse visual cortex. *Cerebral Cortex*, *17*(1), 81–91. <https://doi.org/10.1093/CERCOR/BHJ126>
- Egger, R., Schmitt, A. S., Wallace, D. J., Sakmann, B., Oberlaender, M., & Kerr, J. N. D. (2015). Robustness of sensory-evoked excitation is increased by inhibitory inputs to distal apical tuft dendrites. *Proceedings of the National Academy of Sciences of the United States of America*, *112*(45), 14072–14077. <https://doi.org/10.1073/PNAS.1518773112>
- El Mansari, M., Sakai, K., & Jouviet, M. (1990). Responses of presumed cholinergic mesopontine tegmental neurons to carbachol microinjections in freely moving cats. *Experimental Brain Research*, *83*(1), 115–123. <https://doi.org/10.1007/BF00232199>
- Ellis-Davies, G. C. R. (2019). Two-Photon Uncaging of Glutamate. *Frontiers in Synaptic Neuroscience*, *0*, 48. <https://doi.org/10.3389/FNSYN.2018.00048>
- Ellwardt, E., Pramanik, G., Luchtman, D., Novkovic, T., Jubal, E. R., Vogt, J., Arnoux, I., Vogelaar, C. F., Mandal, S., Schmalz, M., Barger, Z., de Azua, I. R., Kuhlmann, T., Lutz, B., Mittmann, T., Bittner, S., Zipp, F., & Stroh, A. (2018). Maladaptive cortical hyperactivity upon recovery from experimental autoimmune encephalomyelitis. *Nature Neuroscience* *2018 21:10*, *21*(10), 1392–1403. <https://doi.org/10.1038/s41593-018-0193-2>
- Eschenko, O., Mölle, M., Born, J., & Sara, S. J. (2006). Elevated sleep spindle density after learning or after retrieval in rats. *Journal of Neuroscience*, *26*(50), 12914–12920. <https://doi.org/10.1523/JNEUROSCI.3175-06.2006>
- Favre-Bulle, I. A., Preece, D., Nieminen, T. A., Heap, L. A., Scott, E. K., & Rubinsztein-Dunlop, H. (2015). Scattering of Sculpted Light in Intact Brain

- Tissue, with implications for Optogenetics. *Scientific Reports* 2015 5:1, 5(1), 1–9. <https://doi.org/10.1038/srep11501>
- Feldmeyer, D., Egger, V., Lübke, J., & Sakmann, B. (1999). Reliable synaptic connections between pairs of excitatory layer 4 neurones within a single ‘barrel’ of developing rat somatosensory cortex. *The Journal of Physiology*, 521(Pt 1), 169. <https://doi.org/10.1111/J.1469-7793.1999.00169.X>
- Feldmeyer, D., Lübke, J., & Sakmann, B. (2006). *Efficacy and connectivity of intracolumnar pairs of layer 2/3 pyramidal cells in the barrel cortex of juvenile rats*. 575(2), 583–602. <https://doi.org/10.1113/jphysiol.2006.105106>
- Feldmeyer, D., Lübke, J., Silver, R. A., & Sakmann, B. (2002). Synaptic connections between layer 4 spiny neurone- layer 2/3 pyramidal cell pairs in juvenile rat barrel cortex: physiology and anatomy of interlaminar signalling within a cortical column. *The Journal of Physiology*, 538(3), 803–822. <https://doi.org/10.1113/jphysiol.2001.012959>
- Feng, J., Zhang, C., Lischinsky, J. E., Jing, M., Zhou, J., Wang, H., Zhang, Y., Dong, A., Wu, Z., Wu, H., Chen, W., Zhang, P., Zou, J., Hires, S. A., Zhu, J. J., Cui, G., Lin, D., Du, J., & Li, Y. (2019). A Genetically Encoded Fluorescent Sensor for Rapid and Specific In Vivo Detection of Norepinephrine. *Neuron*, 102(4), 745-761.e8. <https://doi.org/10.1016/J.NEURON.2019.02.037>
- Fenko, L., Yizhar, O., & Deisseroth, K. (2011). The development and application of optogenetics. *Annual Review of Neuroscience*, 34, 389–412. <https://doi.org/10.1146/annurev-neuro-061010-113817>
- Field, K. J., & Lang, C. M. (1988). Hazards of urethane (ethyl carbamate): a review of the literature. *Laboratory Animals*, 22(3), 255–262. <https://doi.org/10.1258/002367788780746331>
- Fleischmann, T., Jirkof, P., Henke, J., Arras, M., & Cesarovic, N. (2016). Injection anaesthesia with fentanyl-midazolam-medetomidine in adult female mice: importance of antagonization and perioperative care. *Laboratory Animals*, 50(4), 264–274. <https://doi.org/10.1177/00236772166631458>
- Fois, C., Prouvot, P. H., & Stroh, A. (2014). A roadmap to applying optogenetics in neuroscience. *Methods in Molecular Biology (Clifton, N.J.)*, 1148, 129–147. https://doi.org/10.1007/978-1-4939-0470-9_9

- Fox, K., & Woolsey, T. (2008). Barrel Cortex. *Barrel Cortex*, 1–298. <https://doi.org/10.1017/CBO9780511541636>
- Frank, J. A., Antonini, M. J., Chiang, P. H., Canales, A., Konrad, D. B., Garwood, I. C., Rajic, G., Koehler, F., Fink, Y., & Anikeeva, P. (2020). In Vivo Photopharmacology Enabled by Multifunctional Fibers. *ACS Chemical Neuroscience*, 11(22), 3802–3813. <https://doi.org/10.1021/ACSCHEMNEURO.0C00577>
- Frenkel, M. Y., & Bear, M. F. (2004). How Monocular Deprivation Shifts Ocular Dominance in Visual Cortex of Young Mice. *Neuron*, 44(6), 917–923. <https://doi.org/10.1016/J.NEURON.2004.12.003>
- Fu, Y., Tucciarone, J. M., Espinosa, J. S., Sheng, N., Darcy, D. P., Nicoll, R. A., Huang, Z. J., & Stryker, M. P. (2014). A cortical circuit for gain control by behavioral state. *Cell*, 156(6), 1139–1152. <https://doi.org/10.1016/J.CELL.2014.01.050>
- Funk, C. M., Honjoh, S., Rodriguez, A. V., Cirelli, C., & Tononi, G. (2016). Local slow waves in superficial layers of primary cortical areas during REM sleep. *Current Biology : CB*, 26(3), 396. <https://doi.org/10.1016/J.CUB.2015.11.062>
- Galarreta, M., & Hestrin, S. (1999). A network of fast-spiking cells in the neocortex connected by electrical synapses. *Nature*, 402(6757), 72–75. <https://doi.org/10.1038/47029>
- Galarreta, M., & Hestrin, S. (2002). *Electrical and chemical synapses among parvalbumin fast-spiking GABAergic interneurons in adult mouse neocortex*. 99(19), 12438–12443. <https://doi.org/10.1073/pnas.192159599>
- Garaschuk, O., Milos, R. I., Grienberger, C., Marandi, N., Adelsberger, H., & Konnerth, A. (2006). Optical monitoring of brain function in vivo: From neurons to networks. *Pflugers Archiv European Journal of Physiology*, 453(3), 385–396. <https://doi.org/10.1007/S00424-006-0150-X/FIGURES/8>
- Garaschuk, O., Milos, R. I., & Konnerth, A. (2006). Targeted bulk-loading of fluorescent indicators for two-photon brain imaging in vivo. *Nature Protocols*, 1(1), 380–386. <https://doi.org/10.1038/nprot.2006.58>
- Gargiulo, S., Greco, A., Gramanzini, M., Esposito, S., Affuso, A., Brunetti, A., & Vesce, G. (2012). Mice Anesthesia, Analgesia, and Care, Part I: Anesthetic

- Considerations in Preclinical Research. *ILAR Journal*, 53(1), E55–E69.
<https://doi.org/10.1093/ILAR.53.1.55>
- Gelegen, C., Miracca, G., Ran, M. Z., Harding, E. C., Ye, Z., Yu, X., Tossell, K., Houston, C. M., Yustos, R., Hawkins, E. D., Vyssotski, A. L., Dong, H. L., Wisden, W., & Franks, N. P. (2018). Excitatory Pathways from the Lateral Habenula Enable Propofol-Induced Sedation. *Current Biology*, 28(4), 580–587.e5. <https://doi.org/10.1016/J.CUB.2017.12.050>
- Gentet, L. J. (2012). Functional diversity of supragranular GABAergic neurons in the barrel cortex. *Frontiers in Neural Circuits*, 0(AUGUST 2012), 52. <https://doi.org/10.3389/fncir.2012.00052>
- Gentet, L. J., Kremer, Y., Taniguchi, H., Huang, Z. J., Staiger, J. F., & Petersen, C. C. H. (2012). Unique functional properties of somatostatin-expressing GABAergic neurons in mouse barrel cortex. *Nature Neuroscience*, 15(4), 607–612. <https://doi.org/10.1038/NN.3051>
- Gentet, L. J., Stuart, G. J., & Clements, J. D. (2000). Direct Measurement of Specific Membrane Capacitance in Neurons. *Biophysical Journal*, 79(1), 314–320. [https://doi.org/10.1016/S0006-3495\(00\)76293-X](https://doi.org/10.1016/S0006-3495(00)76293-X)
- Gibson, J. R., Belerlein, M., & Connors, B. W. (1999). Two networks of electrically coupled inhibitory neurons in neocortex. *Nature*, 402(6757), 75–79. <https://doi.org/10.1038/47035>
- Gilbert, C. D., & Wiesel, T. N. (1983a). Clustered intrinsic connections in cat visual cortex. *Journal of Neuroscience*, 3(5), 1116–1133. <https://doi.org/10.1523/JNEUROSCI.03-05-01116.1983>
- Gilbert, C. D., & Wiesel, T. N. (1983b). Functional organization of the visual cortex. *Progress in Brain Research*, 58(C), 209–218. [https://doi.org/10.1016/S0079-6123\(08\)60022-9](https://doi.org/10.1016/S0079-6123(08)60022-9)
- Göppert-Mayer, M. (1931). Über Elementarakte mit zwei Quantensprüngen. *Annalen Der Physik*, 401(3), 273–294. <https://doi.org/10.1002/ANDP.19314010303>
- Gottlieb, J. P., & Keller, A. (1997). Intrinsic circuitry and physiological properties of pyramidal neurons in rat barrel cortex. *Experimental Brain Research*, 115(1), 47–60. <https://doi.org/10.1007/PL00005684>

- Govorunova, E. G., Sineshchekov, O. A., Janz, R., Liu, X., & Spudich, J. L. (2015). Natural light-gated anion channels: A family of microbial rhodopsins for advanced optogenetics. *Science*, *349*(6248), 647–650. <https://doi.org/10.1126/science.aaa7484>
- Grasshoff, C., & Antkowiak, B. (2006). Effects of isoflurane and enflurane on GABAA and glycine receptors contribute equally to depressant actions on spinal ventral horn neurones in rats. *British Journal of Anaesthesia*, *97*(5), 687–694. <https://doi.org/10.1093/BJA/AEL239>
- Grienberger, C., Adelsberger, H., Stroh, A., Milos, R. I., Garaschuk, O., Schierloh, A., Nelken, I., & Konnerth, A. (2012). Sound-evoked network calcium transients in mouse auditory cortex in vivo. *Journal of Physiology*, *590*(4), 899–918. <https://doi.org/10.1113/jphysiol.2011.222513>
- Grienberger, C., & Konnerth, A. (2012). Imaging Calcium in Neurons. In *Neuron* (Vol. 73, Issue 5, pp. 862–885). <https://doi.org/10.1016/j.neuron.2012.02.011>
- Grynkiewicz, G., Poenie, M., & Tsien, R. Y. (1985). THE JOURNAL OF BIOLOGICAL CHEMISTRY A New Generation of Ca²⁺ Indicators with Greatly Improved Fluorescence Properties*. *Journal of Biological Chemistry*, *260*(6), 3440–3450. [https://doi.org/10.1016/S0021-9258\(19\)83641-4](https://doi.org/10.1016/S0021-9258(19)83641-4)
- Hahn, T. T. G., Sakmann, B., & Mehta, M. R. (2006). Phase-locking of hippocampal interneurons' membrane potential to neocortical up-down states. *Nature Neuroscience*, *9*(11), 1359–1361. <https://doi.org/10.1038/nn1788>
- Hamill, O. P., Marty, A., Neher, E., Sakmann, B., & Sigworth, F. J. (1981). Improved patch-clamp techniques for high-resolution current recording from cells and cell-free membrane patches. *Pflügers Archiv : European Journal of Physiology*, *391*(2), 85–100. <https://doi.org/10.1007/BF00656997>
- Hamilton, D. L., & Abremski, K. (1984). Site-specific recombination by the bacteriophage P1 lox-Cre system. Cre-mediated synapsis of two lox sites. *Journal of Molecular Biology*, *178*(2), 481–486. [https://doi.org/10.1016/0022-2836\(84\)90154-2](https://doi.org/10.1016/0022-2836(84)90154-2)
- Han, X., Chow, B. Y., Zhou, H., Klapoetke, N. C., Chuong, A., Rajimehr, R., Yang, A., Baratta, M. V., Winkle, J., Desimone, R., & Boyden, E. S. (2011). A high-light sensitivity optical neural silencer: Development and application to

- optogenetic control of non-human primate cortex. *Frontiers in Systems Neuroscience*, 0(APRIL 2011), 18. <https://doi.org/10.3389/fnsys.2011.00018>
- Hara, K., & Harris, R. A. (2002). The anesthetic mechanism of urethane: The effects on neurotransmitter-gated ion channels. *Anesthesia and Analgesia*, 94(2), 313–318. <https://doi.org/10.1213/00000539-200202000-00015>
- Harris, K. D., Henze, D. A., Csicsvari, J., Hirase, H., & Buzsáki, G. (2000). Accuracy of tetrode spike separation as determined by simultaneous intracellular and extracellular measurements. *Journal of Neurophysiology*, 84(1), 401–414. <https://doi.org/10.1152/jn.2000.84.1.401>
- Harrison, T. C., Sigler, A., & Murphy, T. H. (2009). Simple and cost-effective hardware and software for functional brain mapping using intrinsic optical signal imaging. *Journal of Neuroscience Methods*, 182, 211–218. <https://doi.org/10.1016/j.jneumeth.2009.06.021>
- Hasegawa, E., Miyasaka, A., Sakurai, K., Cherasse, Y., Li, Y., & Sakurai, T. (2022). Rapid eye movement sleep is initiated by basolateral amygdala dopamine signaling in mice. *Science*, 375(6584), 994–1000. <https://doi.org/10.1126/SCIENCE.ABL6618>
- Hazan, L., Zugaro, M., & Buzsáki, G. (2006). Klusters, NeuroScope, NDManager: A free software suite for neurophysiological data processing and visualization. *Journal of Neuroscience Methods*, 155(2), 207–216. <https://doi.org/10.1016/j.jneumeth.2006.01.017>
- Helm, J., Akgul, G., & Wollmuth, L. P. (2013). Subgroups of parvalbumin-expressing interneurons in layers 2/3 of the visual cortex. *Journal of Neurophysiology*, 109(6), 1600–1613. <https://doi.org/10.1152/JN.00782.2012>
- Helmchen, F., Imoto, K., & Sakmann, B. (1996). Ca²⁺ buffering and action potential-evoked Ca²⁺ signaling in dendrites of pyramidal neurons. *Biophysical Journal*, 70(2 I), 1069–1081. [https://doi.org/10.1016/S0006-3495\(96\)79653-4](https://doi.org/10.1016/S0006-3495(96)79653-4)
- Helmstaedter, M., Sakmann, B., & Feldmeyer, D. (2009). Neuronal correlates of local, lateral, and translaminar inhibition with reference to cortical columns. *Cerebral Cortex*, 19(4), 926–937.

- Herreras, O. (2016). Local field potentials: Myths and misunderstandings. *Frontiers in Neural Circuits*, 10(DEC), 101. <https://doi.org/10.3389/FNCIR.2016.00101>
- Hiltunen, T., Kantola, J., Elseoud, A. A., Lepola, P., Suominen, K., Starck, T., Nikkinen, J., Remes, J., Tervonen, O., Palva, S., Kiviniemi, V., & Matias Palva, J. (2014). Infra-slow EEG fluctuations are correlated with resting-state network dynamics in fMRI. *Journal of Neuroscience*, 34(2), 356–362. <https://doi.org/10.1523/JNEUROSCI.0276-13.2014>
- Hodgkin, A. L., Huxley, A. F., & Katz, B. (1952). Measurement of current-voltage relations in the membrane of the giant axon of *Loligo*. *The Journal of Physiology*, 116(4), 424–448. <https://doi.org/10.1113/JPHYSIOL.1952.SP004716>
- Hoess, R., Wierzbicki, A., & Abremski, K. (1985). Formation of small circular DNA molecules via an in vitro site-specific recombination system. *Gene*, 40(2–3), 325–329. [https://doi.org/10.1016/0378-1119\(85\)90056-3](https://doi.org/10.1016/0378-1119(85)90056-3)
- Hoffmann, A., Hildebrandt, V., Heberle, J., & Büldt, G. (1994). Photoactive mitochondria: in vivo transfer of a light-driven proton pump into the inner mitochondrial membrane of *Schizosaccharomyces pombe*. *Proceedings of the National Academy of Sciences of the United States of America*, 91(20), 9367. <https://doi.org/10.1073/PNAS.91.20.9367>
- Horton, J. C., & Adams, D. L. (2005). The cortical column: a structure without a function. *Philosophical Transactions of the Royal Society B: Biological Sciences*, 360(1456), 837. <https://doi.org/10.1098/RSTB.2005.1623>
- Horton, N. G., Wang, K., Kobat, D., Clark, C. G., Wise, F. W., Schaffer, C. B., & Xu, C. (2013). In vivo three-photon microscopy of subcortical structures within an intact mouse brain. *Nature Photonics* 2013 7:3, 7(3), 205–209. <https://doi.org/10.1038/nphoton.2012.336>
- Houweling, A. R., & Brecht, M. (2008). Behavioural report of single neuron stimulation in somatosensory cortex. *Nature*, 451(7174), 65–68. <https://doi.org/10.1038/NATURE06447>
- Hu, H., Gan, J., & Jonas, P. (2014). Fast-spiking, parvalbumin+ GABAergic interneurons: From cellular design to microcircuit function. *Science*, 345(6196). <https://doi.org/10.1126/science.1255263>

- Huber, R., Ghilardi, M. F., Massimini, M., & Tononi, G. (2004). Local sleep and learning. *Nature*, *430*(6995), 78–81. <https://doi.org/10.1038/nature02663>
- Husson, S. J., Liewald, J. F., Schultheis, C., Stirman, J. N., Lu, H., & Gottschalk, A. (2012). Microbial Light-Activatable Proton Pumps as Neuronal Inhibitors to Functionally Dissect Neuronal Networks in *C. elegans*. *PLOS ONE*, *7*(7), e40937. <https://doi.org/10.1371/JOURNAL.PONE.0040937>
- IARC Working Group on the Evaluation of Carcinogenic Risks to Humans., & International Agency for Research on Cancer. (2010). *Alcohol Consumption and Ethyl Carbamate* (Vol. 96). International Agency for Research on Cancer.
- Isaacson, J. S., & Scanziani, M. (2011). How Inhibition Shapes Cortical Activity. *Neuron*, *72*(2), 231–243. <https://doi.org/10.1016/J.NEURON.2011.09.027>
- Jaggard, J. B., Wang, G. X., & Mourrain, P. (2021). Non-REM and REM/paradoxical sleep dynamics across phylogeny. *Current Opinion in Neurobiology*, *71*, 44–51. <https://doi.org/10.1016/J.CONB.2021.08.004>
- Jensen, O., Spaak, E., & Zumer, J. M. (2014). Human Brain Oscillations: From Physiological Mechanisms to Analysis and Cognition. *Magnetoencephalography: From Signals to Dynamic Cortical Networks*, *9783642330452*, 359–403. https://doi.org/10.1007/978-3-642-33045-2_17
- Jercog, D., Roxin, A., Barthó, P., Luczak, A., Compte, A., & De La Rocha, J. (2017). UP-DOWN cortical dynamics reflect state transitions in a bistable network. *ELife*, *6*. <https://doi.org/10.7554/eLife.22425>
- Ji, D., & Wilson, M. A. (2007). Coordinated memory replay in the visual cortex and hippocampus during sleep. *Nature Neuroscience*, *10*(1), 100–107. <https://doi.org/10.1038/nn1825>
- Jiang, X., Shen, S., Cadwell, C. R., Berens, P., Sinz, F., Ecker, A. S., Patel, S., & Tolias, A. S. (2015). Principles of connectivity among morphologically defined cell types in adult neocortex. *Science*, *350*(6264), aac9462–aac9462. <https://doi.org/10.1126/science.aac9462>
- Jiang-Xie, L. F., Yin, L., Zhao, S., Prevosto, V., Han, B. X., Dzirasa, K., & Wang, F. (2019). A Common Neuroendocrine Substrate for Diverse General Anesthetics and Sleep. *Neuron*, *102*(5), 1053–1065.e4. <https://doi.org/10.1016/J.NEURON.2019.03.033>

- Jing, M., Zhang, P., Wang, G., Feng, J., Mesik, L., Zeng, J., Jiang, H., Wang, S., Looby, J. C., Guagliardo, N. A., Langma, L. W., Lu, J., Zuo, Y., Talmage, D. A., Role, L. W., Barrett, P. Q., Zhang, L. I., Luo, M., Song, Y., ... Li, Y. (2018). A genetically encoded fluorescent acetylcholine indicator for in vitro and in vivo studies. *Nature Biotechnology* 2018 36:8, 36(8), 726–737. <https://doi.org/10.1038/nbt.4184>
- Jordan, R. (2021). Optimized protocol for in vivo whole-cell recordings in head-fixed, awake behaving mice. *STAR Protocols*, 2(1), 100347. <https://doi.org/10.1016/J.XPRO.2021.100347>
- Jouvet, M. (1965). Paradoxical Sleep — A Study of its Nature and Mechanisms. *Progress in Brain Research*, 18(C), 20–62. [https://doi.org/10.1016/S0079-6123\(08\)63582-7](https://doi.org/10.1016/S0079-6123(08)63582-7)
- Juczewski, K., Koussa, J. A., Kesner, A. J., Lee, J. O., & Lovinger, D. M. (2020). Stress and behavioral correlates in the head-fixed method: stress measurements, habituation dynamics, locomotion, and motor-skill learning in mice. *Scientific Reports* 2020 10:1, 10(1), 1–19. <https://doi.org/10.1038/s41598-020-69132-6>
- Kaar, S. J., Angelescu, I., Marques, T. R., & Howes, O. D. (2019). Pre-frontal parvalbumin interneurons in schizophrenia: a meta-analysis of post-mortem studies. *Journal of Neural Transmission*, 126(12), 1637–1651. <https://doi.org/10.1007/S00702-019-02080-2/FIGURES/3>
- Kaas, J. H. (2009). Evolution of the Somatosensory System in Mammals. *Encyclopedia of Neuroscience*, 1416–1419. https://doi.org/10.1007/978-3-540-29678-2_3169
- Kajikawa, Y., Schroeder, C. E., & Y Kajikawa, C. S. (2011). How local is the local field potential? *Neuron*, 72(5), 847–858. <https://doi.org/10.1016/j.neuron.2011.09.029>
- Kandori, H. (2015). Ion-pumping microbial rhodopsins. *Frontiers in Molecular Biosciences*, 2(SEP), 52. <https://doi.org/10.3389/FMOLB.2015.00052/BIBTEX>
- Kantevari, S., Hoang, C. J., Ogrodnik, J., Egger, M., Niggli, E., & Ellis-Davies, G. C. R. (2006). Synthesis and two-photon photolysis of 6-(ortho-nitroveratryl)-

- caged IP3 in living cells. *ChemBioChem*, 7(1), 174–180.
<https://doi.org/10.1002/CBIC.200500345>
- Kaplan, J. H., & Ellis-Davies, G. C. (1988). Photolabile chelators for the rapid photorelease of divalent cations. *Proceedings of the National Academy of Sciences of the United States of America*, 85(17), 6571.
<https://doi.org/10.1073/PNAS.85.17.6571>
- Karalis, N., & Sirota, A. (2022). Breathing coordinates cortico-hippocampal dynamics in mice during offline states. *Nature Communications*, 13(1).
<https://doi.org/10.1038/S41467-022-28090-5>
- Karami, P., Nasrollahzadeh, N., Wyss, C., O’Sullivan, A., Broome, M., Procter, P., Bourban, P. E., Moser, C., & Pioletti, D. P. (2021). An Intrinsically-Adhesive Family of Injectable and Photo-Curable Hydrogels with Functional Physicochemical Performance for Regenerative Medicine. *Macromolecular Rapid Communications*, 42(10), 2000660.
<https://doi.org/10.1002/MARC.202000660>
- Kawaguchi, Y., & Kubota, Y. (1997). GABAergic cell subtypes and their synaptic connections in rat frontal cortex. *Cerebral Cortex*, 7(6), 476–486.
<https://doi.org/10.1093/CERCOR/7.6.476>
- Kelz, M. B., Sun, Y., Chen, J., Qing, C. M., Moore, J. T., Veasey, S. C., Dixon, S., Thornton, M., Funato, H., & Yanagisawa, M. (2008). An essential role for orexins in emergence from general anesthesia. *Proceedings of the National Academy of Sciences of the United States of America*, 105(4), 1309–1314.
<https://doi.org/10.1073/pnas.0707146105>
- Kemp, B., & Oliven, J. (2003). European data format ‘plus’ (EDF+), an EDF alike standard format for the exchange of physiological data. *Clinical Neurophysiology : Official Journal of the International Federation of Clinical Neurophysiology*, 114(9), 1755–1761. [https://doi.org/10.1016/S1388-2457\(03\)00123-8](https://doi.org/10.1016/S1388-2457(03)00123-8)
- Kemp, B., Värri, A., Rosa, A. C., Nielsen, K. D., & Gade, J. (1992). A simple format for exchange of digitized polygraphic recordings. *Electroencephalography and Clinical Neurophysiology*, 82(5), 391–393.
[https://doi.org/10.1016/0013-4694\(92\)90009-7](https://doi.org/10.1016/0013-4694(92)90009-7)

- Kerr, J. N. D., De Kock, C. P. J., Greenberg, D. S., Bruno, R. M., Sakmann, B., & Helmchen, F. (2007). Spatial organization of neuronal population responses in layer 2/3 of rat barrel cortex. *Journal of Neuroscience*, *27*(48), 13316–13328. <https://doi.org/10.1523/JNEUROSCI.2210-07.2007>
- Kerr, J. N. D., Greenberg, D., & Helmchen, F. (2005). Imaging input and output of neocortical networks in vivo. *Proceedings of the National Academy of Sciences of the United States of America*, *102*(39), 14063–14068.
- Kerr, J. N. D., & Plenz, D. (2004). Action Potential Timing Determines Dendritic Calcium during Striatal Up-States. *Journal of Neuroscience*, *24*(4), 877–885. <https://doi.org/10.1523/JNEUROSCI.4475-03.2004>
- Killackey, H. P. (1973). Anatomical evidence for cortical subdivisions based on vertically discrete thalamic projections from the ventral posterior nucleus to cortical barrels in the rat. *Brain Research*, *51*(C), 326–331. [https://doi.org/10.1016/0006-8993\(73\)90383-1](https://doi.org/10.1016/0006-8993(73)90383-1)
- Klausberger, T., Marton, L. F., O’Neill, J., Huck, J. H. J., Dalezios, Y., Fuentealba, P., Suen, W. Y., Papp, E., Kaneko, T., Watanabe, M., Csicsvari, J., & Somogyi, P. (2005). Complementary Roles of Cholecystinin- and Parvalbumin-Expressing GABAergic Neurons in Hippocampal Network Oscillations. *The Journal of Neuroscience*, *25*(42), 9782. <https://doi.org/10.1523/JNEUROSCI.3269-05.2005>
- Kodandaramaiah, S. B., Franzesi, G. T., Chow, B. Y., Boyden, E. S., & Forest, C. R. (2012). Automated whole-cell patch-clamp electrophysiology of neurons in vivo. *Nature Methods* *2012* *9*:6, *9*(6), 585–587. <https://doi.org/10.1038/nmeth.1993>
- Komarov, M., Malerba, P., Golden, R., Nunez, P., Halgren, E., & Bazhenov, M. (2019). Selective recruitment of cortical neurons by electrical stimulation. *PLOS Computational Biology*, *15*(8), e1007277. <https://doi.org/10.1371/JOURNAL.PCBI.1007277>
- Kondo, S., Yoshida, T., & Ohki, K. (2016). Mixed functional microarchitectures for orientation selectivity in the mouse primary visual cortex. *Nature Communications* *2016* *7*:1, *7*(1), 1–16. <https://doi.org/10.1038/ncomms13210>
- Kosaka, T., & Heizmann, C. W. (1989). Selective staining of a population of parvalbumin-containing GABAergic neurons in the rat cerebral cortex by

- lectins with specific affinity for terminal N-acetylgalactosamine. *Brain Research*, 483(1), 158–163. [https://doi.org/10.1016/0006-8993\(89\)90048-6](https://doi.org/10.1016/0006-8993(89)90048-6)
- Koutlas, I., Linders, L. E., van der Starre, S. E., Wolterink-Donselaar, I. G., Adan, R. A. H., & Meye, F. J. (2022). Characterizing and TRAPing a Social Stress-Activated Neuronal Ensemble in the Ventral Tegmental Area. *Frontiers in Behavioral Neuroscience*, 0, 280. <https://doi.org/10.3389/FNBEH.2022.936087>
- Kremer, Y., Léger, J.-F. F., Goodman, D., Brette, R., & Bourdieu, L. (2011). *Late Emergence of the Vibrissa Direction Selectivity Map in the Rat Barrel Cortex*. 31(29). <https://doi.org/10.1523/JNEUROSCI.6541-10.2011>
- Kremer, Y., Léger, J.-F., Lapole, R., Honnorat, N., Candela, Y., Dieudonné, S., Bourdieu, L., Li, D. R., Zeng, S. Q., Lv, X. H., Liu, J., Du, R., Jiang, R. H., Chen, W. R., Luo, Q. M., Zeng, S., Li, D., Lv, X., & Luo, Q. (2008). A spatio-temporally compensated acousto-optic scanner for two-photon microscopy providing large field of view. *Optics Express*, Vol. 16, Issue 14, Pp. 10066-10076, 16(14), 10066–10076. <https://doi.org/10.1364/OE.16.010066>
- Krupa, D. J., Brisben, A. J., & Nicolelis, M. A. L. (2001). A multi-channel whisker stimulator for producing spatiotemporally complex tactile stimuli. *Journal of Neuroscience Methods*, 104(2), 199–208. [https://doi.org/10.1016/S0165-0270\(00\)00345-9](https://doi.org/10.1016/S0165-0270(00)00345-9)
- Kubota, Y. (2014). Untangling GABAergic wiring in the cortical microcircuit. In *Current Opinion in Neurobiology* (Vol. 26, pp. 7–14). <https://doi.org/10.1016/j.conb.2013.10.003>
- Kuhne, J., Vierock, J., Tennigkeit, S. A., Dreier, M. A., Wietek, J., Petersen, D., Gavriljuk, K., El-Mashtoly, S. F., Hegemann, P., & Gerwert, K. (2019). Unifying photocycle model for light adaptation and temporal evolution of cation conductance in channelrhodopsin-2. *Proceedings of the National Academy of Sciences of the United States of America*, 116(19), 9380–9389. <https://doi.org/10.1073/PNAS.1818707116>
- Langevin, L. M., Mattar, P., Scardigli, R., Roussigné, M., Logan, C., Blader, P., & Schuurmans, C. (2007). Validating in utero electroporation for the rapid analysis of gene regulatory elements in the murine telencephalon. *Developmental Dynamics: An Official Publication of the American*

- Association of Anatomists*, 236(5), 1273–1286.
<https://doi.org/10.1002/DVDY.21126>
- Laxpati, N. G., Mahmoudi, B., Gutekunst, C. A., Newman, J. P., Zeller-Townson, R., & Gross, R. E. (2014). Real-time in vivo optogenetic neuromodulation and multielectrode electrophysiologic recording with neurorighter. *Frontiers in Neuroengineering*, 7(October). <https://doi.org/10.3389/fneng.2014.00040>
- Lee, S. H., & Dan, Y. (2012). Neuromodulation of Brain States. *Neuron*, 76(1), 209–222. <https://doi.org/10.1016/J.NEURON.2012.09.012>
- Lee, S. H., Kwan, A. C., Zhang, S., Phoumthippavong, V., Flannery, J. G., Masmanidis, S. C., Taniguchi, H., Huang, Z. J., Zhang, F., Boyden, E. S., Deisseroth, K., & Dan, Y. (2012). Activation of specific interneurons improves V1 feature selectivity and visual perception. *Nature* 2012 488:7411, 488(7411), 379–383. <https://doi.org/10.1038/nature11312>
- Lee, S., Kruglikov, I., Huang, Z. J., Fishell, G., & Rudy, B. (2013). *A disinhibitory circuit mediates motor integration in the somatosensory cortex*. 16(11). <https://doi.org/10.1038/NN.3544>
- Lee Weller, W. (1972). Barrels in somatic sensory neocortex of the marsupial *Trichosurus vulpecula* (brush-tailed possum). *Brain Research*, 43(1), 11–24. [https://doi.org/10.1016/0006-8993\(72\)90271-5](https://doi.org/10.1016/0006-8993(72)90271-5)
- Lee, Y., Canales, A., Loke, G., Kanik, M., Fink, Y., & Anikeeva, P. (2020). Selectively Micro-Patternable Fibers via In-Fiber Photolithography. *ACS Central Science*, 6(12), 2319–2325. <https://doi.org/10.1021/ACSCENTSCI.0C01188>
- Lefort, S., Tamm, C., Floyd Sarria, J. C., & Petersen, C. C. H. (2009). The Excitatory Neuronal Network of the C2 Barrel Column in Mouse Primary Somatosensory Cortex. *Neuron*, 61(2), 301–316. <https://doi.org/10.1016/j.neuron.2008.12.020>
- Leong, A. T. L., Chan, R. W., Gao, P. P., Chan, Y. S., Tsia, K. K., Yung, W. H., & Wu, E. X. (2016). Long-range projections coordinate distributed brain-wide neural activity with a specific spatiotemporal profile. *Proceedings of the National Academy of Sciences of the United States of America*, 113(51), E8306–E8315. <https://doi.org/10.1073/pnas.1616361113>

- Lepousez, G., & Lledo, P. M. (2013). Odor discrimination requires proper olfactory fast oscillations in awake mice. *Neuron*, *80*(4), 1010–1024. <https://doi.org/10.1016/J.NEURON.2013.07.025>
- Levin-Arama, M., Abraham, L., Waner, T., Harmelin, A., Steinberg, D. M., Lahav, T., & Harlev, M. (2016). Subcutaneous Compared with Intraperitoneal Ketamine–Xylazine for Anesthesia of Mice. *Journal of the American Association for Laboratory Animal Science: JAALAS*, *55*(6), 794. [/pmc/articles/PMC5113882/](https://pubmed.ncbi.nlm.nih.gov/27113882/)
- Li, L. Y., Ji, X. Y., Liang, F., Li, Y. T., Xiao, Z., Tao, H. W., & Zhang, L. I. (2014). A Feedforward Inhibitory Circuit Mediates Lateral Refinement of Sensory Representation in Upper Layer 2/3 of Mouse Primary Auditory Cortex. *Journal of Neuroscience*, *34*(41), 13670–13683. <https://doi.org/10.1523/JNEUROSCI.1516-14.2014>
- Lindberg, P. G., Térémetz, M., Charron, S., Kebir, O., Saby, A., Bendjemaa, N., Lion, S., Crépon, B., Gaillard, R., Oppenheim, C., Krebs, M. O., & Amado, I. (2016). Altered cortical processing of motor inhibition in schizophrenia. *Cortex*, *85*, 1–12. <https://doi.org/10.1016/J.CORTEX.2016.09.019>
- Lissek, T., Obenhaus, H. A., Ditzel, D. A. W., Nagai, T., Miyawaki, A., Sprengel, R., & Hasan, M. T. (2016). General anesthetic conditions induce network synchrony and disrupt sensory processing in the cortex. *Frontiers in Cellular Neuroscience*, *10*(APR). <https://doi.org/10.3389/fncel.2016.00064>
- Logothetis, N. K., Eschenko, O., Murayama, Y., Augath, M., Steudel, T., Evrard, H. C., Besserve, M., & Oeltermann, A. (2012). Hippocampal-cortical interaction during periods of subcortical silence. *Nature*, *491*(7425), 547–553. <https://doi.org/10.1038/nature11618>
- Lu, J., Nelson, L. E., Franks, N., Maze, M., Chamberlin, N. L., & Saper, C. B. (2008). Role of endogenous sleep-wake and analgesic systems in anesthesia. *Journal of Comparative Neurology*, *508*(4), 648–662. <https://doi.org/10.1002/cne.21685>
- Luppi, P. H., Clément, O., & Fort, P. (2013). Paradoxical (REM) sleep genesis by the brainstem is under hypothalamic control. *Current Opinion in Neurobiology*, *23*(5), 786–792. <https://doi.org/10.1016/J.CONB.2013.02.006>

- MA Busche, A. K. (2015). Neuronal hyperactivity—A key defect in Alzheimer’s disease? *BioEssays*, 37, 624–632. <https://doi.org/10.1002/bies.201500004>
- Maggi, C. A., & Meli, A. (1986). Suitability of urethane anesthesia for physiopharmacological investigations in various systems. Part 1: General considerations. *Experientia*, 42(2), 109–114. <https://doi.org/10.1007/BF01952426>
- Maglie, E., Pisanello, M., Pisano, F., Balena, A., Spagnolo, B., Sabatini, B. L., De Vittorio, M., & Pisanello, F. (2019). Modeling brain tissue scattering for optical neural interfaces. *International Conference on Transparent Optical Networks, 2019-July*. <https://doi.org/10.1109/ICTON.2019.8840259>
- Malmivuo, J., & Plonsey, R. (1995). Bioelectromagnetism: Principles and Applications of Bioelectric and Biomagnetic Fields. *Bioelectromagnetism: Principles and Applications of Bioelectric and Biomagnetic Fields*, 1–506. <https://doi.org/10.1093/ACPROF:OSO/9780195058239.001.0001>
- Mank, M., Reiff, D. F., Heim, N., Friedrich, M. W., Borst, A., & Griesbeck, O. (2006). A FRET-Based Calcium Biosensor with Fast Signal Kinetics and High Fluorescence Change. *Biophysical Journal*, 90(5). <https://doi.org/10.1529/BIOPHYSJ.105.073536>
- Markakis, E. A., Vives, K. P., Bober, J., Leichtle, S., Leranth, C., Beecham, J., Elsworth, J. D., Roth, R. H., Samulski, R. J., & Redmond, D. E. (2010). Comparative transduction efficiency of AAV vector serotypes 1-6 in the substantia nigra and striatum of the primate brain. *Molecular Therapy*, 18(3), 588–593. <https://doi.org/10.1038/mt.2009.286>
- Markram, H., Toledo-Rodriguez, M., Wang, Y., Gupta, A., Silberberg, G., & Wu, C. (2004). Interneurons of the neocortical inhibitory system. *Nature Reviews Neuroscience*, 5(10), 793–807. <https://doi.org/10.1038/nrn1519>
- Marshall, L., Helgadóttir, H., Mölle, M., & Born, J. (2006). Boosting slow oscillations during sleep potentiates memory. *Nature*, 444(7119), 610–613. <https://doi.org/10.1038/nature05278>
- Massimini, M., Huber, R., Ferrarelli, F., Hill, S., & Tononi, G. (2004). The sleep slow oscillation as a traveling wave. *Journal of Neuroscience*, 24(31), 6862–6870. <https://doi.org/10.1523/JNEUROSCI.1318-04.2004>

- Massimini, M., Rosanova, M., & Mariotti, M. (2003). EEG slow (~1 Hz) waves are associated with nonstationarity of thalamo-cortical sensory processing in the sleeping human. *Journal of Neurophysiology*, *89*(3), 1205–1213. <https://doi.org/10.1152/JN.00373.2002>
- Matsui, T., Murakami, T., & Ohki, K. (2016). Transient neuronal coactivations embedded in globally propagating waves underlie resting-state functional connectivity. *Proceedings of the National Academy of Sciences of the United States of America*, *113*(23), 6556–6561. <https://doi.org/10.1073/pnas.1521299113>
- Meffin, H., Tahayori, B., Grayden, D. B., & Burkitt, A. N. (2012). Modeling extracellular electrical stimulation: I. Derivation and interpretation of neurite equations. *Journal of Neural Engineering*, *9*(6), 065005. <https://doi.org/10.1088/1741-2560/9/6/065005>
- Mercier, B. E., Legg, C. R., & Glickstein, M. (1990). Basal ganglia and cerebellum receive different somatosensory information in rats. *Proceedings of the National Academy of Sciences of the United States of America*, *87*(11), 4388–4392. <https://doi.org/10.1073/PNAS.87.11.4388>
- Minert, A., Yatziv, S. L., & Devor, M. (2017). Location of the Mesopontine Neurons Responsible for Maintenance of Anesthetic Loss of Consciousness. *Journal of Neuroscience*, *37*(38), 9320–9331. <https://doi.org/10.1523/JNEUROSCI.0544-17.2017>
- Miranda, C., Howell, M. R., Lusk, J. F., Marschall, E., Eshima, J., Anderson, T., & Smith, B. S. (2021). Automated microscope-independent fluorescence-guided micropipette. *Biomedical Optics Express*, *12*(8), 4689. <https://doi.org/10.1364/BOE.431372>
- Mirvish, S. S. (1969). The Carcinogenic Action and Metabolism of Urethan and N-Hydroxyurethan. *Advances in Cancer Research*, *11*(C), 1–42. [https://doi.org/10.1016/S0065-230X\(08\)60386-3](https://doi.org/10.1016/S0065-230X(08)60386-3)
- Moazen, M., Peskett, E., Babbs, C., Pauws, E., & Fagan, M. J. (2015). Mechanical Properties of Calvarial Bones in a Mouse Model for Craniosynostosis. *PLoS ONE*, *10*(5). <https://doi.org/10.1371/JOURNAL.PONE.0125757>
- Mocanu, V. M., & Shmuel, A. (2021). Optical Imaging-Based Guidance of Viral Microinjections and Insertion of a Laminar Electrophysiology Probe Into a

- Predetermined Barrel in Mouse Area S1BF. *Frontiers in Neural Circuits*, 15. <https://doi.org/10.3389/fncir.2021.541676>
- Moller, P. (1991). Electric Fish. *BioScience*, 41(11), 794–796. <https://doi.org/10.2307/1311732>
- Mondino, A., González, J., Li, D., Mateos, D., Osorio, L., Cavelli, M., Costa, A., Vanini, G., Mashour, G., & Torterolo, P. (2021). Urethane Anesthesia Exhibits Neurophysiological Correlates of Unconsciousness and is Distinct from Sleep. *BioRxiv*, 2021.09.21.461281. <https://doi.org/10.1101/2021.09.21.461281>
- Mosconi, T. M., & Rice, F. L. (1991). Sensory innervation of the mystacial pad fur of the ferret. *Neuroscience Letters*, 121(1–2), 199–202. [https://doi.org/10.1016/0304-3940\(91\)90684-L](https://doi.org/10.1016/0304-3940(91)90684-L)
- Mukovski, M., Chauvette, S., Timofeev, I., & Volgushev, M. (2007). Detection of active and silent states in neocortical neurons from the field potential signal during slow-wave sleep. *Cerebral Cortex*, 17(2), 400–414. <https://doi.org/10.1093/CERCOR/BHJ157>
- Murphy, M., Bruno, M. A., Riedner, B. A., Boveroux, P., Noirhomme, Q., Landsness, E. C., Brichant, J. F., Phillips, C., Massimini, M., Laureys, S., Tononi, G., & Boly, M. (2011). Propofol anesthesia and sleep: A high-density EEG study. *Sleep*, 34(3). <https://doi.org/10.1093/sleep/34.3.283>
- Nagel, G., Brauner, M., Liewald, J. F., Adeishvili, N., Bamberg, E., & Gottschalk, A. (2005). Light activation of channelrhodopsin-2 in excitable cells of *Caenorhabditis elegans* triggers rapid behavioral responses. *Current Biology : CB*, 15(24), 2279–2284. <https://doi.org/10.1016/J.CUB.2005.11.032>
- Nagel, G., Ollig, D., Fuhrmann, M., Kateriya, S., Musti, A. M., Bamberg, E., & Hegemann, P. (2002). Channelrhodopsin-1: A light-gated proton channel in green algae. *Science*, 296(5577), 2395–2398. <https://doi.org/10.1126/science.1072068>
- Nagel, G., Szellas, T., Huhn, W., Kateriya, S., Adeishvili, N., Berthold, P., Ollig, D., Hegemann, P., & Bamberg, E. (2003). Channelrhodopsin-2, a directly light-gated cation-selective membrane channel. *Proceedings of the National Academy of Sciences*, 100(24), 13940–13945. <https://doi.org/10.1073/PNAS.1936192100>

- Nagel, G., Szellas, T., Kateriya, S., Adeishvili, N., Hegemann, P., & Bamberg, E. (2005). Channelrhodopsins: Directly light-gated cation channels. *Biochemical Society Transactions*, *33*(4), 863–866. <https://doi.org/10.1042/BST0330863>
- Nakai, J., Ohkura, M., & Imoto, K. (2001). A high signal-to-noise Ca²⁺ probe composed of a single green fluorescent protein. *Nature Biotechnology* *2001* *19*:2, *19*(2), 137–141. <https://doi.org/10.1038/84397>
- Nakazawa, K., Zsiros, V., Jiang, Z., Nakao, K., Kolata, S., Zhang, S., & Belforte, J. E. (2012). GABAergic interneuron origin of schizophrenia pathophysiology. *Neuropharmacology*, *62*(3), 1574. <https://doi.org/10.1016/J.NEUROPHARM.2011.01.022>
- Ngo, H. V. V., Martinetz, T., Born, J., & Mölle, M. (2013). Auditory closed-loop stimulation of the sleep slow oscillation enhances memory. *Neuron*, *78*(3), 545–553. <https://doi.org/10.1016/j.neuron.2013.03.006>
- Niethard, N., Brodt, S., & Born, J. (2021). Cell-Type-Specific Dynamics of Calcium Activity in Cortical Circuits over the Course of Slow-Wave Sleep and Rapid Eye Movement Sleep. *Journal of Neuroscience*, *41*(19), 4212–4222. <https://doi.org/10.1523/JNEUROSCI.1957-20.2021>
- Niethard, N., Ngo, H. V. V., Ehrlich, I., & Born, J. (2018). Cortical circuit activity underlying sleep slow oscillations and spindles. *Proceedings of the National Academy of Sciences of the United States of America*, *115*(39), E9220–E9229. www.pnas.org/cgi/doi/10.1073/pnas.1805517115
- Nimmerjahn, A., Kirchhoff, F., Kerr, J. N. D., Helmchen, F., A Nimmerjahn, F Kirchhoff, JN Kerr, F. H., Nimmerjahn, A., Kirchhoff, F., Kerr, J. N. D., & Helmchen, F. (2004). *Sulforhodamine 101 as a specific marker of astroglia in the neocortex in vivo*. *1*(1), 31–37. <https://doi.org/10.1038/nmeth706>
- Nir, Y., Staba, R. J., Andrillon, T., Vyazovskiy, V. V., Cirelli, C., Fried, I., & Tononi, G. (2011). Regional Slow Waves and Spindles in Human Sleep. *Neuron*, *70*(1), 153–169. <https://doi.org/10.1016/j.neuron.2011.02.043>
- Normand, E. A., Crandall, S. R., Thorn, C. A., Murphy, E. M., Voelcker, B., Browning, C., Machan, J. T., Moore, C. I., Connors, B. W., & Zervas, M. (2013). Temporal and Mosaic Tsc1 Deletion in the Developing Thalamus Disrupts Thalamocortical Circuitry, Neural Function, and Behavior. *Neuron*, *78*(5), 895–909. <https://doi.org/10.1016/J.NEURON.2013.03.030>

- Oesch, L. T., Gazea, M., Gent, T. C., Bandarabadi, M., Herrera, C. G., & Adamantidis, A. R. (2020). REM sleep stabilizes hypothalamic representation of feeding behavior. *Proceedings of the National Academy of Sciences of the United States of America*, *117*(32), 19590–19598. <https://doi.org/10.1073/pnas.1921909117>
- Oesterhelt, D., & Stoerkenius, W. (1971). Rhodopsin-like Protein from the Purple Membrane of Halobacterium halobium. *Nature New Biology* *1971* *233*:39, *233*(39), 149–152. <https://doi.org/10.1038/newbio233149a0>
- Otsu, Y., Bormuth, V., Wong, J., Mathieu, B., Dugué, G. P., Feltz, A., & Dieudonné, S. (2008). Optical monitoring of neuronal activity at high frame rate with a digital random-access multiphoton (RAMP) microscope. *Journal of Neuroscience Methods*, *173*(2), 259–270. <https://doi.org/10.1016/J.JNEUMETH.2008.06.015>
- Packer, A. M., Russell, L. E., Dalglish, H. W. P., & Häusser, M. (2015). Simultaneous all-optical manipulation and recording of neural circuit activity with cellular resolution in vivo. *Nature Methods*, *12*(2), 140–146. <https://doi.org/10.1038/NMETH.3217>
- Pagliardini, S., Funk, G. D., & Dickson, C. T. (2013). Breathing and brain state: Urethane anesthesia as a model for natural sleep. *Respiratory Physiology & Neurobiology*, *188*(3), 324–332. <https://doi.org/10.1016/J.RESP.2013.05.035>
- Pal, D., Lipinski, W. J., Walker, A. J., Turner, A. M., & Mashour, G. A. (2011). State-specific Effects of Sevoflurane Anesthesia on Sleep Homeostasis Selective Recovery of Slow Wave but Not Rapid Eye Movement Sleep. *Anesthesiology*, *114*(2), 302–310. <https://doi.org/10.1097/ALN.0B013E318204E064>
- Panzer, L. C., & Hoppa, M. B. (2019). Genetically encoded voltage indicators are illuminating subcellular physiology of the axon. *Frontiers in Cellular Neuroscience*, *13*, 1–9. <https://doi.org/10.3389/FNCEL.2019.00052>
- Papagiakoumou, E., Anselmi, F., Bègue, A., De Sars, V., Glückstad, J., Isacoff, E. Y., & Emiliani, V. (2010). Scanless two-photon excitation of channelrhodopsin-2. *Nature Methods* *2010* *7*:10, *7*(10), 848–854. <https://doi.org/10.1038/nmeth.1505>

- Park, S., Guo, Y., Jia, X., Choe, H. K., Grena, B., Kang, J., Park, J., Lu, C., Canales, A., Chen, R., Yim, Y. S., Choi, G. B., Fink, Y., & Anikeeva, P. (2017). One-step optogenetics with multifunctional flexible polymer fibers. *Nature Neuroscience*, *20*(4), 612–619. <https://doi.org/10.1038/NN.4510>
- Patterson, G. H., & Piston, D. W. (2000). Photobleaching in two-photon excitation microscopy. *Biophysical Journal*, *78*(4), 2159–2162. [https://doi.org/10.1016/S0006-3495\(00\)76762-2](https://doi.org/10.1016/S0006-3495(00)76762-2)
- Pauca, A. L., & Dripps, R. D. (1973). CLINICAL EXPERIENCE WITH ISOFLURANE (FORANE trademark of Ohio Medical Products, division of Airco, Inc.). *British Journal of Anaesthesia*, *45*, 697–703. <https://doi.org/10.1093/bja/45.7.697>
- Pechère, J. F., Derancourt, J., & Haiech, J. (1977). The participation of parvalbumins in the activation-relaxation cycle of vertebrate fast skeletal-muscle. *FEBS Lett.*, *75*(1–2), 111–114. [https://doi.org/10.1016/0014-5793\(77\)80064-1](https://doi.org/10.1016/0014-5793(77)80064-1)
- Peixoto, H. M., Cruz, R. M. S., Moulin, T. C., & Leão, R. N. (2020). Modeling the Effect of Temperature on Membrane Response of Light Stimulation in Optogenetically-Targeted Neurons. *Frontiers in Computational Neuroscience*, *14*, 5. <https://doi.org/10.3389/FNCOM.2020.00005>
- Pettit, D. L., Wang, S. S. H., Gee, K. R., & Augustine, G. J. (1997). Chemical Two-Photon Uncaging: a Novel Approach to Mapping Glutamate Receptors. *Neuron*, *19*(3), 465–471. [https://doi.org/10.1016/S0896-6273\(00\)80361-X](https://doi.org/10.1016/S0896-6273(00)80361-X)
- Pfeffer, C. K., Xue, M., He, M., Huang, Z. J., & Scanziani, M. (2013). Inhibition of Inhibition in Visual Cortex: The Logic of Connections Between Molecularly Distinct Interneurons. *Nature Neuroscience*, *16*(8), 1068. <https://doi.org/10.1038/NN.3446>
- Pisanello, M., Pisano, F., Hyun, M., Maglie, E., Balena, A., De Vittorio, M., Sabatini, B. L., & Pisanello, F. (2019). The Three-Dimensional Signal Collection Field for Fiber Photometry in Brain Tissue. *Frontiers in Neuroscience*, *13*(FEB). <https://doi.org/10.3389/FNINS.2019.00082>
- Porter, J. T., Johnson, C. K., & Agmon, A. (2001). Diverse Types of Interneurons Generate Thalamus-Evoked Feedforward Inhibition in the Mouse Barrel

- Cortex. *Journal of Neuroscience*, 21(8), 2699–2710.
<https://doi.org/10.1523/jneurosci.21-08-02699.2001>
- Pouille, F., & Scanziani, M. (2001). Enforcement of temporal fidelity in pyramidal cells by somatic feed-forward inhibition. *Science*, 293(5532), 1159–1163.
<https://doi.org/10.1126/science.1060342>
- Poulet, J. F. A., & Petersen, C. C. H. (2008). Internal brain state regulates membrane potential synchrony in barrel cortex of behaving mice. *Nature*, 454(7206), 881–885. <https://doi.org/10.1038/NATURE07150>
- Prigge, M., Schneider, F., Tsunoda, S. P., Shilyansky, C., Wietek, J., Deisseroth, K., & Hegemann, P. (2012). Color-tuned channelrhodopsins for multiwavelength optogenetics. *Journal of Biological Chemistry*, 287(38), 31804–31812.
<https://doi.org/10.1074/jbc.M112.391185>
- Pritchett, D. L., Siegle, J. H., Deister, C. A., & Moore, C. I. (2015). For things needing your attention: The role of neocortical gamma in sensory perception. In *Current Opinion in Neurobiology* (Vol. 31, pp. 254–263). Elsevier Ltd.
<https://doi.org/10.1016/j.conb.2015.02.004>
- Prönneke, A., Scheuer, B., Wagener, R. J., Möck, M., Witte, M., & Staiger, J. F. (2015). Characterizing VIP Neurons in the Barrel Cortex of VIPcre/tdTomato Mice Reveals Layer-Specific Differences. *Cerebral Cortex (New York, NY)*, 25(12), 4854. <https://doi.org/10.1093/CERCOR/BHV202>
- Puig, M. V., Ushimaru, M., & Kawaguchi, Y. (2008). Two distinct activity patterns of fast-spiking interneurons during neocortical UP states. *Proceedings of the National Academy of Sciences of the United States of America*, 105(24), 8428–8433. <https://www.pnas.org/doi/abs/10.1073/pnas.0712219105>
- Rall, W. (1962). Theory of Physiological Properties of Dendrites. *Annals of the New York Academy of Sciences*, 96(4), 1071–1092.
<https://doi.org/10.1111/J.1749-6632.1962.TB54120.X>
- Reig, R., & Sanchez-Vives, M. V. (2007). Synaptic transmission and plasticity in an active cortical network. *PLoS ONE*, 2(8).
<https://doi.org/10.1371/journal.pone.0000670>
- Reyes-Puerta, V., Kim, S., Sun, J. J., Imbrosci, B., Kilb, W., & Luhmann, H. J. (2015). High Stimulus-Related Information in Barrel Cortex Inhibitory

- Interneurons. *PLoS Computational Biology*, 11(6).
<https://doi.org/10.1371/journal.pcbi.1004121>
- Reyes-Puerta, V., Sun, J. J., Kim, S., Kilb, W., & Luhmann, H. J. (2015). Laminar and Columnar Structure of Sensory-Evoked Multineuronal Spike Sequences in Adult Rat Barrel Cortex in Vivo. *Cerebral Cortex*, 25(8), 2001–2021.
<https://doi.org/10.1093/cercor/bhu007>
- Reyes-Puerta, V., Yang, J. W., Siwek, M. E., Kilb, W., Sun, J. J., & Luhmann, H. J. (2016). Propagation of spontaneous slow-wave activity across columns and layers of the adult rat barrel cortex in vivo. *Brain Structure and Function*, 221(9), 4429–4449. <https://doi.org/10.1007/s00429-015-1173-x>
- Rice, F. L. (1985). *An attempt to find vibrissa-related barrels in the primary somatosensory cortex of the cat.* 53(2), 169–172.
[https://doi.org/10.1016/0304-3940\(85\)90180-6](https://doi.org/10.1016/0304-3940(85)90180-6)
- Rice, F. L. (1993). Structure, vascularization, and innervation of the mystacial pad of the rat as revealed by the lectin Griffonia simplicifolia. *The Journal of Comparative Neurology*, 337(3), 386–399.
<https://doi.org/10.1002/CNE.903370304>
- Rice, F. L., Gomez, C., Barstow, C., Burnet, A., & Sands, P. (1985). A Comparative analysis of the development of the primary somatosensory cortex: Interspecies similarities during barrel and laminar development. *Journal of Comparative Neurology*, 236(4), 477–495. <https://doi.org/10.1002/CNE.902360405>
- Rickgauer, J. P., & Tank, D. W. (2009). Two-photon excitation of channelrhodopsin-2 at saturation. *Proceedings of the National Academy of Sciences of the United States of America*, 106(35), 15025.
<https://doi.org/10.1073/PNAS.0907084106>
- Rocheftort, N. (2009). Sparsification of neuronal activity in the visual cortex at eye-opening. *Proc. Natl. Acad. Sci. USA*, 106, 15049–15054.
<https://doi.org/10.1073/pnas.0907660106>
- Rosales Jubal, E., Schwalm, M., dos Santos Guilherme, M., Schuck, F., Reinhardt, S., Tose, A., Barger, Z., Roesler, M. K., Ruffini, N., Wierczeiko, A., Schmeisser, M. J., Schmitt, U., Endres, K., & Stroh, A. (2021). Acitretin reverses early functional network degradation in a mouse model of familial

- Alzheimer's disease. *Scientific Reports*, *11*(1), 1–16.
<https://doi.org/10.1038/s41598-021-85912-0>
- Rudy, B., Fishell, G., Lee, S., & Hjerling-Leffler, J. (2011). Three Groups of Interneurons Account for Nearly 100% of Neocortical GABAergic Neurons. *Developmental Neurobiology*, *71*(1), 45.
<https://doi.org/10.1002/DNEU.20853>
- Rungta, R. L., Osmanski, B. F., Boido, D., Tanter, M., & Charpak, S. (2017). Light controls cerebral blood flow in naive animals. *Nature Communications* *2017* *8:1*, *8*(1), 1–9. <https://doi.org/10.1038/ncomms14191>
- Sachidhanandam, S., Sermet, B. S., & Petersen, C. C. H. (2016). Parvalbumin-Expressing GABAergic Neurons in Mouse Barrel Cortex Contribute to Gating a Goal-Directed Sensorimotor Transformation. *Cell Reports*, *15*(4), 700–706.
<https://doi.org/10.1016/j.celrep.2016.03.063>
- Sakuma, T., Barry, M. A., & Ikeda, Y. (2012). Lentiviral vectors: basic to translational. *The Biochemical Journal*, *443*(3), 603–618.
<https://doi.org/10.1042/BJ20120146>
- Salomé, R., Kremer, Y., Dieudonné, S., Léger, J. F., Krichevsky, O., Wyart, C., Chatenay, D., & Bourdieu, L. (2006). Ultrafast random-access scanning in two-photon microscopy using acousto-optic deflectors. *Journal of Neuroscience Methods*, *154*(1–2), 161–174.
<https://doi.org/10.1016/J.JNEUMETH.2005.12.010>
- Sanchez-Vives, M. V., Massimini, M., & Mattia, M. (2017). Shaping the Default Activity Pattern of the Cortical Network. *Neuron*, *94*(5), 993–1001.
<https://doi.org/10.1016/J.NEURON.2017.05.015>
- Sanchez-Vives, M. V., & McCormick, D. A. (2000). Cellular and network mechanisms of rhythmic recurrent activity in neocortex. *Nature Neuroscience*, *3*(10), 1027–1034. <https://doi.org/10.1038/79848>
- Scheffold, F. (2014). Principles and fundamentals of optical imaging. *Neuromethods*, *85*, 19–32. https://doi.org/10.1007/978-1-62703-785-3_2
- Schiffman, H. R., Lore, R., Passafiume, J., & Neeb, R. (1970). Role of vibrissae for depth perception in the rat (*Rattus norvegicus*). *Animal Behaviour*, *18*(PART 2), 290–292. [https://doi.org/10.1016/S0003-3472\(70\)80040-9](https://doi.org/10.1016/S0003-3472(70)80040-9)

- Schlatter, J., & Lutz, W. K. (1990). The carcinogenic potential of ethyl carbamate (urethane): Risk assessment at human dietary exposure levels. *Food and Chemical Toxicology*, 28(3), 205–211. [https://doi.org/10.1016/0278-6915\(90\)90008-B](https://doi.org/10.1016/0278-6915(90)90008-B)
- Schmid, F., Wachsmuth, L., Schwalm, M., Prouvot, P. H., Jubal, E. R., Fois, C., Pramanik, G., Zimmer, C., Faber, C., & Stroh, A. (2016). Assessing sensory versus optogenetic network activation by combining (o)fMRI with optical Ca²⁺ recordings. *Journal of Cerebral Blood Flow and Metabolism*, 36(11), 1885–1900. <https://doi.org/10.1177/0271678X15619428>
- Schulz, K., Sydekum, E., Krueppel, R., Engelbrecht, C. J., Schlegel, F., Schröter, A., Rudin, M., & Helmchen, F. (2012). Simultaneous BOLD fMRI and fiber-optic calcium recording in rat neocortex. *Nature Methods*, 9(6), 597–602. <https://doi.org/10.1038/nmeth.2013>
- Schüz, A., & Palm, G. (1989). Density of neurons and synapses in the cerebral cortex of the mouse: NEURONS AND SYNAPSES IN THE MOUSE CORTEX. *Journal of Comparative Neurology*, 286(4), 442–455. <https://doi.org/10.1002/cne.v286:4>
- Schwaller, B. (2010). Cytosolic Ca²⁺ Buffers. *Cold Spring Harbor Perspectives in Biology*, 2(11). <https://doi.org/10.1101/CSHPERSPECT.A004051>
- Schwalm, M., & Easton, C. (2016). Cortical Temperature Change: A Tool for Modulating Brain States? *ENeuro*, 3(3), 608–610. <https://doi.org/10.1523/ENEURO.0096-16.2016>
- Schwalm, M., & Jubal, E. R. (2017). Back to Pupillometry: How Cortical Network State Fluctuations Tracked by Pupil Dynamics Could Explain Neural Signal Variability in Human Cognitive Neuroscience. *ENeuro*, 4(6). <https://doi.org/10.1523/ENEURO.0293-16.2017>
- Schwalm, M., Schmid, F., Wachsmuth, L., Backhaus, H., Kronfeld, A., Jury, F. A., Prouvot, P. H., Fois, C., Albers, F., Van Alst, T., Faber, C., & Stroh, A. (2017). Cortex-wide BOLD fMRI activity reflects locally-recorded slow oscillation-associated calcium waves. *ELife*, 6. <https://doi.org/10.7554/eLife.27602>
- Schwenk, F., Baron, U., & Rajewsky, K. (1995). A cre-transgenic mouse strain for the ubiquitous deletion of loxP-flanked gene segments including deletion in

- germ cells. *Nucleic Acids Research*, 23(24), 5080–5081.
<https://doi.org/10.1093/NAR/23.24.5080>
- Seamari, Y., Narváez, J. A., Vico, F. J., Lobo, D., & Sanchez-Vives, M. V. (2007). Robust off- and online separation of intracellularly recorded up and down cortical states. *PLoS One*, 2(9).
<https://doi.org/10.1371/JOURNAL.PONE.0000888>
- Sharma, A. V., Wolansky, T., & Dickson, C. T. (2010). A comparison of sleep-like slow oscillations in the hippocampus under ketamine and urethane anesthesia. *Journal of Neurophysiology*, 104(2), 932–939.
<https://doi.org/10.1152/JN.01065.2009>
- Shepherd, G. M. G. (2009). Intracortical cartography in an agranular area. In *Frontiers in Neuroscience* (Vol. 3, Issue DEC, pp. 337–343).
<https://doi.org/10.3389/neuro.01.030.2009>
- Sheroziya, M., & Timofeev, I. (2014). Global Intracellular Slow-Wave Dynamics of the Thalamocortical System. *The Journal of Neuroscience*, 34(26), 8875.
<https://doi.org/10.1523/JNEUROSCI.4460-13.2014>
- Shimogori, T., & Ogawa, M. (2008). Gene application with in utero electroporation in mouse embryonic brain. *Development, Growth & Differentiation*, 50(6), 499–506. <https://doi.org/10.1111/J.1440-169X.2008.01045.X>
- Sileo, L., Bitzenhofer, S. H., Spagnolo, B., Pöplau, J. A., Holzhammer, T., Pisanello, M., Pisano, F., Bellistri, E., Maglie, E., De Vittorio, M., Ruther, P., Hanganu-Opatz, I. L., & Pisanello, F. (2018). Tapered Fibers Combined With a Multi-Electrode Array for Optogenetics in Mouse Medial Prefrontal Cortex. *Frontiers in Neuroscience*, 12. <https://doi.org/10.3389/FNINS.2018.00771>
- Silver, N. R. G., Ward-Flanagan, R., & Dickson, C. T. (2021). Long-term stability of physiological signals within fluctuations of brain state under urethane anesthesia. *PLoS ONE*, 16(10).
<https://doi.org/10.1371/JOURNAL.PONE.0258939>
- Sirota, A., Csicsvari, J., Buhl, D., & Buzsáki, G. (2003). Communication between neocortex and hippocampus during sleep in rodents. *Proceedings of the National Academy of Sciences of the United States of America*, 100(4), 2065–2069. <https://doi.org/10.1073/PNAS.0437938100>

- Sohal, V. S., Zhang, F., Yizhar, O., & Deisseroth, K. (2009). Parvalbumin neurons and gamma rhythms enhance cortical circuit performance. *Nature*, *459*(7247), 698–702. <https://doi.org/10.1038/nature07991>
- Sosulina, L., Graebenitz, S., & Pape, H. C. (2010). GABAergic interneurons in the mouse lateral amygdala: A classification study. *Journal of Neurophysiology*, *104*(2), 617–626. <https://doi.org/10.1152/jn.00207.2010>
- Staiger, J. F., Masannek, C., Schleicher, A., & Zuschratter, W. (2004). Calbindin-containing interneurons are a target for VIP-immunoreactive synapses in rat primary somatosensory cortex. *The Journal of Comparative Neurology*, *468*(2), 179–189. <https://doi.org/10.1002/CNE.10953>
- Steinmetz, N. A., Buetfering, C., Lecoq, J., Lee, C. R., Peters, A. J., Jacobs, E. A. K., Coen, P., Ollerenshaw, D. R., Valley, M. T., De Vries, S. E. J., Garrett, M., Zhuang, J., Groblewski, P. A., Manavi, S., Miles, J., White, C., Lee, E., Griffin, F., Larkin, J. D., ... Harris, K. D. (2017). Aberrant Cortical Activity in Multiple GCaMP6-Expressing Transgenic Mouse Lines. *ENeuro*, *4*(5), 207–224. <https://doi.org/10.1523/ENEURO.0207-17.2017>
- Steriade, M. (1993). Cholinergic blockage of network- and intrinsically generated slow oscillations promotes waking and REM sleep activity patterns in thalamic and cortical neurons. *Progress in Brain Research*, *98*(C), 345–355. [https://doi.org/10.1016/S0079-6123\(08\)62418-8](https://doi.org/10.1016/S0079-6123(08)62418-8)
- Steriade, M., & Amzica, F. (1998). Coalescence of sleep rhythms and their chronology in corticothalamic networks. *Sleep Research Online*, *1*(1), 1–10.
- Steriade, M., Nunez, A., & Amzica, F. (1993). A novel slow (< 1 Hz) oscillation of neocortical neurons in vivo: Depolarizing and hyperpolarizing components. *Journal of Neuroscience*, *13*(8), 3252–3265. <https://doi.org/10.1523/JNEUROSCI.13-08-03252.1993>
- Stosiek, C., Garaschuk, O., Holthoff, K., & Konnerth, A. (2003). In vivo two-photon calcium imaging of neuronal networks. *Proc. Natl. Acad. Sci. USA*, *100*, 7319–7324.
- Stroh, A. (2018). Optogenetics: A Roadmap. *Neuromethods*, *133*. <https://doi.org/10.1007/978-1-4939-7417-7>
- Stroh, A., Adelsberger, H., Groh, A., Rühlmann, C., Fischer, S., Schierloh, A., Deisseroth, K., & Konnerth, A. (2013). Making Waves: Initiation and

- Propagation of Corticothalamic Ca²⁺ Waves In Vivo. *Neuron*, 77(6), 1136–1150. <https://doi.org/10.1016/j.neuron.2013.01.031>
- Stüttgen, M. C., Nonkes, L. J. P., Geis, H. R. A. P., Tiesinga, P. H., & Houweling, A. R. (2017). Temporally precise control of single-neuron spiking by juxtacellular nanostimulation. *Journal of Neurophysiology*, 117(3), 1363–1378. <https://doi.org/10.1152/JN.00479.2016>
- Sun, F., Zeng, J., Jing, M., Zhou, J., Feng, J., Owen, S. F., Luo, Y., Li, F., Wang, H., Yamaguchi, T., Yong, Z., Gao, Y., Peng, W., Wang, L., Zhang, S., Du, J., Lin, D., Xu, M., Kreitzer, A. C., ... Li, Y. (2018). A Genetically Encoded Fluorescent Sensor Enables Rapid and Specific Detection of Dopamine in Flies, Fish, and Mice. *Cell*, 174(2), 481-496.e19. <https://doi.org/10.1016/J.CELL.2018.06.042>
- Sun, F., Zhou, J., Dai, B., Qian, T., Zeng, J., Li, X., Zhuo, Y., Zhang, Y., Wang, Y., Qian, C., Tan, K., Feng, J., Dong, H., Lin, D., Cui, G., & Li, Y. (2020). Next-generation GRAB sensors for monitoring dopaminergic activity in vivo. *Nature Methods* 2020 17:11, 17(11), 1156–1166. <https://doi.org/10.1038/s41592-020-00981-9>
- Sun, Q. Q., Huguenard, J. R., & Prince, D. A. (2006). Barrel cortex microcircuits: Thalamocortical feedforward inhibition in spiny stellate cells is mediated by a small number of fast-spiking interneurons. *Journal of Neuroscience*, 26(4), 1219–1230. <https://doi.org/10.1523/JNEUROSCI.4727-04.2006>
- Tang, L., & Fang, C. (2019). Elucidating Excited-State Hydrogen-Bonding Dynamics and Proton Transfer inside Fluorescent Protein Calcium Biosensors. *Hydrogen-Bonding Research in Photochemistry, Photobiology, and Optoelectronic Materials*, 55–91. https://doi.org/10.1142/9781786346087_0003
- Tasaka, G. I., Guenther, C. J., Shalev, A., Gilday, O., Luo, L., & Mizrahi, A. (2018). Genetic tagging of active neurons in auditory cortex reveals maternal plasticity of coding ultrasonic vocalizations. *Nature Communications* 2018 9:1, 9(1), 1–14. <https://doi.org/10.1038/s41467-018-03183-2>
- Tian, L., Hires, S. A., Mao, T., Huber, D., Chiappe, M. E., Chalasani, S. H., Petreanu, L., Akerboom, J., McKinney, S. A., Schreier, E. R., Bargmann, C. I., Jayaraman, V., Svoboda, K., & Looger, L. L. (2009). Imaging neural

- activity in worms, flies and mice with improved GCaMP calcium indicators. *Nature Methods*, 6(12), 875–881. <https://doi.org/10.1038/NMETH.1398>
- Timofeev, I., Grenier, F., Bazhenov, M., Sejnowski, T. J., & Steriade, M. (2000). Origin of slow cortical oscillations in deafferented cortical slabs. *Cerebral Cortex*, 10(12), 1185–1199. <https://doi.org/10.1093/CERCOR/10.12.1185>
- Tung, A., Bergmann, B. M., Herrera, S., Cao, D., & Mendelson, W. B. (2004). Recovery from Sleep Deprivation Occurs during Propofol Anesthesia. *Anesthesiology*, 100(6), 1419–1426. <https://doi.org/10.1097/00000542-200406000-00014>
- Tung, A., Szafran, M. J., Bluhm, B., & Mendelson, W. B. (2002). Sleep Deprivation Potentiates the Onset and Duration of Loss of Righting Reflex Induced by Propofol and Isoflurane. *Anesthesiology*, 97(4), 906–911. <https://doi.org/10.1097/00000542-200210000-00024>
- Uematsu, M., Hirai, Y., Karube, F., Ebihara, S., Kato, M., Abe, K., Obata, K., Yoshida, S., Hirabayashi, M., Yanagawa, Y., & Kawaguchi, Y. (2008). Quantitative Chemical Composition of Cortical GABAergic Neurons Revealed in Transgenic Venus-Expressing Rats. *Cerebral Cortex*, 18(2), 315–330. <https://doi.org/10.1093/CERCOR/BHM056>
- Van De Werd, H. J. J. M., Rajkowska, G., Evers, P., & Uylings, H. B. M. (2010). Cytoarchitectonic and chemoarchitectonic characterization of the prefrontal cortical areas in the mouse. *Brain Structure and Function*, 214(4), 339–353. <https://doi.org/10.1007/s00429-010-0247-z>
- Van Der Loos, H., & Woolsey, T. A. (1973). Somatosensory cortex: Structural alterations following early injury to sense organs. *Science*, 179(4071), 395–398. <https://doi.org/10.1126/science.179.4071.395>
- Vijayan, S., Hale, G. J., Moore, C. I., Brown, E. N., & Wilson, M. (2010). Activity in the Barrel Cortex During Active Behavior and Sleep. *Journal of Neurophysiology*, 103(4), 2074. <https://doi.org/10.1152/JN.00474.2009>
- Villette, V., Chavarha, M., Dimov, I. K., Bradley, J., Pradhan, L., Mathieu, B., Evans, S. W., Chamberland, S., Shi, D., Yang, R., Kim, B. B., Ayon, A., Jalil, A., St-Pierre, F., Schnitzer, M. J., Bi, G., Toth, K., Ding, J., Dieudonné, S., & Lin, M. Z. (2019). Ultrafast Two-Photon Imaging of a High-Gain Voltage

- Indicator in Awake Behaving Mice. *Cell*, 179(7), 1590-1608.e23. <https://doi.org/10.1016/J.CELL.2019.11.004>
- Vo-Dinh, T., Raton, B., New, L., & Washington, Y. (2003). *Biomedical Photonic handbook*. www.crcpress.com
- Vogt, M. (1948). Mutation Triggered In *Drosophila* By Ethyl Urethane. *Experientia*, 4(2), 68–69. <https://doi.org/10.1007/BF02155987>
- Vyazovskiy, V. V., Olcese, U., Hanlon, E. C., Nir, Y., Cirelli, C., & Tononi, G. (2011). Local sleep in awake rats. *Nature* 2011 472:7344, 472(7344), 443–447. <https://doi.org/10.1038/nature10009>
- Waite, P. M. E., Marotte, L. R., & Mark, R. F. (1991). Development of whisker representation in the cortex of the tammar wallaby *Macropus eugenii*. *Developmental Brain Research*, 58(1), 35–41. [https://doi.org/10.1016/0165-3806\(91\)90234-A](https://doi.org/10.1016/0165-3806(91)90234-A)
- Wang, T., Ouzounov, D. G., Wu, C., Horton, N. G., Zhang, B., Wu, C. H., Zhang, Y., Schnitzer, M. J., & Xu, C. (2018). Three-photon imaging of mouse brain structure and function through the intact skull. *Nature Methods* 2018 15:10, 15(10), 789–792. <https://doi.org/10.1038/s41592-018-0115-y>
- Ward-Flanagan, R., & Dickson, C. T. (2019). Neurobiological Parallels, Overlaps, and Divergences of Sleep and Anesthesia. *Handbook of Behavioral Neuroscience*, 30, 223–236. <https://doi.org/10.1016/B978-0-12-813743-7.00015-3>
- Ward-Flanagan, R., Lo, A. S., Clement, E. A., & Dickson, C. T. (2022). A Comparison of Brain-State Dynamics across Common Anesthetic Agents in Male Sprague-Dawley Rats. *International Journal of Molecular Sciences* 2022, Vol. 23, Page 3608, 23(7), 3608. <https://doi.org/10.3390/IJMS23073608>
- Comparative analyses of adeno-associated viral vector serotypes 1, 2, 5, 8 and 9 in marmoset, mouse and macaque cerebral cortex, 93 *Neuroscience Research* 144 (2015). <https://doi.org/10.1016/j.neures.2014.09.002>
- Watakabe, A., Ohtsuka, M., Kinoshita, M., Takaji, M., Isa, K., Mizukami, H., Ozawa, K., Isa, T., & Yamamori, T. (2015). Comparative analyses of adeno-associated viral vector serotypes 1, 2, 5, 8 and 9 in marmoset, mouse and

- macaque cerebral cortex. *Neuroscience Research*, 93, 144–157.
<https://doi.org/10.1016/j.neures.2014.09.002>
- Weber, F., Hoang Do, J. P., Chung, S., Beier, K. T., Bikov, M., Saffari Doost, M., & Dan, Y. (2018). Regulation of REM and Non-REM Sleep by Periaqueductal GABAergic Neurons. *Nature Communications* 2018 9:1, 9(1), 1–13.
<https://doi.org/10.1038/s41467-017-02765-w>
- Welker, E., Soriano, E., & Van der Loos, H. (1989). Plasticity in the barrel cortex of the adult mouse: Effects of peripheral deprivation on GAD-immunoreactivity. *Experimental Brain Research*, 74(3), 441–452.
<https://doi.org/10.1007/BF00247346>
- Wietek, J., Beltramo, R., Scanziani, M., Hegemann, P., Oertner, T. G., & Simon Wiegert, J. (2015). *An improved chloride-conducting channelrhodopsin for light-induced inhibition of neuronal activity in vivo*. 5(1), 1–11.
<https://pubmed.ncbi.nlm.nih.gov/26443033/>
- Wietek, J., Wiegert, J. S., Adeishvili, N., Schneider, F., Watanabe, H., Tsunoda, S. P., Vogt, A., Elstner, M., Oertner, T. G., & Hegemann, P. (2014). Conversion of channelrhodopsin into a light-gated chloride channel. *Science (New York, N.Y.)*, 344(6182), 409–412. <https://doi.org/10.1126/SCIENCE.1249375>
- Wilson, D. C. (2008). Up and down states. *Scholarpedia Journal*, 3(6), 1410.
<https://doi.org/10.4249/SCHOLARPEDIA.1410>
- Woolsey, T. A., & Van der Loos, H. (1970). The structural organization of layer IV in the somatosensory region (S I) of mouse cerebral cortex: The description of a cortical field composed of discrete cytoarchitectonic units. *Brain Research*, 17(2), 205–242. [https://doi.org/10.1016/0006-8993\(70\)90079-X](https://doi.org/10.1016/0006-8993(70)90079-X)
- Woolsey, T. A., Welker, C., & Schwartz, R. H. (1975). Comparative anatomical studies of the Sml face cortex with special reference to the occurrence of “barrels” in layer IV. *Journal of Comparative Neurology*, 164(1), 79–94.
<https://doi.org/10.1002/CNE.901640107>
- Wright, A. K., Norrie, L., & Arbuthnott, G. W. (2000). Corticofugal axons from adjacent ‘barrel’ columns of rat somatosensory cortex: cortical and thalamic terminal patterns. *The Journal of Anatomy*, 196(3), 379–390.
<https://doi.org/10.1046/J.1469-7580.2000.19630379.X>

- Wright, A. K., Norrie, L., Ingham, C. A., Hutton, E. A. M., & Arbuthnott, G. W. (1999). Double anterograde tracing of outputs from adjacent “barrel columns” of rat somatosensory cortex. Neostriatal projection patterns and terminal ultrastructure. *Neuroscience*, *88*(1), 119–133. [https://doi.org/10.1016/S0306-4522\(98\)00186-9](https://doi.org/10.1016/S0306-4522(98)00186-9)
- Wu, F., Stark, E., Im, M., Cho, I. J., Yoon, E. S., Buzsáki, G., Wise, K. D., & Yoon, E. (2013). An implantable neural probe with monolithically integrated dielectric waveguide and recording electrodes for optogenetics applications. *Journal of Neural Engineering*, *10*(5). <https://doi.org/10.1088/1741-2560/10/5/056012>
- Wyss, C. S., Karami, P., Demongeot, A., Bourban, P. E., & Pioletti, D. P. (2021). Silk granular hydrogels self-reinforced with regenerated silk fibroin fibers. *Soft Matter*, *17*(29), 7038–7046. <https://doi.org/10.1039/D1SM00585E>
- Xue, Y., Waller, L., Adesnik, H., & Pégard, N. (2022). Three-dimensional multi-site random access photostimulation (3D-MAP). *ELife*, *11*. <https://doi.org/10.7554/ELIFE.73266>
- Yang, J. W., Kilb, W., Kirischuk, S., Unichenko, P., Stüttgen, M. C., & Luhmann, H. J. (2018). Development of the whisker-to-barrel cortex system. *Current Opinion in Neurobiology*, *53*, 29–34. <https://doi.org/10.1016/j.conb.2018.04.023>
- Yang, J. W., Prouvot, P. H., Stroh, A., & Luhmann, H. J. (2018). Combining optogenetics with MEA, depth-resolved LFPs and assessing the scope of optogenetic network modulation. *NeuroMethods*, *133*, 133–152. https://doi.org/10.1007/978-1-4939-7417-7_8
- Yang, J.-W., Prouvot, P.-H., Reyes-Puerta, V., Stüttgen, M. C., Stroh, A., & Luhmann, H. J. (2017). Optogenetic Modulation of a Minor Fraction of Parvalbumin-Positive Interneurons Specifically Affects Spatiotemporal Dynamics of Spontaneous and Sensory-Evoked Activity in Mouse Somatosensory Cortex in Vivo. *Cerebral Cortex*, *27*(12), 5784–5803. <https://doi.org/10.1093/cercor/bhx261>
- Yang, M., Zhou, Z., Zhang, J., Jia, S., Li, T., Guan, J., Liao, X., Leng, B., Lyu, J., Zhang, K., Li, M., Gong, Y., Zhu, Z., Yan, J., Zhou, Y., Liu, J. K., Varga, Z., Konnerth, A., Tang, Y., ... Jia, H. (2019). MATRIEX imaging: multiarea two-

- photon real-time in vivo explorer. *Light: Science & Applications* 2019 8:1, 8(1), 1–11. <https://doi.org/10.1038/s41377-019-0219-x>
- Yang, X., Wei, X., Mu, Y., Li, Q., & Liu, J. (2020). A review of the mechanism of the central analgesic effect of lidocaine. *Medicine*, 99(17), e19898. <https://doi.org/10.1097/MD.00000000000019898>
- Yizhar, O., Fenno, L. E., Davidson, T. J., Mogri, M., & Deisseroth, K. (2011). Optogenetics in Neural Systems. In *Neuron* (Vol. 71, Issue 1, pp. 9–34). <https://doi.org/10.1016/j.neuron.2011.06.004>
- Yona, G., Meitav, N., Kahn, I., & Shoham, S. (2016). Realistic Numerical and Analytical Modeling of Light Scattering in Brain Tissue for Optogenetic Applications. *Eneuro*, 3(1), ENEURO.0059-15.2015. <https://doi.org/10.1523/ENEURO.0059-15.2015>
- Zariwala, H. A., Borghuis, B. G., Hoogland, T. M., Madisen, L., Tian, L., de Zeeuw, C. I., Zeng, H., Looger, L. L., Svoboda, K., & Chen, T. W. (2012). A Cre-dependent GCaMP3 reporter mouse for neuronal imaging in vivo. *The Journal of Neuroscience: The Official Journal of the Society for Neuroscience*, 32(9), 3131–3141. <https://doi.org/10.1523/JNEUROSCI.4469-11.2012>
- Zemelman, B. V., Lee, G. A., Ng, M., & Miesenböck, G. (2002). Selective photostimulation of genetically chARGed neurons. *Neuron*, 33(1), 15–22. [https://doi.org/10.1016/S0896-6273\(01\)00574-8](https://doi.org/10.1016/S0896-6273(01)00574-8)
- Zhang, F., Wang, L. P., Brauner, M., Liewald, J. F., Kay, K., Watzke, N., Wood, P. G., Bamberg, E., Nagel, G., Gottschalk, A., & Deisseroth, K. (2007). Multimodal fast optical interrogation of neural circuitry. *Nature*, 446(7136), 633–639. <https://doi.org/10.1038/nature05744>
- Zhang, W.-T., Chao, T.-H. H., Yang, Y., Wang, T.-W., Lee, S.-H., Oyarzabal, E. A., Zhou, J., Nonneman, R., Pegard, N. C., Zhu, H., Cui, G., & Shih, Y.-Y. I. (2022). Spectral fiber photometry derives hemoglobin concentration changes for accurate measurement of fluorescent sensor activity. *Cell Reports Methods*, 2(7), 100243. <https://doi.org/10.1016/J.CRMETH.2022.100243>
- Zhang, Z., Russell, L. E., Packer, A. M., Gauld, O. M., & Häusser, M. (2018). Closed-loop all-optical interrogation of neural circuits in vivo. *Nature Methods*, 15(12), 1037–1040. <https://doi.org/10.1038/S41592-018-0183-Z>

- Zhang, Z. W., & Deschênes, M. (1997). Intracortical Axonal Projections of Lamina VI Cells of the Primary Somatosensory Cortex in the Rat: A Single-Cell Labeling Study. *Journal of Neuroscience*, *17*(16), 6365–6379. <https://doi.org/10.1523/JNEUROSCI.17-16-06365.1997>
- Zhu, Y., Qiao, W., Liu, K., Zhong, H., & Yao, H. (2015). Control of response reliability by parvalbumin-expressing interneurons in visual cortex. *Nature Communications*, *6*. <https://doi.org/10.1038/ncomms7802>
- Zhu, Y., Stornetta, R. L., & Zhu, J. J. (2004). Chandelier Cells Control Excessive Cortical Excitation: Characteristics of Whisker-Evoked Synaptic Responses of Layer 2/3 Nonpyramidal and Pyramidal Neurons. *Journal of Neuroscience*, *24*(22), 5101–5108. <https://doi.org/10.1523/JNEUROSCI.0544-04.2004>
- Zimmerli, B., & Schlatter, J. (1991). *Ethyl carbamate: analytical methodology, occurrence, formation, biological activity and risk assessment*. *259*(3–4), 325–350. [https://doi.org/10.1016/0165-1218\(91\)90126-7](https://doi.org/10.1016/0165-1218(91)90126-7)
- Zucca, S., D’Urso, G., Pasquale, V., Vecchia, D., Pica, G., Bovetti, S., Moretti, C., Varani, S., Molano-Mazón, M., Chiappalone, M., Panzeri, S., & Fellin, T. (2017). An inhibitory gate for state transition in cortex. *ELife*, *6*. <https://doi.org/10.7554/eLife.26177>
- Zurek, A. A., Yu, J., Wang, D. S., Haffey, S. C., Bridgwater, E. M., Penna, A., Lecker, I., Lei, G., Chang, T., Salter, E. W. R., & Orser, B. A. (2014). Sustained increase in α 5GABAA receptor function impairs memory after anesthesia. *The Journal of Clinical Investigation*, *124*(12), 5437–5441. <https://doi.org/10.1172/JCI76669>

Glossary:

AAV Adeno-associated virus

ACSF Artificial cerebrospinal fluid

A/D Analog/Digital

AM Acetoxymethyl ester

AMPA α -Amino-3-Hydroxy-5-Methyl-4-Isioxazolepropionic Acid

AP Anteroposterior

ArchT archeorhodopsin variant TP009

ATP adenosine triphosphate

BAPTA 1, 2-bis-[2-aminophenoxy]-ethane-N,N,N',N''-tetra-acetic acid
BOLD blood oxygenation level dependent (signal)
Brm Breath per minute
Ca²⁺ Calcium ions
CamKII calmodulin Kinase II
ChR2 Channelrhodopsin-2
CSD Current source density (analysis)
CW Continuous wave
DMSO Dimethyl sulfoxide
DV Dorso-ventral
DVN Deep vibrissal nerve
EcoG Electro corticogram
EEG Electro encephalography
EGTA Ethylene glycol-bis(β -aminoethyl ether)-N,N,N',N'-tetraacetic acid
fMRI Functional magnetic resonance imaging
Fps Frames per second
GABA: Gamma amino butyric acid
GECI Genetically encoded calcium indicator
GFP Green fluorescent protein
GRIN Gradient index (lens)
HDD Hard disk drive
hSyn Human synapsin
LFP Local field potential
LDT latero-dorsal tegmentum
MEA Multi electrode array
MEG Magneto encephalo graphy
MI Primary motor cortex
ML Mediolateral mM
Millimolar
MRI Magnetic resonance imaging
MUA Multi-unit activity
NA Numerical aperture
Na⁺ Sodium ion
NMDA N-Methyl-D-Aspartate

NREM non rapid eye movement
OGB-1 Oregon green BAPTA 1 AM ester
OGB-1 Oregon-Grenn-Bapta-1
PBS Phosphate buffer saline
PBS phosphate buffered saline
PFA Paraformaldehyde
PMT photo-multiplier tube
Pom Postero-medial nucleus of the sensory thalamus
PPT pedunculo pontine tegmentum
PS principal shank
PV: Parvalbumin
REM rapid eye movement
SI, SII primary,secondary sensory cortex SNR
signal to noise ratio
SOM somatostatin
SSD solid state drive
SST somatostatin (immunoreactive neurons)
SVN superficial vibrissal nerve
Vi nucleus interpolaris of the fifth cranial nerve
VIP vaso-intestinal peptide (immunoreactive neurons) VIP: vaso intestinal peptide
Vo nucleus oralis of the fifth cranial nerve
VPm Ventro-Postero-medial nucleus of the sensory thalamus
VTA Ventra tegmental area
 $\Delta f/f$ Fluorescence change

List of figures

Figure 1-1: Whisker field and barrel cortex.

Figure 1-2: Frequency bands in EEG.

Figure 1-3: Membrane potential changes during slow.

Figure 1-4: Overview of the different types of superficial cortical interneurons.

Figure 1-5: Generalized schematic of interneuron connectivity in the mouse cortex.

Figure 1-6: Principle of two-photon excitation compared to classical fluorescence.

Figure 1-7: Schematic of the cavity within a chameleon ultra laser head.

Figure 1-8: Schematic of the mechanism of chirp compensation.

Figure 1-9: Methods of calcium photometry.

Figure 1-10: Overview Sources of calcium entry into the cytoplasm.

Figure 1-11: Molecular mechanisms of Gcamp.

Figure 1-12: OGB-1 Fluorescence correlate of action potentials in a neuron

Figure 1-13: Schematic of the ChR2 photocycle Figure 1-14: Kinetics of ChR2.

Figure 1-15: General photocycle of pump rhodopsins,

Figure 2-1: Simplified methodology for cortical virus injections without using a stereotactic frame.

Figure 2-2: Protocol for the virus injection.

Figure 2-3: Stereotactic positioning of the barrel.

Figure 2-4: Determination of optimal filter settings for elimination of light induced artifacts.

Figure 2-5. Effect of green light pulse illumination on evoked response by single whisker stimulation in non-ArchT expressing control mice.

Figure 2-6: The laser system designed in-house for optogenetic stimulation.

Figure 2-7: General representation of calculating the efficiently excited volume.

Fig 2-8: Basic design of our fiber photometry system.

Figure 3-1. Optical recordings of slow oscillation-associated comparing signal between OGB1, Gcamp6f and LFP.

Figure 3-2: Correlation of simultaneous Ca²⁺ and LFP recordings.

Figure 3-3: Similar signals between sensory and optogenetic stimulation.

Figure 3-4: Neuronal response patterns upon sensory stimulation for slow wave and persistent activity.

Figure 3-5: Cortical optogenetic stimulation did not result in a widespread secondary recruitment of the neuronal network.

Figure 4-1: Experimental setup for combining in vivo multielectrode recordings, optogenetic manipulation and mechanical stimulation of single whiskers in adult mice.

Figure 4-2: Layer and cell type specificity of ArchT expression in mouse barrel cortex.

Figure 4-3: Expression of ChR2.

Figure 4-4: Optogenetic inactivation of PV inhibitory interneurons causes increase in spontaneous neocortical activity.

Figure 4-5: Optogenetic inactivation of PV interneurons causes amplitude and broad spectrum increases in stimulus-evoked cortical responses.

Figure 4-6: Effect of increasing disinhibition duration and influence of different timing of transient disinhibition on sensory-evoked cortical responses.

Figure 4-7: Impact of inhibiting PV interneurons on slow oscillations.

Figure 4-8. Impact of activating PV interneurons on slow oscillations.

Figure 4-9. Optogenetic inactivation of PV interneurons causes a global increase in neocortical responses to single whisker stimulation.

Figure 4-10: Optogenetic activation of PV interneurons lead to global decrease in neocortical responses to single whisker stimulation.

Figure 4-11: Effect of increasing PV-inhibition duration and influence of different timing of transient PV-inhibition on sensory-evoked cortical responses.

Figure 4-12: Optogenetic activation of PV interneurons causes amplitude decreases in stimulus-evoked cortical responses.

Figure 4-13 light propagation in fresh mouse brain tissue at 488nm.

Fig 4-14: Spatial distribution of MUA activity induced by optogenetic activation of PV interneurons.

Figure 4-15: Optogenetic inactivation of a small number of PV interneurons exerts a global increase in neocortical activity.

Figure 5-1: Schematic representations of the in vivo and in vitro setups.

Figure 5-2: Assessing the number of optogenetically inhibited newborn neurons.

Figure 6-1: Intrinsic optical imaging of PRG-1 KO mice.

Figure 6-2: Intrinsic optical imaging identification of whiskers.

Figure 6-3: Single barrel expression of ArchT.

Figure 6-4: General schematic of the Trimscope II.

Figure 6-5: Typical OGB1 staining in the barrel cortex.

Figure 6-6: Recording of spontaneous activity using a galvanometric scanner.

Figure 6-7: Anesthetized recordings upon single whisker deflection.

Figure 6-8: Single cell participation to neuropil signal.

Figure 6-9: Similar patterns of activity in the neuropil signal using OGB1 and GCamp6f.

Figure 6-10: anesthetized recording mouse installation.

Figure 6-11: Head fixation system for awake recordings.

Figure 6-12: Overview of the awake visual stimulation system.

Figure 6-13: Example fluorescent traces of Gcamp fluorescence combined with measurement of mouse velocity.

Figure 6-14: Surface calcium imaging identification of barrels.

Figure 6-15: Whisker evoked activity in the primary identified barrel field.

Figure 6-16: Whisker evoked activity in the neuropil upon whisker deflection in the barrel cortex.

Figure 6-17: Cumulative delay between imaging and stimulation.

Figure 6-18: Visually evoked activity in awake mice submitted to drifting grating stimuli.

Figure 7-1: The influence of the PV-mediated disinhibition on the signal processing of the response evoked by single whisker stimulation.

Figure 8-1. 4-Hz high-pass filtering eliminates light-induced artifacts in spontaneous and evoked LFP activity.

Figure 8-2. Layer representation of Induced slow oscillation during PV inactivation.

Figure 8-3. MUA activity upon optogenetic inhibition of PV interneurons does not differ between cortical layers in the principal shank.

Figure 8-4. Analysis of spike-sorting data to identify putative inhibitory and excitatory neurons.

Acknowledgments

I am extremely grateful to all these people:

- Prof. Dr. [REDACTED] for supporting me during my stay in his lab in the University of Mainz and during the following years. Providing outstanding and continuous guidance and training over these formative years.
- Prof. Dr. [REDACTED] for very nicely accepting to be my thesis supervisor and for his patience in between versions.
- Prof. Dr. [REDACTED] for providing me with an intermediary position while I finished writing and for introducing me to the fascinating field of sleep research.

- Dr. [REDACTED] for the invaluable teachings on rodent surgery, electrophysiology and general experimental science. I would have not succeeded in half this work without his collaboration.
- My colleagues from [REDACTED] for all our conversations, the happy ones, the fruitful work ones and even the bad ones. I learned much more than I realized all those years with you. Thank you for the fruitful discussions. I particularly would like to thank [REDACTED] for tolerating me early on and being an incredible friend and support all these years. [REDACTED] for her help, the fruitful collaborations and for still helping me even years later. [REDACTED] for the analysis support and for staying true to his principles in the face of conflict. [REDACTED] for, after a rocky start being an amazing friend you can count on and an extremely helpful colleague. [REDACTED] for the long repetitions of difficult experiments that bore fruits in the end. [REDACTED] for his patience with me and all the technical support he provided. [REDACTED] for the moral support. Finally, all my other colleagues for the great work environment [REDACTED]
[REDACTED]
[REDACTED] for the help with immunostainings.
- Prof. [REDACTED] for the excellent early collaboration.
- Prof. Dr. [REDACTED] for the fruitful collaboration and the motivation for excellence.
- Our workshop team [REDACTED] for creating lots of incredibly functional tools from our simple drawings and discussions.
- The Institute of Microscopy, Anatomy and Neurobiology of the Universitätsmedizin Mainz and Prof. Dr. [REDACTED].
- The FTN, Universitätsmedizin Mainz and the DFG for Funding.
- Dr. [REDACTED] for the encouragement, the advice and correcting my English.
- Dr. [REDACTED] for all the encouragement and the invaluable help navigating the administration I couldn't have done it without you.
- My Family, they provided me with the opportunity to study what I love and for the crucial support during the final push.
- Maeve Kerdraon-Byrne for everything but especially supporting me through the hard times and helping me take a step back to do something else before I completely crashed. Thank you for everything, you make everything so much better.

Copyright agreements

All figures from J.-W. Yang et al., 2017 by permission with Oxford university press license
number: 5644830858568

All figures from J. W. Yang, Prouvot, et al., 2018 reproduced with permission from Springer
Nature

Figure from Grienberger & Konnerth, 2012) reproduced with permission from Elsevier License
number 5546520701816

Figure from Woolsey & Van der Loos, 1970 reproduced with permission from Elsevier License
number5644810033680

Figure from almivuo & Plonsey, 1995) Reproduced with permission of the Licensor through
PLSclearCopyright Oxford Publishing limited PLSclear Ref No: 82047

Figure from Adelsberger et al., 2014 photometry Reproduced with permission from Cold Spring
harbor Laboratory press

All other published figures are under creative commons licenses

Collaborative figures are with agreement of the co-authors.

Pierre-Hugues Prouvot
Prouvot.pierrehugues@gmail.com
10, rue des jardins 1018 Lausanne +41762214381
Born 12/07/1989
Doctoral dissertation pending
Languages: French (Native), German, English, Japanese(N3)



Professional experience:

Research assistant with [REDACTED], Université de Lausanne, DSB 2021-2022

Systematic optical dissection of Pontine cholinergic regulation of REM sleep circuitry.

- Electro-encephalography and fiber photometry in freely moving rodents
- Sleep stage classification

Cleaning and maintenance Cabosu House Hotel Beppu, Kyushu, Japan 2019-2020

Service cooking, Kayak guide Sakazuki Terrace, Tomari, Hokkaido Japan Juin-septembre 2019

Electrophysiology consultant January-Mai 2019

JGU Mainz - Universitetshospital Aarhus - ZAP surgical

Testing and redesign of a prototype untethered, integrated MEA and stimulation probe in Göttingen Minipigs. Use of the probe in the context of the evaluation of low level radiation induced damage using a gamma knife.

- Project planning, team coordination and prototyping
- Anesthetized recordings in Göttingen minipigs

Dr. rer. nat. under Prof. Dr. [REDACTED] Johannes Gutenberg university Mainz 2012-2018

Studying the lateral extent of Parvalbumin interneurons inhibition in the mouse barrel cortex using a combination of two-photon calcium imaging, optogenetics and electrophysiology.

- Two-photon calcium imaging and fiber photometry in anesthetized and headfixed rodents
- Microscope prototype testing and maintenance
- MUA et LFP recordings *in vivo*

- Data analysis (spike2, Igor pro, Matlab, Graphpad prism)

Master's dissertation under Dr. [REDACTED]

October-July 2012

Combination of Calcium imaging with optogenetics in brain slices to study the influence of molecular layer parvalbumin interneurons on purkinje cells in the rodent cerebellum. (CNRS UMR 8118 Paris Descartes director: Prof. Dr. [REDACTED])

- Patch-Clamp *ex vivo*
- Rodent colony maintenance
- Optical physiology: optogenetics and calcium imaging
- Adenovirus CNS injections

Internship under Prof. Dr. [REDACTED]

April-Mai 2011

Imaging of mitochondrial Membrane potential dynamics in an in vitro model of Alzheimer's disease (CNRS UMR 8250 Paris Descartes Director: Prof. Dr. [REDACTED])

Internship under Dr. Cécile Jeanpierre

June-July 2010

Sequencing of EYA-1 Variants in a cohort of Patients with branchio-oto-renal syndrome (Inserm UMR 983 Necker Hospital directrice: Prof. Dr. med. [REDACTED]) Méthodes acquises:

- Genotyping of human and animal samples
- Sequencing

Secondary professional experience:

Tutor for biochemistry and cell biology L1-L3 2009-2012

Creation and organization of a tutoring system between master's and bachelor's degree students financed by the faculty (with Amicale Paris Sciences)

Master's and phd student representative at the biomedical faculty council 2010-2012 FELASA B certification

Publication record:

1: Yang JW*, Prouvot PH*, Reyes-Puerta V, Stüttgen MC, Stroh A, Luhmann HJ.

Optogenetic Modulation of a Minor Fraction of Parvalbumin-Positive Interneurons Specifically Affects Spatiotemporal Dynamics of Spontaneous and Sensory-Evoked

Activity in Mouse Somatosensory Cortex in Vivo. Cereb Cortex. 2017 Dec

1;27(12):5784-5803. doi: 10.1093/cercor/bhx261. PubMed PMID: 29040472; PubMed Central PMCID: PMC5939210. (*equally contributing authors)

2: Schwalm M*, Schmid F*, Wachsmuth L, Backhaus H, Kronfeld A, Aedo Jury F, **Prouvot PH**, Fois C, Albers F, van Alst T, Faber C, Stroh A. **Cortex-wide BOLD fMRI activity reflects locally-recorded slow oscillation-associated calcium waves.** 238

Elife. 2017 Sep 15;6. pii: e27602. doi: 10.7554/eLife.27602. PubMed PMID: 28914607; PubMed Central PMCID: PMC5658067. (*equally contributing authors)

3: Schmid F, Wachsmuth L, Schwalm M, **Prouvot PH**, Jubal ER, Fois C, Pramanik G, Zimmer C, Faber C, Stroh A. **Assessing sensory versus optogenetic network activation by combining (o)fMRI with optical Ca²⁺ recordings.** J Cereb Blood Flow Metab. 2016 Nov;36(11):1885-1900. Epub 2015 Nov 30. PubMed PMID: 26661247; PubMed Central PMCID: PMC5094300.

4: Cheng J, Sahani S, Hausrat TJ, Yang JW, Ji H, Schmarowski N, Endle H, Liu X, Li Y, Böttche R, Radyushkin K, Maric HM, Hoerder-Suabedissen A, Molnár Z, **Prouvot PH**, Trimbuch T, Ninnemann O, Huai J, Fan W, Visentin B, Sabbadini R, Strømgaard K, Stroh A, Luhmann HJ, Kneussel M, Nitsch R, Vogt J. **Precise Somatotopic Thalamocortical Axon Guidance Depends on LPA-Mediated PRG-2/Radixin Signaling.** Neuron. 2016 Oct 5;92(1):126-142. doi: 10.1016/j.neuron.2016.08.035. Epub 2016 Sep 15. PubMed PMID: 27641493; PubMed Central PMCID: PMC5065528.

5: Zaer H, Deshmukh A, Orłowski D, Fan W, **Prouvot PH**, Glud AN, Jensen MB, Worm ES, Lukacova S, Mikkelsen TW, Fitting LM, Adler JR Jr, Schneider MB, Jensen MS, Fu Q, Go V, Morizio J, Sørensen JCH, Stroh A. **An Intracortical Implantable Brain-Computer Interface for Telemetric Real-Time Recording and Manipulation of Neuronal Circuits for Closed-Loop Intervention.** Front Hum Neurosci. 2021 Feb 3;15:618626. doi: 10.3389/fnhum.2021.618626. PMID: 33613212; PMCID: PMC7887289.

6: Kur IM, **Prouvot PH**, Fu T, Fan W, Müller-Braun F, Das A, Das S, Deller T, Roeper J, Stroh A, Momma S. **Neuronal activity triggers uptake of hematopoietic extracellular vesicles in vivo.** PLoS Biol. 2020 Mar 16;18(3):e3000643. doi: 10.1371/journal.pbio.3000643. PMID: 32176686; PMCID: PMC7075544.

Methodological chapters:

1: Yang JW*, **Prouvot PH***, Stroh A, Luhmann HJ. **Combining Optogenetics with MEA, Depth-Resolved LFPs and Assessing the Scope of Optogenetic Network Modulation** Springer Neuromethods Optogenetics: a roadmap 2018 ISBN 978-4-4939-7417-7 (*equally contributing authors)

2: Fois C, **Prouvot PH**, Stroh A. **A roadmap to applying optogenetics in neuroscience.** Methods Mol Biol. 2014;1148:129-47. doi: 10.1007/978-1-4939-0470-9_9. PubMed PMID: 24718799.